DOCTOR OF SCIENCES

Study of germanium diffusion and nanoclustering in Si-based host matrices for optoelectronic applications such as photovoltaic cells

Nelis, Adrien

Award date:
2021

Awarding institution:
University of Namur

University of Namur – Faculty of Sciences

Namur Institute of Structured matter (NISM)

Study of germanium diffusion and nanoclustering in Si-based host matrices for optoelectronic applications such as third generation photovoltaic cells

Dissertation presented by
Nélis Adrien
for the degree of doctor of sciences

Jury members:

Prof. Guy TERWAGNE (Supervisor)
Laboratoire d'Analyse par Réactions Nucléaires (LARN - NISM)
UNamur, Namur, Belgium

Dr. Ian VICKRIDGE
Institut des nanosciences de Paris (INSP)
Sorbonne Université
Paris, France

Prof. Olivier DEPARIS
Laboratoire de Physique du Solide (LPS – NISM)
UNamur, Namur, Belgium

Prof. François SCHIETTEKATTE
Regroupement Québécois sur les Matériaux de Pointe (RQMP)
UdeM, Montréal, Canada

Prof. Denis FLANDRE
Institute of Information and Communication Technologies – Electronics and Applied Mathematics
UCL, Louvain-la-Neuve, Belgium

Prof. Robert SPORKEN (Chairman)
Laboratoire Interdisciplinaire de Spectroscopie Electronique (LISE/LPME - NISM)
UNamur, Namur, Belgium

UNamur - 2021

Study of germanium diffusion and nanoclustering in Si-based host matrices for optoelectronic applications such as third generation photovoltaic cells

Abstract

The development of modern optoelectronic devices undoubtedly involves the study of the properties of materials at the nanoscale. In this context, the association of germanium and silicon nanocrystals, or quantum dots, incorporated in a dielectric film, offers new possibilities thanks to manifold attractive optoelectronic properties. This is particularly the case in the field of photovoltaics, which will be taken as an example throughout this manuscript. Quantum confinement, multiple exciton generation (MEG) or tunable bandgap are all properties associated with quantum dots that can make it possible to exceed the theoretical conversion limit of Shockley-Queisser calculated for a single-junction cell (~33%) (1), to achieve theoretical efficiencies up to 66% in the most ideal case (2).

Among the armada of experimental techniques available to form semiconductor quantum dots, we opted in this work for ion implantation followed by thermal treatment in an inert atmosphere. The implantations were mainly carried out using the ALTAÏS particles accelerator available at LARN laboratory. This technique enables a great flexibility in the formation of nanocrystals via experimental parameters such as the energy or fluence of the ion beam.

This purely experimental thesis aims to propose solutions to precisely control the formation of germanium nanocrystals (location, size, distribution) in SiO_2/Si films. The results presented in this thesis are based on the characterization of thin films via the combination of several analysis techniques, ranging from ion beam analysis to optical spectroscopies, including electronic microscopy. In particular, it has been shown that it was possible to completely annihilate the diffusion of germanium, occurring during post-implantation annealing, by judiciously generating a local excess of silicon by co-implantation, the particular affinity of germanium with silicon playing a preponderant role in the trapping effects highlighted in this thesis. It has been demonstrated that this singular relation between Ge and Si could allow controlling the position and the size distribution of the Ge nanocrystals (Ge-ncs) through the dielectric layer. For photovoltaic applications, the idea is to form a size gradient, ranging from 0.6 to 4-5 nm, to optimize absorption over almost the entire solar spectrum. The mechanisms responsible for the diffusion of germanium have also been brought to light, with special attention to the involvement of oxygen in the redistribution of germanium atoms during thermal treatments.

The possibility of forming $Si_{1-x}Ge_x$ crystalline alloys by Ge implantation in silicon substrates has also been investigated. As expected from results obtained in SiO_2 films and due to the miscibility of Ge in silicon, it is shown that these implantations do not give rise to the formation of Ge nanocrystals in c-Si, nevertheless with a glimmer of hope when the sample is heated during the implantation.

Étude de la diffusion du germanium et de la formation de nanocristaux dans des matrices hôtes à base de silicium pour des applications optoélectroniques telles que les cellules photovoltaïques de troisième génération

Résumé

Le développement des dispositifs opto-électroniques modernes passe indéniablement par l'étude des propriétés des matériaux à l'échelle nanométrique. Dans ce contexte, l'association de nanocristaux – ou boites quantiques - de germanium et silicium, incorporés dans une couche diélectrique, offre de nouvelles possibilités grâce aux nombreuses propriétés opto-électroniques qui leur sont associées. C'est particulièrement le cas dans le domaine du photovoltaïque, qui sera pris en exemple tout au long de ce manuscrit. Confinement quantique, génération d'excitons multiples (MEG) ou encore bande interdite modulable sont autant de propriétés associées aux boites quantiques pouvant permettre de dépasser la limite théorique de conversion de Shockley-Queisser pour une cellule simple jonction (~33%) (1), pour atteindre des rendements théoriques de plus de 66% dans le cas d'une configuration idéale (2).

Parmi l'armada de techniques expérimentales disponibles pour former des nanocristaux semiconducteurs, nous avons opté dans ce travail pour l'implantation ionique suivie d'un traitement thermique sous atmosphère inerte. Les implantations ont été principalement réalisées grâce à l'accélérateur de particules ALTAÏS dont dispose le LARN. Cette technique permet une grande flexibilité au niveau de la formation des nanocristaux via des paramètres expérimentaux tels que l'énergie ou la fluence des ions implantés.

Cette thèse purement expérimentale a pour but de proposer des solutions pour contrôler avec précision la formation des nanocristaux de germanium (localisation, taille, distribution) dans des couches SiO_2/Si. Les résultats présentés dans cette thèse sont basés sur la caractérisation de couches minces via la combinaison de nombreuses techniques d'analyse, allant de l'analyse par faisceaux d'ions à l'analyse par spectroscopie optique, en passant par de la microscopie électronique. Il a notamment été démontré qu'il était possible d'annihiler complètement la diffusion du germanium, se produisant lors des traitements thermiques post-implantation, en générant de manière judicieuse un excès local de silicium par co-implantation, l'affinité du germanium avec le silicium jouant un rôle prépondérant dans les effets de piégeage mis en évidence dans cette thèse. Il a été démontré que cette relation singulière entre Ge et Si pouvait permettre de contrôler la position et la distribution de taille des nanocristaux de Ge (Ge-ncs) à travers la couche diélectrique. Pour les applications photovoltaïques, un gradient de taille doit être formé. Celui-ci doit s'étaler de 0.6 à 4-5 nm pour optimiser l'absorption sur presque l'entièreté du spectre solaire. Les mécanismes responsables de la diffusion du germanium ont également été mis en lumière, avec une attention toute particulière pour l'implication de l'oxygène dans la redistribution des atomes de germanium observée lors des traitements thermiques.

La possibilité de former des alliages cristallins $Si_{1-x}Ge_x$ par implantation de germanium dans des substrats de silicium a également été investiguée. En accord avec les résultats obtenus dans les couches SiO_2 et du fait de la miscibilité du germanium dans le silicium, il a été démontré que ce type d'implantation ne donnait pas lieu à la formation de nanocristaux de Ge, avec cependant une lueur d'espoir lorsque l'échantillon est chauffé lors de l'implantation.

Remerciements

Après un peu plus de 6 ans, voici venu le temps de clôturer ce beau chapitre qu'aura représenté cette thèse. Une thèse qui n'aurait pas été aussi fructueuse et épanouissante, autant d'un point de vue scientifique qu'humain, sans la contribution d'un grand nombre de personnes que je tiens à remercier avec ces quelques lignes.

En premier lieu, j'aimerais remercier mon promoteur, Guy, pour la confiance qu'il m'a accordée toutes ces années (mémoire + doctorat !) au cours desquelles il a su m'accompagner. Cette thèse n'aurait littéralement pas eu lieu s'il n'avait pas cru en moi lors de ma recherche de financement. Merci pour la liberté scientifique que tu m'as accordée avec toujours un œil avisé sur mes manips. Merci également pour les bons souvenirs engrangés en conférence, je retiens particulièrement la conférence IBA à Shanghai, ainsi que pour les discussions scientifiques et footballistiques que nous avons pu partager.

Je tiens à remercier tous les membres de mon jury pour leur relecture attentive de mon manuscrit et leurs commentaires pertinents et constructifs visant à améliorer ce travail, ainsi que la discussion scientifique lors de la défense privée.

Je pense que l'environnement de travail joue un rôle important sur la qualité du travail réalisé et sur la motivation à le mener à bien au quotidien. Je n'aurais pas pu imaginer meilleur entourage que l'équipe du LARN pour réaliser cette thèse. J'ai une pensée et un souvenir particuliers avec chacun d'entre vous, que ce soit lors de nos week-ends LARN, les verres après boulot, les pauses café de 10h30 … voire 16h00, ce nombre incalculable de tartes partagées, … Un grand merci à chacun d'entre vous, actuels et anciens.

Merci à mes collègues extraterritoriaux avec qui j'ai eu l'opportunité de collaborer. Je pense en premier lieu à David Barba pour toute l'expertise qu'il a apportée à la première partie de ce travail, notamment concernant les résultats qui ont menés à l'écriture des deux premiers articles publiés dans le cadre de cette thèse. Merci à l'équipe SAFIR (Ian, Jean-Jacques, Emrick, Sébastien, Hervé, Isabelle) pour leur magnifique accueil et le travail fourni lors de mon séjour de quelques mois à Paris. Toute ma gratitude également à François et Martin pour leur contribution à ce travail et pour leur chaleureux accueil lors de mon passage à Montréal, ainsi qu'à Jean-Philippe Masse pour les résultats TEM.

Je remercie la plateforme Welcome, de l'UCL, de m'avoir permis de réaliser la plupart des mesures par spectroscopie Raman présentées dans ce manuscrit.

Merci à tous mes collègues du département de physique et à l'équipe des assistants. Merci aussi à Fernande Frising et Laurent Zanotto pour leur aide et leur encadrement durant ces six années d'assistanat.

J'ai une pensée particulière pour Louis, Cécé, Romain, Lucas et Damien avec qui j'ai commencé mes études il y a déjà 13 ans ! Merci pour votre amitié tout au long de ces années et celles à venir. Dans la même lignée, comment ne pas citer mon binôme (je te pique l'expression), Polo, sans qui cette thèse n'aurait pas été aussi agréable. Merci pour tous ces bons moments, pour ton amitié précieuse et pour ces (très) nombreuses soirées. Nous avons

pendant longtemps formé la fameuse « équipe de Guy » avant que Coco ne vienne gonfler nos rangs !

Je remercie également Félicien pour ces belles années partagées d'abord dans les auditoires de l'UNamur, dans le paysager du LARN ensuite.

Merci également à Emile pour son aide et ses conseils, ainsi que pour les mesures XPS qu'il a réalisées pour cette thèse.

Un grand merci à Julien Colaux pour son aide tout au long de cette thèse, pour ces moments partagés en conférence et pour sa relecture extrêmement pertinente et pointue de ce manuscrit qui a grandement contribué à son amélioration.

Merci à Tija, dont la porte est toujours ouverte, pour son apport dans ce travail expérimental, ainsi qu'à Sébastien pour tous les moments partagés au labo, à la coloc' ou simplement autour d'un « p'tit godet ». Merci à vous deux pour toutes ces discussions autres que scientifiques que nous avons pu partager et pour ces kilos de sushis engloutis avec le Dr D.

Merci à la « team jeudredis », dont Hélo, Marie, Bru, Rémy ou encore Boulbi qui n'ont pas encore été cités, pour ces soirées passées à écumer les bars de Namur.

J'ai également une pensée pour Richard et son chat au nom si bien choisi !

Merci à ma famille pour leur soutien et pour l'admiration qu'ils m'ont toujours inspiré.

Enfin, je tiens à remercier Mathilde pour son soutien tout au long de ce travail et surtout lors de ces derniers mois de thèse. Je n'ai pas toujours été le plus facile à vivre lors de ces mois de rédaction mais tu as su me soutenir et me supporter. Merci pour ton apport lors de la relecture de ce manuscrit et lors des répétitions avant la défense privée.

Table of content

List of figures

List of tables

List of publications

1. **Nélis A.**, Haye E., Terwagne G.
   "Influence of oxygen co-implantation on germanium out-diffusion and nanoclustering"
   Under review in Thin Solid films (submitted 06/07/2021)
   (Referred as **article I** in this manuscript)

2. **Nélis A.**, Vickridge I., Ganem J-J., Briand E., Terwagne G.
   "$^{18}O(p,\alpha)^{15}N$ isotopic tracing of germanium diffusion in SiO_2/Si films"
   Journal of Applied Physics **130** (2021) 105701
   DOI: 10.1063/5.0057968
   (Referred as **article II** in this manuscript)

3. **Nélis A.**, Barba D., Terwagne G.
   "Control of germanium diffusion using low quantities of co-implanted silicon isotopes"
   Journal of Applied Physics **128** (2020) 125705
   DOI: 10.1063/5.0020368
   (Referred as **article III** in this manuscript)

4. Barba D., Wang C., **Nélis A.**, Terwagne G., Rosei F.
   "Blocking germanium diffusion inside silicon dioxide using a co-implanted silicon barrier"
   Journal of Applied Physics **123** (2018) 161540
   DOI: 10.1063/1.5002693
   (Referred as **article IV** in this manuscript)

Chapter I

General introduction

In a modern world increasingly greedy for energy, fossil fuels (coal, gas, oil), which are currently the main sources of energy and CO_2 emissions, tend to run out in the medium term. Although these natural resources are, for now, essential for the operating and development of our society, they must gradually make room for other sources of renewable and ecologically equitable energies. It is with this in mind that technologies have been developed in recent decades to improve the use of solar, wind, geothermal, biomass or hydroelectric energies. However, there is still a long way to go before renewable energies can start to compete with fossil fuels. As shown in **Figure 1**, the annual worldwilde production of renewable energy represents only about 10% of the total production of primary energy.

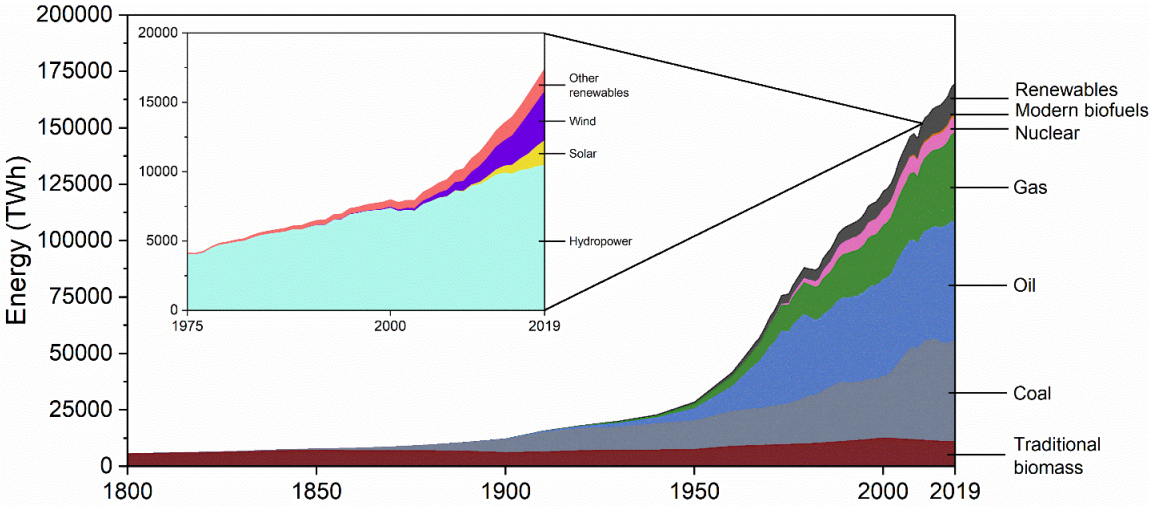

Figure 1 **:** Worldwide production of primary energy in TWh/year with the contributions of the different sources of energy. Insert: annual worldwide production of renewable energy since 1975. Graph produced from data published in *"Our world in data" (3)*.

Among the promising candidates, research has focused in recent years on the use of solar energy. The sun is an inexhaustible source of energy on a human scale that must be harnessed to the best advantage by continuously improving its conversion into an usable energy form. Basic solar collectors generally take advantage of semiconductor materials to convert this energy into electricity.

In a report published in October 2019 (4), the International Energy Agency (IEA) forecasts a growth of 50% in renewable energy production capacity between 2019 and 2024. In these forecasts, photovoltaic represents 60% of this increase, wind power 25%, the rest being shared by other renewable energy sources.

This thesis starts with the presentation of the main factors limiting the effectiveness of photovoltaic (PV) cells and the conversion efficiencies reached by the main technologies, currently dominated by the multi-junction cells. Quantum dots PV cells, part of the so-called "third generation" of solar cells, are developed in more details. It is discussed how their original optoelectronic properties enable to overcome the conversion limit calculated by Shockley and Queisser.

This thesis ensures the continuity of the work carried out as a part of an international collaboration between LARN (G. Terwagne, J. Demarche, M. Yedji) and INRS (G.G. Ross, D. Barba) labs. The original goal of this collaboration was to study the formation of silicon

quantum dots in fused silica matrices by ion implantation. After having demonstrated the relevance of ion implantation for the fabrication of semiconductor quantum dots, the formation of Si quantum dots has been characterized as well as their properties of photoluminescence and ionoluminescence (5). In a second time, the idea of forming Ge quantum dots in silica matrices has been developed because of their most promising properties of quantum confinement and light interaction that are discussed in **chapter II** of this manuscript. This thesis continues the work undertaken on the formation of Ge quantum dots in SiO_2 films by ion implantation, explaining the asymmetric redistribution of Ge during annealing and proposing solutions to control Ge diffusion and nanoclustering.

Chapter II presents several methods commonly used for the fabrication of quantum dots, such as plasma deposition, laser ablation or ion implantation. The latter is discussed further in the third chapter of this manuscript. ALTAÏS[1] accelerator, available at LARN, has been used to carry out the majority of the implantations studied in this thesis. The different methods used to characterize our samples are described in the same chapter (**III**), among which ion beam analyses (IBA), Raman spectroscopy or X-rays photoelectron spectroscopy (XPS). These techniques allowed the study and description of the mechanisms involved in the formation of Ge quantum dots, such as the Ge diffusion taking place during the post-implantation annealing, and the direct visualization of the quantum dots by electronic microscope imaging.

The implantation systems are presented in **chapter III**, while the main results obtained during this PhD thesis are presented in **chapters IV** and **V**, principally under the form of articles published in scientific journals. The results are divided in two major parts:

1. The study of the accurate control of the formation of germanium quantum dots in SiO_2 films (**chapter IV**). Firstly, the mechanisms of germanium diffusion are investigated, notably the influences of irradiation-induced damage and the presence of oxygen in both the annealing atmosphere and the SiO_2 matrix.
   Then, solutions are provided to control this diffusion until its complete annihilation, thanks to the particular affinity of germanium and silicon. This is also demonstrated that the size distribution of the quantum dots can be controlled by Si co-implantation.
   This part was realized in collaboration with INRS.

2. In a second time, the possibility of forming crystalline $Si_{1-x}Ge_x$ top layers by Ge implantation in crystalline silicon is explored (**chapter V**). These preliminary results aim to better define the experimental conditions for future works, showing the possibility of forming such layers by ion implantation.
   Implantations under extreme conditions has also been performed to probe the possibility of forming Ge quantum dots in c-Si.
   This was realized in collaboration with the University of Montréal.

The final chapter of this manuscript presents the conclusions and perspectives.

[1] Accélérateur Linéaire Tandetron pour l'Analyse et l'Implantation des Solides.

Chapter II

State of the art

II.1 Solar spectrum and power

The sun, whose external temperature is about 5778 K, radiates as a black body. The spectral irradiance, at a fixed temperature T, is derived from Planck's equation:

$$L_\lambda = \frac{2hc^2}{\lambda^5} \frac{1}{e^{(hc/\lambda k_B T)} - 1} \qquad (II.1)$$

and corresponds to the power supplied per unit area and wavelength λ by a black body. h, c and k_B are the Planck's constant (6.63 × 10^{-34} m²kg/s), the light velocity in vacuum (~3 × 10^8 m/s) and the Boltzmann's constant (1.38 × 10^{-23} m²kg/s²/K) respectively.

The solar power received by one square meter in the Earth's atmosphere is approximately 1.4 × 10^3 W/m². The attenuation due to light absorption or diffusion in the atmosphere reduces the solar power to ~1 kW/m² at sea level, in AM1.5[2] and total sunshine conditions. Averaged over a full year, taking into account the day/night balance and the seasons, the daily solar power is at best 250 – 300 W/m² at the equator (6). In Belgium, the annual sunshine is ~1000 kWh/m². If we consider the city of Bruxelles, for which all the roofs would be covered with 100% efficient solar panels (representing 48% of the total surface of Bruxelles, *i.e.* ~78 km²), this represents 78 × 10^9 kWh per year. Taking as a reference the average annual consumption of a Belgian two-person household, this could supply about 33 × 10^6 homes a year.

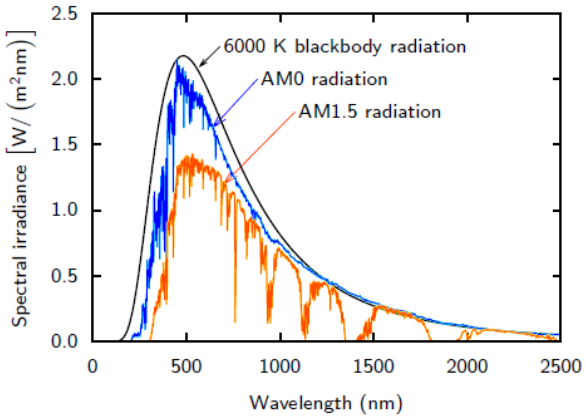

Figure 2 **:** Spectrum of solar irradiance outside the Earth's atmosphere (AM0), at Earth's surface after the crossing of 1.5 atmosphere (AM1.5) and for a perfect black body at 6000 K (black curve) *(7)*.

The wavelength of the maximum of emission of a black body is given by Wien's law ($\lambda_{max} T = 2.898\, x10^{-3}\, m\, K$), which predicts a maximum in the visible range for a temperature of about 6000 K (**Figure 2**). As the solar spectrum is not flat, one has to find a material (or a combination of materials) enabling efficient absorption of solar energy over a wide range of wavelengths.

[2] Air Mass coefficient: $AM \approx \frac{1}{cos\varphi}$, where φ is the zenith angle. AM1.5 corresponds to an angle of ~48.2°, while AM0 means no air between the source and the receiver.

II.2 Silicon and germanium, basic materials for photovoltaic cells

Photovoltaic cells are based on the generation of charge carriers (electron-hole pairs) in materials, such as semiconductors, through the absorption of photons. Semiconductors can be defined as intermediate elements between insulators and conductors, characterized by a relatively low forbidden energy band between the valence and the conduction bands (**Figure 3**). The production of an electric current by the absorption of photons is called the *photovoltaic effect*: a photon is annihilated and all its energy is transferred to an electron in the valence band (VB) to promote it to the conduction band (CB), leaving a hole in the valence band. The forbidden band, also called bandgap, characterizes the lowest amount of energy (E_g) required to promote an electron in the CB. If the photogenerated charges (electrons and holes) are efficiently separated by a *pn junction*, and if the device is integrated in an electric circuit, the photogenerated electron-hole pair can thus contribute to the generation of an electric current and a constant voltage.

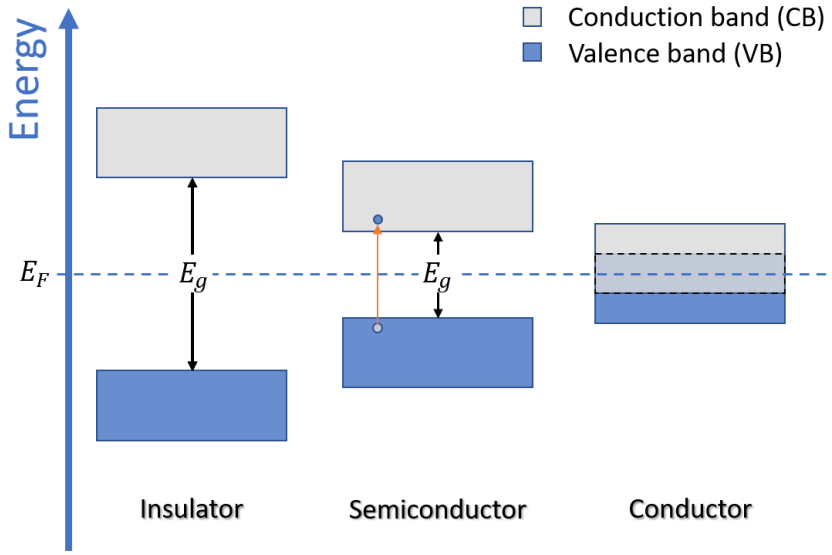

Figure 3 **:** Band diagram of an insulator, a semiconductor and a conductor at 25°C. E_F represents the Fermi level. The intermediate bandgap energy (E_g) of semiconductors enables promotion of electrons in the CB from the VB, letting a hole in the VB, when an energy higher than E_g is transferred to the electron.

Silicon (Si), the second most abundant element in the Earth's crust, is the most widely used semiconductor material in industry. In addition to photovoltaics, its applications are multiple and range from electronics to nano-electronics, including various electro-optic devices such as photo-detectors or light emitting diodes, memory devices, etc. (8)

Material	μ_e [$cm^2V^{-1}s^{-1}$]	μ_h [$cm^2V^{-1}s^{-1}$]	T_{fusion} [°C]
Si	1500	450	1414
Ge	3900	1900	937

Table 1 : Electrons (μ_e) and holes (μ_h) mobilities in intrinsic silicon and germanium at 300K *(9)*, along with their melting points (T_{fusion}).

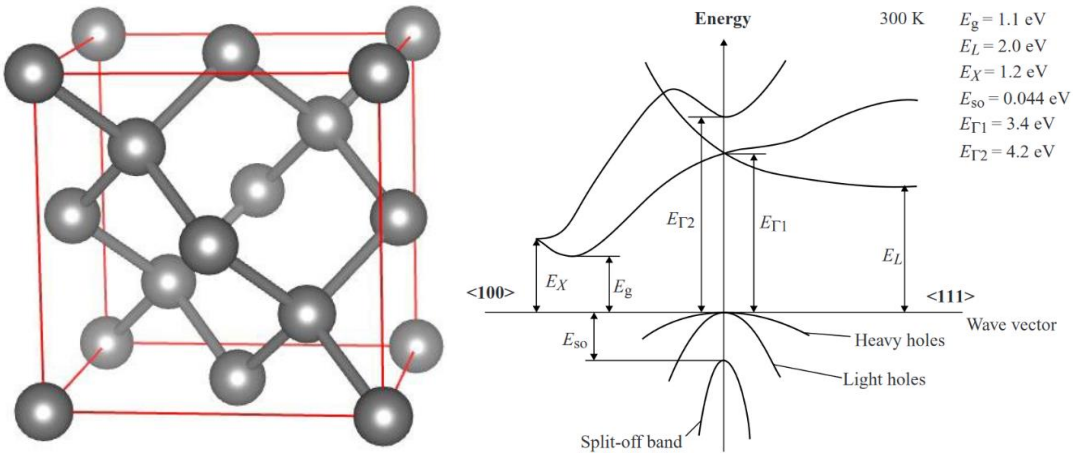

Figure 4 **:** Crystal unit cell of the diamond structure *(10)* and band structure of silicon *(11)*.

Silicon is an indirect bandgap semiconductor: the maximum of its valence band does not match with the minimum of its conduction band (**Figure 4, right**). This means that most of electronic transitions across the bandgap must be phonon-assisted to respect momentum and energy conservation, limiting the effectiveness of radiative recombinations. Silicon has an atomic structure of cubic diamond type (**Figure 4, left**), whose lattice parameter is $a_{Si} =$ 0.5431 nm. The width of the forbidden band of silicon is $E_g = 1.12$ eV ($\lambda_g \approx 1107$ nm) at 300 K, with a first direct transition at 3.4 eV ($\lambda \approx 365$ nm).

Germanium (Ge), a close neighbor of silicon in the periodic table of elements, belongs to the same family: type IV semiconductors. They have the same atomic structure, with a lattice parameter that differs by 4.2% ($a_{Ge} = 0.5658$ nm): $f = (a_{Ge} - a_{Si})/a_{Si} \cong 0.042$. Such as silicon, germanium (**Figure 5, right**) has a relatively low indirect bandgap of $E_g = 0.66$ eV ($\lambda_g \approx 1878$ nm) at 300 K but its first direct bandgap appears at significantly lower energy (0.8 eV, $\lambda \approx 1550$ nm) than silicon (3.4 eV, $\lambda \approx 365$ nm).

As semiconductors are able to absorb photons with energies (wavelengths) higher (lower) than E_g (λ_g), germanium can therefore absorb a wider range of photon energies (wavelengths) from the solar spectrum. However, as discussed in the next section, a wide absorption range does not necessarily mean a high conversion efficiency.

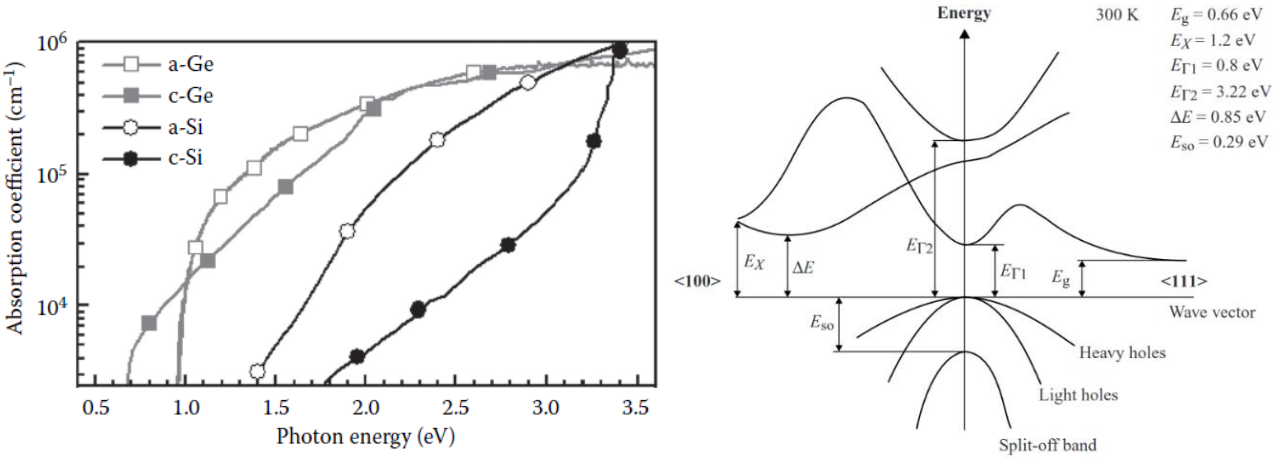

Figure 5 : Absorption coefficient of Si and Ge, in their crystalline or amorphous form, as a function of photons energy *(12)* and band structure of germanium *(11)*.

Germanium has other advantages compared to silicon, as it has higher electrons and holes mobilities (**Table 1**) and a better absorption coefficient in the visible range (1.7 - 3.1 eV; see **Figure 5, left**). Germanium also has a melting point lower than that of silicon (**Table 1**) and a larger dielectric constant (16.2 for Ge and 11.9 for Si), which are two properties that will be interesting while considering the formation and applications of quantum dots (see **section II.5**).

Despite their different lattice constant, Si and Ge are miscible, forming $Si_{1-x}Ge_x$ alloys, whose Ge composition *x* allows the modulation of physical properties from pure silicon to germanium. **Chapter V** of this manuscript is dedicated to the formation of such alloys by Ge implantations in crystalline silicon, and to the study of their crystallinity and state of strain after annealing at high temperature. The $Si_{1-x}Ge_x$ alloy has many applications (solar cells, thermoelectric converters, photo-detectors, etc.) thanks to the numerous electrical, thermal and structural properties resulting from this alloy. Modifying the composition of the alloy will change its bandgap, conductivity, charge carriers mobility or lattice constant. The latter almost follows a Vegard's law (13):

$$a_{SiGe}(x) = a_{Si} + (a_{Ge} - a_{Si})x \qquad \text{(II. 2)}$$

but is better described by Dismukes law (14) (in angstroms):

$$a_{SiGe}(x) = 0.0263x^2 + 0.2005x + 5.43105 \qquad \text{(II. 3)}$$

Due to this lattice constant misfit, $Si_{1-x}Ge_x$ layers formed on top of silicon substrates could be either strained or relaxed, depending on the film thickness and fabrication process. The substrate is assumed to be unstrained as its thickness is much greater than the thickness of the film. Below a critical thickness t_c, the $Si_{1-x}Ge_x$ film is elastically strained and the epilayer is called pseudomorphic. The parallel ($\varepsilon_{//}$) and perpendicular ($\varepsilon_{\perp}$) strains are calculated as a function of the unstrained lattice constant of the epilayer, a_{SiGe}:

$$\varepsilon_{\perp} = \frac{a_{\perp} - a_{SiGe}}{a_{SiGe}} \quad ; \quad \varepsilon_{//} = \frac{a_{//} - a_{SiGe}}{a_{SiGe}} \quad ; \quad \varepsilon_{\perp} = -R\varepsilon_{//} \qquad \text{(II. 4 ; II. 5 ; II. 6)}$$

where R is the biaxial relaxation constant ($R = 1$ for an unstrained film). As discussed in **chapter V**, strain can be estimated experimentally by RBS/Channeling, an ion beam analysis technique presented in **chapter III**.

In a pseudomorphic film, a coherent interface is formed as the lattice parameter of the film is adapted to match the substrate in the direction parallel to the surface (biaxial strain). If the lattice parameter of the substrate is smaller than that of the film, this latter is compressed in the direction parallel to the interface and stretched in the perpendicular direction to conserve the volume of the unit cell. In this configuration, the epilayer is tetragonally distorted

(**Figure 6**). The strain energy per unit area contained in the film increases with its thickness (15):

$$E_\varepsilon = \varepsilon_{//}^2 Y t \qquad \text{(II. 7)}$$

where Y [N/m²] is the biaxial modulus ($Y = \sigma_{//}/\varepsilon_{//}$, with $\sigma_{//}$ the biaxial stress) and t is the film thickness. Above t_c, it becomes energetically more favorable for the epilayer to reduce the strain by gradually relaxing through the formation of misfit dislocations at the film/substrate interface (**Figure 6**).

Several models have been proposed to calculate the critical thickness (**Figure 6, bottom**). In 1974, *Matthews and Blakeslee* (16) calculated the critical thickness based on the assumption of threading dislocations pre-existing in the substrate, and repeated in the film, which glides under the effect of the strain until creating misfit dislocations at the film/substrate interface. In 1985, *People and Bean* (17) proposed another model based on the assumption of $Si_{1-x}Ge_x$ films, initially free of dislocations, with a dislocation generation only determined by energy balance, *i.e.* when the areal strain energy in the film exceeds the minimum energy needed to form a dislocation.

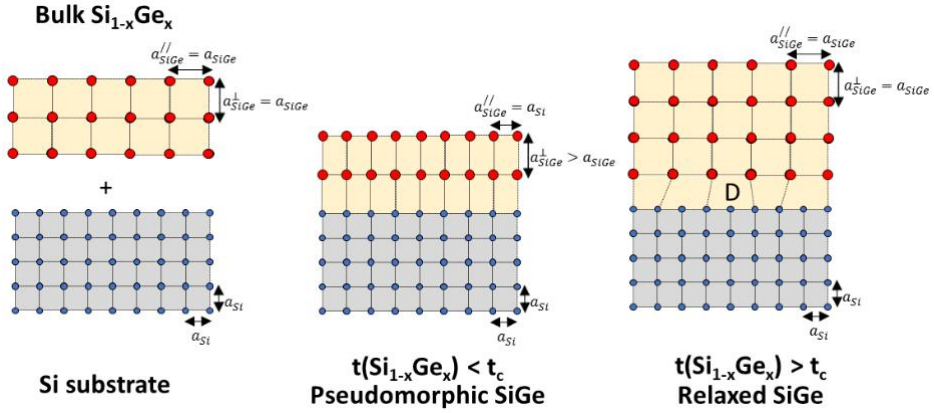

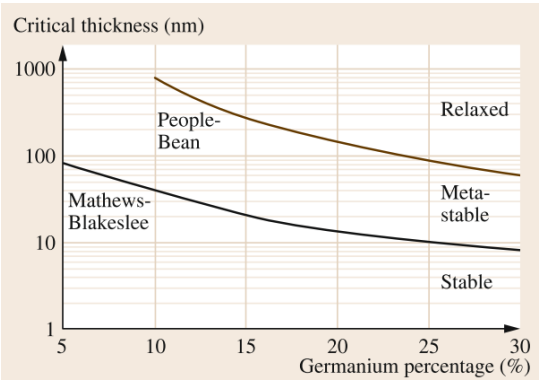

Figure 6 : Top – Schematic representation of $Si_{1-x}Ge_x$/Si layers in strained or relaxed configurations *(18)*. For pseudomorphic films, the $Si_{1-x}Ge_x$ layer is strained and $a_{SiGe}^{//} = a_{Si} < a_{SiGe}^{\perp}$, while the $Si_{1-x}Ge_x$ layer preserves its lattice parameter through the formation of dislocations in relaxed layers. Bottom – Evolution of critical thickness as a function of the Ge concentration in the $Si_{1-x}Ge_x$ film *(19)*. Under the curve calculated by the Matthews-Blakeslee model, the film is considered as fully strained and stable. Above the curve calculated by the People-Bean model, the film is relaxed. Between both curves, the film is metastable and highly sensitive to temperature.

II.3 Efficiency of Si-based photovoltaic cells

The current global photovoltaic (PV) market is dominated by mono-/polycrystalline silicon-based PV cells. However, their efficiency remains relatively low, for non-negligible production costs. The conversion rate of a PV cell is limited by several factors related to the intrinsic properties of the material:

1. Thermalization of carriers photogenerated by high-energy photons: even for photon energies exceeding twice the energy gap or higher, only one electron-hole pair is photogenerated in bulk semiconductors. Despite existing mechanism to produce several electron-hole pairs in semiconductors, called impact ionization, this process is generally inefficient in bulk materials.
   The excess energy from hot electrons is transferred to the crystal lattice by the emission of phonons. Carriers relaxation is therefore responsible for heating up the system which reduces the efficiency of the cell from a thermodynamic point of view.

2. Inefficiency of photons with insufficient energy to generate an electron-hole pair: these sub-bandgap photons do not participate to the generation of charge carriers. As silicon energy gap is $E_g = 1.12$ eV, only photons with energy higher or equal to E_g will transfer enough energy to an electron to promote it from the valence band towards the conduction band.

3. The recombination rate of photo-generated carriers: electrons and holes must be collected before they have a chance to recombine. The recombination pathways are either radiative, by emission of a photon, or non-radiative, through Auger or Shockley-Read-Hall (SRH) effects.
   The purity of the materials is of great importance because the defects/impurities favour the recombination of charge carriers, limiting the conversion efficiency of solar sensors.

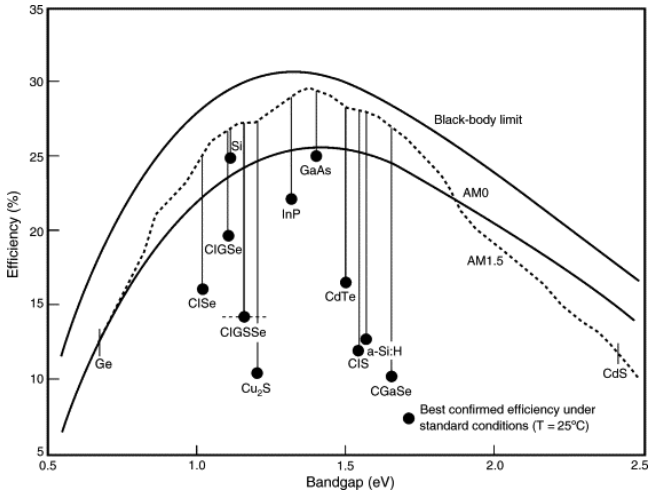

Figure 7 **:** Efficiencies of solar cells for different materials in 2006 *(20)*. Black dots represents the best efficiencies measured for each material and the lines correspond to the values theoretically reachable.

Considering these various limiting factors, the maximum theoretical efficiency for a single-junction PV cell is therefore around 33% (**Figure 7**), as calculated by Shockley and Queisser in 1961, considering an energy gap of ~1.4 eV and AM1.5 solar spectrum (1).

In practice, the type of solar cells currently installed on our roofs (single-junction Si cell) has an efficiency that can approach 27% in laboratory conditions for monocrystalline silicon (see **Figure 8**). Despite the abundance of raw material, mainly silicon, production costs remain significant, in particular because of refinement of the crystals, which is essential to obtain correct conversion rates, and the number of manufacturing steps required to produce a panel.

Single-junction photovoltaic cells are called first generation cells. Two major categories have emerged in recent decades, always with the aim of increasing the efficiency of solar collectors while limiting production costs:

- The second generation, which includes technologies based on the use of thin films, has the advantage of reducing the costs of raw materials. Unfortunately, their efficiencies remain too low and they are not able to exceed the efficiencies of the first generation.
  In addition, these cells sometimes require the use of rare and/or toxic compounds, such as CdTe (best conversion efficiency ~23%), while silicon and germanium are not toxic.

- The third generation, which presents the best conversion yields ever obtained (up to 47%), brings together a whole series of exotic cells such as perovskites or multi-junctions, including PV cells based on quantum dots (QDs) – also called nanocrystals (ncs).

The main researches carried out in the field of photovoltaic cells and the annual evolution of their conversion efficiencies are summarized in **Figure 8**. As shown in this figure, the efficiencies reached by the 3rd generation PV cells vary substantially from one technology to another. This particular ranking is dominated by perovskite PV cells, reaching efficiencies up to 29.5% (Oxford), which is about 10% higher than QDs PV cells.

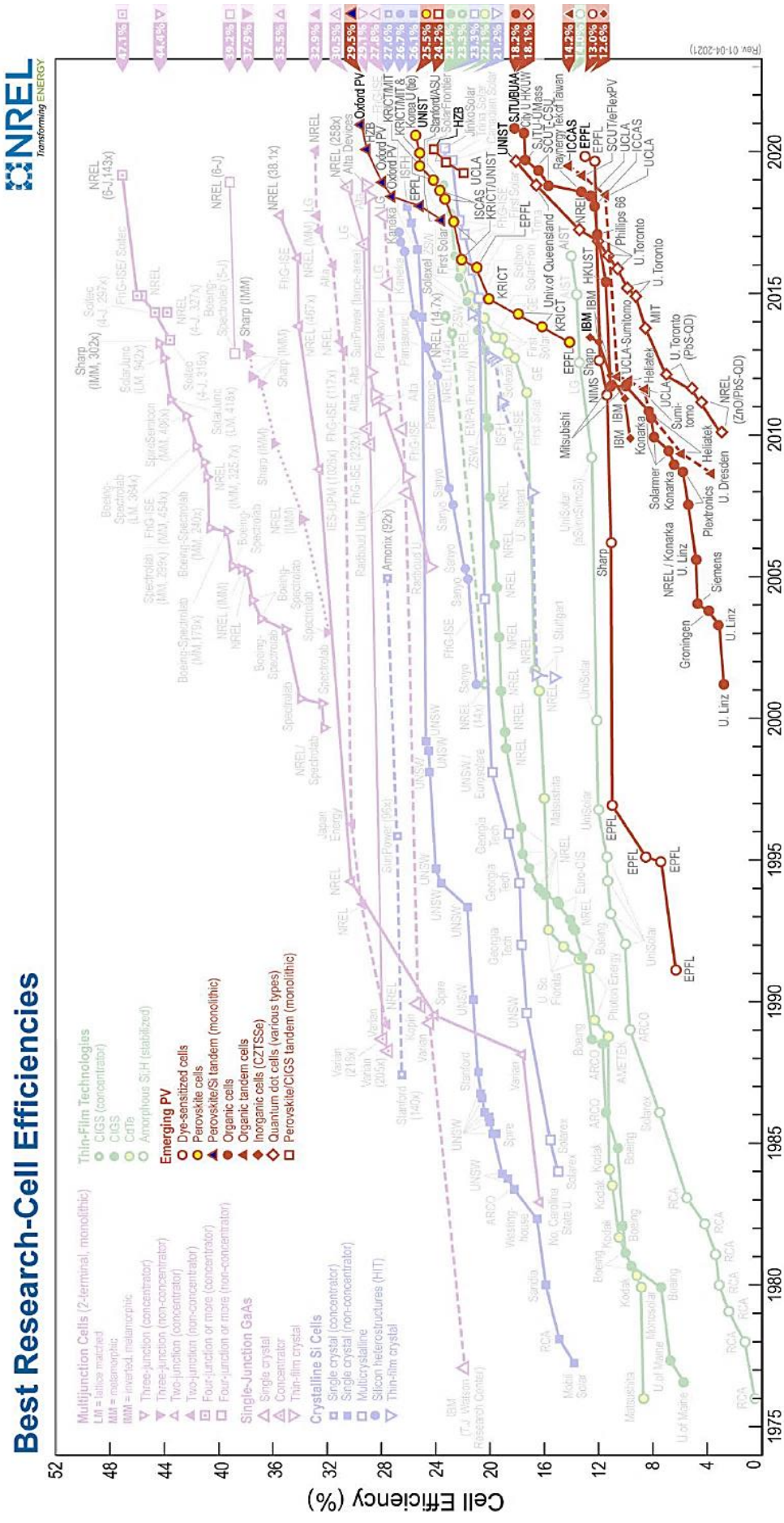

Figure 8 : Evolution of research in the field of PV cells since 1976 *(140)*. The evolution of emerging technologies is highlighted, with the quantum dots (QDs) cells represented by open diamonds. The QDs-based technology exhibits one of the most remarkable efficiency improvements of the last decade.

II.4 Quantum dots (QDs) – Nanocrystals (ncs)

When the dimensions of a material are reduced to the nanoscale, we therefore speak about nanostructures (a quantum dot (QD) - or nanocrystal (nc) - contains of the order of 100 to 10 000 atoms). By shrinking the dimensions of a crystal, its density of state (DOS) approaches that observed for an isolated atom with discrete energy levels, generally called "artificial atom", far from the continuous energy bands observed for bulk crystals (**Figure 9**).

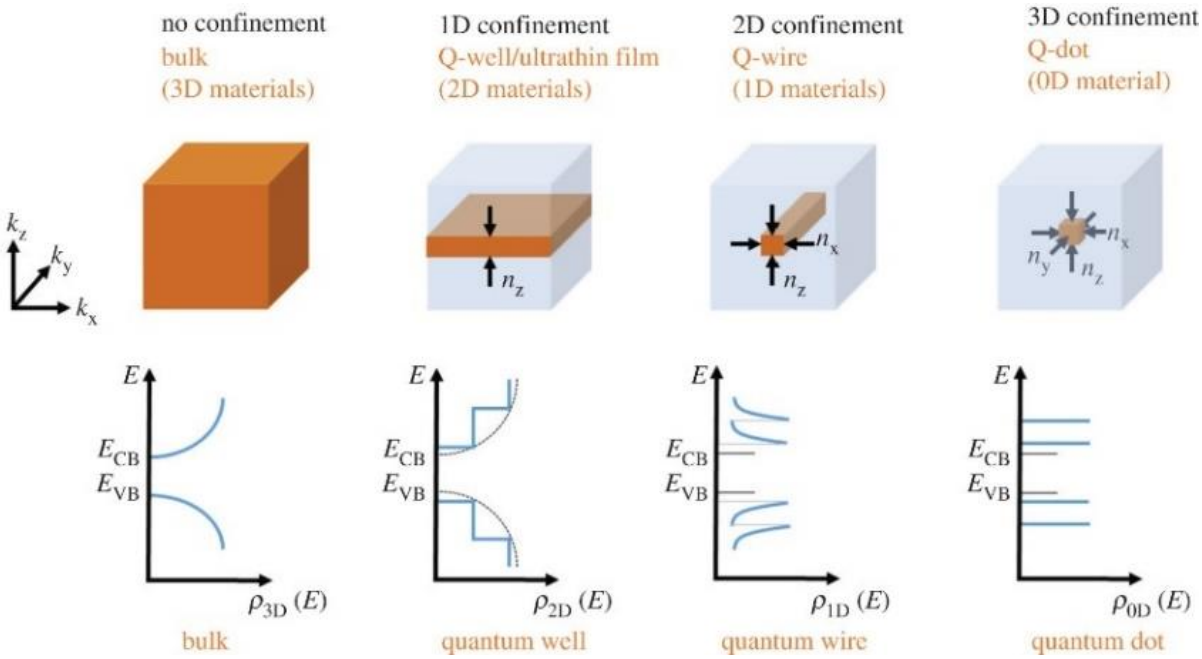

Figure 9 **:** Representation of quantum confinement and associated energy levels. *(21)*

When these nanostructures are integrated into insulating matrices, they are confined in a potential well due to the strong difference in energy that exists between the QDs energy levels and those of the dielectric material. Ge-QDs embedded in silicon dioxide respect a band alignment of type I (**Figure 10**).

For dimensions below the Bohr exciton radius (4.5 nm for silicon, 24 nm for germanium (22)), electron-hole pairs are confined and exist under the form of excitons, which are pairs correlated by a strong Coulomb interaction. The binding energy of an electron-hole pair being inversely proportional to the radius, it is much more intense in quantum dots (hundreds of meV) rather than in bulk material (a few meV to a few tens of meV). As a function of their shape, we will speak about 1D (plane or quantum well), 2D (nanowire or quantum wire) or 3D (nanocrystal or quantum dot) confinement (**Figure 9**).

QDs-based photovoltaic cells are very recent but already present one of the most impressive developments of the last ten years (open diamonds in **Figure 8**). In theory, quantum dots could make it possible to exceed, and even double in an ideal case, the Shockley-Queisser limit (23) by using a unique material, thanks to the manifold optoelectronic properties associated to nanocrystals.

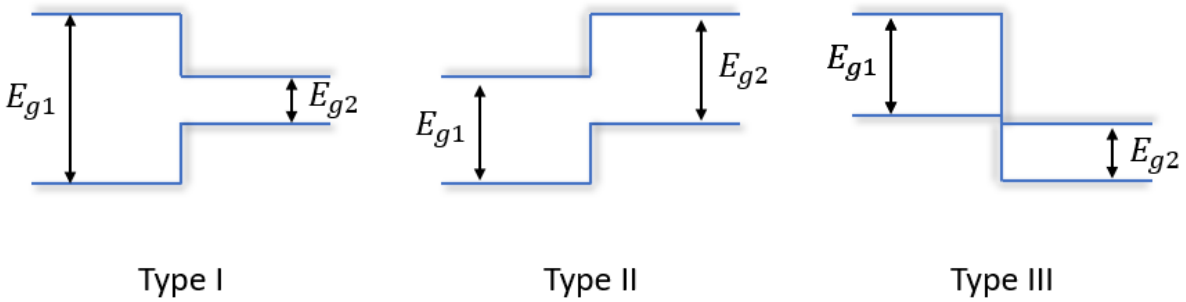

Figure 10 : Different types of band alignment in heterostructures. Ge-ncs embedded in SiO_2 and Si have an alignment of type I and II respectively.

II.5 Properties of quantum dots

Quantum dots have many optoelectronic properties (bandgap engineering, multiple exciton generation and photoluminescence) which are very interesting for optoelectronic devices, such as photovoltaic cells. This section gives a brief reminder of the quantum dots properties relevant for PV cells, in order to help the reader to understand how quantum dots could greatly enhance conversion efficiency in photovoltaic cells.

Bohr exciton radius

Due to smaller effective masses (m_i^*) and a larger dielectric constant (ε_r), Ge nanocrystals are more interesting than Si nanocrystals thanks to a larger Bohr exciton radius, a_B:

$$a_B = \frac{m_e}{\left(\frac{m_e^* m_h^*}{m_e^* + m_h^*}\right)} \varepsilon_r \frac{4\pi\varepsilon_0 \hbar^2}{m_e e^2} = \frac{m_e}{\mu} \varepsilon_r a_0 \qquad \text{(II. 8)}$$

with m_e^* and m_h^* are the effective masses of electrons and holes, $a_0 = 0.53$ Å is the Bohr radius, ε_0 is the vacuum permittivity, $\hbar = \frac{h}{2\pi}$ and $\mu = (m_e^* m_h^*)/(m_e^* + m_h^*)$ is the reduced mass. The dielectric constant ($\varepsilon_r = 16.2$) and reduced mass ($\mu = 2.92 \times 10^{-32}$ kg) for Ge leading to $a_B = 24$ nm, while $a_B = 4.5$ nm for Si ($\varepsilon_r = 11.9$; $\mu = 1.37 \times 10^{-31}$ kg).

As a result, quantum confinement, and subsequent effects, occur at larger dimensions in germanium nanocrystals than in silicon nanocrystals, offering a larger degree of freedom in these size-dependent properties.

Bandgap engineering

As a direct consequence of quantum confinement and energy levels discretization, the reduction of nanocrystals size is accompanied by a widening of the bandgap width. The energy of the nanocrystals bandgap is therefore adjustable according to their dimensions (24). The change in bandgap width can be estimated, as a first approximation, by the effective masses approximation (EMA):

$$E_g = E_{g,bulk} + \frac{\hbar^2\pi^2}{2}\left[\frac{1}{L_x^2}+\frac{1}{L_y^2}+\frac{1}{L_z^2}\right]\left[\frac{1}{m_e^*}+\frac{1}{m_h^*}\right] \quad \text{(II. 9)}$$

with L_i the dimensions in the three directions of space, m_e^* and m_h^* the electron and hole effectives masses respectively. This approximation remains valid only for nanostructures whose diameter is larger than twice the lattice parameter of the material (25), *i.e.* around 1.1 nm when considering silicon and germanium quantum dots. Below this value, experimental results show that EMA systematically overestimates E_g (**Figure 11**).

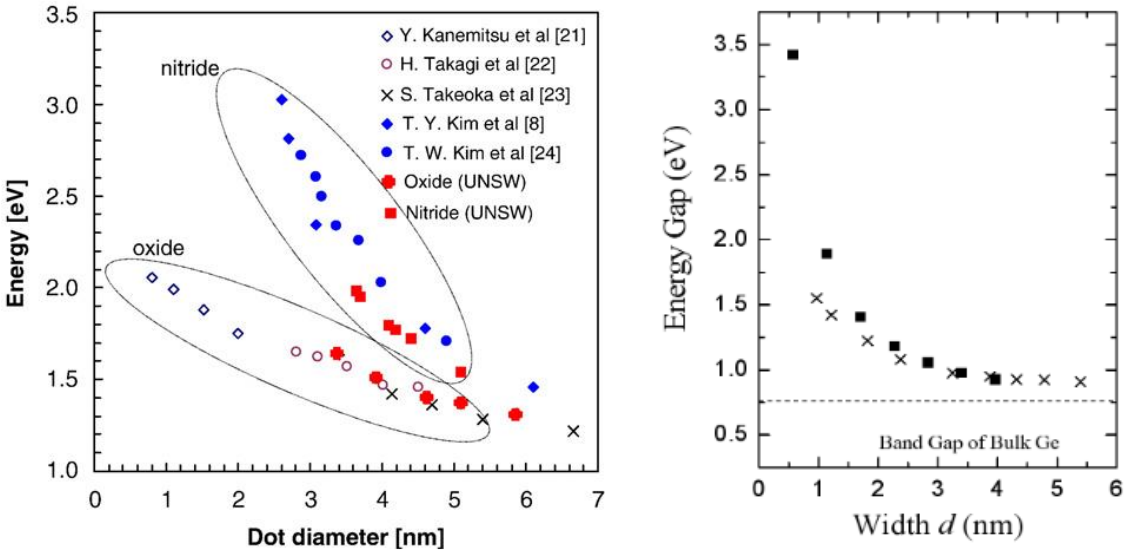

Figure 11 **:** Left - Experimental measurements of the bandgap energy as a function of Si QDs diameter in SiO_2 and Si_3N_4. Right – Experimental (crosses) and simulated by EMA (squares) evolution of the Ge QDs bandgap as a function of their diameter *(26)*.

This quantum dots property can be used to optimize light absorption (or emission) in a wide range of wavelengths, as each nanocrystal diameter corresponds to a different energy gap. In the particular case of PV cells, a well-distributed nanocrystals layer could imitate high-efficiency multi-junction solar cells (purple curves in **Figure 8**) by using a continuous size gradient of nanocrystals increasingly larger as a function of depth. As the quantum dots will be transparent for photons whose energy is lower than their bandgap, high-energy photons will be absorbed by the smallest nanocrystals closer to the top of the active layer, while photons with smaller energies will be progressively absorbed deeper in the layer, imitating the multi-junction solar cells. In theory, germanium quantum dots could cover almost the

entire solar spectrum (360 to 1878 nm). From this point of view, Ge-ncs are more interesting than Si-ncs as they could cover a wider range of the solar spectrum. According to **Figure 11 (right)**, an energy gap of 3.45 eV (360 nm) corresponds to Ge quantum dots diameters as low as 0.6 nm. The upper limit is defined by the Bohr exciton radius, but **Figure 11 (right)** shows that the gain is negligible for diameters higher than 4-5 nm. The grail would therefore consist in forming a size gradient of nanocrystals ranging from 0.6 nm, near the top of the active layer, to 4-5 nm in depth.

Because of the reduction of nanostructures dimensions, and as a consequence of Heisenberg's uncertainty principle, the spatial confinement of charge carriers increases the uncertainty on their momentum in the ***k*** space ($\vec{p} = \hbar\vec{k}$):

$$\Delta x \Delta p \geq \frac{\hbar}{2} \qquad \text{(II. 10)}$$

In these conditions, transitions that are not assisted by phonons become possible, as the momentum conservation rules are broken. As a consequence, direct transitions could become possible even in an indirect semiconductor. The size reduction causes an overlapping of electrons (at the minimum of CB) and holes (at the maximum of VB) wave functions (**Figure 12**). The radiative efficiency is therefore increased by several orders of magnitude in nanostructures with respect to bulk materials.

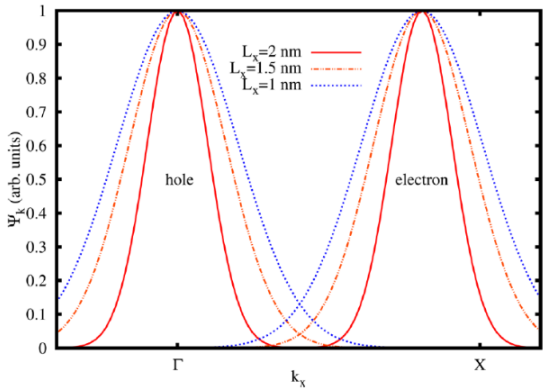

Figure 12 : Representation of electrons and hole wavefunctions and their overlapping while reducing nanocrystlas diameter *(25)*.

Multiple exciton generation (MEG)

Another expected property of quantum dots is the multiple exciton generation (MEG). This consists of creating several electron-hole pairs from a single high-energy photon, whose energy is at least equal to $2E_g$.

The model proposed to explain this phenomenon is the impact ionization. This multiple-particle phenomenon consists in the excitation of at least one additional electron from the valence band as a result of energy transfer between this electron and a hot electron

from the conduction band. A hot electron is an electron receiving enough energy from a photon to reach high-energy levels in the conduction band. Hot electron can de-excite towards the CB edge by transferring its energy either to an electron in the VB (the transferred energy must be at least equivalent to E_g to promote this electron into the CB - **Figure 13a**), or through the emission of phonons (**Figure 13b**). In this latter case, no supplementary electron-hole pairs are produced.

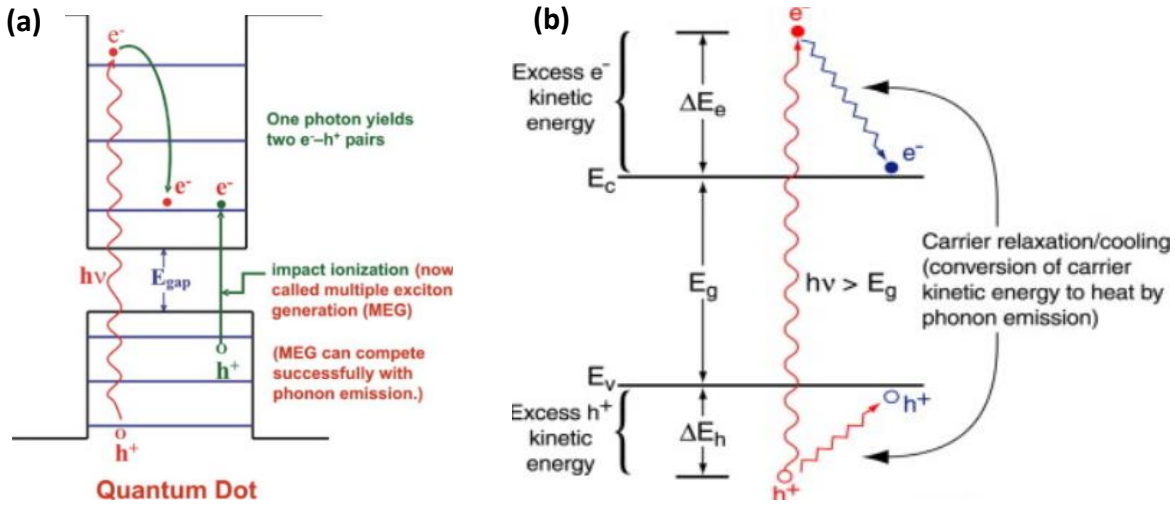

Figure 13 : (a) Principle of multiple exciton generation in quantum dots and (b) carrier relaxation in bulk semiconductor *(27)*.

This process becomes more likely and efficient in nanocrystals compared to bulk materials due to the discretization of energy levels. Hot electrons are less likely to relax by thermalization because the energy difference between two energy levels is greater than the typical energy of phonons (a few meV). Moreover, the wave vector ***k*** should no longer be conserved due to relaxation of momentum conservation in quantum dots, facilitating transitions between valence and conduction bands.

Experimental results quickly demonstrated the potential of MEG (**Figure 14**), notably thanks to *Nozik et al.* (27) and *Klimov et al.* (28) works, with quantum efficiencies up to 700% for PbSe nanocrystals with photons of energy $8E_g$:

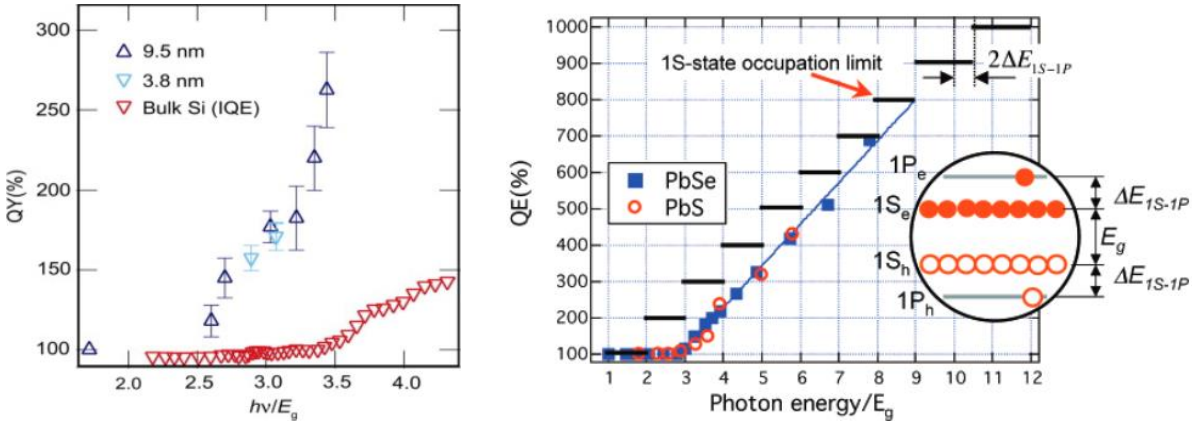

Figure 14 : Experimental results of quantum efficiencies (QE is equivalent to QY – for quantum yields) as a function of photon energy normalized by E_g reported (left) by Nozik in 2008 for bulk silicon and Si-ncs of measured average sizes of 3.8 and 9.5 nm dispersed in tetrachloroethylene or hexane *(27)* and (right) by Klimov in 2006 for PbSe and PbS nanocrystals *(28)*.

The quantum efficiency QE (or quantum yield QY) is the ratio between the number of electron/hole pairs generated and the number of incident photons:

$$QE[\%] = 100.\frac{N_{e^-/h^+}}{N_{photons}} \quad (\text{II. } 11)$$

However, reluctances rapidly appeared concerning the veracity of such results. Other research groups failed to reproduce *Nozik* and *Klimov* findings, neither experimentally nor by simulations (**Figure 15**). Although they recognize the possibility to generate multiple excitons, even the most extreme conditions of simulation do not allow reproduction of the results obtained by *Nozik* and *Klimov*. MEG in quantum dots is not disproved nowadays, but several groups showed that it would not be more efficient in QDs than in bulk materials. Nevertheless, the energy of photons of a particular frequency would be better used in nanocrystals rather than in the bulk material, due to bandgap enlargement, reducing side effects of high-energy photons (29), (30).

Experimental artifacts were invoked to explain *Nozik* and *Klimov* results. The formation of trions (when an exciton is generated in a quantum dot having an electron or a hole trapped at its surface), the successive absorption of several photons or the presence of surface defects are factors that can cause rapid exciton recombination (of the order of one picosecond). Those fast recombination rates are then erroneously associated to the presence of multi-excitons, whose recombination time is also of the order of one picosecond (same magnitude than Auger recombination), whereas the recombination time of a single exciton is rather of the order of the nanosecond (a few tens to a few hundreds).

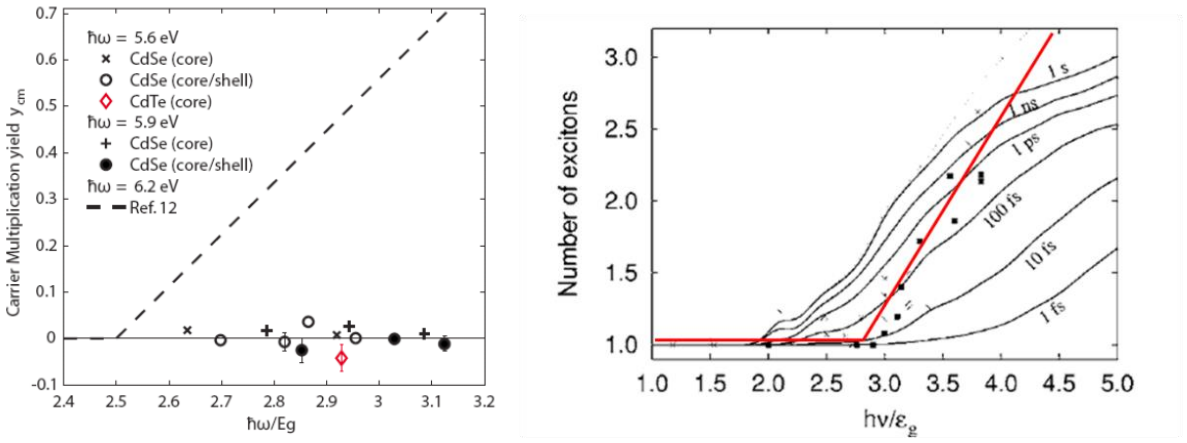

Figure 15 **:** Left – Comparison of Nair and Bawendi results for different CdTe and CdSe QDs diameters and photons energies, showing no MEG, with those obtained by Klimov for PbSe and PbS QDs (presented in **Figure 14** and referenced here as « Ref. 12 ») *(31)*. A carrier multiplication yield higher than 0 corresponds to more than one photogenerated exciton. Right – Comparison of simulations for different lifetimes of multi-excitons with Kilomov's results (red line) *(32)*. One exciton corresponds to a QE of 100%.

How multi-excitons are generated is still a matter of debate nowadays. Other models have emerged, such as the virtual excitonic levels model proposed by *Schaller et al.* (33), or the coherent superposition of excitonic states (34), (35). However, studies carried out a few years after the proposal of these models showed that these two processes would not be

significant compared to impact ionization, which remains the most widespread explanation largely accepted by the scientific community.

Another model describes the possibility of generating several excitons in spatially close quantum dots, whose wavefunctions overlap to form periodic superlattices of nanocrystals (26), (36), (37). Integrated in an insulating host matrix, quantum dots behave like a new material with a *pseudo-direct* bandgap that can be modulated according to the size of the nanostructures.

The probability of transmission of charge carriers by tunnelling effect between two quantum dots spaced by Δx is expressed by (38):

$$T_e \approx 16\, exp\left(-\Delta x \sqrt{\frac{8m^*}{\hbar^2}\Delta E}\right) \qquad \text{(II. 12)}$$

with ΔE the energy difference between the edge of the conduction band of the nanocrystals and the insulating matrix (SiO_2, Si_3N_4, …). This means that spatially close quantum dots must be formed in dielectric films to enhance the probability of transmission of charge carriers between adjacent nanocrystals by tunnelling effect. Therefore, both their probability of collection and their possible contribution to photocurrent increase.

In the ideal case of a single-junction with a MEG threshold approaching $2E_g$, the theoretical efficiency is about 44% for an energy bandgap of 0.7 eV (**Figure 16**). This conversion efficiency can even increase up to 66%, considering a layer containing a stack of well-distributed quantum dots with different diameters (2).

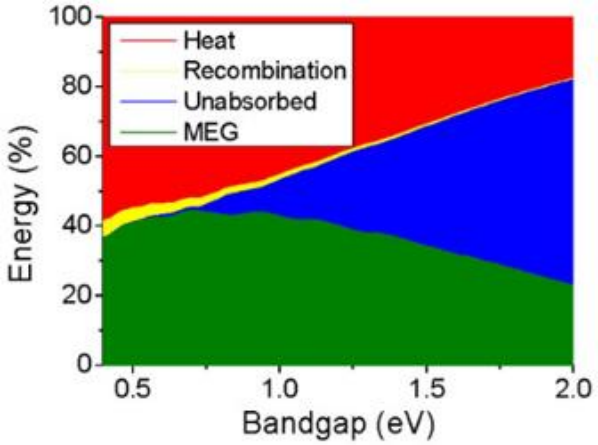

Figure 16 : Calculated conversion efficiency as a function of the QD bandgap for AM1.5 solar spectrum for ideal case, *i.e.* if each photon generates a number of electron/hole pairs proportional to E_g *(29).* The contributions of the major loss mechanisms presented in **section II.3** are represented.

Luminescence

Photoluminescence (PL) and ionoluminescence (IL) of semiconductor nanocrystals open new perspectives for light emitting devices such as lasers or LEDs (24), (39), (40). PL and IL consist in the radiative recombination of an electron/hole pair consecutive to its excitation caused by the absorption of photons or ions energy respectively.

Initially discovered in porous silicon (41), (42), quantum dots luminescence has then been observed for Si and Ge nanocrystals embedded inside dielectric layers (**Figure 17**). The origin of photoluminescence is still a subject of debate nowadays, as we can almost find as many experimental results as there are studies dealing with the subject. However, two possible explanations have been proposed for the origin of the luminescence of quantum dots:

1. Photon emission through radiative recombination, due to the increased probability of not-phonon-assisted radiative transitions, as a result of quantum confinement (because of the relaxation of conservation rules for low-dimensions structures).

2. The presence of a high density of characteristic defects at the QD/dielectric interface, acting as recombination centers in the forbidden band.

In the first case, the wavelength of the emitted light is fixed by the quantum dot energy gap, which is size-dependent as previously discussed. A blueshift has been observed while decreasing nanocrystals size, but systematically at a lower amplitude than calculated by models based on quantum confinement (43), (44), (45), (46), (47). For example, *Takeoka et al.* (48) reported a size-dependent PL in the near-infrared region (from 0.88 to 1.54 eV) for nanocrystals sizes ranging from 5.3 to 0.9 nm.

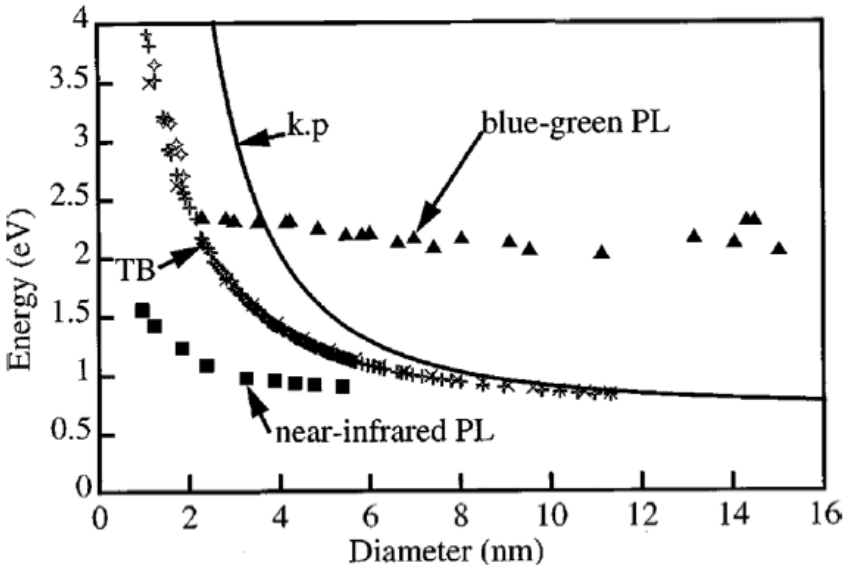

Figure 17 : Evolution of PL emission energy for calculated (by tight binding (TB) and k.p methods of band structure simulation) or experimental (black squares and triangles) values, for germanium nanocrystals of various diameter embedded in SiO_2 *(49)*.

In the second model, which is the most widely adopted, the radiative recombination occurs in the structural defects at the QD/dielectric interface (50), (51), (52), (53), (54). These defects, such as GODC (Germanium-Oxygen Deficiency Center, $\equiv Si - Ge \equiv$) or NBOHC (Non-Bridging Oxygen Hole Center, $\equiv Si - O\bullet$), induce intermediate energy states in the forbidden band of quantum dots. Photoluminescence spectra showed emission bands in the visible range at energies between 2.0 and 2.5 eV or around 3.1 eV.

The real explanation might be midway between both models. It has been proposed that only one carrier confined in the nanocrystal could recombine with a charge carrier located in the energy level of a structural defect (in the forbidden band). This would be consistent with size effects systematically observed at lower energies than calculated values. G*ambaryan et al.* recently observed two different contributions with one in the visible range associated to defects and a second in the NIR range associated to the combination of both defects and confinement effects (50).

From the photovoltaic point of view, nanocrystals luminescence could enable to adjust mismatch between photon energy and bandgap for a better use of UV-regions from the solar spectrum. The idea is to limit the thermalization effect due to high-energy photons by the implementation of an active layer upstream of the solar cell. This optically active layer would absorb UV photons to adapt their wavelength by emitting at least one photon according to one of the following processes:

1. **Down-conversion:** several lower energy photons are produced through the absorption of a high-energy photon (55).

2. **Down-shifting:** the wavelength of a high-energy photon is shifted to a more optimal wavelength (56), (57).

II.6 Experimental methods for fabricating Ge quantum dots in silicon dioxide

Several experimental methods are commonly used to fabricate germanium nanocrystals embedded in silicon dioxide matrices. Among the wide range of techniques, we can mention:

- Ion implantation (58), (59), (60), (61), (62), (63)
- Plasma-enhanced chemical vapour deposition (PECVD) (64), (65), (66)
- Low-pressure chemical vapour deposition (LPCVD) (67), (68)
- Thermal evaporation (69), (70), (71)
- RF magnetron co-sputtering (72), (73), (74)
- Pulsed laser ablation (24), (75), (76)
- Molecular beam epitaxy (MBE) (77), (78)

This thesis focuses on ion implantation, which is detailed in **chapter III**, to form Ge nanocrystals in SiO_2 films. Despite the large variety of techniques available, the purpose of these different methods is always the same: creating germanium supersaturated solid solutions in a dielectric layer, which is SiO_2 in the particular case of this thesis. Ge concentration must be higher than the solubility of the host matrix, which is < 10^{18} at./cm³ in SiO_2. Phase separation and diffusion are then thermally activated to give rise to the formation of nanocrystals. Clusters remain amorphous for low temperature of annealing, with a phase transition to crystalline clusters in the 600 - 800°C range (79).

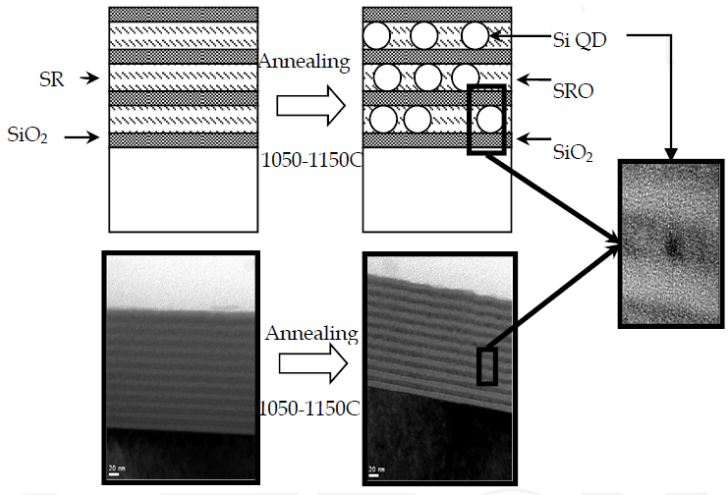

Figure 18 **:** Electronic microscopy images of silicon nanocrystals multi-layers fabricated by plasma deposition *(80)*. A succession of SiO_2 and Si-rich (SR) layers are deposited on a silicon substrate. SR layers are reduced in SiO_2 + Si during annealing. Si atoms in excess diffuse and nucleate to form Si-QDs. The same process is commonly used for the fabrication of Ge quantum dots.

As it has been demonstrated for the growth of silicon nanocrystals, the formation of germanium nanocrystals is ruled by Ostwald ripening process (81), (82): small nanoclusters being more soluble than larger ones, they tend to disappear to the profit of larger more stable nanocrystals.

The formation of germanium nanocrystals in silicon dioxide is a multi-step process:

1. Growth of Ge-rich layers by one of the methods previously cited,
2. Thermal activation of Ge diffusion and nanoclustering,
3. During annealing,
    a. Reduction in elemental Ge of the thermodynamically less stable GeO_x compounds formed during the layer growth or enrichment,
    b. Temperature-dependent diffusion of germanium atoms and GeO molecules,
    c. Formation of small nanocrystals at the early times of the annealing,
    d. Formation of larger nanocrystals to the detriment of small ones by Ostwald ripening process.

The nanocrystals average size increases with the annealing temperature and time and with the local concentration of germanium atoms. According to Ostwald ripening process, the thermodynamically less stable small nanostructures disappear while the larger ones grow up. This occurs by dissolution of very small Ge-ncs, whose Ge/SiO_2 interface is high, or by coalescence of close quantum dots. Consequently, the nanocrystals average radius increases as $\sqrt[3]{t}$ and the nanoclusters density decreases as t^{-1} with respect to the annealing time t (83), until a stable state is reached. The evolution of nanocrystals size and density according to Ostwald ripening process is represented in **Figure 19** as a function of annealing time and temperature. For high germanium concentrations and annealing temperature, the density of nanocrystals formed due to Ostwald ripening process is important. Small nanocrystals can then dilute to the benefit of larger ones, or spatially close nanocrystals can coalesce to form larger nanocrystals (84), (85).

In implanted samples, the average diameter of nanocrystals depends on the local concentration of germanium, which increases with the Ge fluence. However, the percentage of Ge participating to the growth of nanocrystals can decrease at high fluences because of irradiation-induced damage and the consequent silicon trapping effects (81), (82). These features are discussed further in the results presented in **chapter IV** of this manuscript.

As the size and dispersion of nanocrystals highly depend on the fabrication method and conditions, as well as the nature of the host matrix, one can observe large discrepancies in the results reported in literature. Comparison of Ge nanocrystals fabricated by ion implantation in Si_3N_4 or SiO_2 matrices has demonstrated that, for identical temperatures of annealing and Ge concentrations, Ge nanocrystals (Ge-ncs) were smaller and amorphous in Si_3N_4, and larger and crystalline in SiO_2 (86).

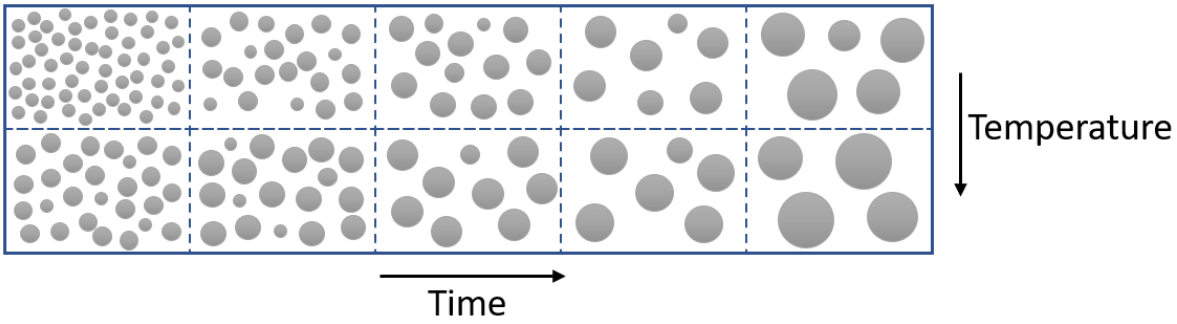

Figure 19 : Shematic representation of Ostwald ripening process as a function of annealing temperature and time. Implanted Ge atoms diffuse through the SiO_2 matrix to form nanocrystals. Smallest nanocrystals, more soluble, dissolve to the benefit of larger nanocrystals. As a result, the density of nanocrystals decreases while the average diameter increases.

Chapter III

Modification and characterization of materials

III.1 Ion implantation

Ion implantation consists to accelerate charged particles, called ions, to incorporate them into a material in order to modify its optical, electrical, structural or chemical properties. To penetrate the target material in depth, these particles are accelerated under vacuum with a kinetic energy ranging from a few to several hundreds of keV. Along their trajectory, incident ions interact with matter in two different processes, which are considered to be independent of each other: nuclear (elastic) and electronic (inelastic) energy losses.

The stopping power, $S(E) = -\,dE/dx$, allows one to quantify the energy loss of ions as a function of the travelled distance through the material, taking into account both nuclear and electronic contributions:

$$\frac{dE}{dx} = \left(\frac{dE}{dx}\right)_n + \left(\frac{dE}{dx}\right)_e = -\,N(\varepsilon_n + \varepsilon_e) \qquad \text{(III. 1)}$$

where N is the material density [at./cm³] and ε_i are the stopping cross sections [eV/(10^{15} at.cm^{-2})]. The stopping power $S(E)$ is an energy loss per unit path length.

Interactions are dominated by electronic stopping power at high energies, or velocities, and nuclear stopping power at low energies, the transition from one to the other occurring when ions are slowed down to velocities lower than Bohr's velocity ($v_{Bohr} = e^2/4\pi\varepsilon_0\hbar \approx 2.2 \times 10^6$ m/s).

Nuclear energy loss is due to Coulomb repulsion between the incident ions and the target nuclei for small impact parameters, b, which leads to the scattering of the impinging particles. Energy and momentum conservation indicates that the energy transferred to the target atom is $E_\phi = E_0 \frac{4M_1M_2}{(M_1+M_2)^2} cos^2\phi$, where ϕ is the recoil angle, E_0 is the energy of the impinging ion, M_1 and M_2 are the masses of the incident and target atoms respectively.

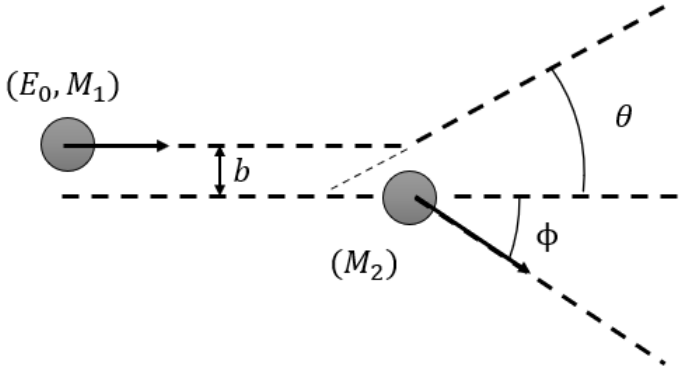

Figure 20 : Binary collision between an impinging ion of mass M_1 et energy E_0 and a target atom of mass M_2 at rest. b is called the impact parameter. θ and ϕ are the scattering and recoil angles respectively.

Electronic energy loss is due to ion-electron interactions and to the generation of plasmons without significant deviation of the ions from their trajectory. The interaction with electrons strongly depends on the ion velocity. The electronic stopping power increases with

the velocity until reaching a maximum when the ion velocity is similar to that of the orbital electrons (**Figure 21**). For higher ions velocities, the time of interaction decreases and the energy loss is inversely proportional the square of the ion velocity, v^2.

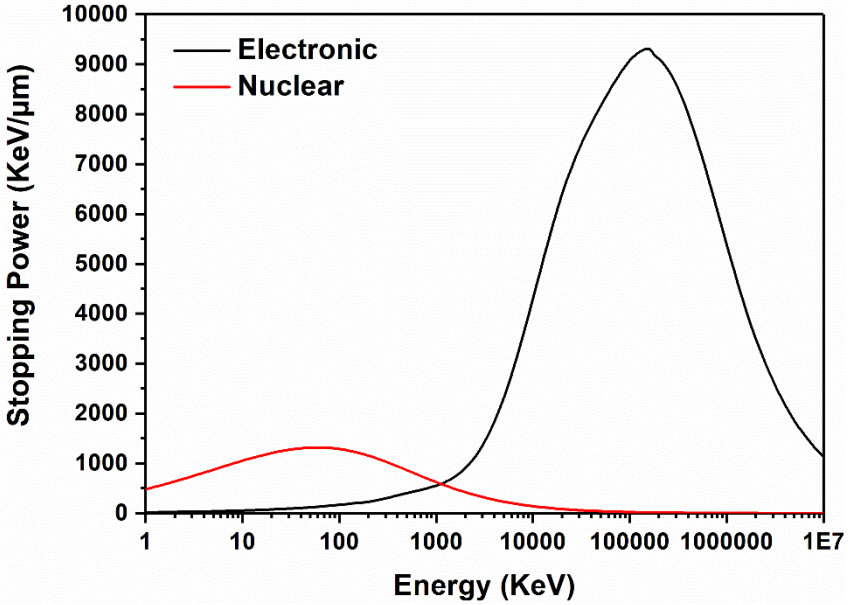

Figure 21 **:** Stopping power is calculated by SRIM-TRIM for ^{74}Ge ions implanted in SiO_2. The energy corresponding to Bohr's velocity for ^{74}Ge is ~1900 keV.

The energy lost by a particle crossing a material over a distance x is estimated by:

$$E_x = E_0 - \int_0^x S(E)dx \qquad \text{(III. 2)}$$

Once their energy is totally dissipated, ions stop their travel through matter and are called "implanted atoms". The energy loss of an ion crossing matter is a statistical phenomenon characterized by longitudinal and transverse fluctuations, which increase with the crossed thickness. The statistical divergences of the energy losses are referred to as energy straggling. For a fixed material, the mean implantation depth, called projected range (R_p), depends on the initial energy and the nature of the incident particle (**Figure 22**). By neglecting flattening (Kurtosis) and asymmetry (Skewness) effects, the ions depth-distribution can be approximated by a Gaussian distribution centred on R_p, with a standard deviation σ ($= \Delta R_p$):

$$C(x) = \frac{\Phi}{\sqrt{2\pi}\sigma} e^{-(x-R_p)^2/2\sigma^2} \qquad \text{(III. 3)}$$

where Φ represents the ion fluence in [at./cm²].

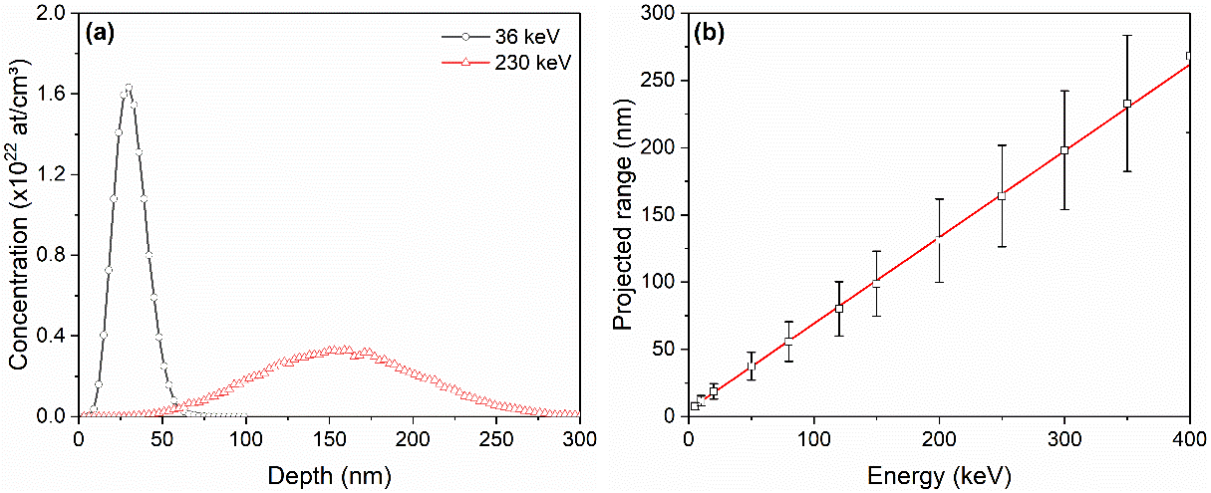

Figure 22 : SRIM-TRIM (version 2013) calculations of Ge ions implanted in SiO_2: (a) depth-profiles for ions energies of 36 and 230 keV with a fluence of 4×10^{16} Ge/cm², and (b) projected ranges for ions energies ranging from 5 to 400 keV (error bars correspond to longitudinal straggling calculated by SRIM *(87)*).

Advantages of ion implantation for the synthesis of nanostructures

1. **Beam purity:** selection of accelerated particles is achieved thanks to the well-known Lorentz force ($\vec{F} = q\vec{v} \times \vec{B}$) through an incurved magnet. The larger the deflection angle, the tighter the selection. Only particles satisfying both mass and energy conditions will efficiently pass through the magnet. Mass resolution enables isotopic selection of the implanted species (a rectangular collimator is placed behind the magnet to ensure isotopic selection). However, the magnet is not able to discretize particles and molecules possessing the same mass, *e.g.* ^{30}Si from $^{29}Si^{1}H$. This can be avoided by the use of isotopically pure ion sources. Therefore, only the desired isotope will be implanted and layer contamination is excluded.
   In this thesis, the following isotopes have been implanted: ^{74}Ge (36% of abundance in natural Ge), ^{29}Si (4.7% in natural Si), ^{30}Si (3.1% in natural Si), ^{28}Si (92.2% in natural Si - used for amorphization) and ^{16}O (99.76% in natural oxygen).

2. **Dose control:** ion implantation enables an accurate control of the implanted dose. Each incident ion of charge state q has "q times" the elementary charge $e = 1.602 \times 10^{-19}$ C (q is generally equal to 1). This charge is positive or negative according to the irradiation station considered (see **section III.2**). The total charge is integrated during the implantation process to estimate the implanted dose, the current reliability being ensured by a repulsive voltage applied on an anode positioned in front of the sample to prevent secondary electrons to escape from the sample surface.

   Controlling the dose allows one to control the doping concentration and, therefore, the size of nanocrystals. For a beam intensity I, the dose D of ions implanted through a surface A during a time t is given by the following relationship:

$$D = \Phi A = \int_0^t \frac{I}{qe} dt \qquad \text{(III. 4)}$$

   where Φ [ions/cm²] is the fluence and q the charge state of the ions. The overall dose D and the fluence Φ are generally used equivalently and both terms are commonly used to designate an ion flux in ions/cm².

   The residual vacuum is important, as residual atoms present in the beam line can neutralize ions, which therefore do not contribute to the beam current at the sample surface. This leads to a modification of the real implanted fluence. Neutral contribution can be strongly limited by applying an offset voltage as close as possible to the sample. This offset will deflect the charged particles beam towards the sample, while neutral atoms will continue in a straight line and are stopped by a collimating system. The use of condensers, cooled by liquid nitrogen, may also

reduce the residual vacuum along the beamline. See **section III.2** for more details on the implantation system.

3. **Control of depth-distribution:** implantation depth can be easily and finely tuned by varying the ions energy. As nanocrystals generally grow in the vicinity of the projected range (assuming low diffusion coefficients), the energy of the incident particles determines the depth-distribution of the nanocrystals.

4. **Homogeneity over a large surface:** implanters enable to implant homogeneously over surfaces of several cm^2 at laboratory scale, and even more at industrial level, thanks to electrostatic scanning (see **section III.2**).

5. **Process adapted to silicon-based industry:** ion implantation is widespread in semiconductor industry since decades, for example for the doping of silicon wafers.

Disadvantages of ion implantation

Ion implantation presents a few disadvantages, whose impact can be strongly limited during implantation or with post-implantation treatments:

1. **Generation of irradiation-induced defects:** by crossing matter, ions induce unavoidable damage. For high fluences, a damage buildup occurs which may lead to the total disorganization of the atomic structure of the target material. This point will be developed further in **section III.3**.

   A post-implantation annealing is generally carried out to restore the structure of the targets.

2. **Sputtering and swelling effects:** A surface exposed to ion flux will be sputtered, resulting in the ejection of atoms from the sample, while damage and implanted ions will induce volume variations through the sample depth. Sputtering is due to the energy transferred to the surface atoms by the impinging ions through cascades of collisions. If the energy transferred is higher than its surface binding energy and if its momentum has a component normal to the sample surface, the atom is ejected from the target.

   These phenomena are generally not taken into account in simulation programs as SRIM-TRIM (87) or SUSPRE (88). These programs only provide values of sputtering yield for simple matrices. Data from these computing programs must be treated downstream to consider sputtering and swelling effects on the final depth-profile.

3. **Channeling:** along their travel through matter, ions may be trapped in channels naturally present in crystals because of their particular atomic structure. In this

case, stopping power and ion/matter interactions decrease, which may induce longer projected ranges. Channeling will be explained further in **section III.5**.

To avoid channeling effect, the target must be tilted a few degrees (about 7° for <100> Si) and twisted (∼22° for <100> Si) with respect to the incident beam direction. Channeling effect is used to our advantage in a particular ion beam analysis technique presented in **section III.5**.

4. **Surface contamination buildup:** even if the implantation is performed under vacuum (∼10^{-7} mbar), heavy ions may collide residual atoms present in the vacuum line, such as carbon, during their path along the beamline. As implantation processes generally involve a significant number of incident ions (> 1×10^{13} ions/s), the probability of colliding with neutral atoms is not negligible. Impinged atoms are driven towards the sample surface, inducing a contamination layer buildup that may be responsible of a variation of ions projected range.

   Surface buildup can be limited by the combination of an LN_2 condenser and an offset voltage.

Computational programs

SRIM-TRIM (87) simulation program, developed by *J.F. Ziegler*, is a software widespread in accelerators physics. This software enables to simulate interactions of impinging ions with matter, allowing one to select the nature and energy of the incident particle and the nature of the irradiated medium, whether it is solid or not.

TRIM part ("*TRansport of Ions in Matter*"), based on KMC method (« *Kinetic Monte Carlo* »), uses binary collision approximation (BCA) to:

- extract 3D depth-profiles of implanted ions,
- simulate irradiation-induced damage,
- estimate sputtering yields for simple compounds,
- …

In BCA approach, the interaction of an ion with matter is considered as a succession of two-body collisions.

SRIM part ("*Stopping and Range of Ions in Matter*") permits to calculate electronic and nuclear stopping powers, projected ranges or longitudinal and transverse divergences.

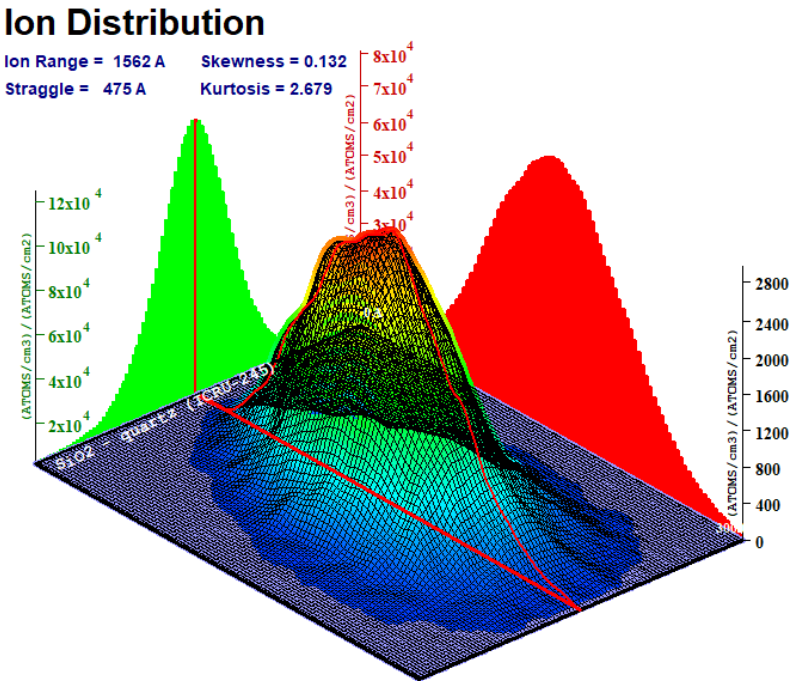

Figure 23 **:** SRIM-TRIM 3D simulation of 230 keV Ge ions implanted into SiO_2.

Disadvantages of SRIM-TRIM:

- It does not take into account the history of the target, *i.e.* ions already implanted in the matrix and damage they have generated. That means that each ion trajectory and sputtering yields are calculated considering a pure and not damaged target,
- It does not take into account effects of surface sputtering or heating of the sample over an implantation depth-profile,

- It does not take into account chemical bonds and their influence on the collision process,
- The material is considered as being a gas, with random interatomic distances.

SUSPRE (88) program developed by the university of Surrey, in collaboration with the universities of Pennsylvania and Karlsuhe, allows one to obtain similar information than SRIM-TRIM but it also enables to predict the fluence required for the complete amorphization of a target sample. However, as **SUSPRE** only takes into account primary collisions and not cascades of collisions, the amorphized thickness is generally underestimated.

SUSPRE and **SRIM-TRIM** do not take into account channeling effects (see **section III.5**) which can change the projected range. Their outputs are therefore only valid for particular experimental conditions avoiding channeling effects. To avoid channeling, the sample can be tilted and twisted. Best tilt and twist angles can be simulated by **Implant Calculator** program from Axcelis (89). For <100> c-Si, a tilt and a twist of 7° and 22° respectively are generally chosen as good conditions to maximize the interactions between the incident ions and the crystal (**Figure 24**).

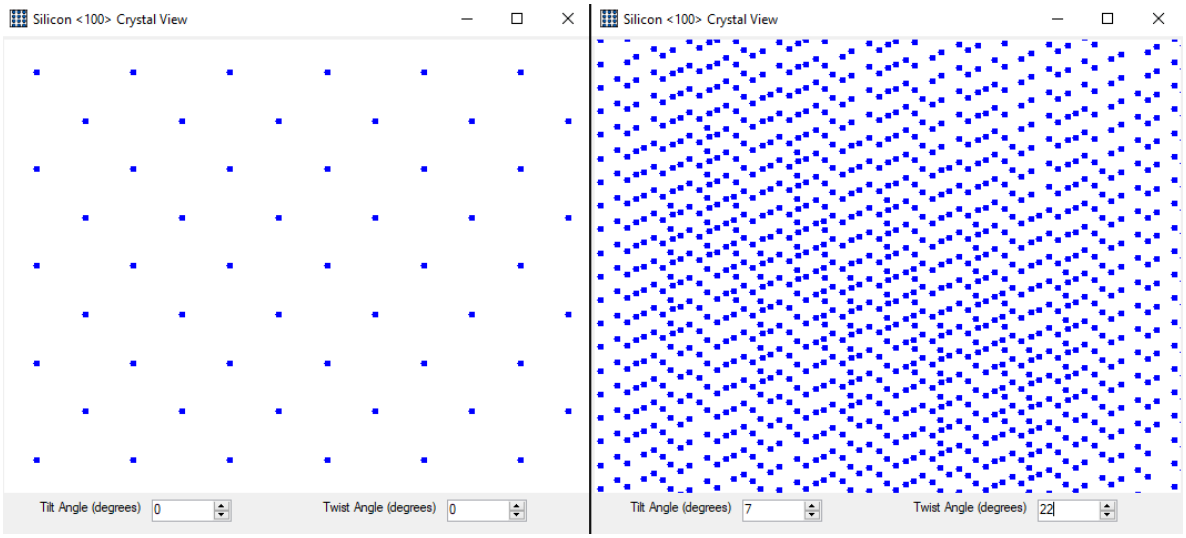

Figure 24 : Crystal view of <100> c-Si from the point of view of incident ions, as simulated by **Implant Calculator** for tilt and twist angles of 0° - 0° (left) and 7° - 22° (right). The simulation considers only the 28 first atomic planes, each blue dot representing one silicon atom.

III.2 Synthesis of germanium nanocrystals by ^{74}Ge implantation

Samples are cut into monocrystalline <100> silicon wafers (thickness ~0.38 mm) or thermally grown SiO_2/Si <100> wafers, which can be commercial or "homemade" oxides.

Samples are systematically cleaned before implantation, to remove surface contamination and to avoid undesired implantation of impurities, with acetone (C_3H_6O) prior to isopropanol (C_3H_8O) into an ultrasonic bath: 10 minutes for each bath at 25°C, 60 W, 35 kHz.

The main part of ion implantations and ion beam analyses (IBA) presented in this thesis has been performed with the ALTAÏS accelerator (**A**ccélérateur **L**inétaire **T**andétron pour l'**A**nalyse et l'**I**mplantation des **S**olides) equipped with 2 MV terminal voltage (**Figure 25**). This particles accelerator is equipped with two implantation beam lines, at low (0 – 40 keV) and high-energy (above 100 keV).

Several analyses were carried out at INSP (Institut des NanoSciences de Paris - France) with a 2.5 MV Van de Graaff accelerator. Few implantations were performed at INRS (Institut National de la Recherche Scientifique - Canada) with an implanter IMC200 ranging from 1 to 400 keV and at UDeM (Université de Montréal - Canada) with an injector converted into an implanter, which can reach implantation energies up to 120 keV.

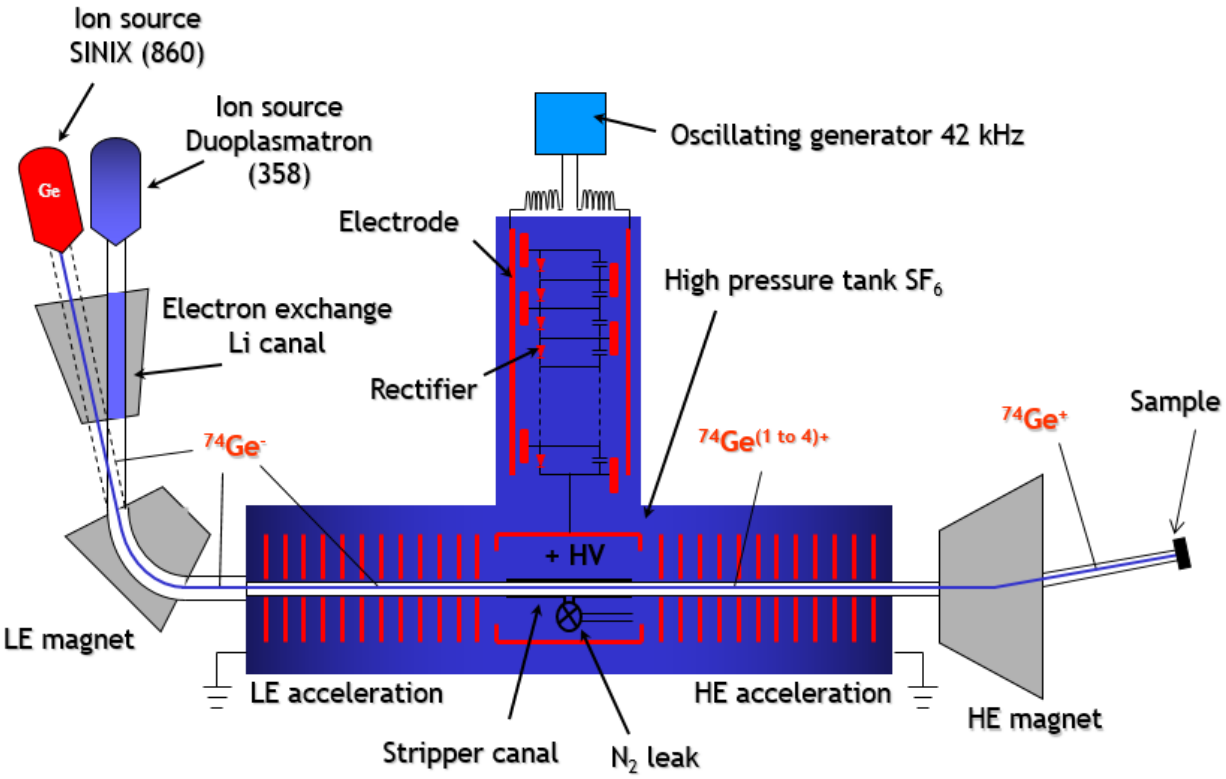

Figure 25 : Schematic representation of ALTAÏS accelerator. The low-energy (LE) station is located just after the LE magnet and the high-energy (HE) station is located in a line after the HE magnet, which ensure the selection of the line and the charge state of the ions.

The high-energy station installed on ALTAÏS is equipped with two pairs of deflector plates (horizontal and vertical), on which triangular tensions are applied (**Figure 26**). This electrostatic scanning system enables homogeneous implantation over surfaces of several cm² from a beam of 1 mm². A collimating system, composed of four tungsten plates, is placed just before the sample to delimit the implanted surface. Implantations are realized under vacuum conditions with pressure of the order of 10^{-7} mbar.

A LN_2 condenser, also called "cold finger", made of a copper cylinder, is cooled with liquid nitrogen (-196°C) and positioned in the vicinity of the sample to avoid carbon buildup by enhancing vacuum thanks to the condensation of residual molecules on the cylinder close to the sample. The sample is shifted by several centimeter with respect to the incident beam axis. An offset is applied on the vertical plates (horizontal scan), as close as possible from the sample, to guide charged particles towards the sample while letting neutral atoms continue in a straight line. In this way, nearly only charged particles reach the sample surface. This enables to limit the contribution of ions eventually neutralized by the capture of one electron on their path towards the sample, which could generate errors in the implanted dose. The LN_2 condenser is generally positioned between the vertical plates and the sample to minimize the contribution of neutral atoms generated in the latest beam line section.

A repulsive voltage is applied just before the sample on a line portion electrically isolated from the rest of the beam line (**Figure 26**). This negative tension (-200 V) ensures the reliability of the measured ionic current by repulsing secondary electrons emitted from the sample towards the sample holder. The beam current is directly measured on the conductive sample holder.

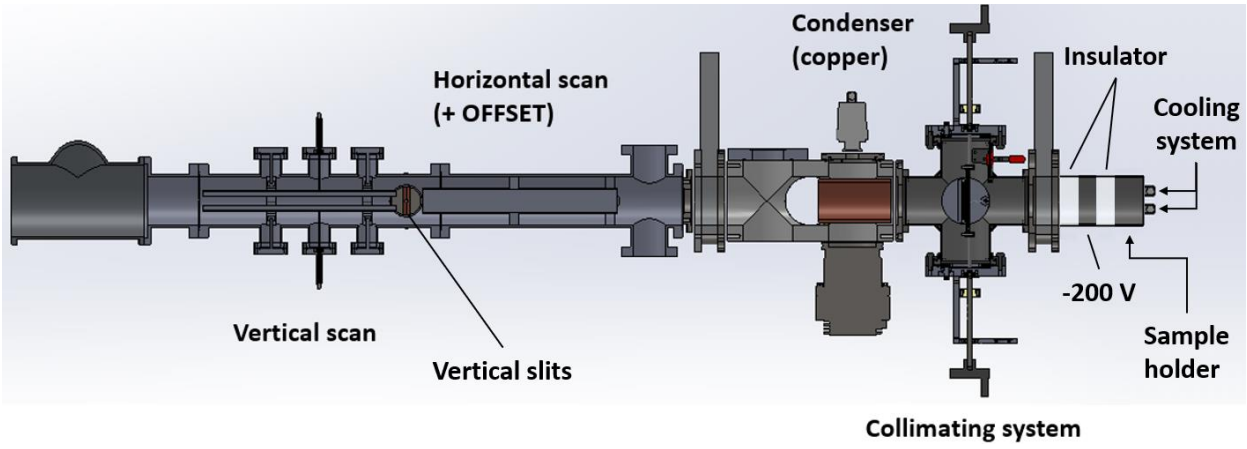

Figure 26 : Side view of the high-energy station available on ALTAÏS accelerator. Horizontal scan and offset are applied as close as possible of the sample, with the LN_2 condenser between the plates and the sample. The collimating system is positioned juste before the sample to delimit the irradiated surface. (Figure provided by T. Tabarrant)

A cooling system enables to cool down the sample holder and, by extension, the irradiated sample. SYLTHERM (90) is used as the insulating coolant, circulating inside the sample holder through an internal circuit.

ALTAÏS injector has been modified in such a way that small samples (around 2 cm²) can be positioned between the injector magnet and the acceleration column, at the faraday cup level. The isotopic selection is ensured by the 90° deflection of magnet and a rectangular collimator placed just before the sample. The cathode (0 – 10 kV) and extraction (0 – 30 kV) voltages are used as accelerating potentials. Injector geometry allows homogeneous implantations over 0.9 cm². Vertical scan is ensured by a triangular signal applied on the injector *Y-Steerer*, while horizontal scan is obtained by varying the current applied to the injector magnet.

Both irradiation stations achieve current densities of several µA/cm² for low-energy and hundreds of nA/cm² to a few µA/cm² for high-energy implanter, depending on the nature and energy of accelerated ions.

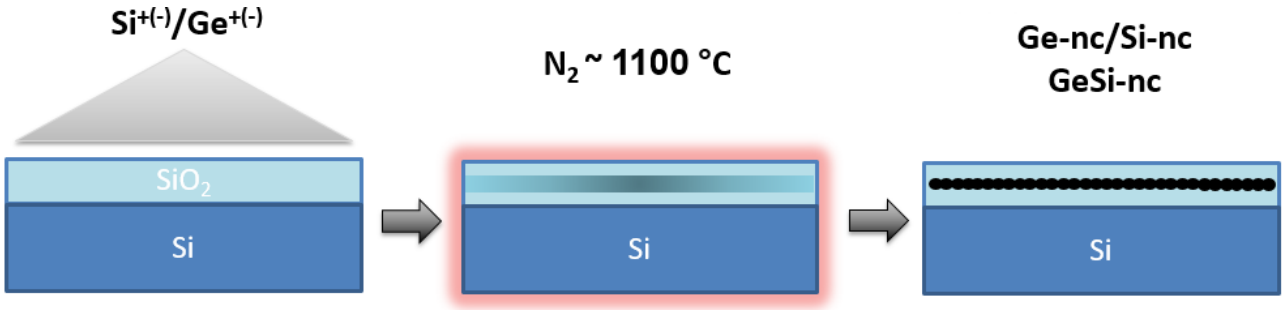

Figure 27 : Principle of Si and Ge-ncs synthesis by ion implantation: 1) implantation in SiO_2/Si over a surface of the order of 1 cm², 2) annealing under controlled atmosphere, 3) nanocrystals embedded in a SiO_2 layer.

Fabrication process of SiO_2/Si layers enriched with germanium nanocrystals is shown in **Figure 27** and presented in reference (63) for the particular case of silicon quantum dots. Nucleation is thermally activated under controlled atmosphere, which can be inert (N_2, Ar, …) or reactive (N_2 + H_2, N_2 + O_2, …), in a quartz tube furnace heated by Joule effect. A vacuum system enables to pump into the sealed tube before injecting gas up to the desired pressure.

III.3 Radiation-induced defects and amorphization

Regardless of the manufacturing process, no matter how refined, solids are always strewn with defects, whose quantity (n_D) is expressed by (91):

$$n_D = Ne^{-\Delta G/k_B T} \quad \text{(III. 5)}$$

where N is the number of atomic sites, ΔG is the Gibbs free energy, k_B is the Boltzmann constant and T is the temperature.

Although the concentration of defects is negligible in crystals at room temperature, incident ions cause a significant increase of the density of damage during the implantation process.

As mentioned in **section III.1**, implanted particles will transfer their energy to the atoms encountered along their trajectory. When the energy transfer is greater than a threshold E_d, called displacement energy, the collided atom will be moved from its atomic site with a kinetic energy $E_k = E_{transferred} - E_d$. Displaced atom will lose its entire energy and rest as an interstitial atom in the matrix. An interstitial atom leaves behind a vacancy, both forming a Frenkel pair. For example, the energy required to form a stable Frenkel pair is of the order of 15 eV in silicon (92). However, Frenkel pairs can recombine at room temperature. On the other hand, if the energy transferred to the impinged atom is high enough, the recoil atom can create another Frenkel pair and so on, generating a cascade of collisions.

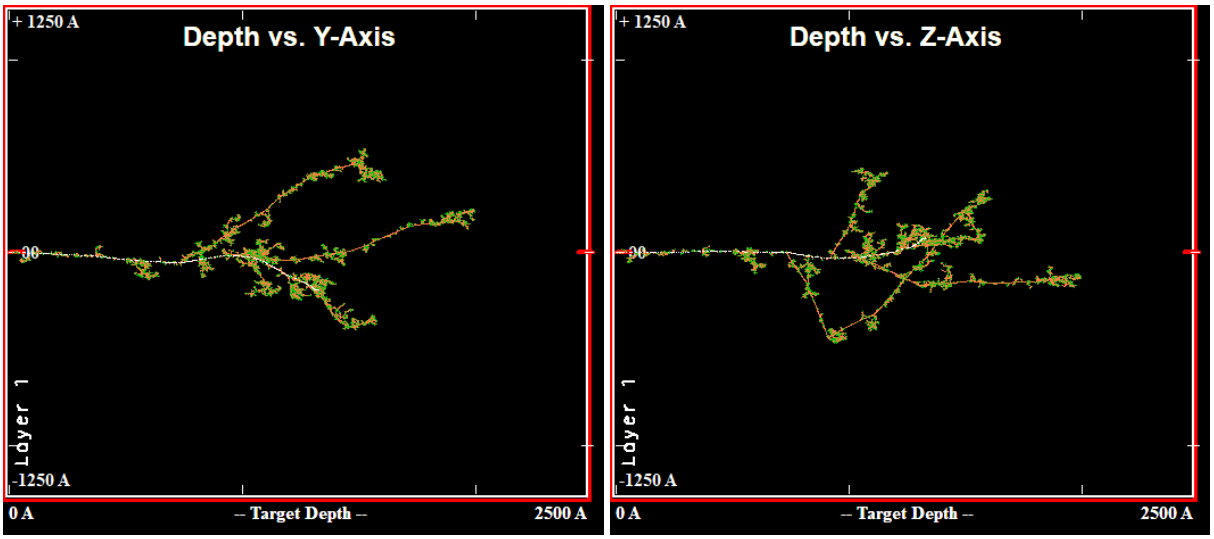

Figure 28 : Simulation SRIM-TRIM (version 2013). Full damage calculation for a single Ge ion of energy 230 keV along its trajectory through a silicon layer. Incident ion trajectory is represented in white, the trajectory of atoms displaced from their original site in red and the final positions of the displaced atoms in green.

The density of displaced atoms $N_d(x)$ can be calculated by using the Norgett-Robinson-Torrens (NRT) model (93). In NRT model, $N_d(x)$ is proportional to the implanted

fluence Φ (**Equation III.4**), to the energy lost by the incident particle by nuclear interaction $\left(\frac{dE}{dx}\right)_n$ and depends on the specific displacement energy E_d of the medium (93):

$$N_d(x) = \Phi \frac{\kappa}{2} \frac{(dE/dx)_n}{E_d} \quad \text{(III. 6)}$$

where κ is the displacement efficiency, whose value is approximately equal to 0.8. This constant is nearly independent of energy and does not depend on the temperature and the target material. Norgett et al. noticed that a vacancy left behind by an atom kicked-out from its atomic site has 20% of chances to be refilled by another kicked-out atom.

The accumulation of damage induced by implantation leads to a substantial disorganization of the implanted layer. Under specified implantation conditions (fluence, temperature, beam intensity), the accumulation of damage can be taken to advantage to generate amorphous layers, *i.e.* fully disordered films.

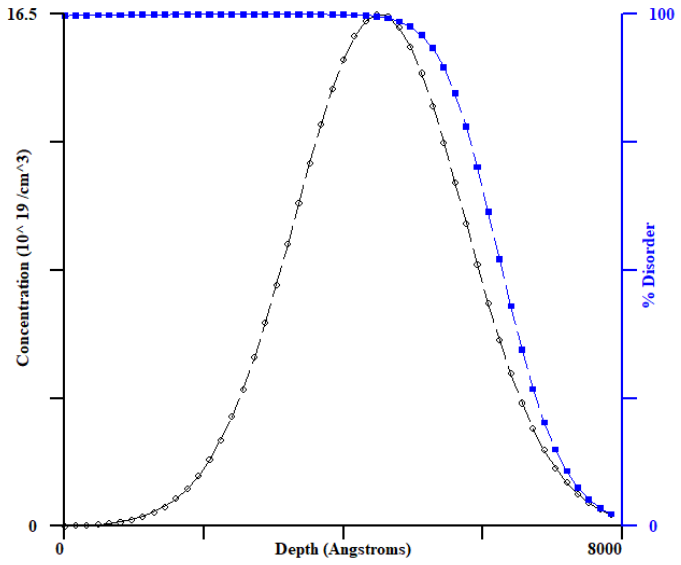

Figure 29 : SUSPRE simultation for ^{28}Si beam on a <100> c-Si substrate for the following parameters : current density 1 µA/cm², fluence 5 × 10^{15} at./cm², energy 300 keV, angle of incidence 7°.

In this thesis, a ^{28}Si (or ^{30}Si) beam is used to amorphize <100> silicon wafers. The energy and fluence of the ions are chosen according to the thickness of the layer to amorphize. For example, a fluence of 6 × 10^{15} Si/cm² is required at an energy of 600 keV to fully amorphize a silicon layer to a thickness of 1 µm (see **Figure 38** in **section III.5**).

Amorphization conditions are extremely critical:

- **Fluence** must be sufficient to induce enough defects to achieve 100 % of disorder.

- Sample must be tilted and twisted in order to optimize the beam-matter interaction and avoid **channeling**. An example of the effect of the sample orientation, from the incident ion point of view, is shown in **Figure 24**.

- **Beam intensity** is important since it defines the energy flux deposited in the sample. This parameter must be scaled along with the cooling system to ensure keeping the **sample temperature** as low as possible during the implantation process. This thermal energy transferred to the medium atoms makes the defects generated by the implantation mobile, which may induce the recombination of Frenkel pairs. The critical temperatures of common semiconductors are reported in **Table 2**. This temperature is relatively low for silicon.

Material	Critical temperature (°C)
Si	120
GaAs	140
GaP	220
SiC	350

Table 2 : Critical temperature for common materials *(92)*. This is no longer possible to amorphize the semiconductor above this temperature.

III.4 Thermal treatments

Annealing and diffusion in solids

Post-implantation annealing has two main objectives: activation of implanted atoms and regeneration of irradiation-induced defects. Elevation of temperature will increase the mobility of extrinsic and intrinsic species, whose time and concentration-dependent diffusion is described by Fick's laws. Second Fick's law expresses the temporal variation of the concentration of a specific species $C(x,t)$ as a function of its spatial variation around a position x, in one dimensional case:

$$\frac{\partial C(x,t)}{\partial t} = D_T \frac{\partial^2 C(x,t)}{\partial x^2} \qquad \text{(III. 7)}$$

where D_T is the coefficient of diffusion, which depends on the annealing temperature *T* according to an Arrhenius law:

$$D_T[cm^2/s] = D_0 e^{-E_A/k_B T} \qquad \text{(III. 8)}$$

where E_A is the activation energy and D_0 is the coefficient of diffusion at infinite temperature in [cm²/s]. For an implantation distributed according to a Gaussian depth-profile, the analytical solution of the second Fick's law is:

$$C(x,t) = \frac{\int_0^{+\infty} C(x,t)dx}{2\sqrt{\pi D_T t}} e^{-\frac{(x-R_p)^2}{4D_T t}} \qquad \text{(III. 9)}$$

where R_p is the projected range and *t* the annealing time.

Thermal treatments will provide enough energy to the implanted species to increase their mobility and initiate the formation of nanocrystals by Ostwald ripening process, thanks to a higher coefficient of diffusion.

As previously discussed, the density of defects is non-negligible in implanted samples. The presence of such defects generally favors diffusion. However, in the particular case of Ge ions implanted in SiO_2 layers, a high density of silicon dangling bonds are formed through the oxide. These unsaturated bonds act as trapping centers and diffusion barriers for Ge, as experimentally demonstrated in **chapter IV**.

In the specific case of photovoltaic cells, defects act as points of recombination for charge carriers. The presence of damage therefore contributes to reduce the efficiency of photovoltaic cells. Annealing can regenerate the crystal structure of the damaged layers by providing enough energy to point defects to make them mobile. The recrystallization rate

(v_{SPE}) of an amorphous layer on top of a crystalline substrate occurs by solid-phase epitaxy (SPE) and is expressed by (92):

$$v_{SPE} = v_0 e^{-E_{SPE}/k_B T} \quad \text{(III. 10)}$$

where k_B is the Boltzmann's constant, T is the temperature, v_0 depends of the crystal orientation and E_{SPE} is an activation energy (~2.70 eV in silicon (94)). During annealing, interstitial atoms and vacancies, forming Frenkel pairs, will recombine. Residual point defects will either diffuse towards the surface or agglomerate to form complex structural defects, called extended defects, such as dislocation loops, clusters of interstitials or vacancies, internal surfaces (2D defects), ect.

Material	E_{SPE} **[eV]**	v_0 **[m/s]**	v_{SPE} **= 0.1 to 10^4 Å/s**
Si	2.70	4.64×10^6	500 - 800°C
Ge	2.15	2.60×10^7	315 - 530°C

Table 3 **:** Values of activation energy and pre-exponential factor for Si and Ge in the direction <100>, and temperature range to obtain a SPE rate ranging from 0.1 to 10000 Å/s *(95)*.

Oxidation

The SiO_2 substrates used in this thesis to host the Ge quantum dots are fabricated by the oxidation of silicon wafers. The oxidation of silicon is a natural phenomenon already occurring at room temperature, whose oxidation rate is enhanced with the elevation of temperature, increasing the mobility of atoms and defects, which is proportional to e^{-1/k_BT} (**Equation III.8**). Oxidation is generally thermally activated in a quartz tube heated under an oxygen atmosphere.

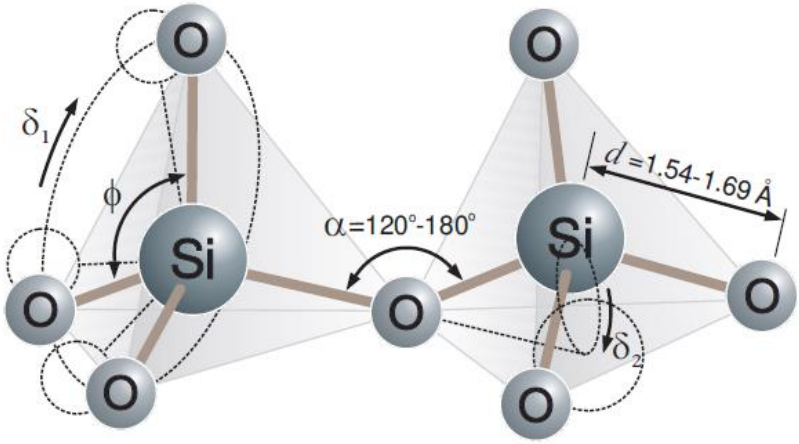

Figure 30 : Tetrahedral structure of SiO_2 *(96)*.

Two types of thermal oxidation can be distinguished: dry or humid. The chemical reactions of oxidation are given by:

$$Si + O_2(g) \rightarrow SiO_2 \qquad \text{in dry conditions}$$

$$Si + 2H_2O(g) \rightarrow SiO_2 + 2H_2(g) \qquad \text{in humid conditions}$$

Even if oxidation rate is higher for humid atmosphere (**Figure 31**), due to higher solubility and diffusivity, dry oxidation is commonly privileged to avoid undesirable hydrogen contamination.

Oxygen is generally considered as the mobile species responsible for oxidation, its mobility is made possible by defects (interstitial or lacunar) present in silicon. The growth kinetics of a thermal oxide can be described by the theory of Deal and Grove (97), which however does not take into account parameters such as surface exchanges or out-diffusion of SiO from the SiO_2/Si interface. Deal and Grove theory predicts a linear parabolic growth expressed by:

$$\frac{X^2}{k_p} + \frac{X}{k_L} = t + \tau \qquad \text{(III. 11)}$$

where X is the oxide thickness, k_p and k_L the parabolic and linear constants, t is the oxidation time and τ is a parameter taking into account the presence of an initial oxide. k_L is proportional to the reaction rate ($Si + O_2 \rightarrow SiO_2$) and k_P is proportional to the coefficient of diffusion of the oxidizing species, both dependent of the temperature. k_L and k_P are also proportional to the gas pressure and inversely proportional to the number of oxidizing species required to form an unit volume of SiO_2 (2.25×10^{22} at./cm³ for O_2 and 4.5×10^{22} at./cm³ for H_2O). $A = k_p/k_L$ represents a critical thickness beyond which linear growth becomes parabolic. Deal and Grove theory well fits experimental results for humid oxidation whatever the oxide thickness and for dry oxidation for thicknesses higher than 20 – 30 nanometers.

Charts based on Deal and Grove theory make possible to estimate, in a relatively reliable way, the time required to form a given thickness of oxide as a function of temperature, gas pressure, type of oxidation (dry, humid), crystal orientation, doping, etc.

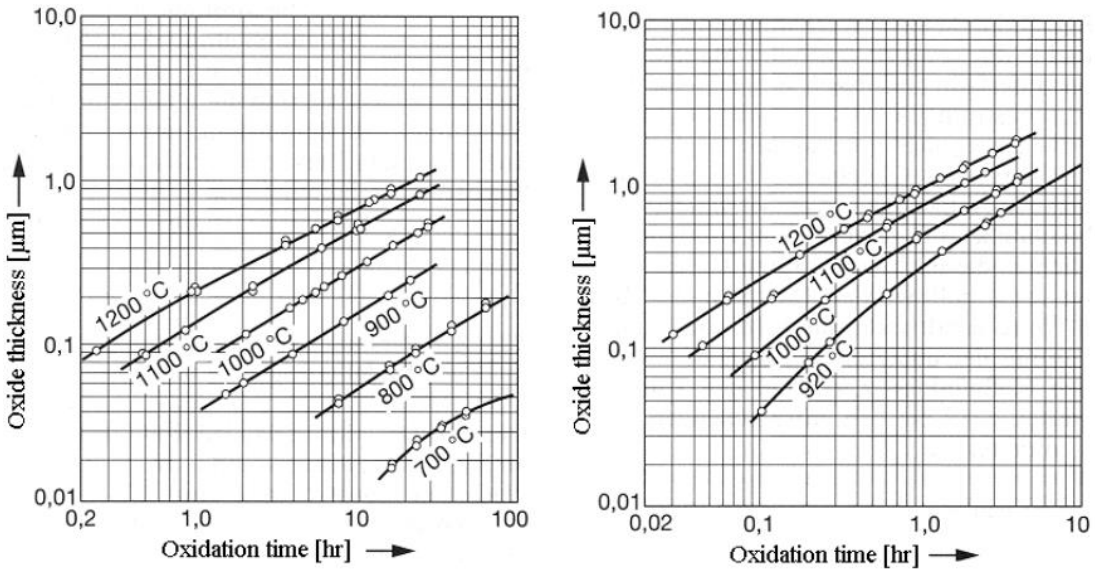

Figure 31 **:** Evolution of oxide thickness, for oxidation of <111> Si, as a function of time and temperature for dry (left) and humid oxidation (right) at 760 Torr *(97), (98), (99)*. Open circles represent experimental data and the solid lines are adjustment by Deal and Grove model.

Thermal oxide growth is the most widely used technique nowadays. However, SiO_2 films can also be obtained by other processes such as plasma deposition techniques (100) or anodic oxidation (101).

In this thesis, we used both thermal growth and plasma deposition, as will be presented in **chapter IV**.

III.5 Ion beam analyses

RBS – Rutherford Backscattering Spectroscopy

Rutherford backscattering spectroscopy is a relevant technique for analyzing heavy chemical elements embedded in a matrix of lighter elements. This non-destructive technique enables to probe a material in order to extract the elemental concentration profile as a function of depth. This technique is particularly suitable for highlighting the implantation depth-profiles of heavy ions in thin films.

RBS is based on a classical binary collision (**Figure 32**), with pure Coulomb interactions, occurring between the incident ions, used for probing matter, and the target atoms constituting the sample. Light ions (mainly protons ($^1H^+$) or α particles ($^4He^+$)) are accelerated with energies of the order of MeV and scattered by the target atoms. In RBS analyses, only backscattered particles are detected, meaning that only scattering angles θ greater than 90° are considered.

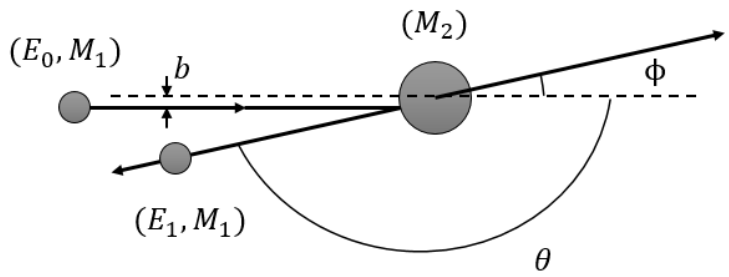

Figure 32 : Schematic representation of a binary collision between the incident projectile and the impinged target atom with a small impact parameter *b*. θ and ϕ are the scattering and recoiling angles respectively.

During the interaction between the incident particle and a target atom, a fraction of the particle energy is transferred to the target. The final energy of the backscattered particle is therefore smaller than its initial energy. Assuming that the projectile (M_1) is lighter than the target atom ($M_1 < M_2$), the ratio between final (E_1) and initial (E_0) energies is given by the kinematic factor *K*:

$$K = \frac{E_1}{E_0} = \left(\frac{\sqrt{\left(\frac{M_2}{M_1}\right)^2 - sin^2\theta} + cos\theta}{1 + \frac{M_2}{M_1}} \right)^2 \qquad \text{(III. 12)}$$

Note that K factor depends on the colliding masses (M_1 and M_2) and the scattering angle θ. Kinematic factors of germanium and silicon targets, for α particles and a scattering angle of 165°, are $K_{Ge} = 0.805$ and $K_{Si} = 0.569$.

This kinematic factor is important since it serves as the basis for elementary identification. The parameters E_0, M_1 and θ being known, it is possible to derive the mass of the target element, M_2, from the energy measurement of the backscattered particles. For example, the tabulated values of the kinematic factor tell us that α particles of energy $E_0 = 3\ MeV$ will be backscattered at 165° with an energy E_1 of about 2.415, 1.707 and 1.098 MeV by ^{74}Ge, ^{28}Si and ^{16}O surface atoms respectively (**Figure 33**).

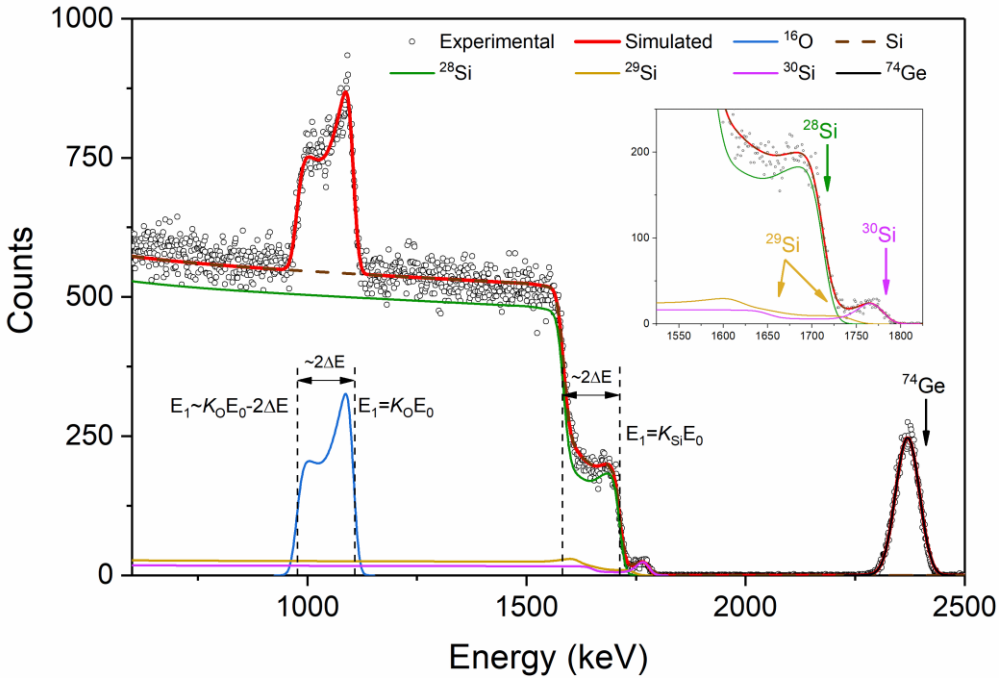

Figure 33 : RBS spectrum of a SiO_2 layer implanted with ^{74}Ge (230 keV, 8 × 10^{16} at./cm²), ^{30}Si (36 keV, 2 × 10^{16} at./cm²) and ^{29}Si (170 keV, 2 × 10^{16} at./cm²) for 3 MeV α particles and a detector angle of 165°, for an integrated charge of 10 µC. The double arrow for ^{29}Si corresponds to ^{29}Si at the sample surface and to the implantation in depth. The layer between 1575 and 1720 keV visible in ^{28}Si signal corresponds to silicon in the SiO_2 layer.

If the scattering does not occur with atoms present at the surface but deeper in the target, the incident ion will lose a fraction of its energy while travelling through the material, as discussed in **section III.1**, before and after the scattering event. The fraction of energy lost depends on the stopping power and is mainly due to electromagnetic interactions with electrons of the target atoms at energies considered for RBS analysis (see **Figure 21**). While travelling through the SiO_2 layer, α particles lose an amount of energy ΔE to reach a depth *x*. The backscattered particles hence have lost an amount of energy of approximately $\sim 2\Delta E$ by crossing the SiO_2 film, where the factor ~ 2 is due to the travel through SiO_2 in forward and backward directions, before and after the scattering event assuming a constant stopping power. In practice, the amount of energy loss will depend on the stopping power, which continuously varies with the ion energy. The measured energy of the backscattered particle therefore depends on the depth at which the scattering event occurs and provides information on the depth-distribution of these target atoms.

Finally, we must consider that the incident ions have a given probability of colliding with target nuclei. This probability is given by the differential elastic scattering cross section, which is, in the laboratory system, expressed by:

$$\left(\frac{d\sigma}{d\Omega}\right)_{lab} = \left(\frac{Z_1 Z_2 e^2}{4E}\right)^2 \frac{4}{sin^4\theta} \frac{\left(\sqrt{1-\left(\frac{M_1}{M_2}\,sin\theta\right)^2} + cos\theta\right)^2}{\sqrt{1-\left(\frac{M_1}{M_2}\,sin\theta\right)^2}} \qquad \text{(III. 13)}$$

where $d\Omega$ is the solid angle of detection

θ is the scattering angle (backscattering if $\theta \geq 90°$)

E is the kinetic energy of the incident ion at which the scattering event occurs in the lab system

Z_1, Z_2 are the atomic numbers of the incident ions and the target atoms respectively

Note that the differential cross section is directly proportional to the square of the atomic number of the target nucleus, Z_2. This analysis technique will therefore be more efficient in detecting heavy atoms such as germanium (Z_2 = 32) rather than silicon atoms (Z_2 = 14), especially in a silicon-based sample. However, for lighter nucleus, it is possible to take advantage of resonances at particular incident energies to highlight their contribution.

RBS quantifies the areal density $N_i.t$ of atoms of a specific element *i* present in the sample from the peak area without the need of reference standards:

$$Y_i = N_i t\; Q\Omega \left(\frac{d\sigma}{d\Omega}\right)_i \frac{1}{cos\alpha} \qquad \text{(III. 14)}$$

where Y_i is the integrated yield of backscattered ions from element *i*, Q is the number of incident ions striking the sample surface and α is the angle of incidence. The product $Q\Omega$ ([particles.sr]) is measured experimentally and the cross section is tabulated. The product $N_i t$ is called the areal density (given in [10^{15} at./cm²]), from which, knowing the layer density N_i, once can derive its thickness *t*.

Although RBS is reputed as being a non-destructive technique, we must mention that the irradiation-induced damage are not null. However, as RBS uses high-energy light particles such as $^1H^+$ or $^4He^+$, the sample deterioration is therefore largely limited. Moreover, if the majority of the particles are implanted in the sample rather than being backscattered, the energies and masses of incident ions result in high projected ranges: R_p is about 11 µm and 85 µm, for $^4He^+$ and $^1H^+$ respectively, in SiO_2 at $E_0 = 3$ MeV. Hence, the incident particles are implanted far from the region of interest, which generally lies within the first micron.

In RBS, the energy separation of backscattered particles ΔE_1, for a fixed angle of detection, is given by (102):

$$\Delta E_1 = E_0 \left(\frac{dK}{dM_2}\right) \Delta M_2 \qquad \text{(III. 15)}$$

where E_0 is the incident particle energy, K is the kinematic factor, M_2 is the target mass and ΔM_2 is the mass difference (in case of compounds or different isotopes). dK/dM_2 is the evolution of K as a function of the mass of the target atoms, which is larger for light elements (**Figure 34**). Energy separation increases with the energy of the incident ions and the difference in mass of the target atoms. The change in K, for a given ΔM_2, is maximal for a scattering angle θ equal to 180°, explaining why large scattering angles are preferred experimentally.

Considering the lowest energy separation achievable by the experimental setup ($\Delta E_1 = \delta E$), the mass resolution of the system is (102):

$$\delta M = \frac{\delta E}{E_0} \left(\frac{dK}{dM_2}\right)^{-1} \qquad \text{(III. 16)}$$

Mass resolution is proportional to the energy resolution δE, which depends on the detector resolution at the sample surface and is dominated by straggling in depth. For a fixed $\frac{\delta E}{E_0}$, δM depends on $\left(\frac{dK}{dM_2}\right)^{-1}$, which is low for masses corresponding to silicon isotopes implanted in this thesis (see **article III** in **chapter IV**).

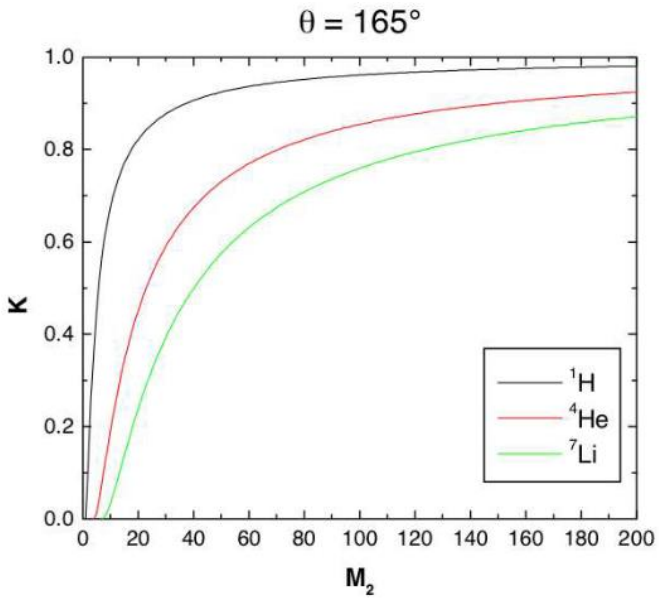

Figure 34 **:** Evolution of kinematic factor as a function of incident ion and target atom masses for a detection angle of 165° *(103)*.

RBS spectra have been fitted with SIMNRA (104) in combination with SIMTarget program (105), developed at LARN. As known from literature and simulations (**section III.1**), implantation profiles can be approximated by Gaussian distributions. SIMTarget enables the creation of Gaussian depth-profiles for SIMNRA simulations. However, one must note that, because of energy straggling and detector resolution, depth resolution is about 300 × 10^{15} at./cm² (or 300 TFU - for Thin Film Units) at the SiO_2/Si interface for an oxide thickness of 300 nm, corresponding to ~2000 TFU (**Figure 35c**). As shown in **chapter IV**, the Ge accumulation at the vicinity of this interface occurring during annealing generally extends on the same order of TFU (**Figure 35a-b**). Therefore, Ge contribution at the interface could be fitted by both a Gaussian and a rectangular function without being able to differentiate them. **Figure 35** shows two fits with Gaussian and rectangular functions with the same FWHM (250 × 10^{15} at./cm²). Although the fit with the rectangular function in not so far from the Gaussian fit, **Figure 35** shows that the tails of the peak are better fitted with a Gaussian function considering an identical FWHM. Moreover, as this accumulation is the consequence of both Ge diffusion and trapping effects near the SiO_2/Si interface, it appears more realistic to consider a germanium distribution which is not abrupt. Therefore, we assume to fit our results with Gaussian functions in **parts IV** and **V**.

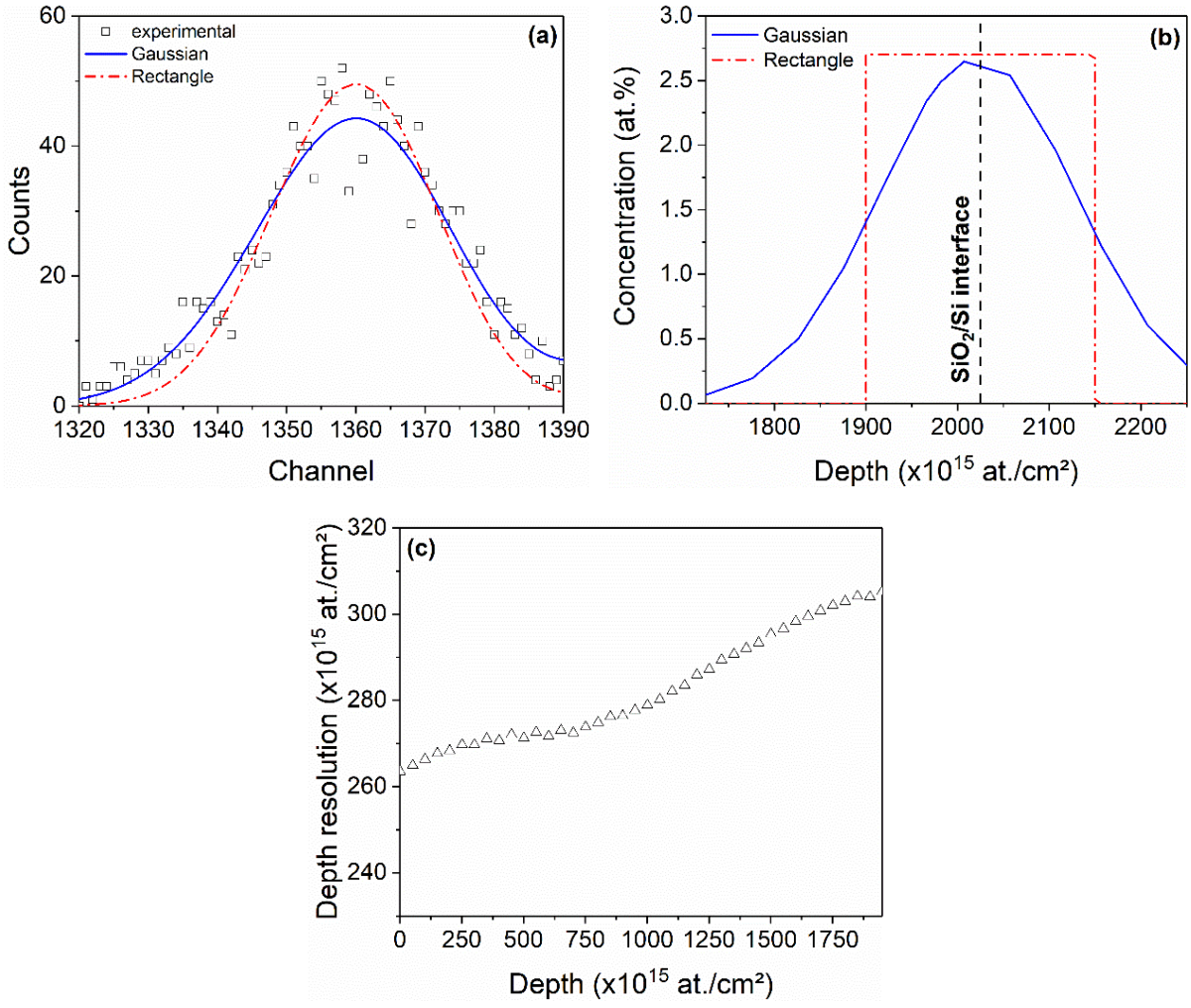

Figure 35 : (a) Fit of experimental data (Ge at the SiO_2/Si interface for an oxide thickness of 300 nm) with the gaussian and rectangular functions presented in (b). (c) Depth resolution for Ge calculated by ResolNRA for a Ge-implanted SiO_2 layer.

RBS/C - Channeling

Channeling provides information on atomic structures and crystallinity, on the depth-distribution of defects and interstitials, and allows one to highlight the presence of low concentrations of elements, which would be hard to observe in “classical” RBS.

RBS/C is a particular application of RBS analysis, which takes advantage of the crystalline structure of matter. There is a finite probability for the trajectory of an ion beam to be aligned with the crystallographic axes or planes of a crystalline sample. When a positive ion penetrates in a crystallographic axis or between planes, it will undergo a succession of repulsive interactions with the nuclei of the atomic rows (**Figure 36**).

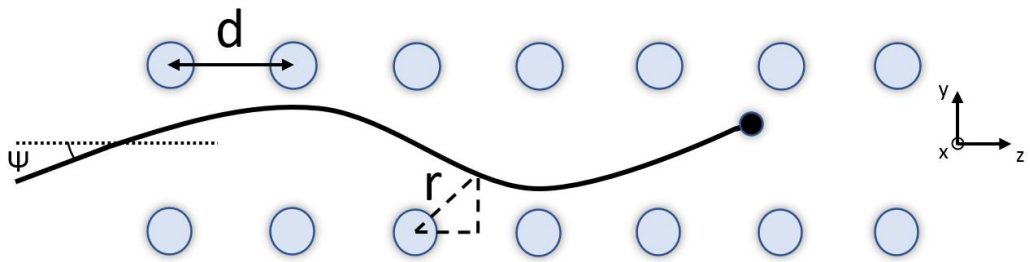

Figure 36 **:** Schematic representation of a charged particle channeled along a crystallographic axis or plane.

According to the model initially introduced by Lindhard in 1965, channeled ions undergo a succession of two-body interactions with network atoms, which can be seen as a continuous potential along the axes and planes of the atomic network (106), (107):

$$U(r) = \frac{Z_1 Z_2 e^2}{d} ln\left[\left(\frac{aC}{r}\right)^2 + 1\right] \qquad \text{(III. 17)}$$

For an axial channeling, where d is the mean interatomic distance, r is the distance between the atoms and the incident ions, C is a constant usually taken equal to $\sqrt{3}$ and a is the screening radius of Thomas-Fermi (106), (107):

$$a = 0.8853 a_0 \left(Z_1^{\frac{1}{2}} Z_2^{\frac{1}{2}}\right)^{-\frac{2}{3}} \qquad \text{(III. 18)}$$

with $a_0 = 5.292\ 10^{-11}\ m$, the Bohr radius.

The ion total energy within the crystal is given by the sum of kinetic and potential energies:

$$E_{TOT} = U(r) + \frac{p_x^2 + p_y^2 + p_z^2}{2M} \qquad \text{(III. 19)}$$

where p_i is the momentum of the non-relativistic particle in the i[th] direction and M is its mass. Since the total energy E_{TOT} and the forward energy $p_z^2/2M$ can be considered constant over the dimensions involved for the steering of a channeled particle, the trajectory can be totally described by solving the projected motion in the *XY* - or transverse - plane where the ions move with a velocity equal to $v_\perp = v\,sin\Psi$, with Ψ the penetration angle. The constant "transverse" energy is given by:

$$E_\perp = U(r) + \frac{p_x^2 + p_y^2}{2M} sin^2\Psi \qquad \text{(III. 20)}$$

The continuum potential approximation is only valid for ions close to the center of the channels, *i.e.* for low penetration angles Ψ. By the small angles approximation, $sin\,\Psi \approx \Psi$, the transverse energy is expressed by:

$$E_\perp = U(r) + E\Psi^2 \qquad \text{(III. 21)}$$

Ions approaching too close to atomic rows have a high probability to be dechanneled. A critical angle of incidence Ψ_c, associated to a minimum approach distance r_{min} between the ions and the atoms in a row, can be defined. It corresponds to the maximum angle for which the incident particles will be channeled. Ψ_c is obtained according to the principle of conservation of the transverse energy, between the penetrating point, for which $U(r) = 0$, and the point closest to the row at which $\Psi = 0°$:

$$E_{inc} = E(r_{min}) \Leftrightarrow E\Psi_c^2 = U(r_{min}) \qquad \text{(III. 22)}$$

$$\Psi_c = \sqrt{\frac{U(r_{min})}{E}} \qquad \text{(III. 23)}$$

For an axial channeling, the critical angle is expressed as:

$$\Psi_c = \frac{\Psi_1}{\sqrt{2}} \sqrt{ln\left[1 + \left(\frac{Ca}{r_{min}}\right)^2\right]} \quad \text{with} \quad \Psi_1 = \sqrt{\frac{2Z_1Z_2e^2}{Ed}} \qquad \text{(III. 24; III. 25)}$$

Ψ_c depends on the atomic numbers Z_i of the nuclei involved and is inversely proportional to the energy of the incident ions E and to the interatomic distance d.

The critical angle value is lower than 1° for $^4He^+$ particles of 1 MeV penetrating in monocrystalline silicon (106).

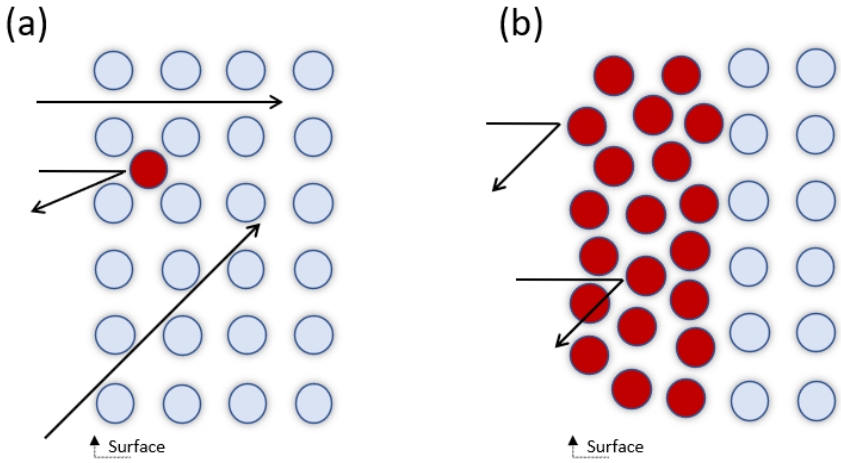

Figure 37 **:** Schematic representation of (a) a monocrystalline structure with one interstitial atom in red, and (b) an amorphous layer on top of a crystalline substrate.

By aligning the ion beam with the main crystallographic axes or planes, the probability of interaction, and therefore the rate of energy loss and elastic backscattering, decreases as more as the material is monocrystalline and exempt of defects (**Figure 37**). Hence, the backscattering yield in RBS/C is smaller compared to classical RBS analyses when the ion beam trajectory is aligned with the crystal. The minimum yield measured in aligned condition is noted χ_{min}. The ions oscillate in these natural channels until they are dechanneled by a defect (such as a dislocation), an interstitial impurity or a self-interstitial nucleus.

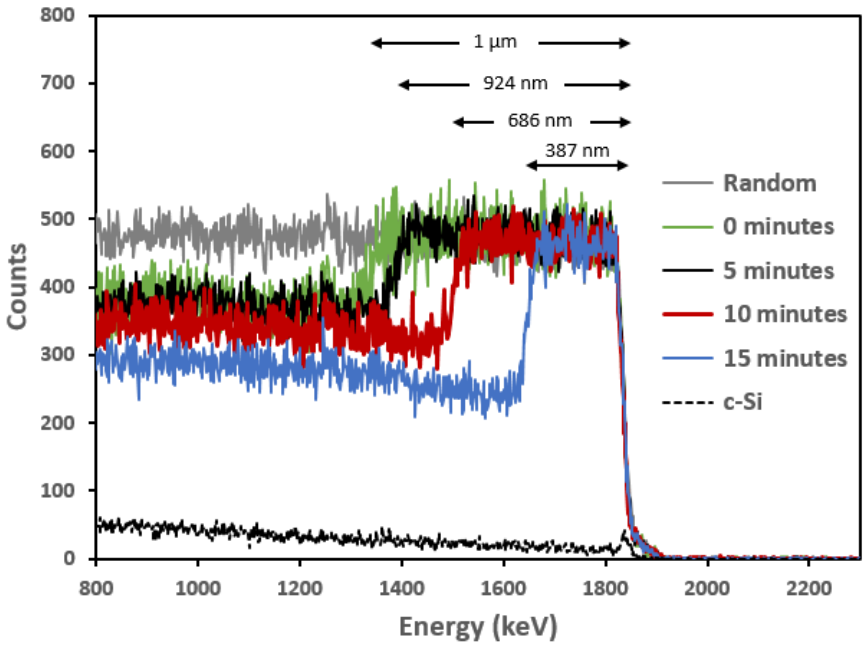

Figure 38 **:** RBS/C spectra of an aligned <100> c-Si sample (black dotted line) and samples amorphized over a thickness of a 1 µm a-Si layer (on a Si substrate) annealed at 600°C for different annealing times. Each time corresponds to the annealing of a different sample. The recrystallization of the a-Si layer is observed from the substrate towards the sample surface. The backscattering yield is drastically reduced in crystalline samples when the beam trajectory is aligned with the crystal.

The experimental recrystallization rate of the Si amorphous layer measured in this work and presented in **Figure 38** is in good agreement with the experimental values measured by *Csepregi et al* (108). This confirms the *SPE* regrowth occurring from the c-Si substrate

discussed in **section III.4**. The yield observed under 1375 keV in the amorphized sample stays high compared to c-Si due to ion dechanneling in the thick a-Si layer. The more the a-Si layer is thick, the more the dechanneling occurs.

Channeling also allows estimation of the strain of a pseudomorphic film by probing the layer through two different crystallographic orientations (109), (110), (111):

$$\theta = \tan^{-1}\left(\frac{a_{//}}{a_{\perp}}\right) \qquad \text{(III. 26)}$$

where θ is the angle between both crystallographic orientations. $a_{//}$ and $a_{\perp}$ are the lattice parameters respectively parallel and perpendicular with respect to the sample surface. The angle shift $\Delta\theta$ between the substrate and the alloy in <110> direction is expressed by:

$$\Delta\theta = \theta_{film} - \theta_{substr.} \qquad \text{(III. 27)}$$

which enables to estimate the tetragonal strain ε_T in a pseudomorphic film:

$$\varepsilon_T = \varepsilon_{//} - \varepsilon_{\perp} = \frac{\Delta\theta}{sin\theta_{substr.}\, cos\theta_{substr.}} \qquad \text{(III. 28)}$$

A negative tetragonal strain (ε_T) indicates a tensile strain in the direction <100> and a compressive strain inside the (100) planes, as represented in **Figure 39**.

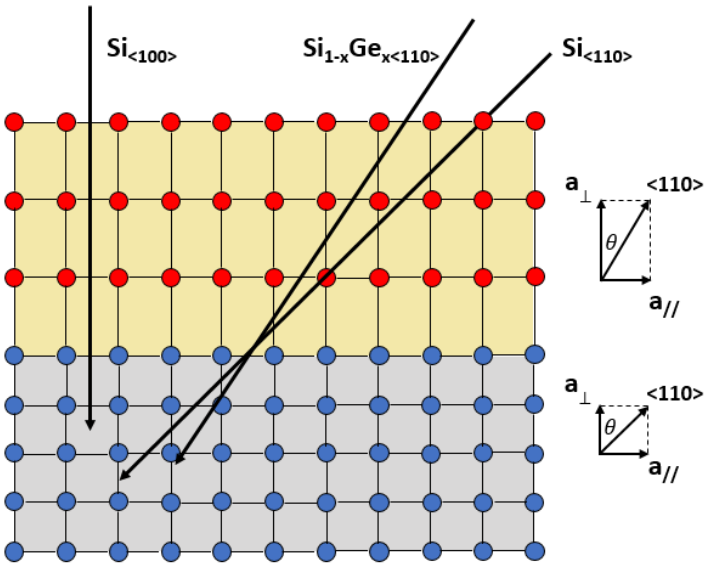

Figure 39 : Schematic representation of channeled particles through a strained $Si_{1-x}Ge_x$ layer on a <100> Si substrate. In this pseudomorphic $Si_{1-x}Ge_x$ layers, the film and the substrate are aligned in the <100> orientation. In the <110> direction strain forces a misalignment of the layer compared to the substrate.

Channeling will be used in **chapter V** to highlight both the crystallinity and the state of strain of the $Si_{1-x}Ge_x$ top layers formed by ion implantation in c-Si substrates.

NRA – Nuclear Reaction Analysis

Nuclear reaction analysis quantifies low *Z* elements in thin films using light ions (^{1}H, d, ^{3}He, α) as a function of depth with a single energy and a single measurement. Such as RBS spectroscopy, NRA is commonly considered as a non-destructive technique.

This technique is based on the detection of charged particles and/or γ rays produced during a nuclear reaction inside the target sample. If the energy of the incident particle (noted a in the following equations) is sufficient to cross the Coulomb barrier of the target nucleus (A) by tunneling effect (*Z* dependent), a nuclear reaction can occur between both nuclei. The reaction product will be either a compound nucleus in an excited state (C^*), which will de-excite by emitting γ radiations, or several nuclei including a heavy nucleus ($B^{(*)}$), called residual (which can be in an excited state) and at least one light nucleus (b).

$$a + A \rightarrow C^* \quad \Rightarrow \quad C^* \rightarrow C + \gamma \tag{III. 29}$$

Or

$$a + A \rightarrow B^{(*)} + b \tag{III. 30}$$

The nuclear reactions of **equations III.29** and **III.30** are generally written as $A(a,\gamma)C$ and $A(a,b)B$ respectively.

The energy balance of the reaction (called $Q\text{-}value$) is given by well-known mass-action law, $E = Mc^2$:

$$Q\text{-}value = [M_A + M_a - M_B - M_b]c^2 \tag{III. 31}$$

The reaction can be either endo-energetic ($Q\text{-}value$ < 0) or exo-energetic ($Q\text{-}value$ > 0). In the latter case, the energy produced during the reaction is distributed between the products under the form of kinetic energy. If the residual nucleus is in an excited state (asterisk in **Equation III.30**), the kinetic energy shared by the residual atom and the light particle decreases by a quantity equal to the energy level of the residual atom.

If the cross section $\frac{d\sigma}{d\Omega}$ for a given nucleus remains constant for a small variation of the incident energy E_i, then the areal density $N_i t$, in [at./cm²], can be quantified in successive thin layers:

$$Y_i = N_i t \; Q\Omega \; \frac{d\sigma}{d\Omega}\frac{1}{cos\alpha} \tag{III. 32}$$

where Y_i is the integrated yield, Q is the number of incident particles, Ω is the solid angle and α is the angle of incidence.

When the cross section $\frac{d\sigma}{d\Omega}$ is unknown, the measurement is generally compared to a well-known sample, called a reference standard:

$$N_i t = \frac{Y_i}{Y_{Stand}} (N_i t)_{stand} \quad \text{(III. 33)}$$

This method can be used for quantitative measurements. In the case of depth profiling, two conditions must be respected:

1. The composition of the standard sample has to be similar to that of the analyzed sample.
2. Standard and analyzed samples must have a uniform composition in depth to avoid cross section integration effects.

NRA results are presented in **chapter IV** – **article II**, with the quantification of ^{16}O and ^{18}O isotopes using $^{16}O(d,\alpha)^{14}N$ and $^{18}O(d,\alpha)^{16}N$ reactions respectively.

RNRA – Resonant Nuclear Reaction Analysis

Resonant nuclear reaction profiling (also called NRP for Narrow Resonant Profiling) is based on the use of nuclear reactions whose cross sections present very narrow resonances ($\Gamma \sim$ 100 eV). These resonances enable isotopic profiling of the material.

If the energy of the incident ion is finely tuned to precisely reach an excited state of the compound nucleus, then the reaction becomes more likely. A first estimate of the probed depth is given by (102):

$$x = \frac{E_0 - E_R}{S(E_R)/cos\alpha} \qquad \text{(III. 34)}$$

with E_0 the energy of the incident ions, $\alpha$the incident angle, E_R the resonance energy and $S(E_R)$ the stopping power of the matrix. The sample is profiled in depth simply by gradually increasing the energy of incident ions, which requires many successive measurements. Depth resolution is given by (102):

$$\Delta x = \frac{\sqrt{\Gamma_R^2 + \frac{x}{cos\alpha}\sigma_{st}^2 + \Delta E_{beam}^2 + \Delta E_{ms}^2}}{S(E_R)/cos\alpha} \qquad \text{(III. 35)}$$

with σ_{st} the energy straggling of the incident ion, Γ_R the width of the resonance, ΔE_{beam} the energy spread of the beam, α is the angle of incidence and ΔE_{ms} the energy spread due to small-angle multiple scattering.

RNRA analyses are presented in **chapter IV** for profiling ^{29}Si, ^{30}Si and ^{18}O isotopes with ^{29}Si(p,γ)^{30}P, ^{30}Si(p,γ)^{31}P and ^{18}O(p,α)^{15}N respectively. The width of ^{29}Si(p,γ)^{30}P resonance is shown in **Figure 40**.

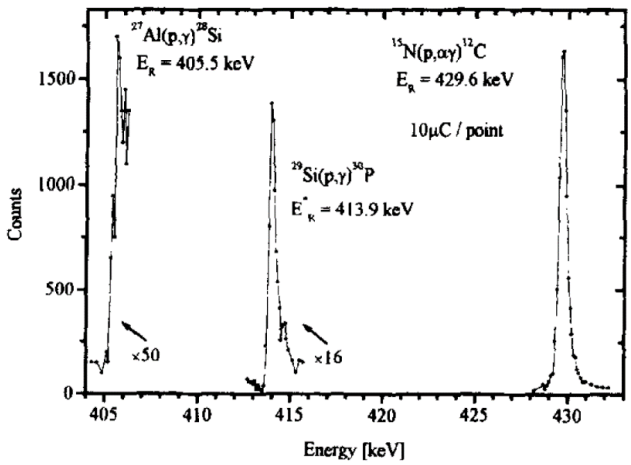

Figure 40 **:** Experimental results of resonance energy measurements for ^{27}Al, ^{29}Si, ^{15}N *(112)*.

III.6 Optical spectroscopies

Raman spectroscopy

Raman spectroscopy is a rapid technique adapted to elemental and chemical bonding identification, as well as to highlight crystallization state, molecular structure or strain. Raman is more adapted to the study of non-polar chemical bonds, *i.e.* for bonds between atoms with similar electronegativities.

This non-destructive technique is based on the inelastic scattering of a monochromatic radiation of energy $E_0 = hv_0 = \frac{hc}{\lambda_0}$ (in the UV-VISIBLE range) by molecules constituting the studied medium. Molecules vibrational states are excited by absorbing photons energy before de-exciting by emission of a new photon, whose frequency may be either equal (Rayleigh scattering) or different from v_0 (Raman scattering). The energy of photons considered in Raman spectroscopy only enables transitions between the vibrational energy levels of the molecules.

The oscillating electric field $\vec{E} = \vec{E}_0 \cos(\omega_0 t)$ of the incident electromagnetic wave induces the creation of an oscillating electric dipolar moment in molecules:

$$\vec{P} = \alpha\vec{E} = \alpha\vec{E}_0 \cos(\omega_0 t) \qquad \text{(III. 36)}$$

where α is the polarizability, defined as the ease with which the electron cloud is distorted by an external electric field and $\omega_0 = 2\pi v_0$ is the angular frequency. α depends on the displacement $q = q_0 \cos(\omega_m t)$ of the oscillating atoms (1D case). For a development in Taylor series around the equilibrium position ($q = 0$):

$$\begin{aligned}\alpha &= \alpha_0 + \frac{1}{1!}\left(\frac{\partial\alpha}{\partial q}\right)_{q=0} q + \frac{1}{2!}\left(\frac{\partial^2\alpha}{\partial q^2}\right)_{q=0} q^2 + \cdots \\ &= \alpha_0 + \left(\frac{\partial\alpha}{\partial q}\right)_{q=0} q_0 \cos(\omega_m t) + \frac{1}{2}\left(\frac{\partial^2\alpha}{\partial q^2}\right)_{q=0} (q_0 \cos(\omega_m t))^2 + \cdots \qquad \text{(III. 37)}\end{aligned}$$

α_0 can be described as a "static" polarizability, while the other terms are due to the variation of α caused by the vibration of the molecule at a frequency $v_m = \omega_m/2\pi$. For small vibrational amplitudes, the response is considered as linear and the dipolar moment is approximated by:

$$\vec{P} = \alpha_0\vec{\xi}_0 \cos(\omega_0 t) + \left(\frac{\partial\alpha}{\partial q}\right)_{q=0} q_0\vec{\xi}_0[\cos(\omega_0 t)][\cos(\omega_m t)]$$

$$\vec{P} = \alpha_0\vec{\xi}_0 \cos(\omega_0 t) + \frac{1}{2}\left(\frac{\partial\alpha}{\partial q}\right)_{q=0} q_0\vec{\xi}_0[\cos([\omega_0 + \omega_m]t) + \cos([\omega_0 - \omega_m]t)] \qquad \text{(III. 38)}$$

The first term corresponds to an oscillating dipole radiating light with a frequency v_0 (called Rayleigh scattering), while other terms correspond to oscillating dipoles radiating light with frequencies different from $v_0 = \omega_0/2\pi$. According to **Equation III.38**, Raman scattering is only active for molecular vibrations generating a 1st order variation of the polarizability, *i.e.* for $(\partial\alpha/\partial q) \neq 0$.

Considering a vibrational angular frequency ω_m, much smaller than ω_0 and characteristic of the molecule, the energy of the emitted photon will be $E_1 = \hbar(\omega_0 - \omega_m)$, if the molecule lays in this vibrational state after de-excitation, or $E_1 = \hbar(\omega_0 + \omega_m)$ if the molecule was in this vibrational state before absorbing the laser radiation (**Figure 41**). These two possibilities correspond to Stokes and anti-Stokes scattering, respectively.

The energy gap between E_0 and E_1 is given by:

$$\Delta E = E_0 - E_1 = hc\left(\frac{1}{\lambda_0} - \frac{1}{\lambda_1}\right) \qquad \text{(III. 39)}$$

This expression can be written in terms of wavenumber, *i.e.* the number of waves per unit length:

$$\Delta k = \frac{\Delta v}{c} = \left(\frac{1}{\lambda_0} - \frac{1}{\lambda_1}\right) \qquad \text{(III. 40)}$$

Raman spectroscopy consists in the measure of this wavenumber shift, called Raman shift or Stokes shift, which is independent of laser frequency. Thus, a shift of 1 cm^{-1} corresponds to an energy of 1.24 $\times 10^{-4}$ eV/molecule.

Rayleigh peak is very intense compared to peaks associated with Raman scattering because of a higher probability of occurring (**Figure 41**). Stokes intensity is also higher than anti-Stokes for similar reason. If we consider a Boltzmann distribution, most of molecules lays in their fundamental state at room temperature instead of a vibrational state. The intensity of the Raman scattered light is (113):

$$I \propto v^4 I_0 N \left(\frac{\partial\alpha}{\partial q}\right)^2 \qquad \text{(III. 41)}$$

where v is the laser frequency, I_0 is the incident light intensity and N is the number of scattering molecules in a given vibrational state.

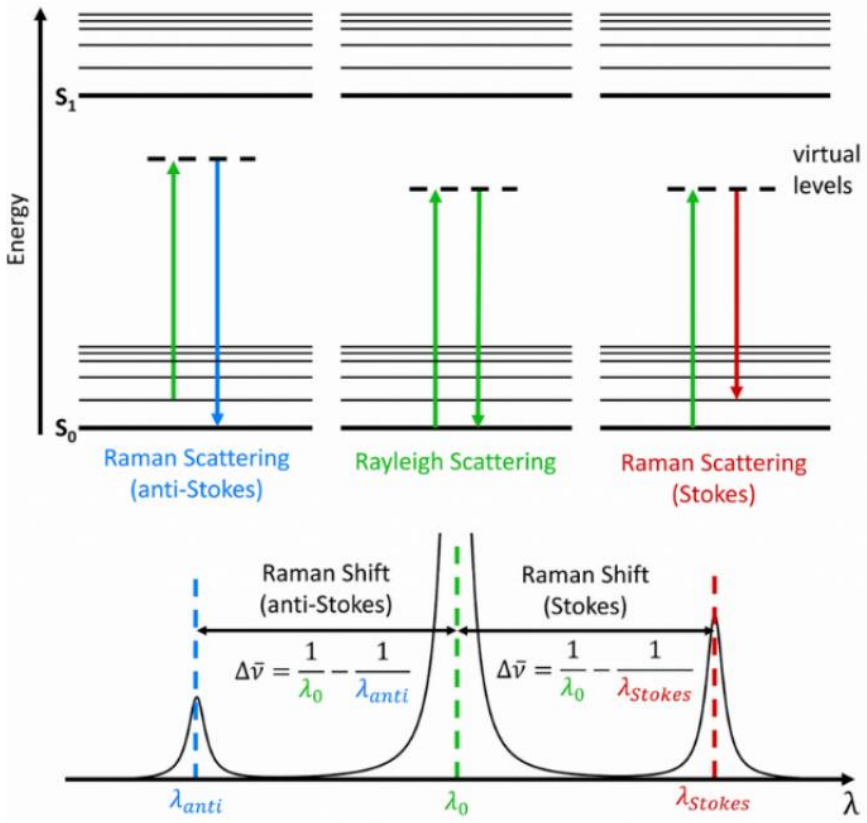

Figure 41 **:** Schematic representation of vibrational states with Raman and Rayleigh transitions, with the corresponding spectrum *(114)*. For anti-stokes scattering, molecules are in an excited state when absorbing the photon and drop in the ground state after the scattering, while molecules are in ground state before the interaction and in an excited state after the interaction in Stokes scattering.

In this thesis, Raman spectrometry has been performed with a low laser power to avoid any changes in the samples caused by heating. Raman was used in this thesis to highlight the presence of Ge-Ge, Ge-Si and Si-Si chemical bonds after annealing, indicating the formation of nanocrystals or alloys. Raman results are presented in **parts IV** and **V** of this manuscript.

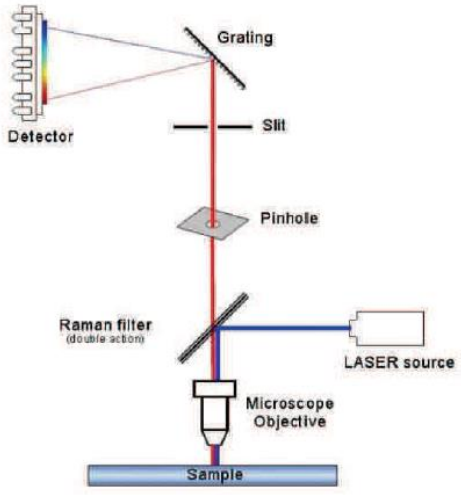

Figure 42 : Basic principle of a Raman spectrometer in backscattering geometry *(5)*.

Two confocal spectrometers were used in this thesis: a *Renishaw RM3000* and a *Horiba LabRAM HR800*, respectively installed at INSR (Varennes, Canada) and at Welcome facility (UCL, Belgium). A classical spectrometer setup (**Figure 42**) is composed of a continuous laser excitation source, a light transport and focusing system, a diffraction grating and a cooled CCD detector. Filters are used along the optical path to ensure a stable excitation wavelength and to eliminate the high intensity Rayleigh scattering (Notch filter). A microscope objective lens can be inserted in the optical path to perform µ-Raman analyses.

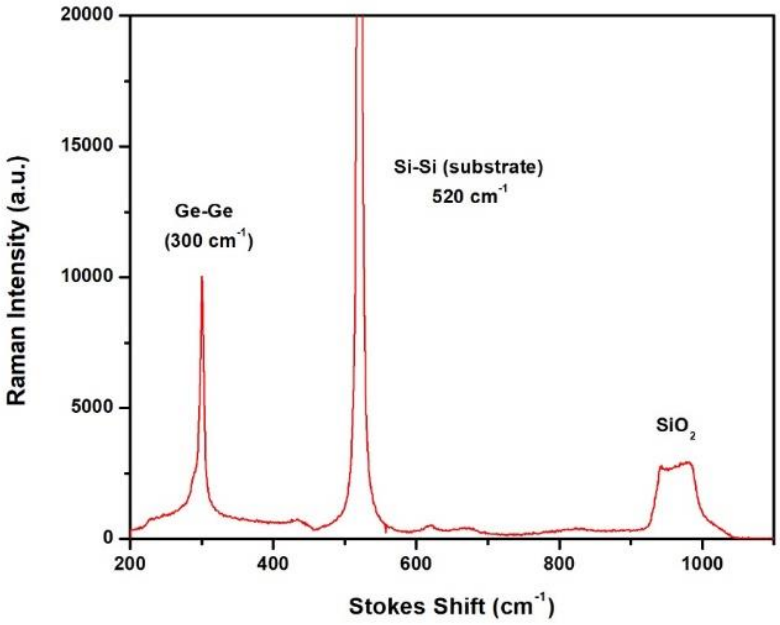

Figure 43 **:** Raman spectrum of Ge quantum dots embedded in a SiO_2/Si layer recorded with LabRAM HR800 spectrometer with x100 objective lens and $\lambda_{Laser} = 514\ nm$.

XRD – X-Ray Diffraction

X-ray diffraction is a technique used to identify the crystalline phases present in a material, crystallite size, lattice parameter, inter-reticular distance, … This analysis technique is based on the elastic scattering of an electromagnetic wave, in the energy range 100 eV to 10 MeV, by a periodic arrangement of atoms, *i.e.* a crystal. It makes it possible to highlight the crystallinity of materials, the orientation of crystals, to determine the lattice parameter or to estimate the size of nanocrystallites. At these energies, light wavelength is of the same order of magnitude than interatomic distances, leading to constructive and destructive interferences.

The intensity of X-rays scattered by an electron is expressed by Thomson's equation (115):

$$I = I_0 \left(\frac{\mu_0}{4\pi}\right)\left(\frac{e^4}{m_e^2 r^2}\right) sin^2\alpha = I_0 \frac{K}{r^2}\left(\frac{1+cos^2 2\theta}{2}\right) \qquad \text{(III. 42)}$$

with $\mu_0 = 4\,\pi \times 10^{-7}$ mkgC^{-2}, θ is the X-rays angle of incidence, α the angle between the direction of scattering and that of the electron accelerated by the electric field, *r* the distance travelled since the scattering and $K = (2.8179 \times 10^{-15})^2$ m². This intensity is weak for an isolated electron but increases with the density of electrons in an atom. As scattering is elastic, the atoms of a crystal behave like coherent sources which will generate interferences.

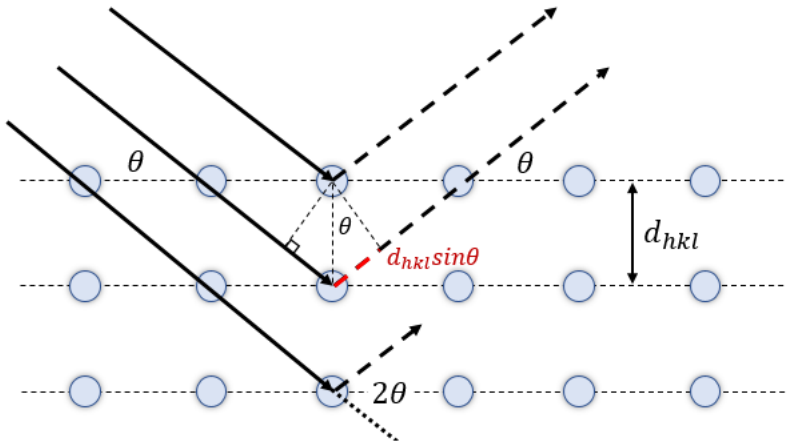

Figure 44 **:** Principle of XRD measurement. X-rays are scattered by atomic planes spaced by an inter-reticular distance *d*.

A periodic arrangement of atoms, arranged along parallel planes (h k l), is assimilated to a diffraction grating (**Figure 44**). According to Bragg's law, the scattering of monochromatic radiation can lead to constructive interference if the difference in optical path for two rays is an integer of times the wavelength:

$$2d_{hkl}sin\theta = n\lambda \qquad \text{(III. 43)}$$

where d_{hkl} represents the inter-reticular distance (distance between two parallel crystallographic planes), λ the wavelength, θ the angle of incidence and n the order of interference.

By combining Bragg's law and the estimation of the inter-planar distance for a cubic lattice, such as silicon or germanium, we obtain the following relations:

$$\frac{sin^2\theta}{h^2+k^2+l^2} = \left(\frac{\lambda}{2a}\right)^2 \quad \text{(III. 44)}$$

$$\frac{4sin^2\theta}{\lambda^2} = \frac{1}{d_{hkl}^2} = \frac{h^2+k^2+l^2}{a^2} \quad \text{(III. 45)}$$

Knowing λ, one can estimate the lattice parameter a and the inter-planar distance d_{hkl} from the position of the peaks on the X-ray diffractogram.

Crystalline nanostructures will also rise to a peak whose width at half height maximum (FWHM) depends on the dimensions of this nanometric structure. When the size of the nanocrystals decreases, a broadening of the peak is observed on the diffractogram, which can also be caused by discrepancies in size distribution. The diameter t of nanocrystals is estimated using the Scherrer's equation:

$$t = \frac{0.9\lambda}{\Delta\theta_{FWHM} cos\theta} \quad \text{(III. 46)}$$

with θ the x-rays angle of incidence and $\Delta\theta_{FWHM}$ the width at half height maximum. Scherrer's equation is used in **chapter IV** for the estimation of the average size of Ge-ncs in SiO_2 films, in **article I** and in **section IV.3**.

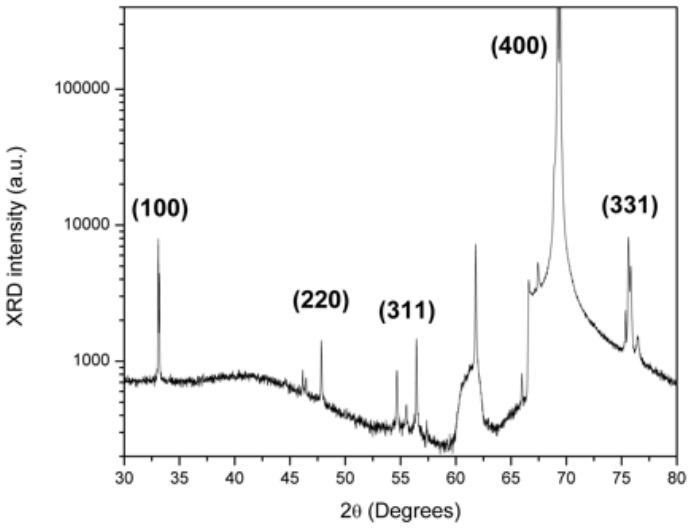

Figure 45 **:** Diffractogram of a monocrystalline silicon wafer <100> in Bragg-Brentano geometry ($\theta - \theta$ mode), with Cu Kα source (1.5406 Å x-rays, rotating sample).

Bragg-Brentano geometry was used in this thesis, with two different configurations possible:

1. Symmetric mode $\theta - \theta$ for which the sample is horizontal and the angles of incidence and diffraction are identical. In this configuration, RX source and detector move together while the angle θ varies.
2. Tilted mode for which the sample is intentionally tilted to reduce the contribution of the atomic planes of the substrate.

III.7 XPS – X-Ray Photoelectrons Spectroscopy

XPS spectroscopy is a quantitative technique for surface characterization (1 – 10 nm). It enables to identify the elemental composition, as well as the chemical and electronic states of the elements within the sample.

Monochromatic X-rays are generated by bombarding a metal anode with high-energy electrons ($K_\alpha = 1486\, eV$ for aluminium) and focused on the sample surface. When the material absorbs a photon X, its energy is entirely transferred to an electron. If the energy transferred is higher than the binding energy of this electron to its electronic orbital, electron is extracted by photoelectric effect. These photoelectrons have a kinetic energy equal to:

$$E_{e^-} = hv - E_b \qquad \text{(III. 47)}$$

Where hv and E_b correspond to the energy of the incident photon and to the electron binding energy, respectively.

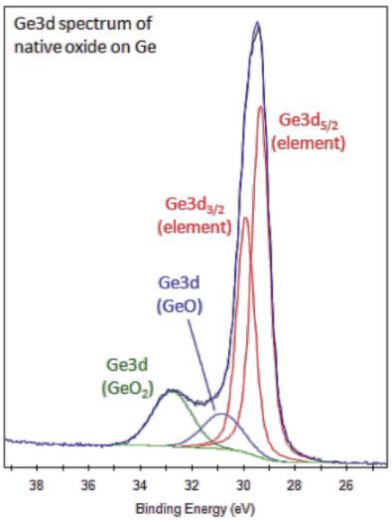

Figure 46 : XPS spectrum of Ge 3d signal *(116)*. Elemental Ge is measured with a binding energy of 29.3 eV, while Ge in an oxided state is measured at higher binding energies.

The quantification of photoelectrons is measured according to their kinetic energy thanks to a hemispherical analyzer coupled to a detector. Each atomic orbital has a characteristic binding energy for each element of the periodic table. Measuring the energy of a photoelectron therefore enables elementary identification of the atoms constituting the sample. Photoelectrons energy is also influenced by chemical environment, which provides information on the chemical bonds formed by an atom as its oxidation state.

Analysis in depth is limited by the extraction of photoelectrons through the surface of the sample from the emission depth. However, XPS spectroscopy can be used to perform depth profiling, using an ion gun allowing sample sputtering between two successive analyses. The use of these monoatomic ions (Ar^+) makes XPS a destructive analysis. In this configuration,

preferential sputtering can affect elementary analyses of chemical compounds and irradiation-induced damage can modify the chemical bonds. This makes XPS a tricky technique for depth-profiling.

XPS analysis has been used in this thesis in **chapter IV** – **article I** to identify the oxidation sate of Ge atoms implanted in SiO_2 films, before and after annealing, in order to explain Ge diffusion through the formation of GeO molecules.

III.8 Electron microscopy

Electron microscopy uses electrons instead of photons to magnify images of samples surfaces and to obtain local information about structure, morphology and composition. Electrons are produced by heating a filament and accelerated by electrodes. Schematic representations of optical and electronic microscopes are shown **Figure 47**. Two types of electron microscopes are commonly used:

- **Transmission electron microscope (TEM):** in this configuration, electron beam is observed through the sample. According to the short mean free path of electrons in matter, only very thin layers can be observed in transmission mode. Samples can be thinned by focused ion beam (FIB), which consists to sputter the sample with low-energy heavy ions (as gallium) to extract a film whose thickness is generally less than 100 nm.

  When the electron beam is focused to a fine spot and scanned point by point in a raster mode over the sample surface, the analysis is called **Scanning Transmission Electron Microscopy (STEM)**.

  In **Bright Field (BF)** mode, which is the most commonly used, unscattered electrons are observed, *i.e.* transmitted electrons. In this mode, the image results from the observation of the direct beam after its interaction with the sample. As scattered electrons are not observed, defects, dense areas or sample regions containing high Z elements appear in dark.

  In **Dark Field (DF)** mode, the direct electron beam is blocked while an aperture selects diffracted beams. Therefore, atoms, defects, high Z elements and dense areas appear brighter.

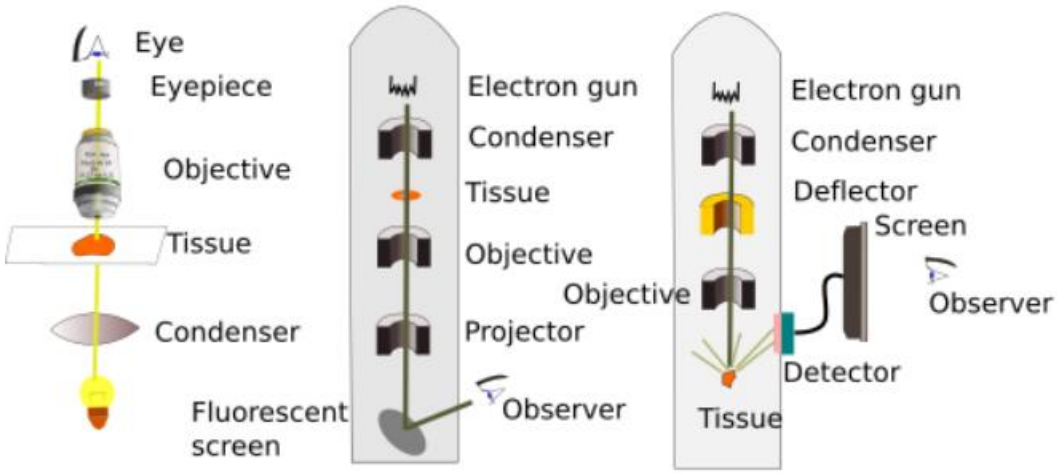

Figure 47 : Main components of optical microscope, TEM and SEM *(117)*.

In **High Angle Annular Dark Field (HAADF)** mode, an annular detector enables the observation of the most scattered electrons. In HAADF, contrast is due to the density multiplied by the sample thickness.

- **Scanning electron microscopy (SEM):** in this configuration, electrons backscattered and secondary electrons emitted from the sample are detected and converted in a digital image.

Electron microscopy also enables **Energy-Dispersive X-ray Spectroscopy (EDS or EDX)**. This technique consists to excite atoms constituting the analysed sample with the microscope electron beam by ejecting core-shell electrons. Outer-shell electrons will fill the void left by the ejected electron by emitting a X-ray characteristic of the atom, whose energy is equal to the difference between both electron shells. A semiconductor detector, as Si(Li) detector, enables to achieve compositional analysis by measuring X-rays energies.

TEM imaging has been used in this thesis to observe the germanium nanocrystals or the $Si_{1-x}Ge_x$ alloys formed after the annealing step. See experimental results in **parts IV** and **V**.

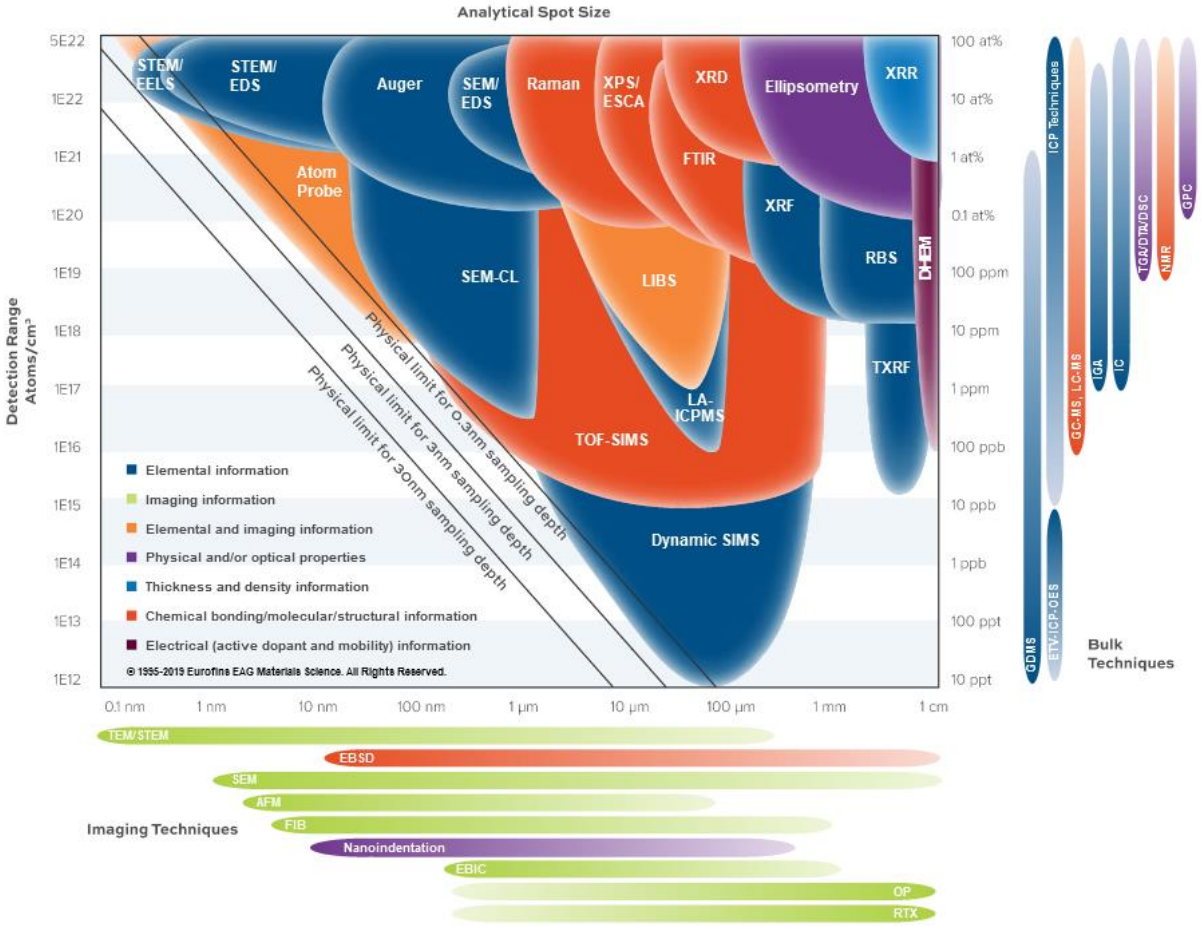

Figure 48 : Summary of the detection limit and spot size of several materials analyses techniques *(118)*. All the techniques used in this thesis are represented except (R)NRA.

Chapter IV

Study of Ge diffusion and nanoclustering in thermally grown silicon dioxide films

IV.1 Study of germanium diffusion mechanisms inside a thermally grown SiO_2 layer

As discussed in this chapter, the thermally activated nucleation of germanium atoms implanted in SiO_2/Si layers is characterized, under certain conditions (dependent of annealing, implantation and host matrix), by a highly asymmetric redistribution of germanium atoms through the SiO_2 matrix. At high annealing temperature, both Ostwald ripening and diffusion mechanisms are in competition due to a high coefficient of diffusion of germanium in silicon dioxide matrices (60), (119). This diffusion can be responsible of long-range germanium redistribution and drastic desorption through the sample surface. This phenomenon is observed especially in Ge-implanted fused silica, leading to the formation of large empty nanostructures, called nanocavities (60), (82). For example, germanium desorption as high as 90% of the implanted fluence in Silica glass and 50% in SiO_2/Si layers have been measured for 60 minutes of annealing at 1150°C under N_2 atmosphere and for similar implantation conditions (120). The difference between thermally grown oxides and fused silica has been explained by a higher concentration of silicon dangling bonds in the first compared to the latter (121). This leads to the stabilization of germanium through the formation of Ge-Si chemical bonds, stronger than Ge-Ge bonds.

An advanced explanation of the mechanisms involved in germanium diffusion and nucleation in SiO_2/Si films is proposed in this chapter, in agreement with results and models reported in literature. Solutions are provided to control Ge thermal diffusion and both size and depth-distribution of Ge nanocrystals.

IV.1.1 Anisotropic diffusion of germanium

Figure 49 and **Figure 50** present three examples of $^{74}Ge^+$ implantations carried out in the middle of SiO_2 layers, 300 nm thick, for three different implantation fluences (0.37, 0.60 and 1.30 × 10^{17} Ge/cm²). Implantations have been performed with a single energy of 230 keV at normal incidence. SRIM-TRIM simulation, represented by a blue solid line in **Figure 50**, indicates that the implantation profile is distributed around a projected range of 156 nm. RBS profiling was performed before and after annealing (1h, 1100°C, N_2 atmosphere) in order to highlight the thermally activated diffusion of these implanted germanium atoms. RBS spectra show that, during thermal treatment, germanium diffuses asymmetrically in both directions: towards the sample surface and in depth.

This highly asymmetric diffusion apparently favours the migration of germanium atoms towards the sample surface. As can be seen in RBS spectra, and more specifically in **Figure 49b** and **Figure 50**, a significant part of the germanium profile is shifted towards the surface and a germanium accumulation occurs at the vicinity of the oxide/substrate interface. In **Figure 49a**, germanium desorption through the sample surface is measured to be of the order of 14-15% of the total amount of Ge atoms measured by RBS before annealing.

The asymmetric shape of the germanium depth-distribution after annealing is the result of a combination of three major factors:

1. The composition and geometry of the implanted medium, which is highly anisotropic,

2. The influence of oxygen through the formation of GeO_x compounds or regeneration of the SiO_2 stoichiometry,

3. The trapping of germanium atoms through the formation of Ge-Si and Ge-Ge chemical bonds.

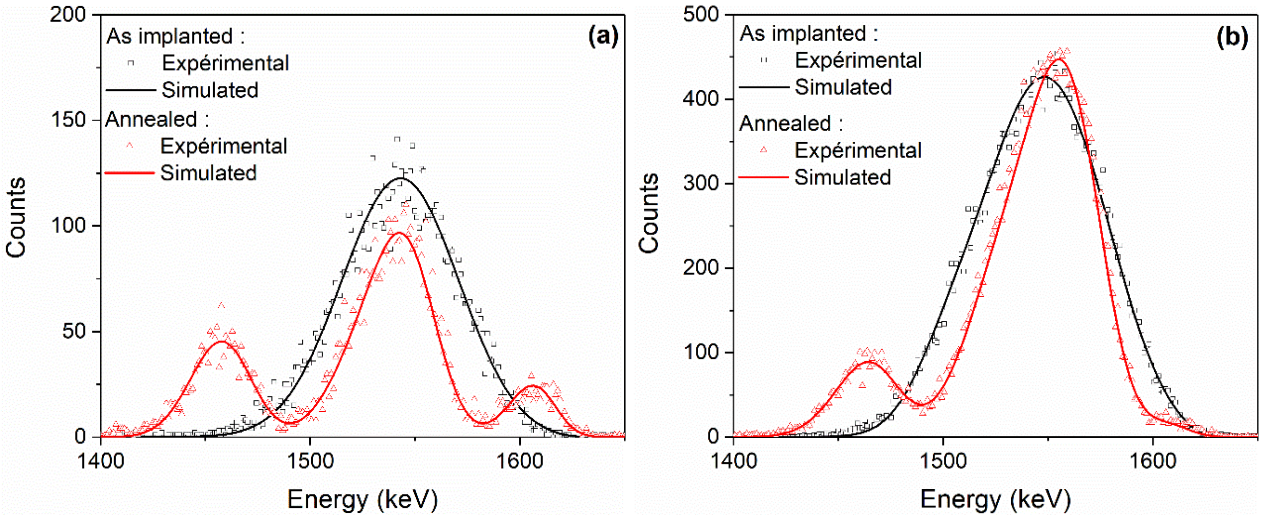

Figure 49 : RBS spectra (^{4}He, 2 MeV, detector at 165°, angle of incidence of 7°), zoomed on the energy range corresponding to germanium signal, fitted before (black) and after (red) 1h of annealing at 1100°C under N_2 for fluences of (a) 3.7 ×10^{16} Ge/cm² and (b) 1.30 ×10^{17} Ge/cm².

1. The layer anisotropy is related to the dose-dependent generation of local defects and reorganization of the oxide induced by the crossing of heavy ions through the dielectric. The irradiation-induced primary damage, mainly localized between the sample surface and the projected range of germanium (yellow squares in **Figure 50**), and the cascades of collisions that follow, will locally affect the stoichiometry of the SiO_2 layer. **Figure 50** shows the Ge depth-profile, extracted from RBS analysis, of a sample implanted with a measured fluence of 6×10^{16} Ge/cm². The displacements per atom (dpa) were simulated using SRIM-TRIM code, which is not able to provide information about the oxide stoichiometry after the implantation.

   As energy is transferred from incident ions to atoms constituting the oxide layer, implantation has also an impact on the oxide region between the germanium projected range and the SiO_2/Si interface. **Article I** discusses the change of stoichiometry in Ge-implanted oxides as a function of Ge fluence and recoiled atoms.

   The combination of these dose-dependent factors makes the composition, density and atomic arrangement of the studied samples non-uniform in depth. The structure of the

implanted SiO_2 films will be a central point discussed in the four articles presented in this section, but more specifically in **article I**.

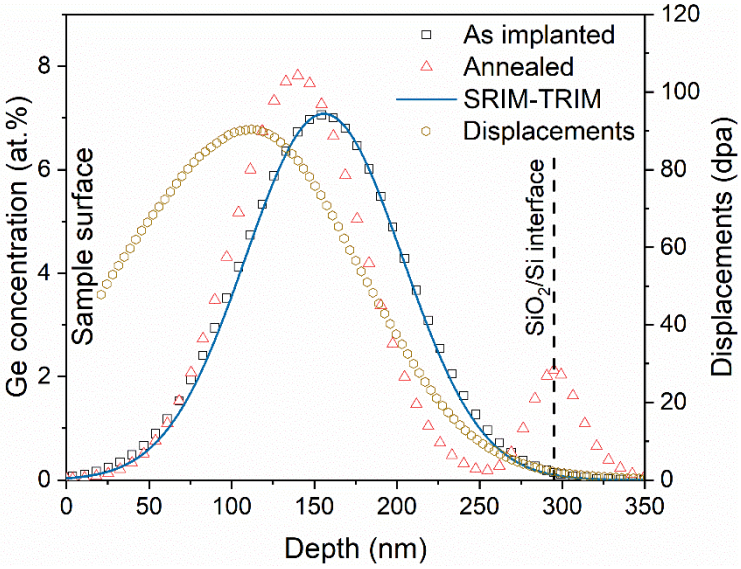

Figure 50 : Ge depth-profiles extracted from RBS analyses before (black open squares) and after (open red triangles) one hour annealing at 1100°C under N_2 for a fluence of 6×10^{16} Ge/cm². The measured "as implanted" profile agrees quite well with SRIM-TRIM 2013 simulation taking into account sputtering and swelling effects (blue curve). Displacements per atoms (from SRIM-TRIM) are represented by open yellow squares (right Y-axis).

2. As frequently reported in literature (59), (61), (121), (122), (123), (124), germanium diffusion is related to the presence of oxygen. As will be discussed in **article II**, the oxygen involved in germanium migration may have two possible origins: it can come from residual contaminants (O_2, H_2O, …) present in the annealing atmosphere, or directly supplied by the SiO_2 film.

   Article II aims first to demonstrate the importance of working under clean annealing environment and the impact of an annealing atmosphere contaminated by oxygen on the species present in the SiO_2 film, particularly for Ge.

   As demonstrated in the first article and discussed in **article II**, a non-negligible fraction of implanted germanium atoms chemically binds to oxygen atoms during the implantation process (51), (122), (125). GeO_x compounds are formed along the entire SiO_2 layer, and notably highly mobile GeO molecules. These GeO molecules are generally appointed as the primary responsible of the desorption and diffusion of germanium visible in **Figure 49** and **Figure 50**.

3. Germanium diffusion and nucleation are also affected by the chemical affinity of germanium, leading to the formation of Ge-Ge and Ge-Si chemical bonds (82), (120), (126). These bonds are responsible for the nucleation of germanium into nanocrystals and barrier effects through Ge/Si trapping. This is discussed in all articles but mainly in **articles III** and **IV**.

IV.1.2 Role of oxygen involved in germanium diffusion

The asymmetric redistribution of germanium in several peaks, reported in literature and visible in **Figure 49** and **Figure 50**, are associated with the presence of oxygen through the formation of partly, or fully, oxidized germanium or with a contaminated atmosphere of annealing. Highly mobile GeO molecules are considered as the major responsible of germanium redistribution and desorption. In **articles I** and **II**, we proposed original methods, using stable isotopes or co-implantations, to demonstrate the different roles played by oxygen atoms during implantation and thermal processes. Our results are in good agreement with models proposed by *Heinig et al.* (123), (127) and *Beyer et al*. (122).

Article I: Influence of oxygen co-implantation on germanium out-diffusion and nanoclustering in SiO_2/Si films

Preliminary to article I

The goal of the first manuscript, entitled "*Influence of oxygen co-implantation on germanium out-diffusion and nanoclustering in SiO_2/Si films*", was to study the mechanisms of Ge diffusion in implanted SiO_2 films and the impact of the implantation step on germanium mobility. We have studied the direct formation of GeO_x compounds during the implantation process due to the atomic reorganization of the SiO_2 layer caused by the implantation of heavy ions, such as germanium. This dose-dependent reorganization is imputed to irradiation-induced damage causing the displacement of atoms constituting the host matrix, *i.e.* silicon and oxygen atoms, and resulting in high stoichiometric discrepancies throughout the SiO_2 layer. The stoichiometric state of the layer and the relative concentration of elemental and oxidized Ge are used together to explain the asymmetric redistribution of Ge.

The impact of oxygen is shown for oxygen atoms naturally present inside the oxide layer and is accentuated by a co-implantation of $^{16}O^-$ ions, whose projected range is between the sample surface and the projected range of germanium. Two different regimes have been identified as a function of oxygen fluence. It is shown that co-implanted oxygen locally participates to both the formation of highly mobile GeO molecules and the restoration of the damaged SiO_2 during annealing, enhancing germanium diffusion, until the over-saturation in oxygen of the oxide layer. Once the stoichiometry of the oxide layer has been restored, and the concentration of remaining O atoms is similar to that of Ge, poorly mobile GeO_2 is formed.

While controlling the size distribution of the QDs to obtain size gradients remains the main goal of this thesis, in order to improve PV cells efficiency, the possibility of reducing quantum dots dispersion in size by oxygen co-implantation is also investigated. This offers the possibility to standardize nanocrystals diameters, which present large discrepancies along the oxide depth in Ge-implanted samples. Due to wide distribution of quantum dots size in implanted samples, which increases with germanium fluence (81), photoluminescence signal is generally extended on a broad range of wavelengths, making them not suitable for

optoelectronic applications such as lasers. Co-implantation, and subsequent size standardization, could be used to reduce the spectral range of emission of germanium quantum dots embedded in SiO_2 films.

Authors' contribution

The idea of co-implanting oxygen ions in addition to germanium to enhance Ge diffusion in damaged SiO_2 films emerged from scientific discussions with Guy Terwagne. I carried out all the Ge implantations with ALTAÏS. I performed and analysed all the RBS, µ-Raman and XRD observations. I assisted Emile Haye during the XPS measurements and the data analysis. Finally, I wrote the article with the comments of Emile Haye and Guy Terwagne.

Influence of oxygen co-implantation on germanium out-diffusion and nanoclustering in SiO_2/Si films

A. Nélis[1,*], E. Haye[1], G. Terwagne[1]

[1] *LARN, Namur Institute of Structured Matter (NISM), University of Namur (UNAMUR), B-5000 Namur, Belgium*

(Under review in Thin Solid Films; submitted 06/07/2021)

Abstract

The thermally activated diffusion of germanium atoms implanted in the middle of SiO_2 layers has been studied by Rutherford Backscattering Spectroscopy (RBS), X-ray Photoelectron Spectroscopy (XPS), μ-Raman spectroscopy and X-Ray Diffraction (XRD), with and without the presence of co-implanted $^{16}O^-$ ions. The important role of implantation-induced defects, in particular atomic recoil of silicon and oxygen atoms, on the well-known asymmetric redistribution of germanium depth-profile is discussed for samples solely implanted with germanium, as a function of the fluence. This is shown how both the stoichiometric state of the implanted SiO_2 layer and their chemical environment influence the mobility of Ge atoms. For samples co-implanted with oxygen, RBS shows an enhancement of germanium diffusion under thermal activation at 1100°C as long as the oxygen over-saturation of the SiO_2 film is not achieved. This enhancement of germanium diffusion is associated to the formation of GeO_x compounds during the implantation, as shown by XPS measurements. This is responsible, during the annealing step, of the formation of highly mobile GeO at low oxygen fluences and less mobile GeO_2 at higher fluences. Combination of XRD and μ-Raman analyses is used to highlight the impact of the co-implanted O atoms on the size dispersion of germanium nanocrystals (Ge-ncs).

Keywords: Rutherford backscattering spectroscopy (RBS); X-Ray photoelectron Spectroscopy (XPS); Ge diffusion; Ge nanocrystals; ion implantation.

I. Introduction

Original approaches are proposed since decades to improve the efficiency of optoelectronic devices [1,2], among which the integration of germanium and silicon nanocrystals in the miniaturization process of such devices [3-7]. Group IV semiconductor nanocrystals open new possibilities thanks to many associated optoelectronic properties. Their tunable bandgap and the potential activation of multiple exciton generation (MEG) can greatly improve energy conversion in photovoltaic cells. This enhanced photovoltaic efficiency strongly depends on the nanocrystals size and their depth-distribution inside the dielectric layer [4,5,8,9].

In this context, germanium is considered as being a better candidate than silicon for the fabrication of third generation photovoltaic cells thanks to a higher charge carriers mobility, a lower energy bandgap (0.66 eV for Ge versus 1.12 eV for Si) and a large absorption in the visible range.

Ge nanocrystals (Ge-ncs) can be synthesized by ion implantation, which has the advantage of being a technique widely used in silicon-based industry, followed by high temperature treatments (> 800°C). It has been shown that the nanostructures size and depth-distribution strongly depend on implantation and annealing conditions [9-14].

This post-implantation annealing is known to be responsible of a long-range germanium diffusion leading to an asymmetric redistribution of the germanium depth-profile. This redistribution is associated to the formation of highly mobile GeO and specific irradiation-induced damage occurring during the implantation process [9,11,15,16,17].

In the present work, Rutherford Backscattering Spectroscopy (RBS) and X-ray Photoelectron Spectroscopy (XPS) measurements investigate the effects of the implantation step on germanium redistribution. In agreement with literature [9,10,15,18,19], it is shown that Ge diffusion is controlled by the formation of GeO_x compounds and Ge/Si chemical trapping effects. Special attention is given to recoiled silicon and oxygen atoms to explain the asymmetric redistribution of Ge observed by RBS.

As germanium diffusion is related to the formation of GeO_x compounds and SiO_2 stoichiometry, its migration can be enhanced by doping, with a co-implantation of oxygen atoms, the under-stoichiometric SiO_x regions where Ge/Si trapping effects generally occur. This leads either to large Ge desorption losses through the gas/SiO_2 interface or germanium oxidation during annealing, depending on the oxygen saturation of the SiO_2 layer.

The effect of oxygen co-implantation on the nanocrystals formation is also investigated by combination of μ-Raman and XRD measurements. This is shown that the co-implantation of oxygen could be used to reduce the nanocrystals size discrepancies, generally resulting from irradiation-induced damage in implanted films [9-11,20].

II. Experiment

300 nm thick wet-oxidized (100) silicon wafers were implanted with $^{74}Ge^+$ prior to $^{16}O^-$ ions at energies of 230 and 39 keV respectively. SRIM-TRIM [21] (Stopping and Range of Ions in Matter-TRansport of Ions in Matter) simulations have been used to calculate projected ranges, which correspond to 156 nm for $^{74}Ge^+$ and 100 nm for $^{16}O^-$ ions. A germanium fluence ranging from 0.37 to 1.30 × 10^{17} Ge/cm^2 is used, corresponding to a measured concentration varying from 4.5 to 16 at.% at maximum. The fluence of co-implanted oxygen varies from 0 to 1.66 × 10^{17} O/cm^2. All implantations were performed with ALTAÏS (Accelerateur Linéaire Tandetron pour l'Analyse et l'Implantation des Solides), the 2 MV Tandetron accelerator installed at LARN (UNamur, Belgium).

A post-implantation annealing was performed for all samples inside a quartz tube furnace heated at 1100°C for 60 minutes under N_2, with the facility installed at LARN. A schematic representation of our fabrication process is available in reference [4].

The fluences and depth-profiles of implanted $^{74}Ge^+$ and $^{16}O^-$ ions were verified by RBS, using 2 MeV $^4He^+$ beams for two scattering angles (165 and 135°). RBS data were treated using SIMNRA program [22] in combination with SimTarget (developed by J.L. Colaux [23]).

The chemistry of the samples was investigated by X-ray photoelectron spectroscopy on a Thermo Fisher Escalab 250Xi spectrometer using Al Kα source (1486.68 eV) and a spot size of 250×250 µm². Samples were profiled using an Ar^+ beam at 1 keV (30°, low current), using a scan mode (pass energy 40 eV, 2 scans) for recording the Ge 3d, Si 2p and O 1s core levels. Fitting is done considering a Shirley background and a Lorentz/Gaussian ratio of 30 and symmetric peak. The authors are aware of the possible damage generation using ion beam, and concentrations obtained are subject to modifications [24,25]. However, ion beam energy has been minimized, and the comparison between samples remains valid, as the same erosion parameters (ion beam energy and current, spot size) have been used.

µ-Raman measurements were carried out using the confocal LabRAM HR800 spectrometer from Horiba Scientific installed at Welcome facility at Université Catholique de Louvain (UCL, Belgium). The spectrometer is equipped with a digital camera, a ×100 objective lens and can perform with three different laser wavelengths (488, 514 and 633 nm). The Ar^+ laser probe (λ = 514 nm) was used for all the analyses presented in this study.

The crystallinity of annealed samples and the mean diameter of germanium nanocrystals were measured by XRD measurements with a Cu Kα source (1.5406 Å x-rays, rotating sample), using a panalytical X'Pert PRO Diffractometer in Bragg-Brentano geometry.

III. Results and discussion

A. Thermally activated diffusion of Ge

Figure 1a shows an example of Ge signal measured by RBS, before (black) and after (red) annealing, obtained for a sample solely implanted with a measured fluence of 1.30 × 10^{17} Ge/cm² in the middle of the SiO_2 layer. Only the energy range related to Ge signal is shown. In agreement with previous works in SiO_2/Si films [9,11,13,15,16,20,26,27], an important thermal diffusion of germanium is observed towards both the surface (upwards) and the SiO_2/Si interface (downwards). This results in a multi-peak redistribution of the germanium depth-profile, characterized by a highly asymmetric diffusion of implanted Ge atoms.

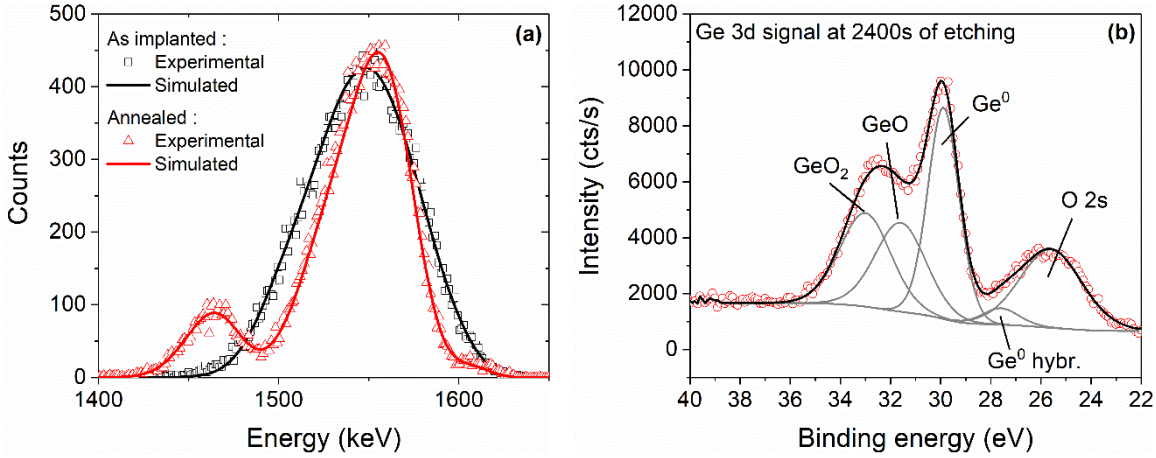

Figure 1: (a) RBS spectra and fitting curves of a sample implanted with 1.30 × 10^{17} Ge/cm², not co-implanted with oxygen, before (black) and after (red) 60 minutes of annealing at 1100°C under N_2. Only the energy range corresponding to germanium signal is shown. (b) Example of XPS fit for the Ge 3d signal for an etching time of 2400 seconds for the same sample (1.30 × 10^{17} Ge/cm² - 230 keV) before annealing.

As already discussed in reference [9], this asymmetric distribution along the sample depth of the germanium profile after annealing results from the combination of three factors : 1) the highly isotropic composition and crystallography of the implanted medium, 2) the influence of oxygen through the formation of extremely mobile GeO [11,15,18] and 3) the trapping of germanium atoms through the formation of $Ge - Si$ and $Ge - Ge$ chemical bonds [10,19].

The contribution of Ge trapping effects by silicon excess has been presented in reference [9] with the co-implantation of silicon isotopes, while the influence of an atmosphere of annealing contaminated with oxygen has been presented in reference [37] with the use of ^{18}O. The reduction of Ge mobility for increasing Ge fluences is discussed in this work and explained as a function of the stoichiometric state of the SiO_2 film (see section 3.2).

The example presented in figure 1a was chosen because of the Ge/Si trapping effects and oxide damaging which both occur at this fluence during annealing, resulting in the asymmetric diffusion of the implanted Ge atoms. As demonstrated in the next section, at lower fluences Ge diffusion is more efficient and trapping effects are less marked, while the opposite is observed for fluences higher 1.30 × 10^{17} Ge/cm². This justifies the use of a fluence of 1.30 × 10^{17} Ge/cm², which allows diffusion and trapping effects to coexist.

B. Formation of GeO_x compounds during Ge implantation

The direct formation of GeO_x compounds during germanium implantations has been observed in SiO_2 layers [15,18,28], but its dependency with germanium fluence is poorly reported in literature, as well as the changes in the SiO_2 stoichiometry.

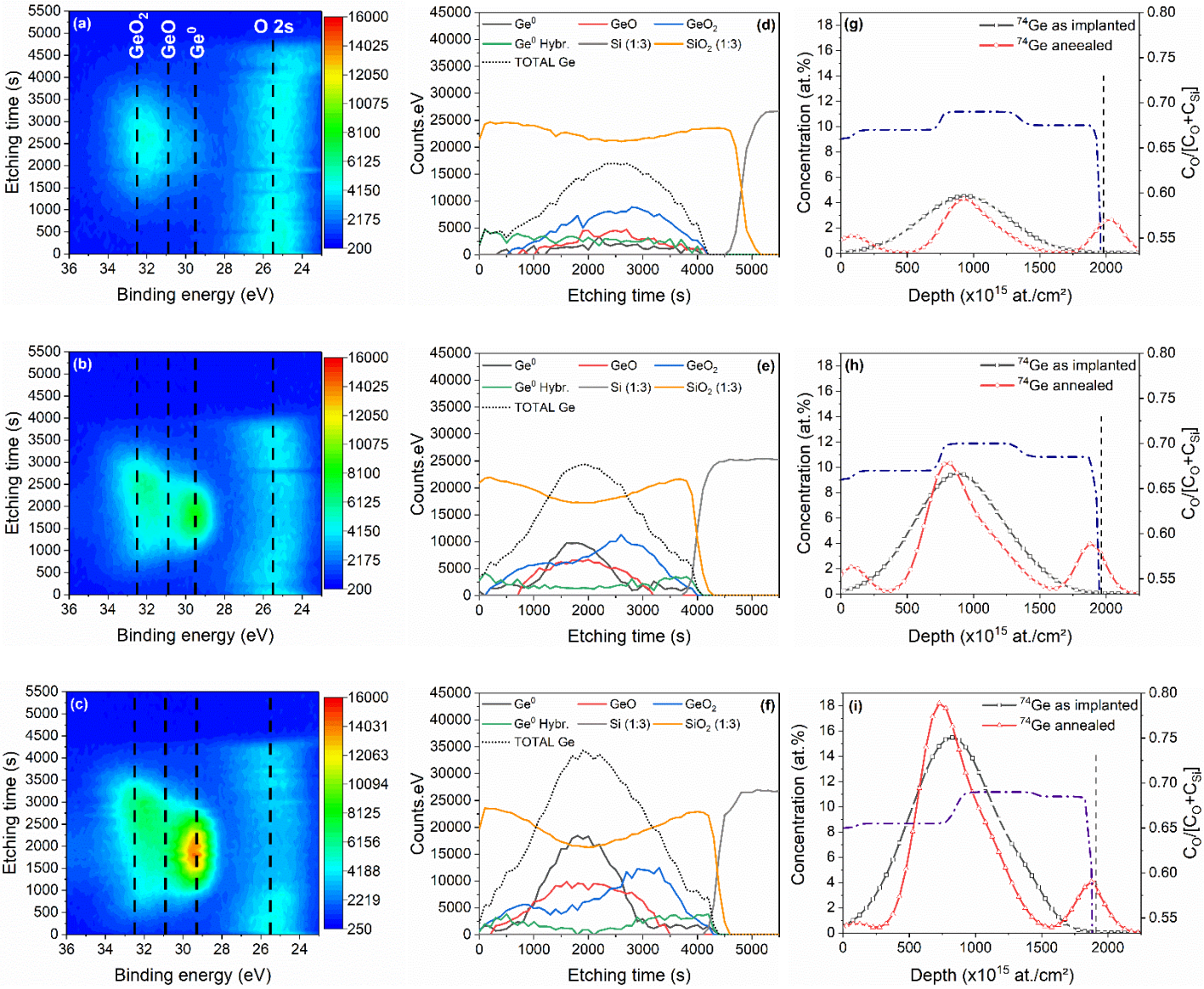

Figure 2: XPS depth-profiles as a function of etching time before annealing (a-f) and RBS depth-profiles before and after annealing (g-i), for samples solely implanted with germanium with 0.37 $\times 10^{17}$ (a,d,g), 0.80 $\times 10^{17}$ (b,e,h) and 1.30 $\times 10^{17}$ Ge/cm² (c,f,i). For better clarity, and due to their strong intensity, Si and SiO_2 signals have been reduced to 1/3 to have representative scale in d-f. $C_O/[C_O + C_{Si}]$ ratio before annealing is plotted by blue dotted line in RBS depth-profiles (right Y-axis).

Figure 1b presents a typical fit of the Ge 3d signal with contributions centered at 29.3, 30.9 and 32.5 eV, corresponding to elemental Ge, GeO, and GeO_2 respectively. The wide peak around 25.5 eV corresponds to O 2s signal. Note that peak position is subject to standard deviation (about 0.3 eV). In some cases, elemental Ge has been observed at binding energies lower than 29.3 eV, probably due to sp^3-like hybridization state resulting in longer chemical

bond lengths, and thus lower binding energies [29]. The Si 2p signal has been fitted with two contributions centered at 99.5 and 103.5 eV, corresponding to Si and SiO_2 respectively [30].

Figures 2a-f present the XPS depth-profiles of not annealed samples solely implanted with germanium for three different fluences, derived from the Ge 3d and Si 2p signals. Figures 2a-c present a heat map of the Ge 3d signal intensity at different binding energies and as a function of etching time, while figures 2d-f present the evolution of the peak area of Ge^0 (black), Ge^0 hybridized (green), GeO (red), GeO_2 (blue), Si (grey) and SiO_2 (yellow) contributions.

XPS data analysis shows that a significant fraction of Ge atoms is present in an oxidized state after the implantation (GeO_x, x being equal to 1 or 2), in the range 30.5 – 33.5 eV. This is consistent with *Oswald et al.* [18] and *Beyer et al.* [15] XPS observations in Ge-implanted SiO_2 layers. These GeO_x compounds formed during the implantation are supposed to be mainly responsible of the long-range diffusion of germanium.

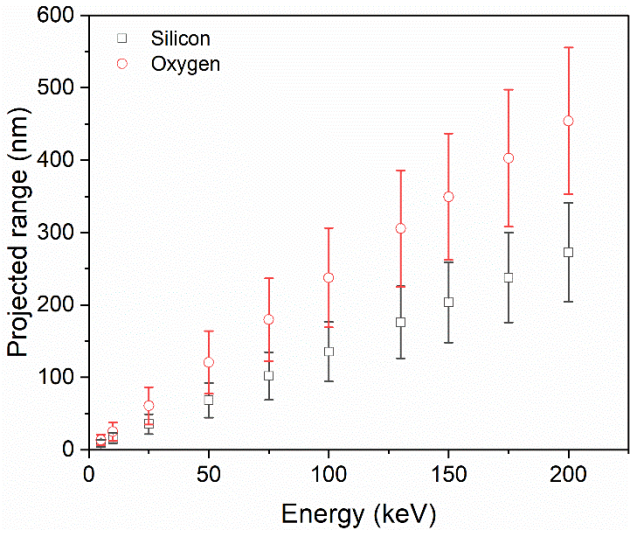

Figure 3: Results of SRIM-TRIM simulations of projected ranges for Si and O atoms of energy varying from 5 to 200 keV in SiO_2. Error bars represent the longitudinal straggling calculated by SRIM-TRIM.

Along their trajectory through the SiO_2 layer, $^{74}Ge^+$ ions will mainly loss their kinetic energy by Coulomb interactions with Si and O atoms, causing the formation of a large density of recoiled atoms throughout the oxide. According to classical mechanics, the energy transferred to an atom at rest in a single collision is $E = 4m_{ion}m_2E_{ion}cos^2(\theta)/(m_{ion}+m_2)^2$, where θ is the recoil angle, m_2 is the mass of the target atom, E_{ion} and m_{ion} are the ion energy and mass. According to this, the maximum energy of recoiled Si and O atoms, involved in the particular case of a head-on collision with 230 keV $^{74}Ge^+$ ions, is around 183 and 135 keV respectively. The projected range of these particles, as calculated by SRIM-TRIM, is ~1.3 times greater for oxygen than silicon atoms. In a more general case and at equivalent energy, the oxygen average projected range is 1.68 times higher than that of silicon over an energy range of 5 – 200 keV (figure 3). The probability of recoiling being similar for Si and O atoms in SiO_2, with displacement energies two times lower for O than Si (9.3 vs 18.6 eV) [31], the density of Si dangling bonds or Si interstitials will be highest in the region before the maximum of Ge depth-distribution, while recoiled O atoms will concentrate behind the germanium projected range.

This structural reorganization of the oxide leads to the formation of a non-uniform SiO_2 layer with high local stoichiometric discrepancies. This is shown in figures 2g-i by blue dotted lines, extracted from RBS analyses and representing the concentration ratio $C_O/[C_O + C_{Si}]$. This ratio is equal to ~0.667 for a stoichiometric oxide. Therefore, RBS confirms the formation of an under-stoichiometric oxide (SiO_x, x < 2) in the first half of the layer and an over-stoichiometric oxide (SiO_x, x > 2) in the second half. This experimental result is in agreement with *Beyer* and *von Borany* Tridyn simulations of recoiled O atoms [15]. This also agrees with XPS observations, which systematically exhibit a shift in the positions of O 2s (see figures 2a-c and 6a), O 1s and Si 2p peaks (see figure 4 for an example of Si 2p energy shift), indicating the formation of under-stoichiometric SiO_x (x < 2). This chemical environment influences the chemical bonds that implanted Ge atoms will be able to form during both the implantation and the annealing steps, and thus their diffusivity. The mobility of Ge atoms is lower in SiO_2 films presenting an excess of Si compared to a stoichiometric oxide or a high concentration of Si dangling bonds [9,10,19,26].

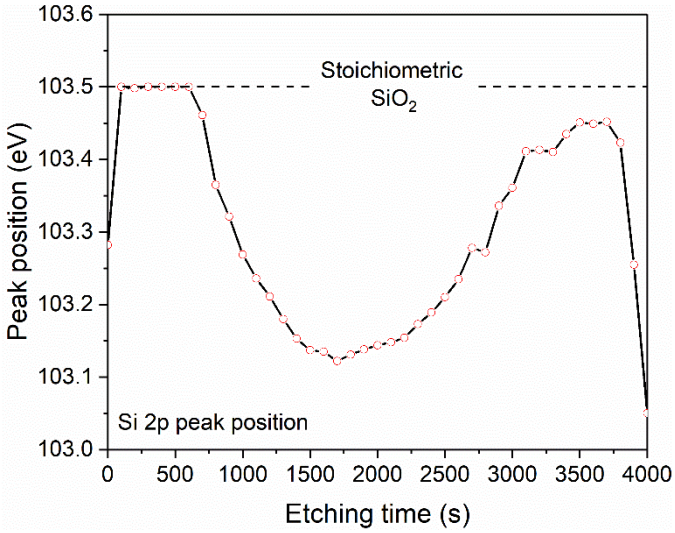

Figure 4: Evolution of the Si 2p energy shift as a function of the etching time, derived from XPS, for a sample solely implanted with 1.30×10^{17} Ge/cm² before annealing.

XPS depth-profiles (Figures 2a-f) confirm that GeO_x compounds are formed throughout the entire SiO_2 film, with a concentration which increases as a function of the etching time (up to 3500 seconds for the highest fluence). This is shown that, for higher Ge fluences, GeO_2 dominates principally just after the projected range of germanium (between 2250 and 4000 seconds of etching – figure 2), while Ge^0 signature becomes dominant in the first part of the Ge depth-profile (between 1000 and 2250 seconds of etching for the higher Ge fluence), in agreement with the behavior of recoiled Si and O atoms previously highlighted by RBS.

As XPS cannot discriminate Ge-Ge and Ge-Si chemical bonds, due to similar binding energies, Ge^0 contains both contributions. Therefore, Ge^0 signal corresponds to the supposed accumulation of recoiled Si (Ge-Si bonds) and overlaps with the maximum of germanium depth-distribution (Ge-Ge bonds). As reported in literature [11,13,16,19], this Ge^0 region will be the center of Ge nucleation.

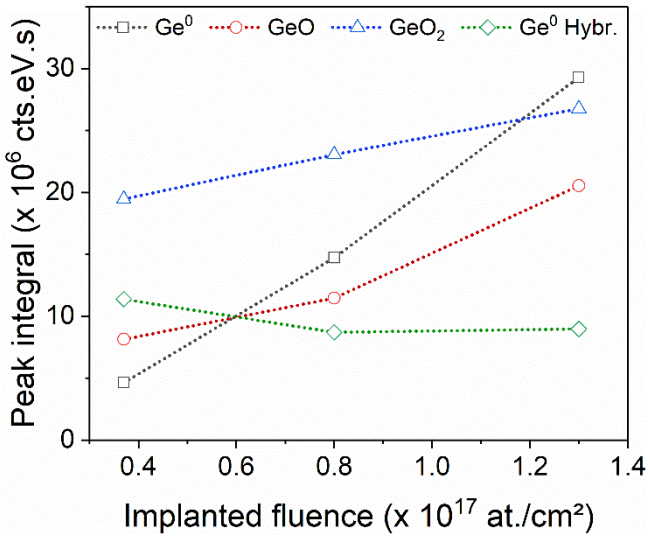

Figure 5: Evolution of Ge^0, Ge^0 hybr., GeO_2 and GeO integrals measured by XPS as a function of co-implanted fluence. Dotted lines are only there to guide the eye.

Figure 5 presents the integrated signals of GeO_2, GeO, Ge^0 and Ge^0 hybr.; a direct correlation with the implanted fluence is observed. It can be inferred from figure 5 that the fraction of germanium in an oxidized state and Ge^0 is proportional to the implanted fluence, within the range used in this work. GeO_x compounds dominate at low Ge fluences, while Ge^0 concentration increases faster with Ge fluence. As GeO is highly mobile and germanium poorly mobile when chemically bonded to Ge or Si atoms (both included in Ge^0), this explains the higher germanium mobility observed by RBS for lower Ge fluences, characterized by an enhanced out-diffusion and a more efficient multi-peak redistribution. Added to the large stoichiometric discrepancies measured throughout the oxide layer, and the different Ge diffusivities associated to these regions of the SiO_2 film, this results in the asymmetric redistribution of Ge observed by RBS. This is visible in Ge depth-profiles after annealing (red curves of figures 2g-i), and in table I which summarizes the contributions of the three peaks observed by RBS after annealing. The decrease of the amount of Ge within the surface and interface peaks confirms the reduction of the long-range redistribution of Ge as the implantation fluence increases. Note that losses, measured by RBS, stay relatively high (7.5%) for the higher fluence due to the increase of Ge concentration at the extreme surface because of sputtering occurring during the implantation. Near-surface GeO molecules are highly volatile and therefore easily subject to desorption through the sample surface [15].

Implanted fluence ($\times 10^{17}$ Ge/cm²)	Surface peak (%)	Central peak (%)	Interface peak (%)	Losses (%)
0.37	**8.5** ±0.2	**56.0** ±1.1	**21.5** ±0.4	**14.0** ±0.3
0.80	**6.0** ±0.1	**69.0** ±1.4	**15.0** ±0.3	**10.0** ±0.2
1.30	**1.5** ±0.1	**80.0** ±1.6	**11.0** ±0.2	**7.5** ±0.2

Table I: Distribution of germanium after annealing, as measured by RBS, for samples presented in figure 2.

C. Enhanced Ge diffusion by co-implantation of oxygen

To improve germanium diffusion during annealing, a co-implantation of $^{16}O^-$ ions has been inserted between Ge implantation and annealing steps. As the implantation energy of the oxygen ions is 39 keV, the oxygen depth-profile is distributed at around 100 nm from the sample surface, *i.e.* in the oxide region most subject to irradiation-induced damaging. Co-implanted oxygen atoms will have three effects: 1) enhancing the Ge diffusion through the formation of GeO molecules [15,18], 2) regenerating the stoichiometry of the damaged SiO_2 layer by oxidizing the Si dangling bonds and Si interstitials [15], or 3) oxidizing Ge when SiO_2 over-saturation is achieved.

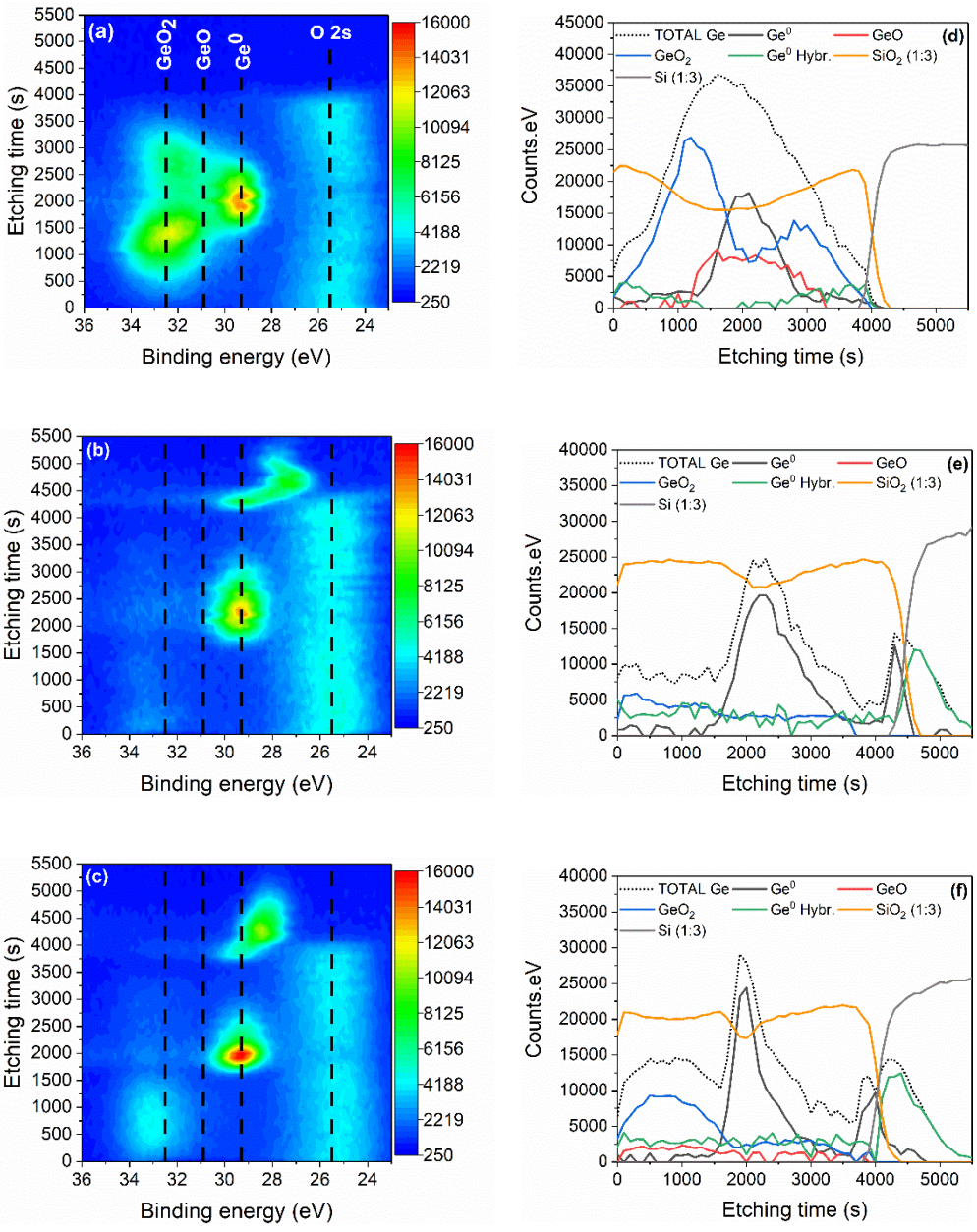

Figure 6: XPS depth-profiles as a function of etching time for samples co-implanted with 1.30×10^{17} Ge/cm² and (a) 1.30×10^{17} O/cm² before annealing, (b) 6.9×10^{16} after annealing and (c) 1.30×10^{17} O/cm² after annealing. For better clarity, and due to their strong intensity, Si and SiO_2 signals have been reduced to 1/3 to have representative scale.

The XPS depth-profile (figures 6a and 6d) of a co-implanted sample, without annealing, shows that co-implanted oxygen chemically binds to germanium to form GeO_2 at a depth where their concentration profiles overlap, namely at etching time of 0 – 2500 seconds. XPS results indicate that GeO_2 depth-distribution exhibits a maximum for an etching time of 1300 seconds, which corresponds to the first third of the SiO_2 layer measured by XPS. This value is consistent with the projected range of $^{16}O^-$ ions calculated by SRIM-TRIM simulation (100 nm).

Seven samples have been co-implanted with fluences ranging from 0 to 1.66×10^{17} O/cm², for a single Ge fluence of 1.30×10^{17} Ge/cm². This range of fluences allows a constant evolution of the relative concentration of implanted oxygen atoms compared to Ge, until the concentration at maximum of added O atoms exceeds that of Ge (figure 7c). To simplify the discussion, Ge depth-distributions of annealed samples are superimposed in figure 7a and normalized integrals are shown in figure 7b. The depth-profiles of oxygen, derived from RBS measurements before annealing, are shown in figure 7c, as well as the $C_O/[C_O + C_{Si}]$ concentration ratio. Several effects on the multi-peak redistribution of Ge, attributed to oxygen co-implantation, are highlighted by RBS (figure 7) and XPS (figure 6) data analysis after thermal treatment:

1. According to XPS, the central peak is mainly composed of elemental Ge after annealing. As oxidized Ge compounds are thermodynamically less stable than oxidized Si at high temperature [32,33], the following oxygen exchange is expected to occur during annealing until the SiO_2 stoichiometry is restored:

$$GeO_x + SiO_x \rightarrow Ge + SiO_2, \quad (1)$$
$$GeO_x + Si \rightarrow Ge + SiO_x. \quad (2)$$

   This tendency of the SiO_2 layer to recover its stoichiometry is confirmed by XPS for annealed samples (figure 6), which shows that the SiO_2 stoichiometry is globally restored after annealing, as O 2s signal is no longer shifted. The central peak integral, measured by RBS, decreases by 95% while O fluence increases from 0 to 1.66×10^{17} O/cm² (figure 7b). This diminution seems to be proportional to the co-implanted fluence over the full range. For low O fluences, additional oxygen will bind with both Si and Ge atoms to form SiO_x and GeO_x compounds during the implantation. During annealing, the SiO_x concentration decreases as the SiO_2 stoichiometry is restored (equation 1), leading to a lower density of Si dangling bonds. At the same time, mobile GeO molecules are formed rather than GeO_2, as long as the oxygen excess stays relatively low compared to the Ge concentration, due to the following reaction [34,35]:

$$GeO_2 + Ge \rightarrow 2GeO. \quad (3)$$

   Therefore, GeO can diffuse easier as the Ge/Si trapping effects [9,10] due to silicon dangling bonds is reduced in this region of the oxide, from 0 to 1000×10^{15} at./cm², for co-implanted samples. These mobile GeO molecules, generally considered as the main responsible of the Ge redistribution, can diffuse towards oxygen-poor regions such as the SiO_2/Si interface or the sample surface. This is confirmed by RBS with the increase

in Ge concentration in these two regions of the SiO_2 layer, accompanied by a reduction in Ge concentration in the central peak, as the O fluence increases (figure 7b).

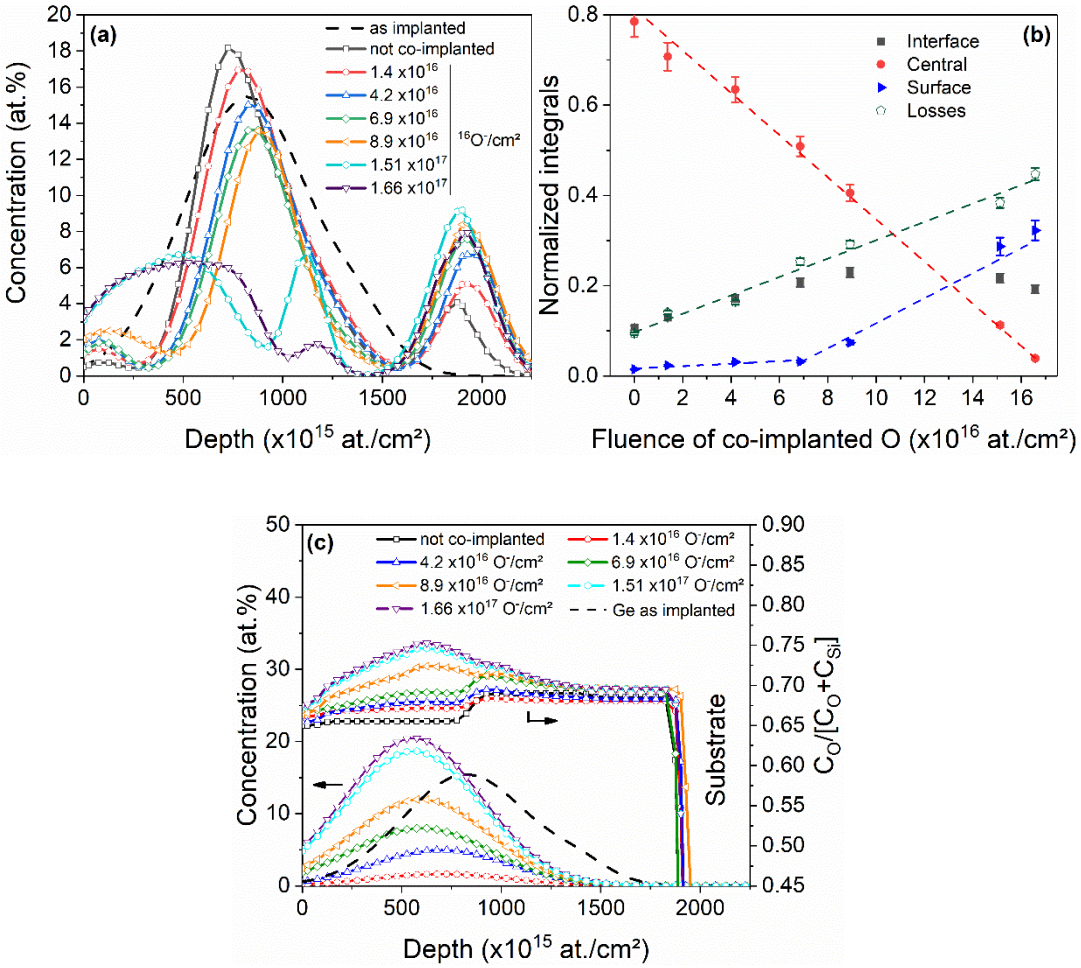

Figure 7: (a) Superposition of Ge depth-profiles measured by RBS after 60 minutes of annealing at 1100°C (N_2) for a fluence of co-implanted oxygen ranging from 0 to 1.66 × 10^{17} O/cm². (b) Normalized integrals of Ge peaks measured by RBS. (c) Oxygen depth-profiles extracted from RBS analysis (left Y-axis) and $C_O/[C_O + C_{Si}]$ ratio (right Y-axis) before annealing. Oxide saturation is observed when the concentration ratio exceeds the ratio of a stoichiometric oxide (~0.667). The Ge depth-profile of the not co-implanted sample is shown to visualize the overlapping of O and Ge depth-profiles.

2. A sub-surface peak of fully oxidized germanium (GeO_2) appears after annealing when the oxygen fluence increases, as indicated in figure 6. For low oxygen concentrations, this peak is supposed to be due to additional oxygen in the damaged layer, leading to the formation of GeO molecules, and to the presence of residual impurities (H_2O, O_2) in the annealing environment [11,13,16,36,37]. The encounter of out-diffusing GeO with in-diffusing O_2 coming from the annealing atmosphere forces the oxidation of Ge. For higher oxygen fluences, the concentration of oxygen is so high that the SiO_2 oxide is saturated, as shown in figure 7c by the $C_O/[C_O + C_{Si}]$ concentration ratios. The saturation is observed when the concentration ratio exceeds the ratio of a stoichiometric oxide (~0.667). The exceeding oxygen is therefore free to oxidize germanium atoms or GeO molecules to form GeO_2 if the concentration of O is at least comparable to that of Ge. The mobility of fully oxidized germanium is highly reduced

compared to that of GeO.

XPS data confirm that GeO_2 formation occurs already during the implantation of oxygen (figure 6d) and that this sub-surface peak is composed of GeO_2 after the annealing step (figure 6f). The formation of this few mobile GeO_2 explains the extension of the sub-surface peak observed for higher oxygen fluences in both RBS and XPS measurements.

3. The integral of the SiO_2/Si interface peak increases with the oxygen fluence before decreasing for higher fluences (black squares in figure 7b). This indicates that the fraction of GeO diffusing in depth also increases with the co-implanted O fluence. This can be attributed to an increase of oxygen concentration, and so GeO concentration, with the oxygen fluence (figure 7c), and to the over-stoichiometric state of the oxide between the Ge projected range and the SiO_2/Si interface which favors diffusion. This demonstrates that GeO also diffuses towards the oxygen-poor regions such as the SiO_2/Si interface, which is known to be under-stoichiometric [38], where it reduces in elemental Ge (equations 1-2). XPS measurement on annealed samples (figures 6b, 6c, 6e, 6f) confirms that this interface peak is composed of Ge-Ge and Ge-Si bonds (Ge^0 and Ge^0 hybr.). However, if *Baranwal et al.* has observed the presence of Ge nanocrystals in the vicinity of the interface [20], using transmission electron microscopy (TEM) investigations, it was evidenced by *Markvitz et al.* that the formation of such bonds would not necessarily lead to the nucleation of Ge [11]. Nevertheless, note that one could imagine to use this accumulation of Ge at the SiO_2/Si interface to reduce the current crowding effects occurring in MOS gate-controlled device structures [39].
4. Figure 7b shows an increase of 450% of desorption losses through the sample surface observed for co-implantation fluences varying from 0 to 1.66×10^{17} O/cm². As already discussed, the presence of additional oxygen atoms saturates the Si dangling bonds and therefore reduces the Ge/Si trapping effects [9,10,26]. This also leads to the formation of mobile GeO, giving rise to a diffusion directed towards the oxygen-poor regions, such as the sample surface. There, the highly volatile GeO molecules desorb through the surface. These losses increase with the concentration of GeO present in the sample and specially in the vicinity of the sample surface in co-implanted samples.

D. Influence on Ge nanoclustering

µ-Raman and XRD analyses were performed to highlight the impact of oxygen co-implantation over Ge nanoclustering. µ-Raman spectra are shown in figure 8a within the spectral range of 270 - 330 cm^{-1}, chosen to eliminate the strong contribution of the TO phonon mode of the Si substrate around 520.7 cm^{-1} and to zoom on the region where Raman phonons related to Ge nanocrystals appear [40]. In agreement with previous studies [9,10,40-41] two contributions are observed at about 291 and 300 cm^{-1} in figure 8a. These peaks are associated to the signature of small Ge nanocrystals (or containing Si impurities) and pure Ge nanocrystals, respectively.

As previously shown by XPS and RBS analyses, the SiO_2 region mainly impacted by co-implanted oxygen ions (for an etching time of 0 - 2000 seconds) is the damaged zone of the

film which corresponds to the growth region of smaller nanocrystals (or nanocrystals containing Si) [10,20].

The evolution of Raman peaks integrals is shown in figure 8b. As absolute intensities are hard to compare in Raman spectroscopy, we use the ratio I_{Ge-Ge}/I_{Ge-Ge^*}, which represents the integrals ratio between pure (Ge-Ge) and Si-contaminated or very small nanocrystals (Ge-Ge*). An important increase of this ratio is observed between 0 and 4.17 ×10^{16} O/cm², which indicates that the density of small nanocrystals (Raman peak around 291 cm^{-1}) decreases continuously, compared to that of pure Ge-ncs, with the fluence of co-implanted oxygen. As the growth region of small nanocrystals coincides with the projected range of co-implanted oxygen ions, this diminution of small nanocrystals signature in Raman spectra is consistent with the increased Ge diffusion highlighted by RBS and XPS measurements in this region for lower oxygen fluences. For higher oxygen concentrations, I_{Ge-Ge}/I_{Ge-Ge^*} ratio decreases with oxygen fluence, meaning a diminution of the density of pure germanium nanocrystals (Raman peak around 300 cm^{-1}), which can be attributed to the direct formation of GeO_2 during the implantation or during annealing, as shown by XPS for higher oxygen fluences (figure 6).

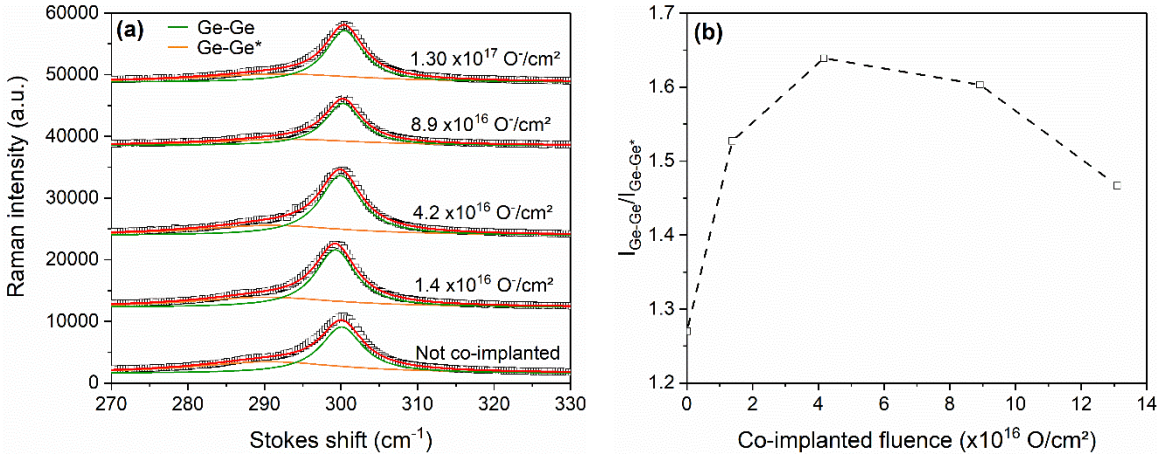

Figure 8: (a) µ-Raman measurements focused on frequencies corresponding to Ge nanocrystals signal, and (b) evolution of I_{Ge-Ge}/I_{Ge-Ge^*} ratio as a function of co-implanted oxygen fluence. Dotted lines are only there to guide the eye.

Note that a very weak Raman signal is measured at around 400-405 cm^{-1} from an oxygen fluence of 4.17 × 10^{16} O/cm², with a slight increase in intensity with oxygen fluence. This peak corresponds to Ge-Si chemical bonds and is supposed to be due to the increase of Ge concentration at the SiO_2/Si interface and the subsequent formation of Ge-Si bonds.

The reduction of small nanocrystals density is confirmed by XRD measurements, with analyses focused on Ge (111) signal around 27.4°, which showed a constant diminution of the peak broadening until the SiO_2 oversaturation. This indicates a standardization of nanocrystals size, which could be consistent with an elimination of small nanocrystals and the conservation of larger nanostructures. Using Scherrer's equation and taking into account instrumental broadening, the Ge nanocrystals average size is calculated and reported in table II and figure 9. It is shown that the nanocrystals average size linearly increases with the co-implanted

fluence, which tends to confirm the disappearance of small nanostructures to the benefit of larger ones, until the SiO_2 oversaturation and the subsequent formation of GeO_2.

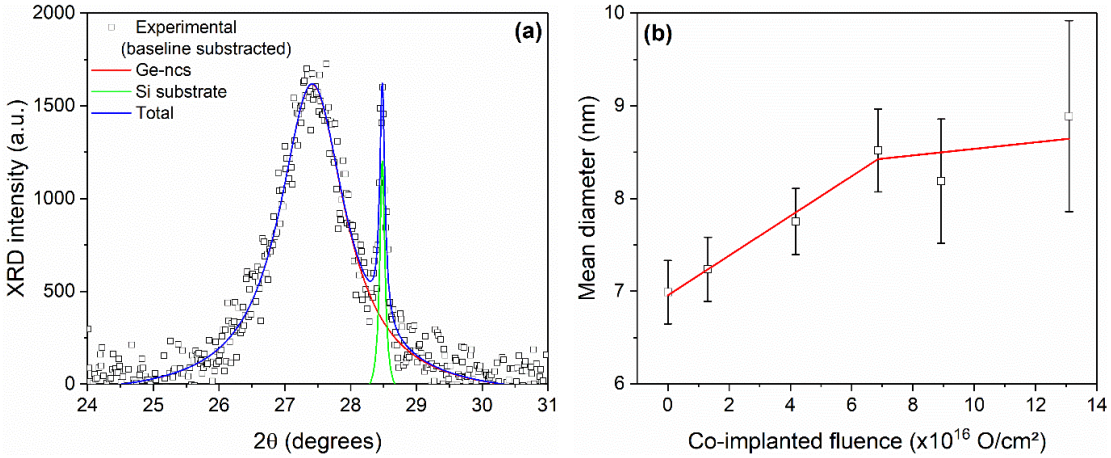

Figure 9: (a) Example of a fit with Ge nanocrystals peak around 27.4° and Si substrate signal around 28.45°. (b) Evolution of nanocrystals mean diameter as a function of the oxygen fluence, the red lines are only there to guide the eye.

These µ-Raman and XRD results indicate that oxygen co-implantation could be used to locally reduce the size dispersion of Ge nanocrystals, which increases with Ge fluence [12], by preserving only the purest Ge-ncs while removing small nanocrystals. After the possibility of controlling the diffusion of Ge and the size distribution in depth of Ge nanocrystals by Si co-implantation [9,10,19], introduction of oxygen excess could be another tool in a precise control of nanocrystals size dispersion. This study demonstrates that the O fluence must stay relatively low to enhance Ge diffusion while limiting its desorption or the formation of GeO_2. As Ge-ncs photoluminescence (PL) could partially depend of the nanocrystals size and their Si contamination [33,42], an uniform size distribution could reduce the broad PL emission observed for Ge-ncs in SiO_2 [43], making them possibly more suitable for applications such as lasers.

Co-implanted fluence ($\times 10^{17}$ O^-/cm^2)	**0**	**0.14**	**0.42**	**0.69**	**0.89**	**1.31**
Mean diameter (nm)	**7.0** ±0.3	**7.2** ±0.4	**7.8** ±0.4	**8.5** ±0.4	**8.2** ±0.7	**8.9** ±1.0

Table II: Evolution of nanocrystals average size as measured by XRD and calculated using Scherrer's equation.

IV. Conclusions

Combination of RBS and XPS investigations confirmed the role played by GeO formation and ion damaging, which both occur simultaneously during germanium implantation, on the thermally activated diffusion of Ge atoms implanted in the middle of SiO_2 films. The results highlight the effects of both the Ge fluence and the stoichiometric state of the implanted SiO_2 film on the diffusion of germanium, explaining the large discrepancies observed in literature. It is shown that the concentrations of GeO_x compounds and Ge^0 linearly increase with the germanium fluence with different slopes, leading to different dominations as a function of the implanted fluence. This explains why germanium diffusion is generally improved in SiO_2 layers implanted with low Ge fluences compared to higher fluences.

As implanted samples are characterized by large discrepancies in the size of the thermally grown nanostructures, due to specific irradiation-induced damage, the use of oxygen co-implantation is suggested to prevent the formation of the smallest nanocrystals. It is shown by RBS and XPS, and supported by µ-Raman and XRD measurements, that the introduction of oxygen excess in the damaged regions of the SiO_2 film can improve the mobility of Ge atoms. At relatively low O concentration, the gain in Ge mobility enables to increase the average size of nanocrystals. At higher O fluences, the high mobility of GeO causes the desorption of germanium through the sample surface until the over-saturation of the oxide, which leads to the formation of fixed GeO_2.

ACKNOWLEDGMENTS

The authors would like to thanks Welcome platform for the accessibility to the spectrometer and especially Ferran Urena Begara for his help, T. Tabarrant for the technical support on ALTAÏS accelerator, SIAM (Synthesis, Irradiation and Analysis of Materials) and PC² (Physico-Chemical Characterization) technological platforms of the university of Namur for XPS and XRD measurements.

DATA AVAILABILITY

The data that support the findings of this study are available from the corresponding author upon request.

REFERENCES

[1] Xu, K., Huang, L., Zhang, Z., Zhao, J., Zhang, Z., Snyman, L. W., & Swart, J. W. (2018). *Light emission from a poly-silicon device with carrier injection engineering.* Materials Science and Engineering: B, 231, 28–31. https://doi.org/10.1016/j.mseb.2018.07.002

[2] Márquez, J., Stange, H., Hages, C. J., Schaefer, N., Levcenko, S., Giraldo, S., Saucedo, E., Schwarzburg, K., Abou-Ras, D., Redinger, A., Klaus, M., Genzel, C., Unold, T., & Mainz, R. (2017). *Chemistry and Dynamics of Ge in Kesterite: Toward Band-Gap-Graded Absorbers.* Chemistry of Materials, 29(21), 9399–9406. https://doi.org/10.1021/acs.chemmater.7b03416

[3] Green, M. A., & Bremner, S. P. (2017). *Energy conversion approaches and materials for high-efficiency photovoltaics*. Nature Materials, 16, 23–34. https://doi.org/10.1038/nmat4676

[4] Yedji, M., Demarche, J., Terwagne, G., Delamare, R., Flandre, D., Barba, D., Koshel, D., & Ross, G. G. (2011). *Method for fabricating third generation photovoltaic cells based on Si quantum dots using ion implantation into SiO_2.* J. Appl. Phys., 109(8), 084337. https://doi.org/10.1063/1.3575325

[5] Beard, M. C., Knustsen, K. P., Yu, P., Song, Q., Luther, J., Ellingson, R., & Nozik, A. J. (2007). *Multiple exciton generation in colloidal silicon nanocrystals*. *Nano Lett.*, *7*, 2506–2512. https://doi.org/10.1021/nl071486l

[6] Nann, T., & Skinner, W. M. (2011). *Quantum Dots for Electro-Optic Devices.* ACS Nano, 5(7), 5291–5295. https://doi.org/10.1021/nn2022974

[7] Hanafi, H. I., Tiwari, S., & Khan, I. (1996). *Fast and long retention-time nano-crystal memory*. IEEE Trans. Electron Devices, 43, 1553–1558. https://doi.org/10.1109/16.535349

[8] Trinh, M. T., Limpens, R., de Boer, W. D. A. M., Schins, J. M., Siebbeles, L. D. A., & Gregorkiewicz, T. (2012). *Direct generation of multiple excitons in adjacent silicon nanocrystals revealed by induced absorption.* Nature Photonics, 6(5), 316–321. https://doi.org/10.1038/nphoton.2012.36

[9] Nélis, A., Barba, D., & Terwagne, G. (2020). *Control of germanium diffusion using low quantities of co-implanted silicon isotopes.* J. Appl. Phys., 128(12), 125705. https://doi.org/10.1063/5.0020368

[10] Barba, D., Wang, C., Nélis, A., Terwagne, G., & Rosei, F. (2018). *Blocking germanium diffusion inside silicon dioxide using a co-implanted silicon barrier*. *J. Appl. Phys.*, *123*(16), 161540. https://doi.org/10.1063/1.5002693

[11] Markwitz, A., Schmidt, B., Matz, W., Grötzschel, R., & Mücklich, A. *(1998). Microstructural investigation of ion beam synthesised germanium nanoclusters embedded in SiO_2 layers.* Nucl. Instrum. Methods Phys. Res. B, 142(3), 338–348. https://doi.org/10.1016/S0168-583X(98)00283-3

[12] Ge, L. H., Wang, C., Cai, R. S., Liang, W. S., Wang, Y. Q., Ross, G. G., & Barba, D. (2017). *Effect of Ge Concentration on the Microstructure of Germanium Nanocrystals Produced by Ion Implantation in SiO_2*. Nanosci. Nanotechno., 17(3), 2196–2200. https://doi.org/10.1166/jnn.2017.12858

[13] Heinig, K. ., Schmidt, B., Markwitz, A., Grötzschel, R., Strobel, M., & Oswald, S. (1999). *Precipitation, ripening and chemical effects during annealing of Ge^+ implanted SiO_2 layers*. Nucl. Instrum. Methods Phys. Res. B, 148(1–4), 969–974. https://doi.org/10.1016/S0168-583X(98)00862-3

[14] Marstein, E. S., Gunnæs, A. E., Serincan, U., Jørgensen, S., Olsen, A., Turan, R., & Finstad, T. G. (2003). *Mechanisms of void formation in Ge implanted SiO_2 films.* Nucl. Instrum. Methods Phys. Res. B, 207(4), 424–433. https://doi.org/10.1016/S0168-583X(03)00965-0

[15] Beyer, V., & von Borany, J. (2008). *Elemental redistribution and Ge loss during ion-beam synthesis of Ge nanocrystals in SiO_2 films*. Phys. Rev. B, 77(1), 014107. https://doi.org/10.1103/PhysRevB.77.014107

[16] von Borany, J., Grötzschel, R., Heinig, K. H., Markwitz, A., Matz, W., Schmidt, B., & Skorupa, W. (1997). *Multimodal impurity redistribution and nanocluster formation in Ge implanted silicon dioxide films*. Appl. Phys. Lett., 71(22), 3215–3217. https://doi.org/10.1063/1.120294

[17] Hao, X., Zhou, C., Yu, R., Wang, B., & Wei, L. (2008). *Characterization of Implantation Induced Defects in Si-Implanted SiO_2 Film*. Nanosci. Nanotechno., 8(3), 1350–1354. https://doi.org/10.1166/jnn.2008.327

[18] Oswald, S., Schmidt, B., & Heinig, K.-H. (2000). *XPS investigation with factor analysis for the study of Ge clustering in SiO_2.* Surf. Interface Anal., 29(4), 249–254. https://doi.org/10.1002/(SICI)1096-9918(200004)29:4<249::AID-SIA735>3.0.CO;2-5

[19] Barba, D., Demarche, J., Martin, F., Terwagne, G., & Ross, G. G. (2012). *Trapping of diffusing germanium by silicon excess co-implanted into fused silica.* Appl. Phys. Lett., 101(14), 143107. https://doi.org/10.1063/1.4757291

[20] Baranwal, V., Gerlach, J. W., Lotnyk, A., Rauschenbach, B., Karl, H., Ojha, S., … Pandey, A. C. (2015). *Embedded Ge nanocrystals in SiO_2 synthesized by ion implantation*. J. Appl. Phys., 118(13), 134303. https://doi.org/10.1063/1.4932151

[21] Ziegler, J. F., Ziegler, M. D., & Biersack, J. P. (2010). *SRIM – The stopping and range of ions in matter (2010).* Nucl. Instrum. Methods Phys. Res. B, 268(11–12), 1818–1823. https://doi.org/10.1016/j.nimb.2010.02.091

[22] *SIMNRA, a simulation program for the analysis of NRA, RBS and ERDA.* Mayer, M. 1999*, AIP Conf. Proc.*

[23] *Characterization of carbon nitride compounds synthesized by simultaneous implantation of carbon and nitrogen in copper.* Colaux, J.L. 2009, Doctoral dissertation, University of Namur.

[24] Greczynski, G., & Hultman, L. (2020). *X-ray photoelectron spectroscopy: Towards reliable binding energy referencing.* Prog. Mater. Sci., 107, 100591. https://doi.org/10.1016/j.pmatsci.2019.100591

[25] *Rassinfosse, L., Colaux, J. L., Pilloud, D., Nominé, A., Tumanov, N., Lucas, S., … Haye, E. (2020). Using ammonia for reactive magnetron sputtering, a possible alternative to HiPIMS? Appl. Phys. Lett., 502, 144176.* https://doi.org/10.1016/j.apsusc.2019.144176

[26] Barba, D., Cai, R. S., Demarche, J., Wang, Y. Q., Terwagne, G., Rosei, F., … Ross, G. G. (2014). *Influence of silicon dangling bonds on germanium thermal diffusion within SiO_2 glass.* Appl. Phys. Lett., 104(11), 111901. https://doi.org/10.1063/1.4868721

[27] Rodríguez, A., Rodríguez, T., Prieto, Á. C., Jiménez, J., Kling, A., Ballesteros, C., & Sangrador, J. (2010). *Crystallization of Amorphous $Si_{0.6}Ge_{0.4}$ Nanoparticles Embedded in SiO2: Crystallinity Versus Compositional Stability*. J. Electon. Mater., 39(8), 1194–1202. https://doi.org/10.1007/s11664-010-1254-9

[28] Kim, H. B., Chae, K. H., Whang, C. N., Yeong, J. Y., Oh, M. S., Im, S., & Song, J. H. (1998). *The origin of photoluminescence In Ge-implanted SiO_2 layers.* J. Lumin., 80, 281–284. https://doi.org/10.1109/IMNC.1998.730045

[29] Tsai, H.-S., Chen, Y.-Z., Medina, H., Su, T.-Y., Chou, T.-S., Chen, Y.-H., … Liang, J.-H. (2015). *Direct formation of large-scale multi-layered germanene on Si substrate.* Phys. Chem. Chem. Phys., 17(33), 21389–21393. https://doi.org/10.1039/C5CP02469B

[30] Jensen, D. S., Kanyal, S. S., Madaan, N., Vail, M. A., Dadson, A. E., Engelhard, M. H., & Linford, M. R. (2013). *Silicon (100)/SiO_2 by XPS.* Surf. Sci. Spectra, 20(1), 36–42. https://doi.org/10.1116/11.20121101

[31] Pfeffer, R. L. (1985). *Damage center formation in SiO_2 thin films by fast electron irradiation.* J. Appl. Phys., 57(12), 5176–5180. https://doi.org/10.1063/1.335252

[32] Prabhakaran, K., Maeda, F., Watanabe, Y., & Ogino, T. (2000). *Distinctly different thermal decomposition pathways of ultrathin oxide layer on Ge and Si surfaces.* Appl. Phys. Lett., 76(16), 2244–2246. https://doi.org/10.1063/1.126309

[33] Gambaryan, M. P., Krivyakin, G. K., Cherkova, S. G., Stoffel, M., Rinnert, H., Vergnat, M., & Volodin, V. A. (2020). *Quantum Size Effects in Germanium Nanocrystals and Amorphous Nanoclusters in $GeSi_xO_y$ Films.* Phys. Solid State, 62(3), 492–498. https://doi.org/10.1134/S1063783420030105

[34] Oh, J., & Campbell, J. C. (2004). *Thermal desorption of Ge native oxides and loss of Ge from the surface.* J. Electon. Mater., 33(4), 364–367. https://doi.org/10.1016/j.mssp.2010.10.009

[35] Hellberg, P.-E., Zhang, S.-L., D'Heurle, F. M., & Petersson, C. S. (1997). *Oxidation of silicon–germanium alloys. II. A mathematical model.* J. Appl. Phys., 82(11), 5779–5787. https://doi.org/10.1063/1.366444

[36] Borodin, V. A., Heinig, K.-H., & Schmidt, B. (1999). *Modeling of Ge nanocluster evolution in ion-implanted SiO_2 layer.* Nucl. Instrum. Methods Phys. Res. B, 147(1–4), 286–291. https://doi.org/10.1016/S0168-583X(98)00562-X

[37] Nélis, A., Vickridge, I., Ganem, J.-J., Briand, E., Terwagne, G. (2021). *$^{18}O(p,a)^{15}N$ isotopic tracing of germanium diffusion in SiO_2/Si films.* J. Appl. Phys. 130 (10), .

[38] Takakuwa, Y., Nihei, M., & Miyamoto, N. (1993). *Outdiffusion and Subsequent Desorption of Volatile SiO Molecules during Annealing of Thick SiO_2 Films in Vacuum.* Jpn J. Appl. Phys., 32(Part 2, No. 4A), L480–L483. https://doi.org/10.1143/JJAP.32.L480

[39] Xu, K. (2021). *Silicon electro-optic micro-modulator fabricated in standard CMOS technology as components for all silicon monolithic integrated optoelectronic systems*. J. Micromech. Microeng. 31, 054001. https://doi.org/10.1088/1361-6439/abf333

[40] Barba, D., Demarche, J., Martin, F., Terwagne, G., & Ross, G. G. (2013). *Control of the Ge nanocrystal synthesis by co-implantation of Si^+.* J. Appl. Phys., 114(7), 074306. https://doi.org/10.1063/1.4817667

[41] Liu, L. Z., Gao, F., Wu, X. L., Li, T. H., & Chu, P. K. (2009). *Influence of GeSi interfacial layer on Ge–Ge optical phonon mode in SiO_2 films embedded with Ge nanocrystals.* Appl. Phys. Lett., 95(17), 171105. https://doi.org/10.1063/1.3257379

[42] Takeoka, S., Toshikiyo, K., Fujii, M., Hayashi, S., & Yamamoto, K. (2000). *Photoluminescence from$Si_{1-x}Ge_x$ alloy nanocrystals*. Phys. Rev. B, 61(23), 15988–15992. https://doi.org/10.1103/PhysRevB.61.15988

[43] Choi, W. K., Ho, Y. W., Ng, S. P., & Ng, V. (2001). *Microstructural and photoluminescence studies of germanium nanocrystals in amorphous silicon oxide films.* J. Appl. Phys., 89(4), 2168–2172. https://doi.org/10.1063/1.1342026

Article II: $^{18}O(p,\alpha)^{15}N$ isotopic tracing of germanium diffusion

Preliminary to article II

Article I explained the diffusion mechanisms as a function of Ge fluence, the stoichiometric state of the oxide and the role of oxygen through the formation of Ge^0, GeO and GeO_2 compounds, already occurring during the implantation process. This leads to the asymmetric diffusion of the implanted Ge atoms because of the presence of mobile and less mobile species, as well as the presence of over and under-stoichiometric SiO_x regions exhibiting different Ge diffusivities.

This second article aims to highlight the different origins of oxygen and their respective impact on the thermally activated diffusion of germanium. As previously mentioned in **article I**, oxygen may have two possible origins, qualified as intrinsic or extrinsic sources. The main supplier of oxygen is obviously the implanted SiO_2 layer, considered as an intrinsic source of oxygen. Germanium atoms chemically bind to oxygen atoms present in the oxide, already during the implantation process (51), (122), (125), causing the formation of GeO molecules considered as the main cause of germanium diffusion. The extrinsic source results of the presence of residual contaminants, as O_2 or H_2O, in the furnace tube under bad vacuum conditions or low purity of the inert gas (122), (123), (127). *Beyer et al.* (122) also established that oxidizing components coming from wet chemical cleaning or ambient atmosphere, penetrate the damaged SiO_2 and are responsible of germanium oxidation and desorption at the extreme surface of implanted SiO_2 films.

In the manuscript entitled "*$^{18}O(p,\alpha)^{15}N$ isotopic tracing of germanium diffusion in SiO_2/Si films*", we proposed to use the ^{18}O stable isotope to trace oxygen diffusion and to correlate this migration to that of germanium, using the $^{18}O(p,\alpha)^{15}N$ resonant nuclear reaction at around 151 keV. As ^{18}O represents only 0.2% of natural oxygen, the use of isotopically sensitive analyses highlighted distinctly the contributions of an oxygen-contaminated atmosphere and oxygen naturally present in the oxide. This narrow resonant reaction ($\Gamma \sim 100$ eV) allowed us to demonstrate the importance of working in a highly pure annealing environment and to bring out the connected diffusion of germanium and oxygen through the oxide film.

Authors' contribution

I proposed the idea of using the ^{18}O stable isotope to trace the oxygen coming from the annealing atmosphere, while the idea of forming ^{18}O-enriched oxides was proposed by Jean-Jacques Ganem. I carried out all the Ge implantations at LARN with ALTAÏS. We worked together with Ian Vickridge, Jean-Jacques Ganem and Emrick Briand to perform the ion beam analyses (NRA, RBS and RNRA) with SAPHIR or ALTAÏS. Supported by Ian and Jean-Jacques, I realized the data analysis. I wrote the article with the comments of the other authors.

$^{18}O(p,\alpha)^{15}N$ isotopic tracing of germanium diffusion in SiO_2/Si films

A. Nélis[1,*], I. Vickridge[2], J.-J. Ganem[2], E. Briand[2], G. Terwagne[1]

[1] LARN, Namur Institute of Structured Matter (NISM), University of Namur (UNAMUR), B-5000 Namur, Belgium

[2] Sorbonne Université, Institut des NanoSciences de Paris, CNRS UMR 7588, 4 place Jussieu, F-75252 Paris cedex 05, France

Published in *Journal of Applied Physics* **130** (2021) 105701.

https://doi.org/10.1063/1.5002693

Abstract

We investigate the effects of oxygen on the thermal diffusion of germanium atoms, implanted inside a thermally grown SiO_2 layer, during high temperature processes (1100°C, 60 minutes). The impact of oxygen presence on Ge diffusion is studied as a function of its origin, as it can come either from the annealing atmosphere (extrinsic source) or from the SiO_2 matrix itself (intrinsic source). ^{18}O labeling of the oxygen either in the annealing atmosphere or in the silica substrate, together with isotopically sensitive Ion Beam Analysis (IBA), shows a clear oxygen-dependence in germanium diffusion. This is especially so when oxygen is present in the annealing atmosphere, where it is responsible for an enhancement of germanium out-diffusion and redistribution into several peaks during annealing, through the formation of GeO molecules. A new three-process model is proposed to explain the impact of a contaminated atmosphere on Ge redistribution. This is notably shown that a third Ge peak arises at the sample surface when the annealing atmosphere is contaminated by oxygen. This peak formation is explained by the oxidation of Ge present at the vicinity of the surface by oxygen coming from the annealing atmosphere. This is also shown that O_2 molecules can diffuse in depth, with a coefficient of diffusion $D_{O_2} \sim 10^{-9} cm^2/s$, until the densities of Ge and irradiation-induced defects increase, causing the progressive oxidation of Ge in depth and the restoration of the SiO_2 stoichiometry.

Keywords: Resonant Nuclear Reaction Analysis; Ge diffusion; ion implantation; GeO formation; stable isotopic tracing.

I. Introduction

Integration of germanium nanocrystals (Ge-ncs), and more widely group IV materials, produced by ion implantation into dielectric layers has been largely studied over last decades thanks to their numerous attractive optoelectronic properties [1-5]. Bandgap engineering, possible multiple exciton generation (MEG) or photoluminescence show great promise for enhancing the conversion efficiency of modern photovoltaic cells.

Fabrication of Ge-ncs by ion implantation requires a thermal activation, with temperatures as high as 800-1100°C under non-reactive atmosphere (N_2 or Ar), which is responsible for long-range germanium redistribution inside the insulator layer, a thermally grown silicon dioxide film in this study [6-14]. Germanium diffusion mechanisms are generally associated in literature to the presence of oxygen [8-13,15,16]. The first origin of the oxygen involved in germanium diffusion is the oxygen directly supplied by the SiO_2 host matrix and released by the dose-dependent damage and atomic rearrangement generated during the implantation and annealing processes. X-ray photoelectron spectroscopy (XPS) measurements demonstrated that implanted germanium ions are chemically bound to oxygen and silicon atoms present in the SiO_2 layer, already during the implantation process [9,12,17]. This is responsible for the formation of GeO_x compounds within the oxide film, including highly volatile GeO, considered to be the main contributor to germanium out-diffusion during thermal treatments. *Heinig et al.* [11] and *Borodin et al.* [18] also proposed that oxygen could be provided by the presence, in the annealing atmosphere, of residual moisture and other oxygen-containing compounds (O_2, H_2O, OH). These oxidizing agents could penetrate through the damaged silica surface and diffuse inside the SiO_2 film.

In this work, we propose to use the ^{18}O isotope to trace oxygen behavior during thermal processes and to correlate it with the diffusion of implanted germanium atoms. Two sets of samples have been prepared. The first set of samples aims to highlight the transport of oxygen atoms originating in the SiO_2 layer, by using an ^{18}O-containing oxide film implanted with Ge and annealed under high purity N_2 atmosphere (100 % of the gas introduced in the furnace tube). The second set of samples is intended to show the impact of oxidizing agents present in the annealing environment on the diffusion of germanium by using commercial thermally-grown SiO_2 layers implanted with germanium and annealed under a controlled atmosphere composed of 99 % of nitrogen and 1 % of $^{18}O_2$. This allows us to highlight the impact of the purity of the annealing environment on the germanium redistribution.

^{74}Ge and ^{18}O depth-distributions before and after annealing are obtained by a combination of Rutherford Backscattering Spectroscopy (RBS), Nuclear Reaction Analysis (NRA) and Resonant Nuclear Reaction Analysis (RNRA) measurements.

II. Experiment

The two sets of samples will be referred as type A, for Ge implantations in $Si^{18}O_2$ layers (sandwiched between two $Si^{16}O_2$ layers – see below) annealed under pure N_2 (after the implantation), and type B, for Ge implantations in commercial SiO_2 films annealed under an atmosphere contaminated by $^{18}O_2$ molecules.

For type A samples, (100) silicon wafers are oxidized before Ge implantation under dry atmosphere in three successive steps ($^{16}O/^{18}O/^{16}O$) to obtain a sandwich configuration. The respective thicknesses of the three layers (from the sample surface to depth), confirmed by RBS, were: 1. ~110 nm $Si^{16}O_2$; 2. ~60 nm $Si^{18}O_2$; 3. ~80 nm $Si^{16}O_2$. They were chosen so that the projected range R_p of about 134 nm (calculated by SRIM-2013 [19]) for the $^{74}Ge^+$ ions implanted at 185 keV is located around the middle of the ^{18}O labelled layer. After implantation, samples were annealed at 1100°C for 60 minutes in pure N_2 (600 mbar) in a quartz tube furnace (INSP), coupled with a turbomolecular pump. Base pressure in the furnace before introduction of N_2 was < 10^{-5} mbar.

For type B samples, 300 nm thick wet-oxidized and 200 nm dry-oxidized (100) silicon wafers were implanted with $^{74}Ge^+$ ions at energies of 230 keV (R_p = 156 nm) and 140 keV (R_p = 156 nm) respectively, for measured fluences varying from 3.5 × 10^{16} to 2.2 × 10^{17} Ge/cm^2. After implantation, the samples are annealed at 1100°C for 60 minutes under a controlled atmosphere of 594 mbar N_2 plus 6 mbar $^{18}O_2$ in INSP quartz tube furnace. Note that anneals just in 6 mbar $^{18}O_2$ without nitrogen gives very similar results, with a weak quantity of additional oxygen incorporated in the presence of nitrogen.

All implantations were carried out with the 2 MV Tandetron ALTAÏS (Accélérateur Linéaire Tandetron pour l'Analyse et l'Implantation des Solides) accelerator available at LARN.

^{74}Ge fluences and depth-profiles were verified by RBS before and after annealing at INSP with the 2.5 MV Van de Graaff accelerator of SAFIR platform (System d'Analyses par Faisceaux d'Ions Rapides) or at LARN with ALTAÏS.

^{18}O depth-profiles were measured via the $^{18}O(p,\alpha)^{15}N$ narrow resonant reaction (width Γ ~ 100 eV) at 151 keV [20-23]. The ^{18}O depth-profiles are deduced from the measured excitation curves by iteratively fitting simulations generated by SPACES [24], assuming a stopping power and a density of 475 keV/(µg/cm²) and 6.65 × 10^{22} at/cm³ respectively for pure SiO_2.

^{16}O and ^{18}O were quantified by NRA before and after annealing, with $^{16}O(d,\alpha)^{14}N$ and $^{18}O(d,\alpha)^{16}N$ reactions at 860 and 750 keV.

III. Results and discussion

A. Annealing under pure N_2: role of the host matrix

The isotopic sandwich structure of the implanted oxide is visible in figure 1, showing the ^{18}O depth-profile of a virgin [$Si^{16}O_2/Si^{18}O_2/Si^{16}O_2$] oxide layer represented by a black solid line. The $Si^{18}O_2$ film is centered at around 130 nm, almost corresponding to the middle of the whole oxide, with a small peak at the sample surface, resulting from $^{18}O/^{16}O$ exchanges taking place during the successive oxidation steps [25].

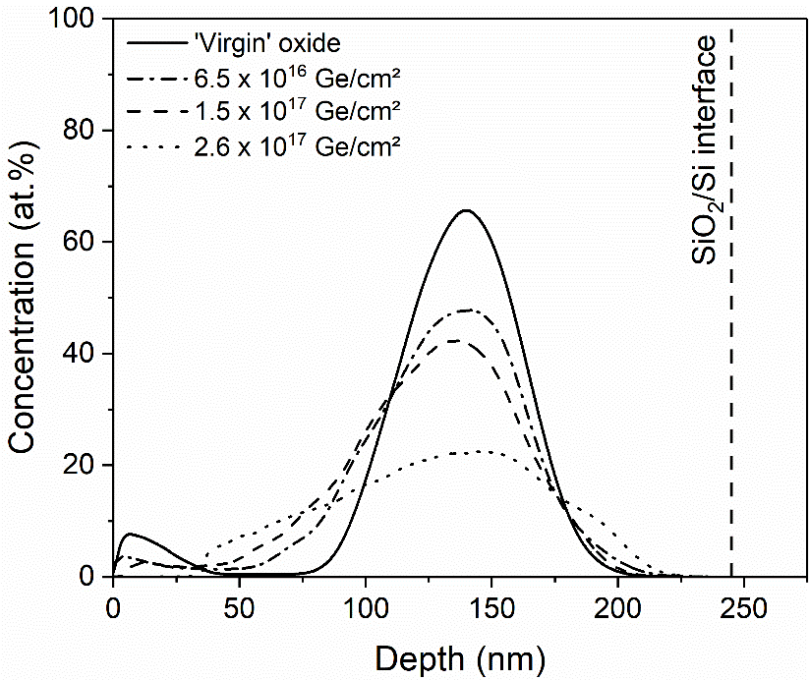

Figure 1: ^{18}O depth-distributions of 245 nm $Si^{16}O/Si^{18}O/Si^{16}O/Si$ layers for virgin oxide (solid line) and for implantation fluences of 6.5×10^{16}, 1.5×10^{17} and 2.6×10^{17} Ge/cm². All profiles have as reference the SiO_2/Si interface.

As shown in figure 1 for three different germanium fluences, the oxide layer undergoes a significant atomic rearrangement during implantation due to recoiled Si and O atoms, and subsequent cascades of collisions, caused by the passage of heavy $^{74}Ge^+$ ions. The beam effect is visible by observing the ^{18}O depth-distribution of the buried $Si^{18}O_2$ layer, showing substantial disorganization of the oxide film for the higher fluence (2.6×10^{17} Ge/cm² - dotted line). This layer rearrangement is consistent with the changes in the SiO_2 stoichiometry calculated by Tridyn simulations in ref. [9]. This dose-dependent atomic rearrangement leads to large stoichiometric discrepancies throughout the SiO_2 film, resulting in silicon excess (with respect to stoichiometric SiO_2) between the sample surface and the Ge projected range, and oxygen excess behind the projected range of germanium (see RBS results in figure S1 in supplementary material and more details in the upcoming ref. [17]). As a significant number of Si-O bonds are broken by the passage of the $^{74}Ge^+$ ions, a high fraction of $^{74}Ge^+$ ions will chemically bind to Si or O during the implantation. The concentrations of Ge-Si and Ge-O bonds increase with germanium fluence, as well as the formation of Ge-Ge bonds [17] (see figure S2 in supplementary material). Ge chemically bound to germanium or silicon is poorly mobile. The presence of germanium in an oxidised state after the implantation step has been largely observed in literature [9,12,17,26]. Among GeO_x compounds, highly volatile GeO molecules are formed. These are generally considered to be the main mobile species responsible of both germanium diffusion and desorption.

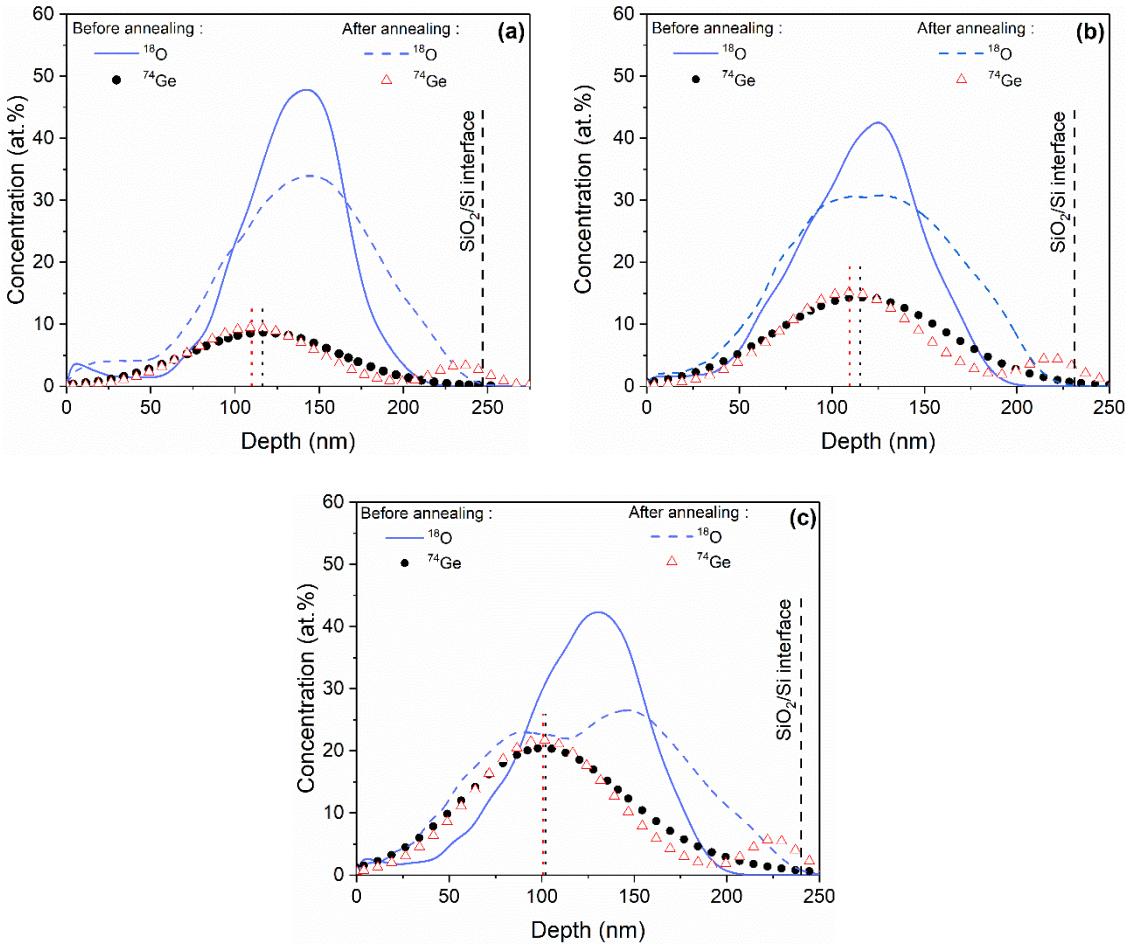

Figure 2: ^{74}Ge depth-profiles, extracted from RBS spectra, before (black dots) and after (red triangles) annealing and ^{18}O RNRA depth-profiles before (blue dashed line) and after (blue solid line) annealing for (a) 6.5×10^{16}, (b) 1×10^{17} and (c) 1.5×10^{17} Ge/cm². The depth position of the main peak is spotted by a dotted line.

As shown in figure 2, after implantation both Ge and ^{18}O profiles practically overlap (black dots and blue solid line respectively). This allows us to study the migration of these two species and highlight a possible connection between their thermally activated diffusion. As germanium atoms locally bind with oxygen atoms to form GeO_x, a fraction of implanted ions chemically binds to ^{18}O and ^{16}O during the implantation.

Three implantation fluences of 6.5×10^{16}, 1.0×10^{17} and 1.5×10^{17} Ge/cm² are shown in figure 2, corresponding to figures 2a, 2b and 2c respectively. After annealing under pure N_2 atmosphere, Ge exhibits a depth-profile (red triangles) consistent with that of samples annealed under pure N_2 (for an example see ref. [7]), *i.e.* a double peak configuration with a major peak slightly shifted towards the sample surface and an accumulation of Ge at the SiO_2/Si interface. This asymmetric diffusion is generally explained by the introduction of GeO molecules, diffusing towards oxygen-poor regions such as the sample surface and the SiO_2/Si interface [8,9,11,17,27]. The formation of these highly volatile GeO molecules could also explain Ge desorption occurring at the sample surface.

We know from previous works that the mobility of Ge is linked to the saturation in oxygen of the SiO_2 layer. As the oxide region between Ge projected range and sample surface is under-stoichiometric (SiO_x, x < 2), metastable GeO_x will reduce in a thermodynamically more stable configuration, while the SiO_2 network tends to recover its stoichiometry [see Refs [28] and [29] for Eq. (1), Ref [16] for Eq. (2), and Ref. [30] for Eq. (3)]:

$$GeO + SiO \rightarrow Ge + SiO_2, \quad (1)$$

$$GeO_x + Si \rightarrow Ge + SiO_x, \quad (2)$$

$$SiO_x \rightarrow \left(1 - \frac{x}{2}\right) Si + \frac{x}{2} SiO_2. \quad (3)$$

All reactions are supposed to be initiated in the first moments of annealing. As the SiO_2 layer recovers its stoichiometry in a region initially presenting a lack of oxygen, the concentration of less mobile elemental Ge and Si increases, leading to the local formation of Ge and SiGe nanocrystals. As the coefficient of diffusion of Ge is two orders of magnitude higher than that of Si in SiO_2 [27], mostly Ge-Si and Ge-Ge chemical bonds will be formed rather than Si-Si [6,7,31]. The chemical evolution of the main RBS peak has been probed by XPS studies [16,17], confirming that GeO_x is reduced to elemental Ge^0 during annealing (*i.e.* Ge chemically bound to Ge or Si, which are not distinguishable by XPS). Only germanium implanted close to the surface is eventually able to desorb through the gas/oxide interface before being trapped by the nucleation process.

On the other side, a Ge accumulation peak is measured at the SiO_2/Si interface, indicating that a part of germanium diffuses inwards. Due to the over-stoichiometric state (SiO_x, x > 2) of the oxide region between the Ge projected range and the Si substrate after implantation, the reduction process of equations 1-3 will restore the SiO_2 stoichiometry while probably maintaining a mixture of elemental Ge and GeO_x compounds less likely to be trapped by Si dangling bonds because of oxygen excess. RBS analyses confirm that Ge mobility is greater in the second half of the Ge depth-profile, as it is this part of the profile which is redistributed during annealing.

The ^{18}O depth-profile after annealing (dashed blue lines) also shows an asymmetric diffusion, whose range is limited to a few nanometers towards the sample surface but is, on the other hand, able to reach the SiO_2/Si interface. This is consistent with the stoichiometric discrepancies previously mentioned, with a high rate of interactions of diffusing species with under-stoichiometric SiO_x (x < 2) between the Ge projected range and the sample surface, which acts as a trapping center for GeO_x ($0 \leq x < 2$) or oxygen, and with over-stoichiometric SiO_x (x > 2) towards the SiO_2/Si interface. Figure 2 shows that annealing perturbs ^{18}O depth-profile more as the Ge fluence increases, with a clear redistribution into two peaks for the sample 2c. As observed by XPS (see figure S2 in supplementay material), these positions correspond to the SiO_2 regions where the concentrations of elemental Ge and GeO_x are

maximum after the implantation. These regions seem to be particular centers for oxygen fixation, due to trapping effects in under-stoichiometric regions and oxygen exchanges in over-stoichiometric regions.

As no real ^{18}O buildup is observed at the SiO_2/Si interface, it can be deduced that only a very small number of ^{18}O atoms reaches the substrate. Three possible interpretations:

1. The interface peak is due to the diffusion of elemental Ge, whose diffusion in depth is not limited by the presence of silicon dangling bonds.
2. If germanium diffuses under the form of GeO_x compounds, this indicates that they could exchange or yield their oxygen before reaching the interface:

$$Ge^{18}O_x + Si^{16}O_2 \rightarrow Ge^{16}O_x + Si^{16(18)}O_2. \quad (4)$$

3. The number of Ge atoms chemically bound to ^{18}O is weak, as Ge will probably bind preferentially with recoiled ^{16}O coming from the first 110 nanometers.

Another possibility proposed in literature is the encounter of GeO coming from the implanted zone and SiO molecules emitted by the substoichiometric interface [9,15,32]:

$$Ge^{18}O + Si^{16}O \rightarrow Ge + Si^{16(18)}O_2. \quad (5)$$

Knowing that the diffusion coefficient of SiO molecules is estimated to be $D_{SiO}(1100°C) = 4 \times 10^{-17} cm^2/s$ [15], this can only occur close to the SiO_2/Si interface.

In any case, oxidized Ge would be reduced upon reaching the substoichiometric SiO_x/Si interface, releasing elemental Ge atoms in the vicinity of the SiO_2/Si interface which is free to bond to Si (mainly) or other Ge atoms. At least a part of this germanium is supposed to penetrate in a shallow layer of the silicon substrate because of the solubility of germanium in silicon due to their similar atomic structure [8,11]. This agrees with XPS observations [12,17], indicating the presence of only Ge-Ge and Ge-Si chemical bonds in the vicinity of the interface region.

B. Annealing under a contaminated environment

Figure 3 shows Ge depth-profiles extracted from RBS analyses, before and after annealing, for type B samples implanted with different Ge fluences inside 200 nm (figure 3a) and 300 nm (figures 3b-d) SiO_2 layers. Figures 3b-d correspond to fluences of 4.5×10^{16}, 1.2×10^{17} and 2.2×10^{17} Ge/cm² respectively. The fluence (3.5×10^{16} Ge/cm²) of the sample presented in figure 3a has been chosen to get similar concentration at maximum to that in the sample presented in figure 3b. The left side of figures 3a-d corresponds to the sample surface.

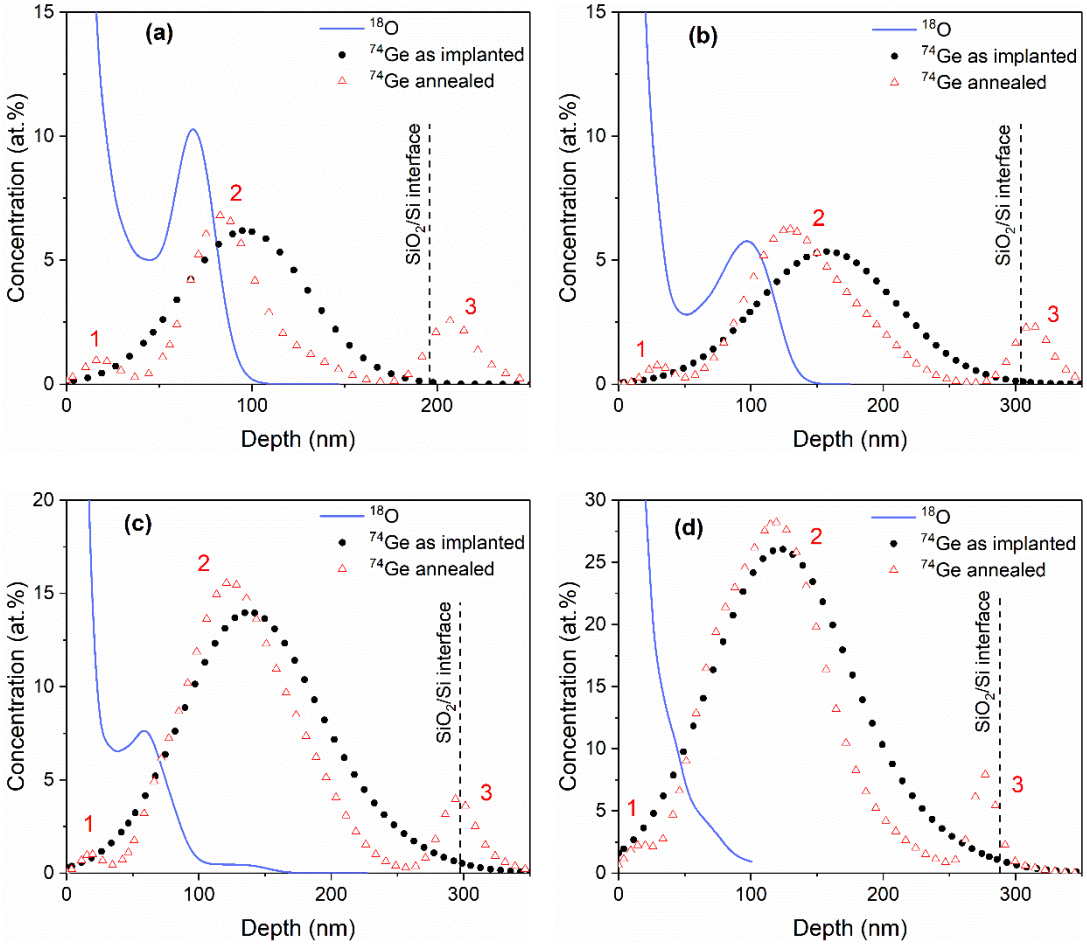

Figure 3: ^{74}Ge depth-profiles, extracted from RBS spectra, before (black dots) and after (red triangles) annealing, and ^{18}O RNRA deconvoluted depth-profiles after annealing (blue solid line), for fluencies of (a) 3.5 × 10^{16}, (b) 4.5 × 10^{16}, (c) 1.2 × 10^{17} and (d) 2.2 × 10^{17} Ge/cm².

For each germanium fluence, the Ge depth-profile after annealing (red triangles in figure 3) is redistributed into three peaks, with the emergence of a subsurface peak (peak 1) that was not observed for annealing under pure nitrogen (figure 2). This three-peak configuration, which is frequently observed in the literature [8,10-12,17], is generally associated with the presence of oxygen in the annealing atmosphere.

As peak 1 is not present for annealing under pure N_2, this peak can be directly associated with the presence of oxygen in the annealing environment. Peaks 2 and 3 are similar to those observed in figure 2, corresponding to a Ge diffusion mainly directed towards the sample surface and a Ge accumulation at the SiO_2/Si interface, but with a clear enhancement of outward diffusion for the intentionally contaminated atmosphere.

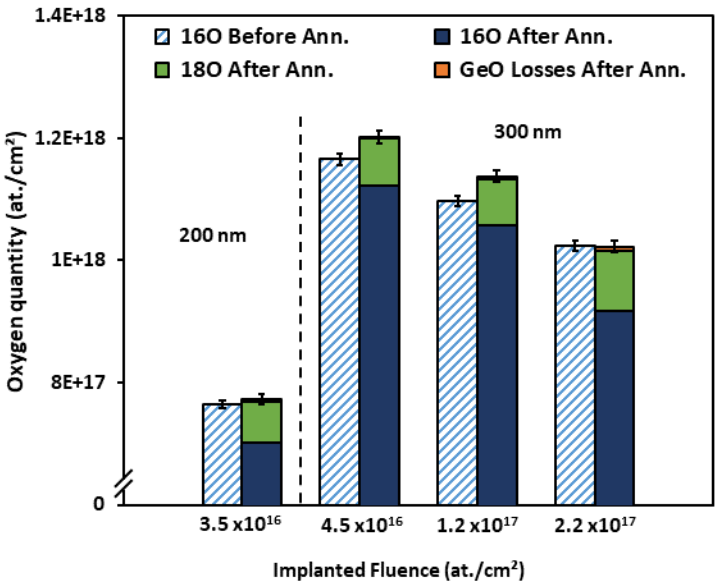

Figure 4: Total oxygen atoms measured by $^{16}O(d,\alpha)^{14}N$ and $^{18}O(d,\alpha)^{16}N$ reactions for 200 nm (left) and 300 nm (right) SiO_2 before and after annealing. Orange boxes represent GeO desorption.

First of all, it can be inferred from NRA measurements (figure 4) that ^{18}O incorporation during annealing is not due only to $^{16}O/^{18}O$ surface exchanges, since the total oxygen amount increases especially for the intermediate fluences. In this calculation, we suppose that each germanium atom desorbs in the form of GeO, carrying one oxygen atom while leaving the sample through the surface (orange boxes in figure 4). The amount of desorbing GeO molecules is deduced from Ge losses measured by RBS after annealing. NRA measurements will allow us to constrain the amount of ^{18}O in our RNRA fits.

In Ge-implanted SiO_2 layers, germanium mobility decreases as the fluence increases due to the formation of Ge-Si and Ge-Ge chemical bonds during implantation and annealing steps. Table I shows the decrease of Ge mobility, manifested by the reduction of the percentage of Ge in peaks 1 and 3, which obviously also depends of the relative distance with both interfaces.

Fluence ($\times 10^{16}$ Ge/cm^2)	Ge Losses (%)	Ge peak 1 (%)	Ge peak 3 (%)	Maximum displacement per atom (dpa)
3.5	12.0	6.4	19.0	55
4.5	2.5	3.7	14.4	72
12	4.2	1.4	9.6	199
22	2.7	1.5	7.9	366

Table I: Percentage of Ge losses and contained in peaks 1 and 3 of figure 3 derived from RBS spectra, and maximum displacement per atom as calculated by TRIM.

^{18}O depth-profiles (blue solid lines) after annealing are superimposed on the Ge depth-profiles in figure 3 and fitted in figure 5 for each fluence. ^{18}O depth-profiles, shown in figure 5, can be decomposed in three contributions (processes I, IIa and IIb).

As the whole diffusion process is complex with the simultaneous diffusion of multiple species occurring at different rates, we will propose a possible explanation based on our experimental observations and literature.

A significant ^{18}O surface peak, noted process I, arises at the gas/SiO_2 interface and is attributed to the irradiation-induced damage and preferential sputtering of oxygen occurring at the sample surface during Ge implantation [9,13,19,26]. Process I depends on the implanted ions energy and fluence, with a tail which extends from 25 to 50 nm. Therefore, a damaged oxygen-poor surface is exposed to $^{18}O_2$ during annealing, highly increasing the oxygen permeability of the surface [9]. Figure 5 shows that ^{18}O saturation is achieved at the extreme surface even for our low oxygen pressure. This surface will act as a constant oxygen provider.

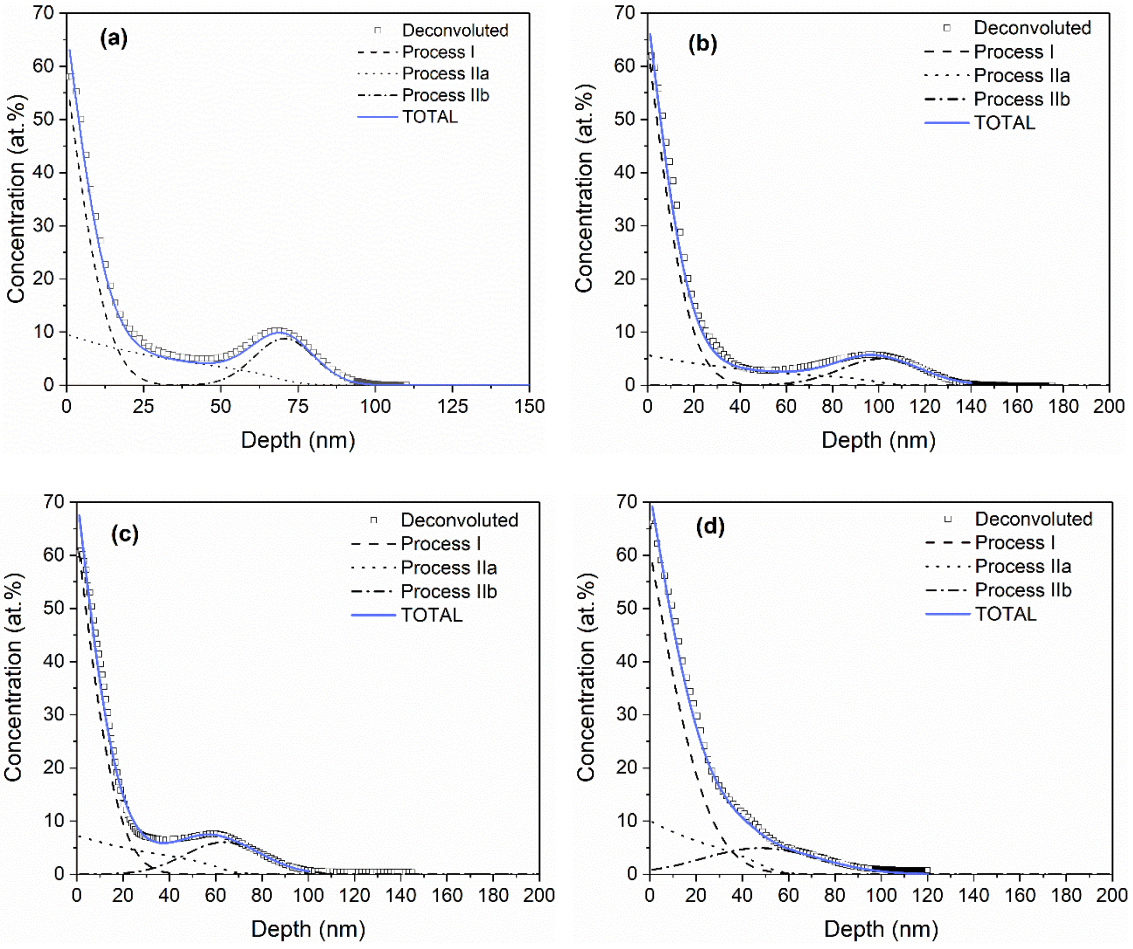

Figure 5: Measured – and deconvoluted - (open squares) and calculated with processes I, IIa and IIb (lines) ^{18}O RNRA depth-profiles for fluencies of (a) 3.5×10^{16}, (b) 4.5×10^{16}, (c) 1.2×10^{17} and (d) 2.2×10^{17} Ge/cm².

Before annealing, the subsurface region is mainly composed of a mixture of partially oxidized silicon or germanium (SiO_x and GeO_x with $x < 2$) and elemental Ge (chemically bound to Ge or Si) whose concentration increases with the Ge fluence [17,26] (see two examples in figure S2 in supplementary material). At 1100°C, SiO_x is supposed to reduce within the first second of

annealing [29] by equation 3. This agrees with *Borodin et al.* model [18], considering only O_2 and the fraction of Ge which did not nucleate as the diffusing species. At the same time, $^{18}O_2$ penetrates the sample through the damaged surface and fully oxidizes all species present, or incoming, in the subsurface region, *e.g.* by reactions such as:

$$2\,GeO + {}^{18}O_{2(g)} \rightarrow 2\,GeO_2, \tag{6}$$

$$Ge + {}^{18}O_{2(g)} \rightarrow GeO_2, \tag{7}$$

$$Si + {}^{18}O_{2(g)} \rightarrow SiO_2. \tag{8}$$

At the temperature considered in this work (1100°C), Ge and Si oxidation occurs at the same time. However, SiO_2 is thermodynamically more stable than GeO_2 in systems involving Si, Ge and O, for which GeO_2 tends to reduce by reactions such as equation 2 in the presence of silicon even for weak Si concentrations [33]. Therefore, ^{18}O atoms will more favorably restore the SiO_2 stoichiometry (equation 8) than form GeO_2. This passivation of silicon dangling bonds also enhances the diffusion of germanium by limiting the formation of Ge-Si bonds, favoring its desorption. RBS spectra show that germanium outward diffusion is initiated before its oxidation to immobile GeO_2, leading to the formation of peak 1. XPS studies confirmed that peak 1 is composed of fully oxidized germanium [9,11,12,26]. *Zatsepin et al.* [26] showed that each germanium atom, implanted near the sample surface (in the first 30-35 nm), is at least partially oxidized after 15 seconds of annealing at 950°C, with a fraction of GeO_2/GeO_x ($x < 2$) which increases with the annealing time (approximately 40-45 % of Ge is fully oxidized after 1 minute in these conditions). As the coefficients of diffusion increase with the temperature, the oxidation of germanium in the subsurface region will occur in a shorter time at 1100°C.

Process I is fitted by an erfc function, resulting from the encounter of incompletely oxidized species and $^{18}O_2$ molecules [22]:

$$\left[{}^{18}O\right]_I(x,t) = \alpha\, erfc(\beta x), \tag{9}$$

where α is the maximum concentration at the sample surface, almost constant for all samples, and β represents the dose-dependent peak width. $\beta = \frac{1}{2\sqrt{Dt}}$, with *D* being proportional to the concentration of incompletely oxidized species and their respective coefficient of diffusion.

As shown in figure 3, peak 1 overlaps with the tail of the ^{18}O surface peak, confirming an encounter between the oxygen molecules present in the annealing atmosphere, penetrating SiO_2 through the surface and diffusing inwards, and out-diffusing GeO_x compounds close to the surface. This is consistent with other works [10-12], which suggested an overlapping between penetrating oxidizing agents and outgassing GeO leading to the formation of fixed GeO_2 close to the sample surface.

Process IIa is hypothesized to be the result of the diffusion of $^{18}O_2$ molecules interacting with the Ge-implanted $Si^{16}O_2$ network. Process IIa is fitted using the following equation, presented in ref. [21]:

$$\left[^{18}O\right]_{IIa}(x,t) = L_g^{18}\left[^{18}O\right]_{c,x=0} \frac{cosh[(x-x_0)/\lambda]}{cosh(x_0/\lambda)}\,\gamma t, \qquad (10)$$

where L_g^{18} is the isotopic labeling of the employed gas, $\left[^{18}O\right]_{c,x=0}$ is the oxygen concentration at the sample surface (depending of the ^{18}O-enrichment and pressure of the gas and the solubility of ^{18}O in SiO_2 [34]), x_0 is the oxide thickness, λ is the characteristic $^{16}O/^{18}O$ exchange length and γ is the average rate at which a diffusing oxygen atom is exchanged with an oxygen atom of the $Si^{16}O_2$ network.

Using λ and γ parameters, we are able to calculate the $^{18}O_2$ diffusion coefficient by the equation: $D_{O_2} = \gamma\lambda^2$. λ, γ and D_{O_2} values are summarized in table II for each sample. $D_{O_2}(1100°C) \sim 10^{-9}\ cm^2/s$ is about one order of magnitude lower than the coefficient found by *F. J. Norton* in case of pure SiO_2 layer [34]: $1.2 \times 10^{-8}\ cm^2/s$ at 1078°C. The difference could be explained by the morphological difference of our Ge-implanted samples compared to a pure SiO_2 layer, probably increasing the interactions between O_2 and the network. This is supported by the decreasing of λ and D_{O_2} with the increasing of Ge fluence (Table II).

Fluence ($\times 10^{16}$ Ge/cm²)	Ox. Thick. (nm)	Process I	Process IIa				Process IIb	
		$\sum_I$ (at./cm²)	λ (nm)	γ (s^{-1})	D_{O_2} (cm²/s)	$\sum_{IIa}$ (at./cm²)	$\sum_{IIb}$ (at./cm²)	x_C (nm)
3.5	200	3.06×10^{16}	50	59	1.48×10^{-9}	2.34×10^{16}	1.43×10^{16}	70.5
4.5	300	4.59×10^{16}	65	35	1.48×10^{-9}	1.91×10^{16}	1.46×10^{16}	101.0
12	300	4.50×10^{16}	50	49	1.31×10^{-9}	1.76×10^{16}	1.69×10^{16}	63.5
22	300	6.15×10^{16}	43	62	1.15×10^{-9}	1.90×10^{16}	2.00×10^{16}	48.0

Table II: Summarize of integrals for processes I, IIa and IIb, with fitting parameters and calculated coefficient of diffusion.

Process IIb, which is related to process IIa, is a buildup of inward diffusing ^{18}O whose integral and depth-position appear to be determined by the local concentration of Ge-Ge and Ge-Si chemical bonds, which dominates in peak 2, *i.e.* the oxide region where nanoclustering occurs [10,11]. Table II shows that, as the ^{74}Ge fluence increases, ^{18}O is trapped close to the surface in larger quantities. This is due to the local concentration of not mobile Ge-Ge and Ge-Si chemical bonds (*i.e.* nanoclusters), which increases with the fluence until dominating the formation of GeO_x compounds during the implantation, as demonstrated by XPS in ref. [17]

(see figure S2 in supplementary material, two examples are shown for Ge fluences of 0.80 and 1.30×10^{17} Ge/cm²).

Process IIb is fitted by a gaussian curve, whose integral is fixed by the total number of ^{18}O atoms present in the sample from the NRA measurements.

Under pure N_2, peak 2 (figure 3) corresponds to the region of nanoclustering, where mostly Ge-Ge or Ge-Si chemical bonds are observed [6-8,10,12,13,17]. When an oxygen contamination is present in the annealing environment, XPS and TEM measurements showed that peak 2 is gradually oxidized and the edge of the Ge nanocrystals band shifts to a greater depth with annealing time. For sufficient annealing time and oxygen supply, the complete oxidation of Ge nanocrystals can be achieved [11,12,18].

This is consistent with our observations, showing that inward diffusing $^{18}O_2$ molecules react with Ge-Ge and Ge-Si bonds as soon as their concentrations increase. For longer annealing time, process IIb should continue to gradually overlap peak 2 until its complete oxidation. However, the shift of peak 2 towards the sample surface and the changes in its shape compared to pure N_2 annealing indicate that fixed GeO_2 is not directly formed. Two mechanisms must be considered. Firstly, the presence of oxygen occupies Si dangling bonds, favoring Ge diffusion. Secondly, the formation of GeO_2 locally depends on the relative amounts of oxygen and germanium. Oxygen arrives gradually from the sample surface, while the local concentration of elemental germanium increases rapidly for the fluences used in this work. As GeO_2 is not stable in the presence of germanium at high temperature ($GeO_2 + Ge \rightarrow 2GeO$) [33,35], a part of GeO molecules could diffuse towards the surface before being oxidized again in regions containing larger amounts of oxygen, either in peak 2 or near the sample surface (peak 1).

Considering the coefficient of diffusion deduced from process IIa, $D_{O_2}(1100°C)$, the number of ^{18}O atoms at a certain depth Δx after an annealing time t, maintaining a constant concentration of ^{18}O at the sample surface, is given by:

$$n_{^{18}O}(x,t) = \mathrm{L}_{\mathrm{g}}^{18}\left[^{18}\mathrm{O}\right]_{c,x=0} D_{O_2}(1100°C)\,\frac{t}{\Delta x}. \qquad (11)$$

This allows us to estimate the quantity of ^{18}O atoms which should accumulate by process IIb. As the integral of process IIb is systematically lower than this calculated value $n_{^{18}O}(x,t)$ for each sample, this supports the idea of an out-diffusion of $Ge^{18}O$, enhanced by the presence of oxygen in the annealing atmosphere.

Considering the weak isotopic labeling of the SiO_2 layer after annealing, corresponding to less than 8% of the total oxygen amount, we assume that processes I and II are independent.

No measurable ^{18}O accumulation has been observed at the SiO_2/Si interface, indicating that all $^{18}O_2$ is consumed in Ge oxidation process of peak 2. Therefore, peak 3, in the vicinity of the SiO_2/Si interface, is rather more influenced by the oxide thickness and Ge fluence than the presence of ^{18}O in the annealing atmosphere. For a similar atomic concentration, Ge buildup

at the interface is more significant for thinner samples (table I), which can be explained by the proximity to the SiO_2/Si interface and the lower implantation fluence.

IV. Conclusions

We studied the origin of oxygen involved in germanium diffusion into a SiO_2/Si layer, by a combination of stable isotopic tracing and three IBA techniques: RBS, RNRA and NRA.

A new experimental proof is provided that, compared to a pure N_2 environment, a low percentage of O_2 in the annealing atmosphere enhances Ge out-diffusion, through the formation of GeO molecules. It is shown that this oxygen contamination causes the oxidation of diffusing species close to the sample surface, as well as in the region of nanocrystals growth, in agreement with models proposed in literature. This underlines the importance of working in pure and non-reactive atmosphere.

SUPPLEMENTARY MATERIAL

See supplementary material for RBS analyses highlighting the changes in the SiO_2 stoichiometry after the Ge implantation (figure S1). Figure S2 shows Ge depth-profiles in SiO_2 measured by XPS for two different Ge fluences. The chemical state of implanted Ge ions after the implantation is shown in figure S2.

ACKNOWLEDGMENTS

This work was made possible thanks to the Fédération Wallonie-Bruxelles (FWB) travel grant (BV17-54). The authors would like to thank SIAM (Synthesis, Irradiation and Analysis of Materials) technological platform for the use of ALTAÏS and T. Tabarrant for his technical support on the accelerator. This work had benefitted from access to the SAFIR platform of the CNRS and Sorbonne University. A.N. would like to personnaly thank Hervé Tancrez.

DATA AVAILABILITY

The data that support the findings of this study are available from the corresponding author upon request.

REFERENCES

[1] Green, M. A., Bremner, S. P. (2017). *Energy conversion approaches and materials for high-efficiency photovoltaics*. Nature Materials, 16, 23–34. https://doi.org/10.1038/nmat4676

[2] Yedji, M., Demarche, J., Terwagne, G., Delamare, R., Flandre, D., Barba, D., Koshel, D., Ross, G. G. (2011). *Method for fabricating third generation photovoltaic cells based on Si quantum dots using ion implantation into SiO_2.* J. Appl. Phys., 109(8), 084337. https://doi.org/10.1063/1.3575325

[3] Beard, M. C., Knustsen, K. P., Yu, P., Song, Q., Luther, J., Ellingson, R., Nozik, A. J. (2007). *Multiple exciton generation in colloidal silicon nanocrystals*. *Nano Lett.*, *7*, 2506–2512. https://doi.org/10.1021/nl071486l

[4] Trinh, M. T., Limpens, R., de Boer, W. D. A. M., Schins, J. M., Siebbeles, L. D. A., Gregorkiewicz, T. (2012). *Direct generation of multiple excitons in adjacent silicon nanocrystals revealed by induced absorption.* Nature Photonics, 6(5), 316–321. https://doi.org/10.1038/nphoton.2012.36

[5] Smith, C., Binks, D. (2013). *Multiple Exciton Generation in Colloidal Nanocrystals.* Nanomaterials, 4(1), 19–45. https://doi.org/10.3390/nano4010019

[6] Barba, D., Wang, C., Nélis, A., Terwagne, G., Rosei, F. (2018). *Blocking germanium diffusion inside silicon dioxide using a co-implanted silicon barrier*. *J. Appl. Phys.*, *123*(16), 161540. https://doi.org/10.1063/1.5002693

[7] Nélis, A., Barba, D., Terwagne, G. (2020). *Control of germanium diffusion using low quantities of co-implanted silicon isotopes.* J. Appl. Phys., 128(12), 125705. https://doi.org/10.1063/5.0020368

[8] Markwitz, A., Schmidt, B., Matz, W., Grötzschel, R., Mücklich, A. *(1998). Microstructural investigation of ion beam synthesised germanium nanoclusters embedded in SiO_2 layers.* Nucl. Instrum. Methods Phys. Res. B, 142(3), 338–348. https://doi.org/10.1016/S0168-583X(98)00283-3

[9] Beyer, V., von Borany, J. (2008). *Elemental redistribution and Ge loss during ion-beam synthesis of Ge nanocrystals in SiO_2 films*. Phys. Rev. B, 77(1), 014107. https://doi.org/10.1103/PhysRevB.77.014107

[10] von Borany, J., Grötzschel, R., Heinig, K. H., Markwitz, A., Matz, W., Schmidt, B., Skorupa, W. (1997). *Multimodal impurity redistribution and nanocluster formation in Ge implanted silicon dioxide films*. Appl. Phys. Lett., 71(22), 3215–3217. https://doi.org/10.1063/1.120294

[11] Heinig, K. H., Schmidt, B., Markwitz, A., Grötzschel, R., Strobel, M., Oswald, S. (1999). *Precipitation, ripening and chemical effects during annealing of Ge^+ implanted SiO_2 layers*. Nucl. Instrum. Methods Phys. Res. B, 148(1–4), 969–974. https://doi.org/10.1016/S0168-583X(98)00862-3

[12] Oswald, S., Schmidt, B., Heinig, K.-H. (2000). *XPS investigation with factor analysis for the study of Ge clustering in SiO_2.* Surf. Interface Anal., 29(4), 249–254. https://doi.org/10.1002/(SICI)1096-9918(200004)29:4<249::AID-SIA735>3.0.CO;2-5

[13] Barba, D., Cai, R. S., Demarche, J., Wang, Y. Q., Terwagne, G., Rosei, F., Ross, G. G. (2014). *Influence of silicon dangling bonds on germanium thermal diffusion within SiO_2 glass.* Appl. Phys. Lett., 104(11), 111901. https://doi.org/10.1063/1.4868721

[14] Baranwal, V., Gerlach, J. W., Lotnyk, A., Rauschenbach, B., Karl, H., Ojha, S., Avasthi, D. K., Kanjilal, D., Pandey, A. C. (2015). *Embedded Ge nanocrystals in SiO_2 synthesized by ion implantation*. J. Appl. Phys., 118(13), 134303. https://doi.org/10.1063/1.4932151

[15] Uematsu, M., Kageshima, H., Takahashi, Y., Fukatsu, S., Itoh, K. M., Shiraishi, K., Gösele, U. (2004). *Modeling of Si self-diffusion in SiO_2: Effect of the Si/SiO2 interface including time-dependent diffusivity.* Appl. Phys. Lett., 84(6), 876–878. https://doi.org/10.1063/1.1644623

[16] Choi, W. K., Ho, V., Ng, V., Ho, Y. W., Ng, S. P., Chim, W. K. (2005). *Germanium diffusion and nanocrystal formation in silicon oxide on silicon substrate under rapid thermal annealing.* Appl. Phys. Lett., 86(14), 1–3. https://doi.org/10.1063/1.1891290

[17] Nélis, A., Haye, E., Terwagne, G. (2021). *Influence of oxygen co-implantation on germanium out-diffusion and nanoclustering in SiO_2/Si films*. (To be published)

[18] Borodin, V. A., Heinig, K. H., Schmidt, B. (1999). *Modeling of Ge nanocluster evolution in ion-implanted SiO_2 layer.* Nucl. Instrum. Methods Phys. Res. B, 147(1–4), 286–291. https://doi.org/10.1016/S0168-583X(98)00562-X

[19] Ziegler, J. F., Ziegler, M. D., Biersack, J. P. (2010). *SRIM – The stopping and range of ions in matter (2010).* Nucl. Instrum. Methods Phys. Res. B, 268(11–12), 1818–1823. https://doi.org/10.1016/j.nimb.2010.02.091

[20] Amsel, G., Samuel, D. (1967). *Microanalysis of the Stable Isotopes of Oxygen by Means of Nuclear Reactions.* Anal. Chem., 39(14), 1689–1698. https://doi.org/10.1021/ac50157a027

[21] Cavellin, C. D., Trimaille, I., Ganem, J. J., D'Angelo, M., Vickridge, I., Pongracz, A., Battistig, G. (2009). *An ^{18}O study of the interaction between carbon monoxide and dry thermal SiO_2 at 1100 °C.* J. Appl. Phys., 105(3), 1–7. https://doi.org/10.1063/1.3072679

[22] Trimaille, I., Rigo, S. (1989). *Use of 18O isotopic labelling to study thermal dry oxidation of silicon as a function of temperature and pressure.* Appl. Surf. Sci., 39(1–4), 65–80. https://doi.org/10.1016/0169-4332(89)90420-0

[23] Battistig, G., Amsel, G., d'Artemare, E., Vickridge, I. (1991). *A very narrow resonance in $^{18}O(p, \alpha)^{15}N$ near 150 keV: Application to isotopic tracing. I. Resonance width measurement.* Nucl. Instrum. Methods Phys. Res. B, 61(4), 369–376. https://doi.org/10.1016/0168-583X(91)95308-Z

[24] Vickridge, I., Amsel, G. (1990). *SPACES: A PC implementation of the stochastic theory of energy loss for narrow-resonance depth profiling.* Nucl. Instrum. Methods Phys. Res. B, 45(1–4), 6–11. https://doi.org/10.1016/0168-583X(90)90772-M

[25] Ganem, J.-J., Trimaille, I., André, P., Rigo, S., Stedile, F. C., Baumvol, I. J. R. (1997). *Diffusion of near surface defects during the thermal oxidation of silicon.* J. Appl. Phys., 81(12), 8109–8111. https://doi.org/10.1063/1.365420

[26] Zatsepin, A. F., Zatsepin, D. A., Zhidkov, I. S., Kurmaev, E. Z., Fitting, H. J., Schmidt, B., Mikhailovich, A.P., Lawniczak-Jablonska, K. (2015). *Formation of Ge^0 and GeO_x nanoclusters in Ge^+ -implanted SiO_2/Si thin-film heterostructures under rapid thermal annealing.* Appl. Surf. Sci., 349, 780–784. https://doi.org/10.1016/j.apsusc.2015.05.090

[27] Minke, M. V., Jackson, K. A. (2005). *Diffusion of germanium in silica glass*. J. Non-Crystalline Solids, 351(27–29), 2310–2316. https://doi.org/10.1016/j.jnoncrysol.2005.04.052

[28] Gambaryan, M. P., Krivyakin, G. K., Cherkova, S. G., Stoffel, M., Rinnert, H., Vergnat, M., Volodin, V. A. (2020). *Quantum Size Effects in Germanium Nanocrystals and Amorphous Nanoclusters in $GeSi_xO_y$ Films.* Phys. Solid State, 62(3), 492–498. https://doi.org/10.1134/S1063783420030105

[29] Dan'ko, V. A. (2005). *Kinetics of Structural and Phase Transformations in Thin SiO_x Films in the Course of a Rapid Thermal Annealing.* Semiconductors, 39(10), 1197. https://doi.org/10.1134/1.2085270

[30] Prabhakaran, K., Maeda, F., Watanabe, Y., Ogino, T. (2000). *Distinctly different thermal decomposition pathways of ultrathin oxide layer on Ge and Si surfaces.* Appl. Phys. Lett., 76(16), 2244–2246. https://doi.org/10.1063/1.126309

[31] Barba, D., Demarche, J., Martin, F., Terwagne, G., Ross, G. G. (2012). *Trapping of diffusing germanium by silicon excess co-implanted into fused silica.* Appl. Phys. Lett., 101(14), 143107. https://doi.org/10.1063/1.4757291

[32] Takakuwa, Y., Nihei, M., Miyamoto, N. (1993). *Outdiffusion and Subsequent Desorption of Volatile SiO Molecules during Annealing of Thick SiO_2 Films in Vacuum.* Jpn J. Appl. Phys., 32(Part 2, No. 4A), L480–L483. https://doi.org/10.1143/JJAP.32.L480

[33] Hellberg, P.-E., Zhang, S.-L., D'Heurle, F. M., Petersson, C. S. (1997). *Oxidation of silicon–germanium alloys. II. A mathematical model.* J. Appl. Phys., 82(11), 5779–5787. https://doi.org/10.1063/1.366444

[34] Norton, F. J. (1961). *Permeation of Gaseous Oxygen through Vitreous Silica.* Nature, 191(4789), 701–701. https://doi.org/10.1038/191701a0

[35] Oh, J., Campbell, J. C. (2004). *Thermal desorption of Ge native oxides and loss of Ge from the surface.* J. Electon. Mater., 33(4), 364–367. https://doi.org/10.1016/j.mssp.2010.10.009

$^{18}O(p,\alpha)^{15}N$ isotopic tracing of germanium diffusion in SiO_2/Si films

A. Nélis[1,*], I. Vickridge[2], J.-J. Ganem[2], E. Briand[2], G. Terwagne[1]

[1]LARN, Namur Institute of Structured Matter (NISM), University of Namur (UNAMUR), B-5000 Namur, Belgium

[2]Sorbonne Université, Institut des NanoSciences de Paris, CNRS UMR 7588, 4 place Jussieu, F-75252 Paris cedex 05, France

- Supplementary material -

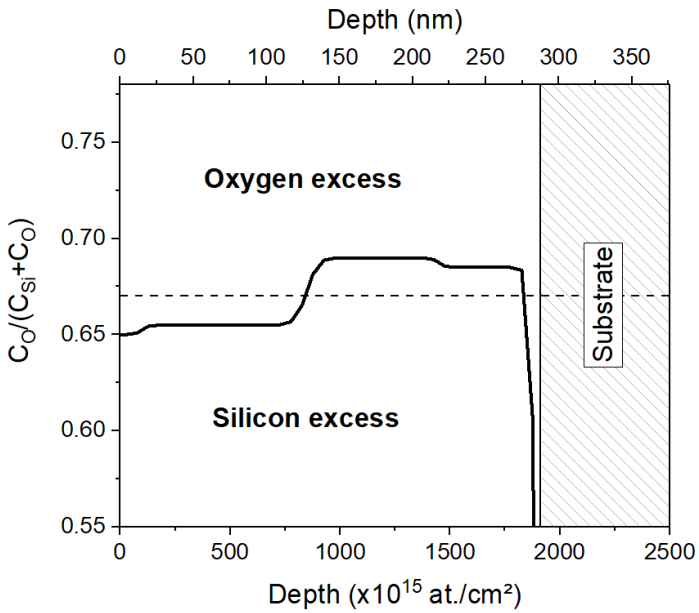

Figure S1.

$C_O/(C_{Si} + C_O)$ concentration ratio extracted from RBS analysis of a SiO_2/Si layer (~300 nm) implanted with 1.30 × 10^{17} Ge/cm² at an energy of 230 keV. RBS measurement is performed after the implantation. A ratio lower than 0.67 corresponds to a silicon excess with respect to stoichiometric SiO_2, while a ratio higher than 0.67 corresponds to an oxygen excess.

Remark: RBS measurements have been carried out with 2 MeV alpha particles for detection angles of 135 and 165°. The conversion between both X-axes assumes a SiO_2 density of 6.65 × 10^{22} at./cm² because of the low Ge concentration for these implantation parameters.

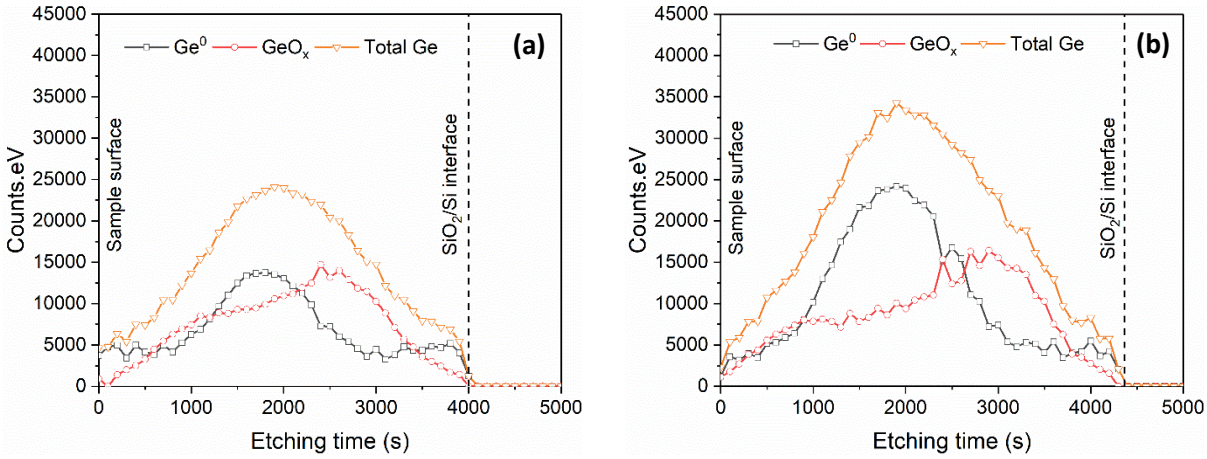

Figure S2.

Ge depth-profiles measured by XPS after the implantation (orange curve) as a function of etching time. Ge^0 (black curve) corresponds to Ge atoms chemically bonded to Ge or Si atoms. GeO_x (red curve) corresponds to Ge in an oxidized state. GeO_x are formed through the entire oxide but dominates in the second part of the Ge depth-profile, while Ge-Ge and Ge-Si bonds dominate in the first part of the Ge depth-profile. Implantations have been carried out at an energy of 230 keV in a SiO_2/Si sample, the SiO_2 thickness being ~300 nm, for a fluence of (a) 0.80×10^{17} Ge/cm² and (b) 1.30×10^{17} Ge/cm². This effect is dose-dependent, as more detailed in the upcoming ref. [17].

Remark: XPS measurements presented in ref. [17] were carried out with a Thermo Fisher Escalab 250Xi spectrometer using Al Kα source (1486.68 eV) and a spot size of 250×250 µm². Samples were profiled using an Ar^+ beam at 1 keV (30°, low current). The authors are aware of the possible damage generation using ion beam, and measured concentrations are subject to variations. However, ion beam energy has been minimized, and the comparison between samples remains valid in ref. [17], as the same erosion parameters (ion beam energy and current, spot size) have been used.

IV.2 Stabilization of Ge diffusion and nucleation by Si co-implantation in SiO_2/Si films

We propose to use the Ge/Si trapping effect introduced in **section IV.1** to control both germanium diffusion and nucleation. In previous articles, we discussed about the role of silicon excess, with respect to stoichiometric SiO_2, in a diminution of germanium mobility through the formation of Ge-Si chemical bonds during implantation or annealing. This reduced mobility and the strength of Ge-Si bonds could be used to control both the diffusion of germanium and the quantum dots size distribution.

Article III: Control of germanium diffusion using low-quantities of co-implanted silicon isotopes

Preliminary to article III

Previous works, carried out as a part of our collaboration between LARN and INRS, showed that, more than simply irradiation-induced damage, it is the affinity of silicon and germanium which was responsible of the reduction of germanium mobility at high temperature (120). It was demonstrated that silicon co-implantation could drastically reduce the large out-diffusion and long-range redistribution observed during annealing for Ge implanted in fused silica (120), (126). The amount of germanium retained in the sample during annealing linearly depends on the fluence of co-implanted silicon with a slope ~1 until the saturation close to the Ge implanted fluence, while the same density of defects generated by N^+ ions does not reduce desorption losses. Ge-Si chemical bonds (2.40 Å) are shorter than Ge-Ge bonds (2.44 Å), resulting in stronger binding energies of 301 kJ/mol versus 264 kJ/mol for Ge-Ge bonds. Ge*-ncs, *i.e.* very small Ge nanocrystals or nanocrystals containing Si, and pure Ge nanocrystals co-exist in co-implanted samples until a threshold for which the formation of Ge-Si bonds dominates. This was demonstrated by electron microscopy that Si co-implantation was even able to prevent the diffusion and nucleation of germanium in silica (120). For low Si fluence, large nanocavities are formed in fused silica and the density of large nanocrystals increases with the Si fluence until a threshold for which the formation of Ge-Si bonds leads to the formation of smaller germanium nanocrystals (82), (126). In practice, Ostwald ripening process is limited by the lower germanium mobility due to its affinity with silicon.

Preliminary results, reported by *Barba et al.* (82), (121), showed that, due to a higher density of dangling bonds, lower co-implantation fluences would be necessary in thermally grown SiO_2/Si layers compared to fused silica to annihilate germanium out-diffusion. In fact, even in not co-implanted oxides, silicon impurities are observed in germanium nanocrystals formed in SiO_2/Si films while they are not observed in fused silica, resulting in shorter interplanar distances (82).

The goal of this study was to co-implant silicon isotopes in addition to germanium in thermally grown SiO_2/Si films. The aim is to reduce germanium mobility until the complete

annihilation of its asymmetrical diffusion. ^{29}Si and ^{30}Si are therefore implanted on both sides of germanium profile to prevent migration in both directions, *i.e.* towards the sample surface and towards the SiO_2/Si interface. Germanium diffusion is studied as a function of silicon co-implanted fluence to determine a lower limit for the complete annihilation of Ge diffusion. Note that this lower bound is only valid for a defined sample configuration, as it strongly depends on the implantation parameters of the three co-implanted species (energy, fluence) and their relative depth-distributions.

The use of isotopes is motivated by the possibility to distinguish implanted silicon to silicon originally present in the sample, thanks to isotopically sensitive techniques or good energy and mass separation due to suitable analysis conditions. Considering the discussion of **section III.5** about RBS mass and energy resolutions, an energy of 3 MeV is used in this article to discriminate the RBS signal originating from ^{30}Si atoms implanted at the vicinity of the sample surface from silicon naturally present in the SiO_2 film.

Authors' contribution

I carried out all the ^{29}Si, ^{30}Si and Ge implantations at LARN with ALTAÏS. I performed all the RBS and RNRA analyses. I performed magnetron sputtering and thermal evaporations (this idea was proposed by Ian Vickridge during one of our discussions). µ-Raman analyses were performed by David Barba and Guy Terwagne at Varennes (INRS) or by myself at Louvain-la-Neuve (UCL – Welcome). Assisted by David Barba, I was in charge of the data interpretation and I wrote the article.

Control of germanium diffusion using low quantities of co-implanted silicon isotopes

A. Nélis[1,*], D. Barba[2], G. Terwagne[1]

[1] *LARN, Namur Institute of Structured Matter (NISM), University of Namur (UNAMUR), B-5000 Namur, Belgium*

[2] *INRS-EMT, 1650 boul. Lionel-Boulet, Varennes, Québec J3X 1S2, Canada*

Published in *Journal of Applied Physics* **128** (2020) 125705.

https://doi.org/10.1063/1.5002693

Abstract

The thermal diffusion of Ge implanted into SiO_2 films growth on Si substrate have been studied by nuclear analyses and μ-Raman spectroscopy with and without the presence of co-implanted ^{30}Si and ^{29}Si barriers, each located from both sides of the Ge implanted distribution. Combination of Rutherford Backscattering Spectroscopy (RBS) and Resonant Nuclear Reaction Analysis (RNRA) shows that, under thermal activation at 1100°C, implanted Ge diffuses differently towards the sample surface and the SiO_2/Si interface due to the occurrence of Ge outgassing effects, as well as the non-homogenous distributions of the implanted ion species and the defects they have generated inside SiO_2. A maximum local atom concentration of co-implanted silicon as low as ~1.6 at.%, is found to completely block the germanium diffusion in both directions, leading to the formation of Ge nanocrystals and Si/Ge aggregates evidenced by μ-Raman spectroscopy. In addition to highlighting the role of Si excess on the Ge trapping mechanism, such a result makes the nominal silicon oxide stoichiometry and composition two crucial parameters to stabilize Ge during high temperature annealing, which explains the strong discrepancies reported for the Ge thermal diffusion coefficient in the literature.

Keywords: Rutherford backscattering spectroscopy, Narrow resonance profiling, Ge diffusion, Ge nanocrystals, ion implantation.

I. Introduction

Research in the field of group IV semiconductors has been of great interest during the last few decades for their applications in memory devices, nanoelectronic or optoelectronic, as photovoltaic (PV) cells [1-3]. Germanium is a good candidate thanks to a very low energy bandgap, large absorption in the visible range and an adaptability to silicon-based industry due to a similar atomic structure.

Semiconductor nanocrystals, integrated into dielectric layers by ion implantation, offer new possibilities thanks to manifold associated optoelectronic properties. Their tunable bandgap and the potential activation of multiple exciton generation (MEG) can greatly improve energy conversion in PV cells. This enhanced photovoltaic efficiency strongly depends on the size of the nanocrystals and their depth-distribution inside the dielectric layer [1-5].

Controlling the nanocrystals distribution, size and purity is a great challenge to tune their physical properties for specific applications. The co-implantation of silicon excess was found to be an efficient solution to annihilate the Ge thermal diffusion for temperatures as high as 1000-1100°C [6-12], and thus control the Ge nanocrystals (Ge-ncs) depth-distribution after annealing. It has been shown that the production of silicon excess using this technique can reduce the long-range redistribution of implanted Ge during high temperature annealing [5], and annihilate its release from the fused silica or thermally grown SiO_2 oxides matrices.

In this work, both the diffusion of Ge atoms implanted into a thermally grown SiO_2 layer and the diffusion barrier effect of co-implanted ^{30}Si and ^{29}Si isotopes are investigated by Rutherford Backscattering Spectroscopy (RBS) and Resonant Nuclear Reaction Analysis (RNRA) measurements.

The highly asymmetric upward and downward diffusion of the Ge nominally implanted in the middle of the SiO_2 layer is evidenced by RBS/RNRA, showing an accumulation of Ge after thermal annealing, within the sample regions where both the concentration of implanted Ge and the ion damaging are maximum. The role played by the ion-induced depth-dependent structural and composition changes on the Ge diffusion mechanism is discussed by comparing the profiles of Ge-implanted samples to those recorded for Ge thin layers embedded in SiO_2/Si systems, prepared by thermal evaporation and physical vapor deposition (PVD).

When the implanted Ge is sandwiched between two Si co-implanted sublayers, both the diffusion toward the sample surface and the SiO_2/Si interface are blocked. In order to distinguish the effects related to the blocking of diffusing Ge by the upper and lower Si barriers, two different ^{30}Si and ^{29}Si isotopes were implanted into the top and bottom parts of the SiO_2 layer, respectively. Whereas the diffusion barrier effect becomes effective for low fluences of co-implanted Si and complete for implanted Si-excess of 1.6 at.% at maximum, a continuous growth of the Ge nanocrystallites is observed by µ-Raman upon Si co-implantation. This Ge-ncs nucleation is accompanied by the one of $Si - Ge$ chemical bonds, suggesting that the local reduction of the Ge thermal coefficient evidenced by RBS/RNRA results from enhanced Si/Ge chemical trapping effects and Ge nanoclustering in the ion-damaged sublayers. These features can be explained from the different effects that contribute to the

thermal diffusion mechanism, which are discussed here to describe both the RBS/RNRA and μ-Raman measurements.

II. Experiment

300 nm thick wet-oxidized (100) silicon wafers were implanted with $^{30}Si^-$ prior to $^{29}Si^+$ ions at energies of 35 and 170 keV respectively, and fluences varying from 1 to 8 × 10^{16} Si/cm^2. Projected ranges of $^{30}Si^-$ and $^{29}Si^+$ in SiO_2 are around 20 and 275 nm respectively (depending on implantation fluences). $^{74}Ge^+$ ions were later implanted with a single energy of 230 keV in order to obtain a main depth around the middle of the SiO_2 layer. A $^{74}Ge^+$ fluence varying from 6 × 10^{16} to 2.5 × 10^{17} $^{74}Ge/cm^2$ has been used. All implantations were performed with ALTAIS (Accelerateur Linéaire Tandetron pour l'Analyse et l'Implantation des Solides), the 2 MV Tandetron accelerator installed at LARN (UNamur). SRIM-TRIM (Stopping and Range of Ions in Matter-TRansport of Ions in Matter [16]) calculations have been used to calculate projected ranges taking account of surface sputtering and swelling effects, considering a sputtering yield of 0.85 at./Ge.

After implantation, all samples were annealed inside a quartz tube furnace heated at 1100°C for 60 minutes under ultra-high purity nitrogen (N_2) environment, using a gas purifier and a hermetic set-up to limit contamination and oxidation from air ambient. Annealing were performed with the facilities installed at INRS-EMT center (Varennes, Québec) and at LARN (UNamur).

The fluences and depth-profiles of implanted Ge ions and Si isotopes were measured by RBS, using 2 and 3 MeV $^4He^+$ beams for two scattering angles (165 and 170°). The choice of 3 MeV alpha beam is justified by the mass resolution observed for the subsurface implanted ^{30}Si ions. RBS data were treated using SIMNRA [29] (combined with SimTarget, developed by J.L. Colaux [36]) and DataFurnace [30] (NDF) programs.

^{30}Si and ^{29}Si depth-profiles were measured by using $^{29}Si(p,\gamma)^{30}P$ and $^{30}Si(p,\gamma)^{31}P$ narrow resonant reactions, around 414 and 620 keV respectively [17], into a low-background system coupled with a NaI(Tl) well detector installed on ALTAIS. γ-rays are detected in energy windows (4-6 MeV for $^{29}Si(p,\gamma)^{30}P$ and 3.5-9.5 MeV for $^{30}Si(p,\gamma)^{31}P$) given in reference [17].

PVD depositions and thermal evaporation were performed into a vacuum chamber. Samples are made in three successive steps without breaking vacuum: (1) SiO_2 plasma deposition using silicon cathode submitted to a reactive atmosphere composed of Ar with 5 sccm of O_2, (2) thermal evaporation of natural germanium powder under vacuum (10^{-4} Pa) with a deposition rate of 1 Angstrom/s, and (3) SiO_2 deposition under the same conditions than step 1.

μ-Raman measurements were performed using a confocal Renishaw RM 3000 spectrometer equipped with a digital camera, a x50 objective lens of 0.75 numerical aperture, and a 514 nm laser probe.

III. Implantation depth-profiles

Powerful ion beam analysis (IBA) techniques are used to highlight the implantation profiles. Figure 1a shows the result of a 3 MeV alpha particles RBS spectra of a triply implanted sample, i.e., with two silicon implantations followed by a single germanium implantation. In this configuration, Ge implantation will always be localized at the same projected range. In figure 1a, germanium peak (at high energies) and subsurface implanted ^{30}Si atoms can easily be fitted on RBS spectra. This last one is well untied from Si-contained SiO_2 signal, thanks to good mass resolution at 3 MeV. ^{29}Si contribution is less obvious to highlight owing to peak drowning into the substrate signal. This issue justifies the use of isotope sensitive analysis techniques, as RNRA [37,38].

In addition to being isotopically sensitive, the depth resolution is better for RNRA than RBS [32], as described in reference [31]. For backscattering analysis, the depth resolution is essentially ruled by the energy resolution of the detector (Passivated Implanted Planar Silicon), which is typically around 15 keV for Si-based PIPS detectors. For resonance profiling, depth resolution is mainly controlled by the energy spread of the incident beam (~ hundreds eV) and by the resonance width (< 100 eV in our cases [17]). An example of the evolution of RNRA depth-resolution is shown in figure 1 of reference [38].

Weak percentages of ^{29}Si and ^{30}Si contained in natural silicon (^{28}Si : 92.2% ; ^{29}Si : 4.7% ; ^{30}Si : 3.1%) allow us to bring out implanted species by RNRA measurements. Figures 1b and 1c illustrate respectively depth-profiles of ^{29}Si and ^{30}Si isotopes obtained using $^{29}Si(p,\gamma)^{30}P$ and $^{30}Si(p,\gamma)^{31}P$ reactions (open squares). In figure 1c, RNRA measurements are in good agreement with RBS fitted profiles (black dots). The RNRA data obtained by $^{29}Si(p,\gamma)^{30}P$ (figure 1b) were used to adjust the fit of ^{29}Si peak in RBS spectra.

RNRA raw data ($Y(E_0)$), which are a convolution of the beam energy spread, the straggling function and the resonance width (all included in $F(E_0, x)$), are decovoluated using Vavlov program developed at LARN [28]:

$$Y(E_0) = \int_0^x c(x)F(E_0, x)dx, \quad (1)$$

where $c(x)$ is the concentration depth-profile and $x = \frac{E_0 - E_R}{S_{E_R}}$ with S_{E_R} the stopping power, E_0 and E_R are the induced and resonant energies respectively. The Vavlov program enables us to get the concentration profile $c(x)$ as a function of depth (described in references [28,37,38]).

Combination of both techniques, RBS and RNRA, allows us to completely define the three implantation profiles of $^{29}Si^+$, $^{30}Si^-$ and $^{74}Ge^+$.

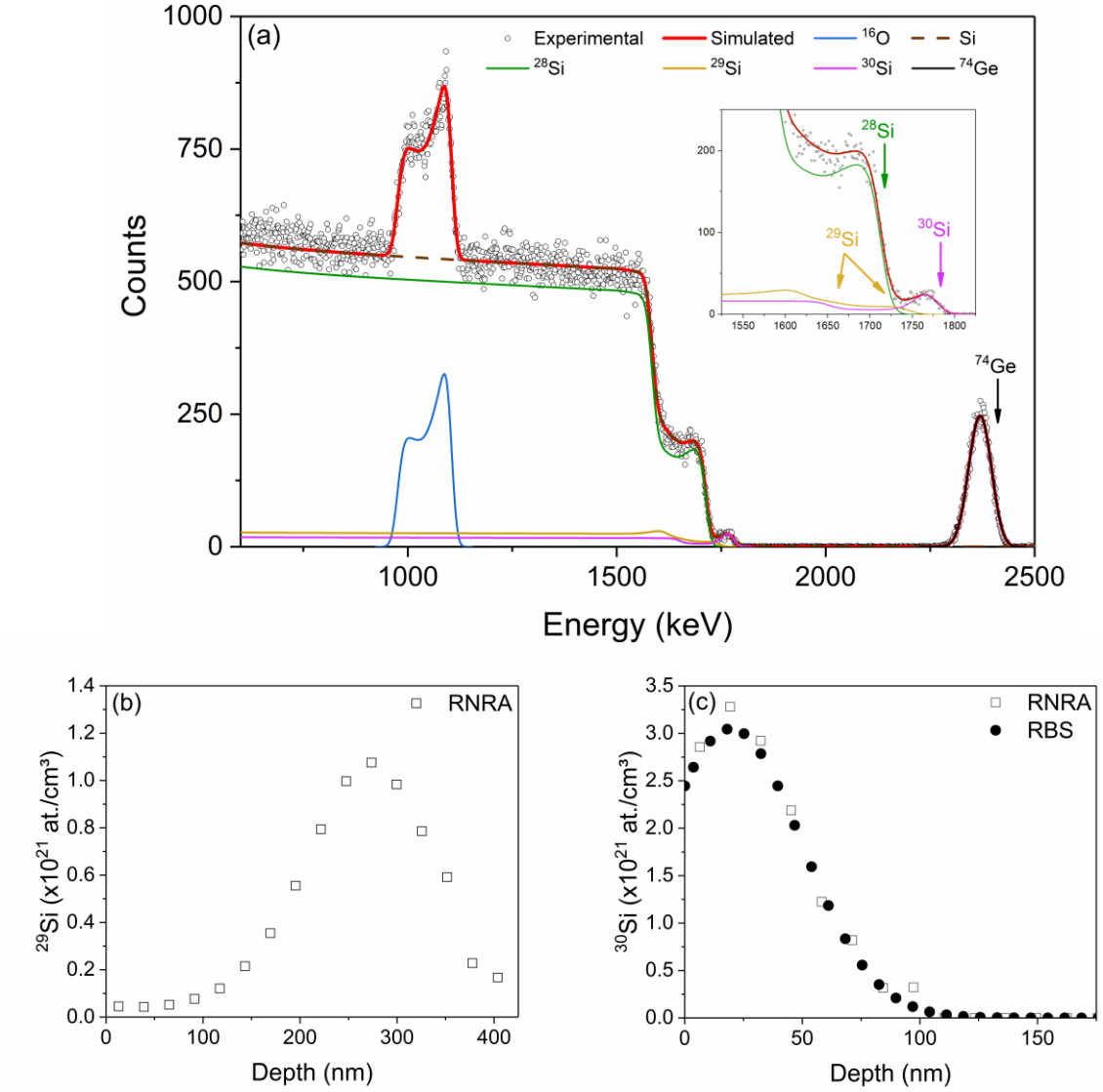

Figure 1: (a) RBS analysis of a 8 × 10^{16} $^{74}Ge/cm^2$ implanted sample, co-implanted with 2 × 10^{16} Si/cm^2 on either side of Ge, where ^{30}Si is well untied from substrate signal with a maximum about 1767 keV. RNRA extracted using the Vavlov program for ^{29}Si (b) and ^{30}Si (+ RBS) (c) for the same sample.

IV. Results and discussion

A. Anisotropic thermal diffusion of Ge

Figure 2 shows the germanium depth-profile obtained by RBS in a sample implanted solely with a measured fluence of 6 × 10^{16} $^{74}Ge/cm^2$, before and after 1 h annealing. The "as implanted" profile (blue dots) is consistent with SRIM-TRIM simulations (black solid line), taking into account interactions between the energetic ions and the substrate, with an eroded SiO_2 thickness of ~10 nm. The origin of the x axis corresponds to the sample surface (through which the Ge ions have penetrated) and the right part to the silicon substrate whose SiO_2/Si interface is located 295 nm below the surface. As shown in previous works [5-7], an important thermal diffusion of Ge is observed in both directions. After annealing, the Ge depth-profile

exhibits two peaks of the Gaussian shape. This migration is highly asymmetric with a major peak (peak 1) centered at a depth of 140 nm, which is shifted upwards by about 15 nm with respect to the center of the as-implanted depth-distribution. The second peak (peak 2) is located at the SiO_2/Si interface, where diffusing Ge have accumulated (red triangles). These features are consistent with the RBS measurements obtained by Minke et al. and Markvitz et al. in thermal SiO_2 fused and crystallized silica, who also found that the diffusing Ge accumulate in the vicinity of the sample surface [6,7] and at the SiO_2/Si interface [7]. Contrary to fused silica implanted with Ge and annealed above 900°C [9-11,14], no drastic outgassing-like comportment are reported. As measured by RBS, less than 4 % of germanium loss is measured which is consistent with the ones we have measured in other thermally grown silicon oxides [4,5].

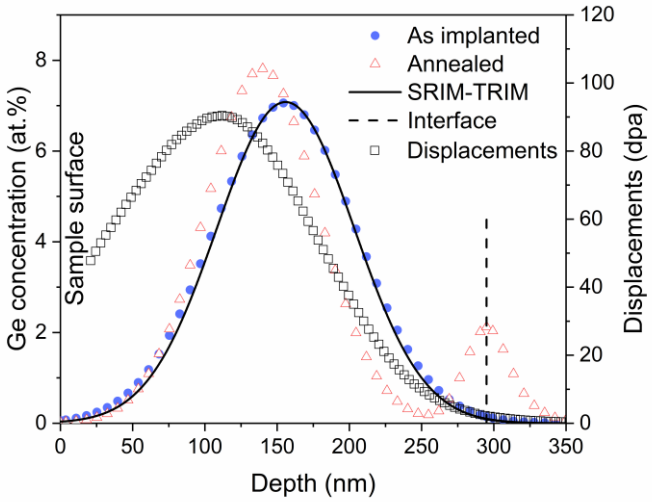

Figure 2: Fitting curves of RBS analyses of germanium depth-profile evolution before (blue dots) and after (red triangles) 1 h annealing at 1100°C for a sample not co-implanted with Si, supported by SRIM-TRIM calculations. Displacements (calculated from TRIM simulation) are represented by open squares (right y-axis).

In figure 2, the Ge that migrated upward during annealing is found to accumulate in the region where most the defects generated by the Ge implantation are located. On the other hand, about 11.5 % of the total amount of Ge is observed at the SiO_2/Si interface after thermal activation. This asymmetric shape along the sample depth of the Ge distribution after annealing results from the combination of three factors: [1] the composition and geometry of the implanted medium, which is highly anisotropic, [2] the influence of oxygen and [3] the trapping of diffusing germanium through the formation of $Ge-Si$ and $Ge-Ge$ chemical bonds.

[1] The layer anisotropy results from the as implanted germanium depth-profile which is located around the center of the SiO_2 layer, as measured by RBS (blue dots in figure 2), the depth-distribution of implantation-induced damage which is maximal between the surface and the Ge projected range (represented by open squares in figure 2 and calculated by SRIM-TRIM [16]), and the nature of the implanted medium: a 300 nm homogeneous SiO_2 layer edged by SiO_2/Si and gas/SiO_2 interfaces. The combination of these three contributions makes the composition,

density and atom ordering of the studied samples non-uniform in depth.

[2] As stated by the results published in the literature [7,8,11,12,18,19], Ge atoms were found to link with O inside SiO_2 layers after implantation [27], as a side effect of irradiation damages or during annealing, to form gaseous GeO. With the GeO density being smaller than that of air, Ge migration is favored toward the sample surface. This oxygen has two possible origins: it can come from residual moistures present in the annealing atmosphere or from the oxide itself and released by the damages induced by implantation. In this study, thermal processes are performed under ultra-high purity atmosphere, thus atmosphere contribution is limited and we consider that oxygen mostly comes from the SiO_2 matrix.

[3] Finally, chemical trapping effect evidenced in similar systems have shown that the diffusion of germanium is strongly affected by the formation of $Ge - Si$ and $Ge - Ge$ bonds, leading to nanoclustering and blocking barrier effects [5,13-15].

In agreement with the models proposed to describe the Ge diffusion mechanism inside SiO_2, we infer that the Ge implanted should preferentially diffuse upward and its motion would be affected by the nature of crossed medium. Such a scenario is supported by the data reported on figure 2, where the region containing the greatest concentration of Ge after annealing (peak 1) corresponds to the region where Ge atoms have greater probability to nucleate, and the accumulation of Ge found at the SiO_2/Si interface (peak 2) is a direct consequence of the Si/Ge trapping [5,14,15]. This SiO_2/Si interface is known to release SiO molecules that react with GeO through the following reaction [24]:

$$GeO + SiO \rightarrow Ge + SiO_2, \quad (2)$$

as confirmed by XPS measurements showing the formation of $Ge - Ge$ and $Ge - Si$ chemical bonds [12,27]. However, it was evidenced by Markvitz *et al.* using transmission electron microscopy (TEM) investigations, that the formation of such bonds would not necessary lead to the nucleation of Ge [7].

Trapping effect is less dominant in the subsurface region where Ge is close to the gas/SiO_2 interface. This allows low quantities of highly volatile GeO to desorb through the surface.

Despite the presence of strong material density variations originating from recoiled Si and O target atoms [16], the structural defects generated by implantation are not responsible of the anisotropic Ge diffusion. This remark is consistent with previous works, highliting the poor contribution of grain boundary diffusion and cracking layer to the Ge displacement [6]. It is also consistent with the fact that most of the damage induced by ion implantation is restored for SiO_2 and silica films annealed at temperatures higher than 1000 °C [33] (not fully efficient at the high fluences used in this work). Hence, although the efficiency of this structural recovery process may differ in the different sample regions, the Ge diffusion mechanism appears to be mostly dominated by factors [2] and [3]. This is confirmed by the thinning of peak 1 after annealing in figure 2, suggesting Si/Ge trapping and nanoclustering during the upwards diffusion of Ge.

For fluences as high as 2.5×10^{17} $^{74}Ge/cm^2$, the density of defects is increased by factor 4, and the damage and Ge depth-profiles superimpose due to erosion (30 nm). In these conditions, peak 1 is measured to shift only by 4 nm with respect to the as implanted peak position, which is four times less than for 6×10^{16} $^{74}Ge/cm^2$, and ~9 % of the total implanted Ge atoms accumulate at the SiO_2/Si interface, confirming the participation of damage in Si/Ge trapping during Ge diffusion.

B. Ge diffusion through non-implanted SiO_2/Si samples

In order to highlight the significant role of implantation-induced effects discussed above on Ge diffusion, a sample free of ion damaging was prepared by thermal evaporation and plasma vapor deposition (PVD). This sample is composed of a thin germanium layer thermally evaporated inside a vacuum chamber (10^{-4} Pa). This evaporation step is inserted between two SiO_2 plasma depositions to obtain a germanium layer of about 15-20 nm thickness embedded into a homogeneous medium exempt of implanted ions and atoms displaced by collision with impinging ions.

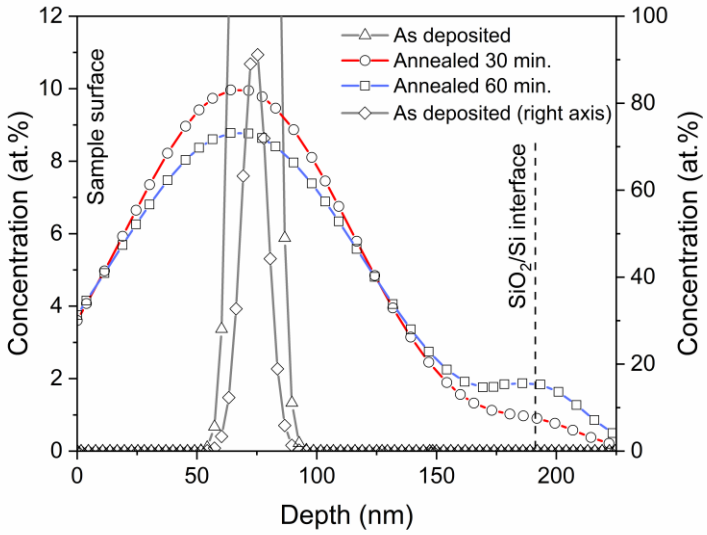

Figure 3: Ge depth-profiles (RBS) of deposited samples (SiO_2/Ge/SiO_2) before and after 30 and 60 min annealing at 1100 °C under pure N_2 atmosphere.

Figure 3 shows the RBS spectra, measured before and after annealing, of non-implanted samples. Two samples were annealed at 1100°C under pure nitrogen atmosphere, for 30 and 60 minutes respectively. After thermal treatment, the Ge is found to diffuse through the two deposited SiO_2 layers. The diffusion process occurs at the same rate upward and downward, leading to a final depth-distribution that is almost symmetric with respect to the Ge layer. In the absence of implantation, only a poor fraction of Ge atoms are supposed to be chemically bonded to oxygen to form highly volatile GeO responsible for upward diffusion. As for the Ge implanted sample shown in figure 2, a buildup of the Ge concentration is observed with the increase of the annealing time in the vicinity of the Si substrate, which can be attributed to Si/Ge trapping effects, resulting from the abrupt increase of the Si concentration. Nevertheless, in absence of ion-induced effects within the first 50 nm of the sample, no accumulation of Ge is observed between the sample surface and the deposited Ge layer,

resulting in 12-13% of Ge outgassing. Such a behavior is consistent with the expected result, since for the non-implanted samples, the Ge diffusing upward is not affected by the presence of local defects and excess atoms, which both reduce its displacement and contribute to its clustering [5,13-15].

Using figure 3 and the second Fick's law, we are able to calculate the diffusion coefficient of germanium in this deposited oxide, $D_{1100°C}$:

$$C(x,t) = \frac{C_0}{2\sqrt{D_{1100°C}t}} e^{-(x-x_0)^2/4D_{1100°C}t}, \quad (3)$$

with C_0 the initial concentration (t = 0 s), x_0 the position of the distribution maximum and t the annealing time. At 1100°C, this coefficient is found to be $D_{1100°C} \sim 10^{-14}\ cm^2/s$, which is several orders of magnitude higher than current coefficients referenced in the literature [6,10]. These coefficients are generally obtained on implanted samples whose diffusion is influenced by the three factors explained in the previous section. Diffusion coefficient strongly depends on implantation and annealing conditions as well as host matrix quality, which explains the discrepancies reported in the literature and the large difference measured in this work with deposited samples less influenced by GeO formation and irradiation damage.

C. Co-implantation of Si

To control the diffusion and position of germanium atoms after annealing, we take advantage of the Si/Ge trapping effect explained above. $^{29}Si^+$ and $^{30}Si^-$ isotopes were implanted on either side of the Ge depth-distribution prior to the thermal annealing to act as diffusion barrier for Ge [5,13-15].

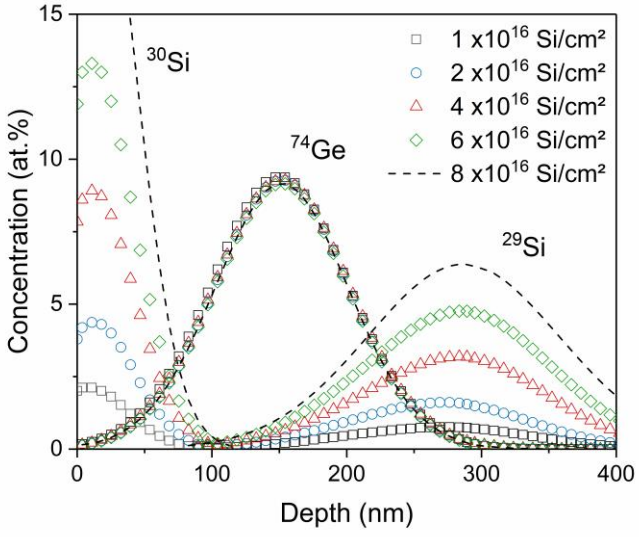

Figure 4: ^{74}Ge, ^{29}Si and ^{30}Si depth-profiles (curves used to fit RBS/RNRA data), measured by RBS/RNRA, of co-implanted samples for fluences varying from 1 to 6 × 10^{16} Si/cm². The implantation sequence permits to obtain the same Ge depth-profile for each sample with different overlaps when the ^{30}Si and ^{29}Si fluences increase.

Figure 4 illustrates the depth-profiles of five samples implanted with Ge at a fluence of 8 × 10 ^{16} ^{74}Ge/cm^2 and co-implanted at silicon fluences ranging from 1 × 10^{16} to 8 × 10^{16} Si/cm², as measured by RBS. Although the central positions of the Si depth-distribution may vary from several nanometers with the ion fluences due to ion erosion [16], the silicon excess introduced by ion implantation into the samples is basically localized between the first 100 nm of the sample for ^{30}Si and deeper than 100 nm for ^{29}Si. As the silicon diffusion is negligible compared to that of germanium [6], the depth-profiles of co-implanted Si remain unchanged after thermal treatment. For each co-implanted sample, no germanium losses are measured after annealing within the accuracy limits of the RBS technique. As shown by the Ge depth-profiles presented in figure 5, the germanium diffusion is completely stopped for Si co-implanted fluences greater than 2 × 10^{16} Si/cm². This shows that, as for the upward diffusion [5], the in-depth diffusion of Ge can be blocked using Si co-implantation. The value at which the diffusion barrier effects become optimal on RBS profiles corresponds to a maximum Si excess atom concentration of about 4.5 at.% and 1.6 at.% for low and high energies of implantation respectively. Such a density is very low compared to the one previously reported in fused silica, where each co-implanted Si atom is found to block one diffusing Ge on average [14]. We infer that the need of a smaller amount of Si excess to stop the diffusion of Ge in the SiO_2/Si samples is due to the higher concentration of silicon dangling bonds, whose presence within the thermal oxide also contributes to the Si/Ge trapping via the formation of $Ge - Si$ chemical bonds [5,11].

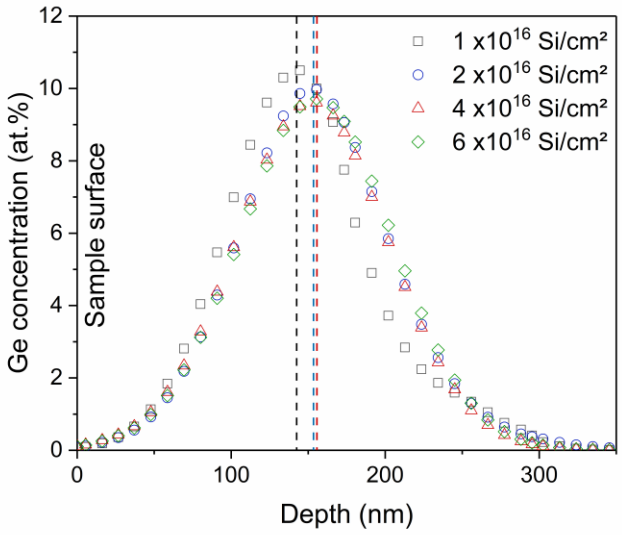

Figure 5: Concentration of ^{74}Ge after 1 h annealing at 1100 °C under N_2 atmosphere for samples co-implanted with fluences varying from 1 to 6 × 10^{16} Si/cm² (fitted from RBS/RNRA spectra).

Under 2 × 10^{16} Si/cm², diffusion in both directions appears to be the dominant regime. The excess of co-implanted silicon is not sufficient and the diffusion process is marked upward and ruled the same way than for not co-implanted samples shown in figure 2.

A configuration without the low energy implantation at 35 keV has been tested to highlight the in-depth blocking and the potential effect on upwards diffusion. The ^{29}Si$^+$ implantation at 170 keV was replaced by ^{30}Si$^+$ because of a resonance more intense by a factor 2.5. Two

samples implanted with measured fluences of 1.2×10^{17} $^{74}Ge/cm^2$, co-implanted with 2 and 6 $\times 10^{16}$ $^{30}Si/cm^2$ respectively, were annealed at 1100°C during 1 h. Figure 6 shows a completely annihilated Ge diffusion in regions where Si excess was co-implanted, while Ge upwards diffusion dominates in the 70 - 85 first nanometers (depending on the ^{30}Si fluence) where no Si excess has been implanted. A fluence-dependent effect is observed due to surface erosion and the increased density of damage with the fluence. The high energy implantation is not sufficient to block upward diffusion in the subsurface region even for a fluence of 6×10^{16} $^{30}Si/cm^2$, corresponding to a local concentration of 4.5 at.%. This confirms the strong upward diffusion of Ge in regions not co-implanted with Si excess and the importance of co-implanted Si as a barrier for Ge diffusion. ^{30}Si induced-defects are distributed throughout the Ge profile, as well as damage induced by ^{74}Ge due to surface erosion (~15 nm), as calculated by TRIM. Damage contribution is less significant due to matrix restoration occurring during annealing. This additional result is consistent with an upward diffusion of Ge annihilated by the formation of Si/Ge chemical bonds due to co-implanted Si and irradiation defects.

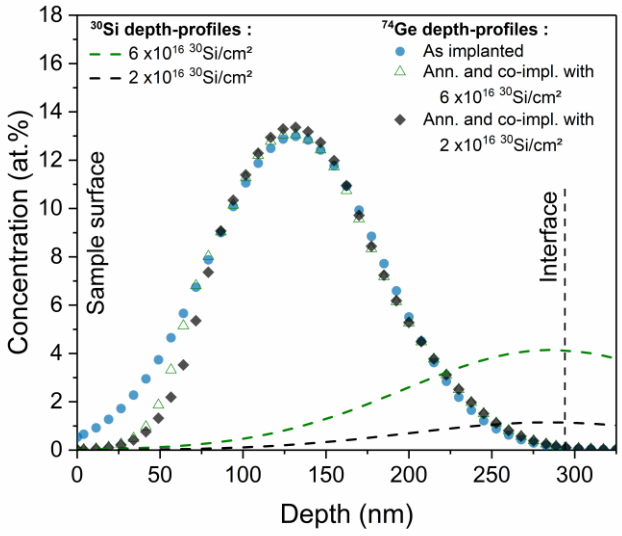

Figure 6: Fitting curves of RBS/RNRA analysis of 1.2×10^{17} $^{74}Ge/cm^2$ co-implanted with 2 and 6×10^{16} $^{30}Si/cm^2$. ^{30}Si is implanted at 170 keV to annihilate the in-depth diffusion of Ge.

D. Nanoclustering

In order to bring out the role of each silicon isotope, µ-Raman analyses have been performed. Figure 7 shows the Raman signature of Ge implanted samples co-implanted with $^{30}Si^-$ and $^{29}Si^+$ after 1 h annealing at 1100°C. The spectral range of 270 - 420 cm^{-1} was chosen to eliminate the strong contribution of the TO phonon mode of the Si substrate around 520 cm^{-1}, to zoom on the region where Raman phonons related to Ge-ncs and Ge/Si clusters appear [14]. In agreement with previous studies [5,13,20-24], peaks 1 and 2 observed at 280 and 295 cm^{-1} on figure 7a are associated with the signature of Ge nanocrystals containing Si impurities and pure Ge nanocrystals, respectively. The increase of peak 1 with the increase of the co-implanted Si fluence supports this assignation. $Ge - Si$ phonons peaks, around 400 cm^{-1}, are the phonons related to the formation of ^{30}Si-Ge (peak 3), ^{29}Si-Ge (peak 4) and ^{28}Si-Ge (peak 5)

bonds. Their positions of 391, 398 and 406 cm^{-1} were maintained constant during spectral deconvolution, and correspond to the wavenumbers calculated for isotopic effect using the $M^{-1/2}$ dependence of the phonon frequency [39].

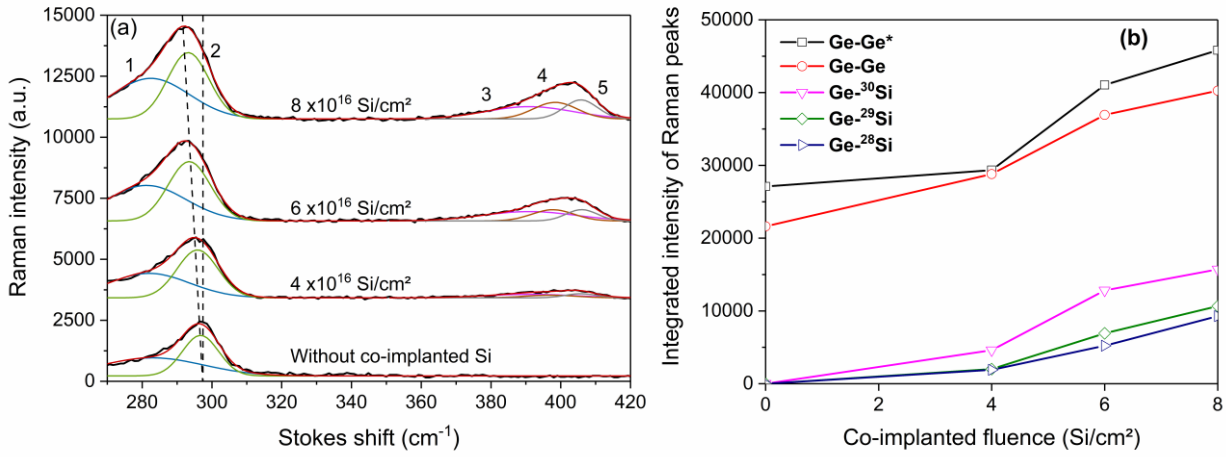

Figure 7: µ-Raman spectra of samples co-implanted with 4, 6, 8 × 10^{16} Si/cm² and without Si (a), and integrated intensity of Raman peaks (b).

While the contributions of co-implanted Si for ion fluences lower 4 × 10^{16} Si/cm² are below the µ-Raman detection limit, both the signals related to the Ge nanoclusters and the Si/Ge aggregates are found to increase with the increase of the ^{30}Si and ^{29}Si concentrations. This trend is consistent with the reduction of the thermal diffusion of Ge throughout the whole SiO_2 matrix shown in figure 5 and discussed in section IV.C, which promotes the clustering of Ge within the region where the concentration of implanted Ge is the highest.

The presence of the two $Ge{-}^{30}Si$ and $Ge{-}^{29}Si$ Raman peaks confirm that silicon excess participates actively to the blocking of implanted germanium atoms. The evolution of $Ge{-}^{30}Si$, $Ge{-}^{29}Si$ and $Ge{-}^{28}Si$ peaks is presented in figure 7b, indicating that the formation of Si/Ge clusters is dominated by the formation of $Ge{-}^{30}Si$ bonds. As the intensity of the phonon Raman peaks is usually proportional to the density of chemical bonds related to this vibration, such a feature would be a direct consequence of the preponderant Ge upward diffusion, through the formation of GeO. This result is supported by RBS measurements, showing in figure 2 that a majority of Ge diffuses toward the sample surface, where the presence of ^{30}Si excess in co-implanted samples promote locally its trapping. Such a feature is further pronounced by the fact that according to overlap of the ^{30}Si/Ge and ^{29}Si/Ge depth-distribution, evaluated from the RBS spectra of figure 4 and reported on figure 8, the quantity of co-implanted Si introduced into the Ge-implanted region is nominally greater for ^{29}Si than for ^{30}Si. Due to ion erosion, this overlap increases with the fluence of co-implanted Si. In figure 8, the relative spatial superposition of the $Ge{-}^{30}Si/Ge{-}^{29}Si$ depth-profiles is twice lower for a co-implantation at 8 × 10^{16} Si/cm² than 4 × 10^{16} Si/cm², while the concentration of $Ge{-}^{30}Si$ bonds found by µ-Raman on figure 7b still remains 50% higher than that of $Ge{-}^{29}Si$ bonds. This confirms that even if there are more ^{29}Si in the surrounding of implanted Ge the formation

of $Ge-^{30}Si$ in the first 50 nm of the samples still dominates, due to the greater upward diffusion of Ge.

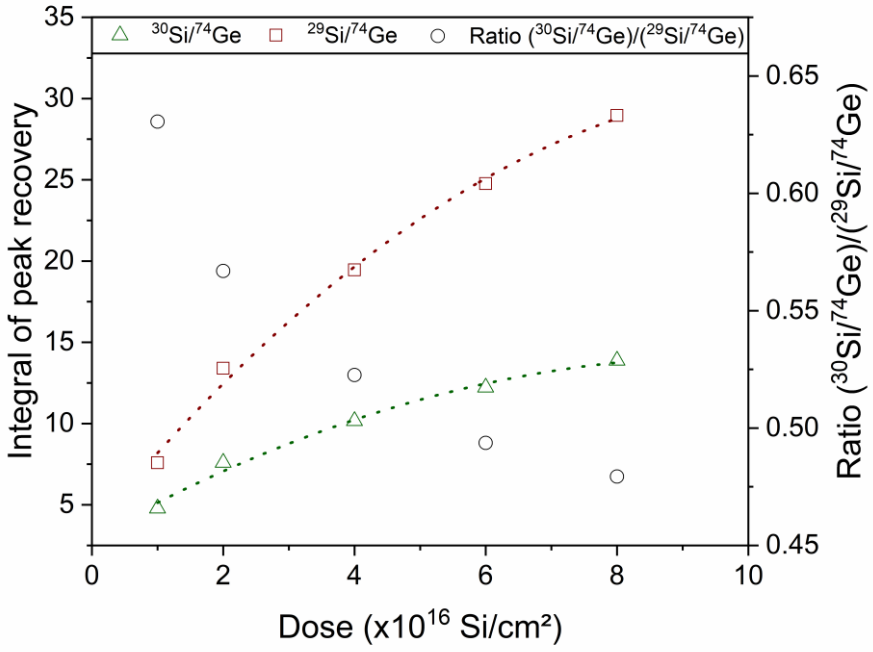

Figure 8: $^{29}Si/^{74}Ge$ (·· □ ··) and $^{30}Si/^{74}Ge$ (·· Δ ··) profiles overlapping measured by RBS (deduced from figure 4). The overlap ratio (○) decreases due a faster increase of $^{29}Si/^{74}Ge$ compared to $^{30}Si/^{74}Ge$.

The increase of the $Ge-^{28}Si$ Raman peak with co-implantation fluence suggests a "kick-out" effect generated by the implanted species: a fraction of implanted Si can substitute to ^{28}Si atoms in the SiO_2 matrix, inducing an increase of ^{28}Si excess through the dioxide layer.

The influence of Si co-implantation on Ge nanocrystal size and purity has been investigated by TEM and discussed in references [5] and [14]. The more the Si fluence is increasing, the more the Ge-ncs diameter is reducing due to the decrease of Ge thermal diffusion, which is consistent with the current results. As a consequence, the concentration of co-implanted Si can be set to control the size of the formed nanocrystals and their distribution over the SiO_2 layer. In addition, samples co-implanted with Si were found to contain Ge-ncs with interplanar spacings 2-3% smaller than that of not co-implanted samples [5]. These two features contribute to both the redshift and the spectral broadening of the Ge-nc Raman peak, in agreement with our measurements.

V. Conclusions

RBS/RNRA investigations showed that the thermally activated diffusion of Ge atoms implanted in the middle of a SiO_2/Si layer occurs upward (surface) and downward (interface). This diffusion is asymmetric due to the formation of highly volatile GeO, which favors out-diffusion. It is brought out that low quantities of co-implanted Si excess (from 2×10^{16} Si/cm², corresponding to 4.5 at.% at low energy and 1.6 at.% at high energy), implanted on either side of Ge, are sufficient to completely annihilate Ge diffusion in both directions for a Ge fluence of 8×10^{16} ^{74}Ge/cm² (10 at.% at maximum). Silicon isotopes were used in order to highlight the contribution of the two Si implantations, with ^{30}Si and ^{29}Si implanted at 35 and 170 keV respectively. Upward diffusion observed by RBS was confirmed by µ-Raman analyses systematically presenting a larger density of $Ge{-}^{30}Si$ chemical bonds. µ-Raman analysis showed the importance of co-implantation of Si excess in Si/Ge trapping and nanoclustering by measuring a dependence, as a function of the fluence of co-implanted Si, on the density of $Ge{-}^{30}Si$ and $Ge{-}^{29}Si$ bonds.

The important role of implantation induced-defects has been highlighted using a deposited sample free of irradiation damage. In the absence of implantation, Ge diffusion is less limited by the density of defects and a coefficient of diffusion as high as $D_{1100°C} \sim 10^{-14}\ cm^2/s$ is found. This value is two orders of magnitude higher than coefficients generally measured for implanted samples, due to structural differences of the SiO_2 layer and absence of implantation induced-defects. Deposition also prevents from GeO formation, responsible of upward diffusion, resulting in a symmetric Ge diffusion in both directions.

ACKNOWLEDGMENTS

The authors would like to thanks I. Vickridge for his advises during our discussions, T. Tabarrant for the technical support on ALTAÏS accelerator, and the SIAM (Synthesis, Irradiation and Analysis of Materials) technological platform of the university of Namur.

DATA AVAILABILITY

The data that support the findings of this study are available from the corresponding author upon request.

REFERENCES

[1] Green, M. A., Bremner, S. P. (2017). *Energy conversion approaches and materials for high-efficiency photovoltaics*. Nature Materials, 16, 23–34. https://doi.org/10.1038/nmat4676

[2] Yedji, M., Demarche, J., Terwagne, G., Delamare, R., Flandre, D., Barba, D., Koshel, D., Ross, G. G. (2011). *Method for fabricating third generation photovoltaic cells based on Si quantum dots using ion implantation into SiO_2.* J. Appl. Phys., 109(8), 084337. https://doi.org/10.1063/1.3575325

[3] Beard, M. C., Knustsen, K. P., Yu, P., Song, Q., Luther, J., Ellingson, R., Nozik, A. J. (2007). *Multiple exciton generation in colloidal silicon nanocrystals*. *Nano Lett.*, *7*, 2506–2512. https://doi.org/10.1021/nl071486l

[4] Trinh, M. T., Limpens, R., de Boer, W. D. A. M., Schins, J. M., Siebbeles, L. D. A., Gregorkiewicz, T. (2012). *Direct generation of multiple excitons in adjacent silicon nanocrystals revealed by induced absorption.* Nature Photonics, 6(5), 316–321. https://doi.org/10.1038/nphoton.2012.36

[5] Barba, D., Wang, C., Nélis, A., Terwagne, G., Rosei, F. (2018). *Blocking germanium diffusion inside silicon dioxide using a co-implanted silicon barrier*. *J. Appl. Phys.*, *123*(16), 161540. https://doi.org/10.1063/1.5002693

[6] Minke, M. V., Jackson, K. A. (2005). *Diffusion of germanium in silica glass*. J. Non-Crystalline Solids, 351(27–29), 2310–2316. https://doi.org/10.1016/j.jnoncrysol.2005.04.052

[7] Markwitz, A., Schmidt, B., Matz, W., Grötzschel, R., Mücklich, A. *(1998). Microstructural investigation of ion beam synthesised germanium nanoclusters embedded in SiO_2 layers.* Nucl. Instrum. Methods Phys. Res. B, 142(3), 338–348. https://doi.org/10.1016/S0168-583X(98)00283-3

[8] Beyer, V., von Borany, J. (2008). *Elemental redistribution and Ge loss during ion-beam synthesis of Ge nanocrystals in SiO_2 films*. Phys. Rev. B, 77(1), 014107. https://doi.org/10.1103/PhysRevB.77.014107

[9] Barba, D., Martin, F., Demarche, J., Terwagne, G., & Ross, G. G. (2012). *Nanocavities and germanium nanocrystals produced by Ge ion implantation in fused silica.* Nanotechnology, 23(14). https://doi.org/10.1088/0957-4484/23/14/145701

[10] Li, C., Feng, H., Liu, B., Liang, W., Liu, G., Ross, G. G., Wang, Y., & Barba, D. (2017). *Effect of nanocavities on Ge nanoclustering and out-diffusion in SiO_2.* Nanotechnology, 28(3), 035707. https://doi.org/10.1088/1361-6528/28/3/035707

[11] Barba, D., Cai, R. S., Demarche, J., Wang, Y. Q., Terwagne, G., Rosei, F., Ross, G. G. (2014). *Influence of silicon dangling bonds on germanium thermal diffusion within SiO_2 glass.* Appl. Phys. Lett., 104(11), 111901. https://doi.org/10.1063/1.4868721

[12] Heinig, K. H., Schmidt, B., Markwitz, A., Grötzschel, R., Strobel, M., Oswald, S. (1999). *Precipitation, ripening and chemical effects during annealing of Ge^+ implanted SiO_2 layers*. Nucl. Instrum. Methods Phys. Res. B, 148(1–4), 969–974. https://doi.org/10.1016/S0168-583X(98)00862-3

[13] Barba, D., Demarche, J., Martin, F., Terwagne, G., Ross, G. G. (2012). *Trapping of diffusing germanium by silicon excess co-implanted into fused silica.* Appl. Phys. Lett., 101(14), 143107. https://doi.org/10.1063/1.4757291

[14] Barba, D., Demarche, J., Martin, F., Terwagne, G., & Ross, G. G. (2013). *Control of the Ge nanocrystal synthesis by co-implantation of Si^+*. J. Appl. Phys., 114(7), 074306. https://doi.org/10.1063/1.4817667

[15] Cai, R. S., Wang, Y. Q., Shang, L., Liu, X. H., Zhang, Y. J., Ross, G. G., & Barba, D. (2014). *Inhibitive formation of nanocavities by introduction of Si atoms in Ge nanocrystals produced by ion implantation.* Journal of Applied Physics, 115(20). https://doi.org/10.1063/1.4880661

[16] Ziegler, J. F., Ziegler, M. D., Biersack, J. P. (2010). *SRIM – The stopping and range of ions in matter (2010).* Nucl. Instrum. Methods Phys. Res. B, 268(11–12), 1818–1823. https://doi.org/10.1016/j.nimb.2010.02.091

[17] Amsel, G., D'Artemare, E., Battistig, G., Girard, E., Gosset, L. G., & Révész, P. (1998). *Narrow nuclear resonance position or cross section shape measurements with a high precision computer-controlled beam energy scanning system.* Nuclear Instruments and Methods in Physics Research Section B: Beam Interactions with Materials and Atoms, 136–138, 545–550. https://doi.org/10.1016/S0168-583X(97)00870-7

[18] Baranwal, V., Gerlach, J. W., Lotnyk, A., Rauschenbach, B., Karl, H., Ojha, S., Avasthi, D. K., Kanjilal, D., Pandey, A. C. (2015). *Embedded Ge nanocrystals in SiO_2 synthesized by ion implantation*. J. Appl. Phys., 118(13), 134303. https://doi.org/10.1063/1.4932151

[19] von Borany, J., Grötzschel, R., Heinig, K. H., Markwitz, A., Matz, W., Schmidt, B., Skorupa, W. (1997). *Multimodal impurity redistribution and nanocluster formation in Ge implanted silicon dioxide films*. Appl. Phys. Lett., 71(22), 3215–3217. https://doi.org/10.1063/1.120294

[20] Rodríguez, A., Ortiz, M. I., Sangrador, J., Rodríguez, T., Avella, M., Prieto, A. C., Torres, A., Jiménez, J., Kling, A., & Ballesteros, C. (2007). *Comparative study of the luminescence of structures with Ge nanocrystals formed by dry and wet oxidation of SiGe films.* Nanotechnology, 18(6), 065702. https://doi.org/10.1088/0957-4484/18/6/065702

[21] Pagès, O., Souhabi, J., Torres, V. J. B., Postnikov, A. V., & Rustagi, K. C. (2012). *Re-examination of the SiGe Raman spectra: Percolation/one-dimensional-cluster scheme and ab initio calculations.* Physical Review B, 86(4), 045201. https://doi.org/10.1103/PhysRevB.86.045201

[22] Vasin, A. S., Vikhrova, O. V., & Vasilevskiy, M. I. (2015). *Effects of alloy disorder and confinement on phonon modes and Raman scattering in Si_xGe_{1-x} nanocrystals: A microscopic modeling.* J. Appl. Phys. 115, 143505. Journal of Applied Physics, 118(18), 189902. https://doi.org/10.1063/1.4935816

[23] Liu, L. Z., Gao, F., Wu, X. L., Li, T. H., & Chu, P. K. (2009). *Influence of GeSi interfacial layer on Ge–Ge optical phonon mode in SiO_2 films embedded with Ge nanocrystals.* Appl. Phys. Lett., 95(17), 171105. https://doi.org/10.1063/1.3257379

[24] Rodríguez, A., Rodríguez, T., Prieto, Á. C., Jiménez, J., Kling, A., Ballesteros, C., & Sangrador, J. (2010). *Crystallization of Amorphous $Si_{0.6}Ge_{0.4}$ Nanoparticles Embedded in SiO_2: Crystallinity Versus Compositional Stability.* Journal of Electronic Materials, 39(8), 1194–1202. https://doi.org/10.1007/s11664-010-1254-9

[25] Barba, D., Koshel, D., Martin, F., Ross, G. G., Chicoine, M., Schiettekatte, F., Yedji, M., Demarche, J., & Terwagne, G. (2010). *Silicon nanocrystal synthesis by implantation of natural Si isotopes.* Journal of Luminescence, 130(4), 669–673. https://doi.org/10.1016/j.jlumin.2009.11.014

[26] Cardona, M. (2000). *Isotopic Effects in the Phonon and Electron Dispersion Relations of Crystals.* Physica Status Solidi (B), 220(1), 5–18. https://doi.org/10.1002/1521-3951(200007)220:1<5::AID-PSSB5>3.0.CO;2-K

[27] Oswald, S., Schmidt, B., Heinig, K.-H. (2000). *XPS investigation with factor analysis for the study of Ge clustering in SiO_2.* Surf. Interface Anal., 29(4), 249–254. https://doi.org/10.1002/(SICI)1096-9918(200004)29:4<249::AID-SIA735>3.0.CO;2-5

[28] Deconninck, G., & Van Oystaeyen, B. (1983). *High resolution depth profiling of F, Ne and Na in materials.* Nucl. Instrum. Methods in Phys. Res., 218(1–3), 165–170. https://doi.org/10.1016/0167-5087(83)90974-2

[29] *SIMNRA, a simulation program for the analysis of NRA, RBS and ERDA.* ***Mayer, M.*** *1999*, AIP Conf. Proc.

[30] Jeynes, C., Barradas, N. P., Marriott, P. K., Boudreault, G., Jenkin, M., Wendler, E., & Webb, R. P. (2003). *Elemental thin film depth profiles by ion beam analysis using simulated annealing - A new tool.* J. Phys. D Appl. Phys., 36(7). https://doi.org/10.1088/0022-3727/36/7/201

[31] Vickridge, I. C. (2003). *Depth resolution and narrow nuclear resonance profiling.* Curr. Appl. Phys., 3(1), 51–55. https://doi.org/10.1016/S1567-1739(02)00235-3

[32] Y. Wang and M. Nastasi (Eds.), Handbook of modern ion beam materials analysis, Materials Research Society, 2009 (2nd edition).

[33] Hao, X., Zhou, C., Yu, R., Wang, B., & Wei, L. (2008). *Characterization of Implantation Induced Defects in Si-Implanted SiO_2 Film*. J. Nanosci. Nanotechno., 8(3), 1350–1354. https://doi.org/10.1166/jnn.2008.327

[34] Takakuwa, Y., Nihei, M., Miyamoto, N. (1993). *Outdiffusion and Subsequent Desorption of Volatile SiO Molecules during Annealing of Thick SiO_2 Films in Vacuum.* Jpn J. Appl. Phys., 32(Part 2, No. 4A), L480–L483. https://doi.org/10.1143/JJAP.32.L480

[35] Doğan, İ., & van de Sanden, M. C. M. (2013). *Direct characterization of nanocrystal size distribution using Raman spectroscopy.* J. Appl. Phys., 114(13), 134310. https://doi.org/10.1063/1.4824178

[36] J.L. Colaux, (2009) *Characterisation of carbon nitride compounds synthesized by simultaneous implantation of carbon and nitrogen in copper*. [Doctoral dissertation, University of Namur]

[37] Terwagne, G., Piette, M., & Bodart, F. (1987). *Comparison between diffusion of ^{15}N and ^{14}N in implanted iron.* Nucl. Instrum. Methods Phys. Res. B: Beam Interactions with Materials and Atoms, 19–20, 145–149. https://doi.org/10.1016/S0168-583X(87)80030-7

[38] Lucas, S., Bodart, F., Terwagne, G., Sorensen, G., & Jensen, H. (1989). *Modifications by rare gas bombardment of aluminium nitride formed by direct implantation.* Mater. Sci. Eng. B, 2(1–3), 183–187. https://doi.org/10.1016/0921-5107(89)90094-9

Article III: supplementary information

In **article III**, we have shown that low fluences of co-implanted silicon could be used to completely control germanium diffusion in both directions. The two samples presented in figure 6 of **article III** indicated that the high-energy co-implantation (at 170 keV) was the main responsible of the annihilation of germanium diffusion. This can be explained by two factors:

1. Silicon is co-implanted in the SiO_2 region with the highest germanium mobility, *i.e.* behind the germanium projected range (cfr **articles I and II**). Si co-implantation reduces the over-stoichiometric state observed in this region, limiting the formation of highly mobile GeO.
2. Additional damage are induced in the oxide region where Ge atoms are implanted, increasing the density of silicon dangling bonds.

As GeO has been confirmed as the main responsible of Ge diffusion, and knowing that oxygen preferentially binds with silicon rather than germanium at high temperature while not mobile Ge-Si chemical bonds are formed, the presence of additional silicon drastically reduces germanium mobility.

In the particular case of samples presented in figure 6 of **article III**, we must mention that implanted germanium is initially less mobile due to a higher germanium fluence compared to figure 5 (1.2×10^{17} versus 8×10^{16} Ge/cm²). As discussed in **article I**, Ge^0 and GeO_x concentrations are dose-dependent and tend to be dominated by Ge-Ge and Ge-Si chemical bonds for the higher germanium fluences. This explains the very low concentrations of co-implanted silicon ions required to drastically limit the Ge long-range redistribution for the sample presented in figure 6 of **article III**.

Article IV: Blocking Ge diffusion inside silicon dioxide using a co-implanted Si barrier

Preliminary to article IV

After having demonstrated in **article III** that germanium diffusion could be completely annihilated by silicon co-implantation under right conditions, this fourth manuscript, entitled "*Blocking germanium diffusion inside silicon dioxide using a co-implanted Si barrier*", aims to investigate the effects of this co-implantation on the nanocrystals formation and on the control of their size distribution. HRTEM measurements are carried out to highlight the effects on quantum dots formation with and without the presence of silicon excess, for single or double Si co-implantations. The final objective of this article is to use this co-implantation to form a size gradient ranging from 0.6 to 4-5 nm.

As the energy gap of quantum dots depends on their dimensions (24), (26), a well-distributed size gradient could be used to mimic high-efficiency multi-junction photovoltaic cells. As the gap increases while the nanocrystals diameter is reduced (**Figure 11** in **chapter III**), the quantum dots average size should increase as a function of the depth to optimize the absorption of solar spectrum over a wide range of wavelengths. This enables to limit efficiency losses due to the emission of phonons (cfr **Figure 13**).

Authors' contribution

David Barba carried out the Ge implantations for samples co-implanted with one Si isotope, while I performed the ^{30}Si implantations for these samples. I realized all the implantations for the samples co-implanted with ^{29}Si and ^{30}Si isotopes. Chao Wang carried out TEM imaging. David performed and interpreted the µ-Raman analyses. I performed and analysed the RBS measurements. Assisted by all the authors, David Barba was in charge of writing the article.

Blocking germanium diffusion inside silicon dioxide using a co-implanted silicon barrier

D. Barba[1,*], C. Wang[1], A. Nelis[2], G. Terwagne[2], F. Rosei[1]

[1] *INRS-EMT, 1650 boul. Lionel-Boulet, Varennes, Québec J3X 1S2, Canada*

[2] *LARN, Centre de Recherche en Physique de la Matière et du Rayonnement, University of Namur (FUNDP), B-5000 Namur, Belgium*

Published in *Journal of Applied Physics* **123** (2018) 161540.

https://doi.org/10.1063/1.5002693

Abstract

We investigate the effect of co-implanting a silicon sublayer on the thermal diffusion of germanium ions implanted into SiO_2 and the growth of Ge nanocrystals (Ge-ncs). High-resolution imaging obtained by transmission electron microscopy and energy dispersive spectroscopy measurements supported by Monte-Carlo calculations show that the Si-enriched region acts as a diffusion barrier for Ge atoms. This barrier prevents Ge outgassing during thermal annealing at 1100 ^{o}C. Both the localization and the reduced size of Ge-ncs formed within the sample region co-implanted with Si are observed, as well as the nucleation of mixed Ge/Si nanocrystals containing structural point defects and stacking faults. Although it was found that the Si co-implantation affects the crystallinity of the formed Ge-ncs, this technique can be implemented to produce size-selective and depth-ordered nanostructured systems by controlling the spatial distribution of diffusing Ge. We illustrate this feature for Ge-ncs embedded within a single SiO_2 monolayer, whose diameters were gradually increased from 1 nm to 5 nm over a depth of 100 nm.

Keywords: Transmission electron microscopy, Ge diffusion, Si and Ge nanocrystals, ion implantation, atom ordering.

I. Introduction

The visible (1.12 eV) and near-infrared (0.66 eV) optical bandgaps of silicon and germanium make these elements attractive for applications in photovoltaics (PV). [1, 2] When Si and Ge nanocrystals (Si-ncs and Ge-ncs) are synthesized inside a silicon dioxide layer, the range of their optical absorption can be extended over the sun's whole emission spectrum, and multiple exciton generation (MEG) can greatly reduce energy losses. [3-5] This light-to-current conversion efficiency of Ge-nc and Si-nc strongly depends on the geometrical dimensions and the crystallinity of the formed nanoparticles, as well as their depth distribution inside the active layer of the PV cell. [6]

To optimize both light absorption and photocurrent extraction, stacked nanoparticles arranged inside a single monolayer have been suggested. [7] Nevertheless, the design of such architecture is very challenging for group IV nanostructured systems, notably because Si-ncs and Ge-ncs form at temperatures higher than 800 °C, [8, 9] for which strong thermal diffusion effects can be activated. [10, 11] In particular, the arrangement of Si-ncs and Ge-ncs inside thin SiO_2 films requires the development of efficient methods that enable us to control the atom diffusion mechanisms at the nanoscale and permit the growth of nanoparticles in predetermined locations. In Ge-based fused silica glass heated to temperatures higher than 900 °C, it was established that a reduction of Ge thermal diffusion is also essential to prevent Ge outgassing. [13-15] This effect was found to be responsible for critical Ge desorption, leading to the formation of large nanoscale cavities and the disappearance of Ge-ncs. [12-19] Our recent investigations of mixed Ge/Si and Si-enriched systems prepared by ion implantation have shown the occurrence of a trapping mechanism of diffusing Ge atoms by Si excess atoms and/or Si dangling bonds, which can strongly reduce Ge mobility during thermal annealing. [15-18] The methods we have implemented consist of Ge ion implantation performed into unsaturated SiO_2 targets, or conducted after co-implantation of Si ions into fused silica films. Both techniques offer a better monitoring of the Ge-nc nucleation process, with the possibility to produce Ge-ncs of specific sizes in predetermined sample regions. [15] However, the presence of Si excess atoms in the sample regions where these Ge-ncs have growth and/or agglomerated raises some central questions regarding their chemical composition and their crystallinity. The presence of Si impurities inside the formed Ge-ncs is strongly suspected, due to the poor mobility of Si ions compared to the one of Ge, [10] as well as the high rate of chemical Ge-Si bonds formation in Si-enriched systems implanted with Ge. [15, 16]

The objective of our present work is threefold: (i) demonstrate that a SiO_2 sublayer co-implanted with Si can act as a diffusion barrier for Ge, (ii) characterize the geometry and crystallinity of the formed Ge and Ge/Si aggregates, and (iii) showing how Si co-implantation can be used to design size-selected dispersed Ge nanoparticles inside a submicrometric SiO_2 monolayer. To this end, we conducted a comparative analysis between one SiO_2/Si sample implanted with Ge^+ ions and co-implanted with Si^+ ions (labelled 'Ge/Si sample'), and one sample only implanted with Ge ('Ge sample'). Our experimental investigations include observations by transmission electron microscopy (TEM) and energy dispersive spectroscopy (EDS) supported by Monte-Carlo calculations, as well as complementary measurements by

Raman and Rutherford Backscattering Spectroscopy (RBS). In addition to evidence the blocking of Ge by the co-implanted Si sublayer, we characterized the effects of such a diffusion barrier on both the size and the nature of the formed nanoclusters.

II. Experiment

Silicon dioxide layers (~ 200 nm thickness) were thermally grown on (100) silicon wafers by dry oxidation, performed at 1100 °C under 4.3 grade oxygen flux. $^{74}Ge^+$ ions were implanted into SiO_2/Si samples at an ion energy of 160 keV and a fluency of $1.5x10^{17}$ ion/cm^2, using the IMC commercial implanter available at INRS center. Si co-implantation experiments were conducted before Ge^+ implantation in the Ge/Si sample, for an ion implantation dose of $8.0x10^{16}$ ion/cm^2, using a 35 kV ion beam of isotopic $^{30}Si^+$, delivered by a 2 MV Tandetron accelerator, available at LARN – University of Namur (Belgium). This silicon isotope was preferred to $^{28}Si^+$ to facilitate the distinction between implanted Si ions and Si atoms nominally present within the SiO_2 film. According to Stopping Range of Ions in Solids and TRansport of Ions in Matter (SRIM-TRIM) calculations, [20] the projected ranges of normal incident 160 keV Ge^+ ions and 35 keV Si^+ ions into a SiO_2 target are found to be 90 nm and 50 nm, with maximum penetration depths of 200 nm and 120 nm, respectively. These values account for surface erosion and volume expansion effects, which can be estimated from the ion sputtering yield (given by SRIM) and the amount of ions introduced into the target. [13-18] After implantation, all studied specimens were annealed inside a quartz tube furnace heated at 1100 °C for 1 h, in ultra-high purity N_2 atmosphere. The doses of implanted $^{74}Ge^+$ and $^{30}Si+$ were verified by RBS at LARN using a 2 MeV He^+ beam.

All the studied samples were prepared for TEM imaging along their cross-sectional direction, using conventional techniques of mechanical polishing and ion thinning carried out with a Gatan model 691 precision ion polishing system. Bright-field (BF) imaging, and high-resolution TEM and EDS measurements were conducted on a JEOL JEM2100F microscope, with an electron beam voltage of 200 kV. Backscattering micro-Raman measurements were performed with the 514 nm laser excitation, using a confocal Renishaw RM 3000 spectrometer equipped with a digital camera and a ×50 objective lens of 0.75 numerical aperture.

III. Results and discussion

Figure 1a shows the cross-sectional TEM micrograph of a sample implanted with Ge and co-implanted with Si (Ge/Si sample), while figure 1b displays the one related to the sample implanted only with Ge (Ge sample). The top of these images corresponds to the sample surface (where impinging ions have penetrated) and the bottom to the Si substrate. Dark clusters observed inside SiO_2 after thermal annealing indicate that a significant fraction of the implanted species has precipitated into nanoparticles. To simplify the analysis of the observed objects, we divided their depth-distribution in three different zones, labelled «A» between 20 and 50 nm depths, «B» between 50 and 80 nm, and «C» between 80 and 180 nm, respectively. Both dimension and shape of the formed nanoparticles are observed to be very different in these two samples. While the size of the nanoclusters observed in zone B is maximum in the pure Ge sample (Fig. 1b), it is minimum in the Ge/Si sample (Fig. 1a). These important features will be analyzed and discussed in a later paragraph of this section (see figures 2 and 3).

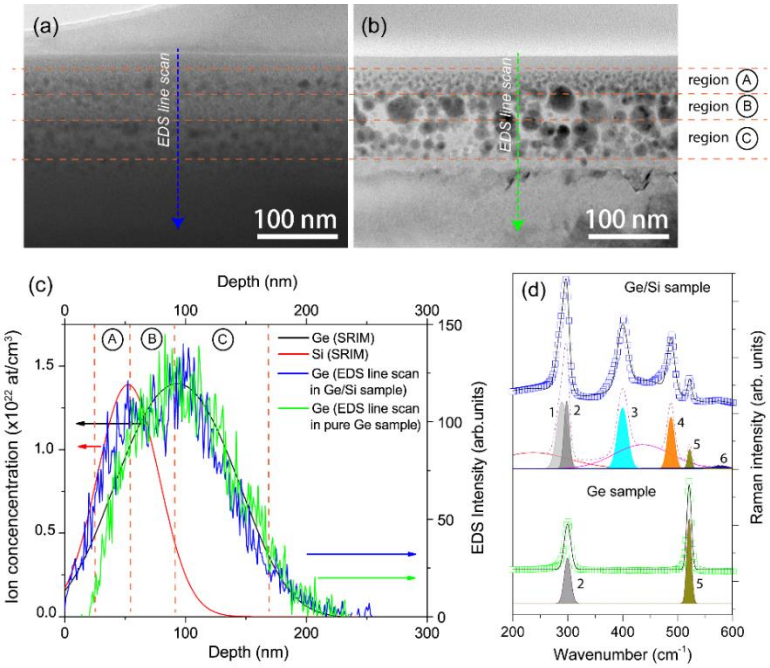

Figure 1: BF TEM images of the Ge/Si sample (a) and Ge sample (b). EDS line scans of the Ge content measured in each sample and compared with the implantation profiles predicted by SRIM-TRIM (c). Raman spectra recorded in Ge/Si and Ge samples (d).

According to the depth-profiles of implanted Si (drawn in red on figure 1c) and the one of implanted Ge (black line), calculated using SRIM-TRIM simulations: [14, 15, 20] zone A refers to a sample region where the concentration of implanted Si is higher than the concentration of implanted Ge; zone B, to a region where both concentrations of implanted Si and Ge are roughly equivalent; and zone C, to a region where the concentration of implanted Si is lower than the concentration of implanted Ge. After integrating the ^{30}Si depth-profile over regions A and B and comparing its value calculated over the whole SiO_2 layer, we find that about 80% of the co-implanted Si is located in the first 80 nm of the Ge/Si sample. On the other hand, the surface density of Ge measured in the Ge sample after annealing is 1.44×10^{17} at/cm^2, which corresponds to 96 % of the Ge dose nominally introduced by ion implantation into the target.

The EDS line scans of the Ge content measured along the two directions indicated by vertical arrows on figures 1a and 1b are superimposed on the SRIM-TRIM Si and Ge depth-distributions on figure 1c. Close to the surface of the Ge/Si sample, an accumulation of Ge is clearly detected in the region containing co-implanted Si, whereas a significant decrease in Ge concentration is reported in the Ge sample, due to Ge desorption effects. [10-19] These two features are supported by figures 1a and 1b, showing the presence of small dark nanograins within the first 25 nm of the Ge/Si sample, and the absence of such nanoscale objects in the pure Ge sample. Since the Ge atoms detected in the vicinity of the Ge/Si sample's surface are located closer than the Ge ions introduced into the SiO_2 layer, they can be associated with implanted Ge ions that have diffused towards the top of the sample. In figure 1c, we observe that after thermal treatment, their depth-distribution is centered with respect to the depth-profile of co-implanted Si. As the motion of implanted Si during annealing can be neglected with respect to the one of Ge, [10] this means that the Ge retained within the first eighty nanometers of the Ge/Si sample mainly originates from Ge diffusing atoms that have been blocked by the co-implanted Si ions, in agreement with the Ge-Si trapping mechanism evoked in Refs. [15, 16]. As indicated by complementary RBS analyses conducted on SiO_2 thin films of 300 nm thickness, thermally grown by wet oxidation and implanted with Ge of 230 keV, Ge ions may also diffuse towards the SiO_2/Si interface during thermal annealing (see an example of Ge in-depth diffusion in figure 4). This effect has already been reported by Markwitz *et al* in wet SiO_2 films, [11] but it is not clearly evidenced in the Ge sample (figure 1c), where the shape of the Ge depth-profile measured by EDS is closer to the Ge concentration distributions reported by Minke. [10] The smaller diffusion lengths of Ge observed in our samples are due most likely to the presence of a greater concentration of Si dangling bonds in the silicon oxide matrix, as previously measured by X-ray photoelectron spectroscopy in dry oxide films prepared in our laboratory. [18] Nevertheless, we anticipate that the blocking of diffusing Ge by co-implanted Si should also reduce the in-depth diffusion of Ge in Ge/Si sample (as evidenced in wet SiO_2 films where Si has been co-implanted on both sides of the Ge distribution, inset of figure 4). This could explain why the Ge concentration measured by EDS in region C (blue line) appears to be slightly smaller than the one measured in the Ge sample (green line) in figure 1c.

The formation of Ge-Si chemical bonds resulting from Ge-Si trapping is also evidenced in figure 1d, which shows the Raman signatures of the Ge/Si sample (top) and pure Ge sample (bottom). In agreement with previous studies, [16, 21-23] the optical vibration modes observed after spectral deconvolution are assigned to: Ge-Ge chains containing Si impurities (peak 1, around 290 cm^{-1}), pure Ge-Ge phonon (peak 2, around 295 cm^{-1}), Ge-Si phonon (peak 3, around 400 cm^{-1}), Si-Si phonon (peak 4, around 490 cm^{-1}) and Ge-Ge two-phonon mode (peak 6, around 580 cm^{-1}). The peak observed at 521 cm^{-1} (peak 5) corresponds to the TO phonon mode of the Si (001) substrate. Its wavenumber is similar in the two studied samples. This mode contributes to the spectral signature of each system because the penetration depth of the Raman probe is around 1.5 µm, [24] which is quite larger than the thickness of the thermally growth SiO_2 layer, between 150 and 200 nm. As expected in nanocluster systems due to quantum confinement effects, [24-26] peaks 2 and 3 are redshifted by ~2-5 cm^{-1} with respect to their positions measured in bulk materials. The greater redshift of 30 cm^{-1} reported

for the wavenumber of peak 4 with respect to the position of peak 5 (521 cm^{-1}) is due to the additional contribution of isotopic effects, [27, 28] which means that most of the Si-ncs nucleated in Ge/Si sample contain ^{30}Si-^{30}Si chemical bonds.

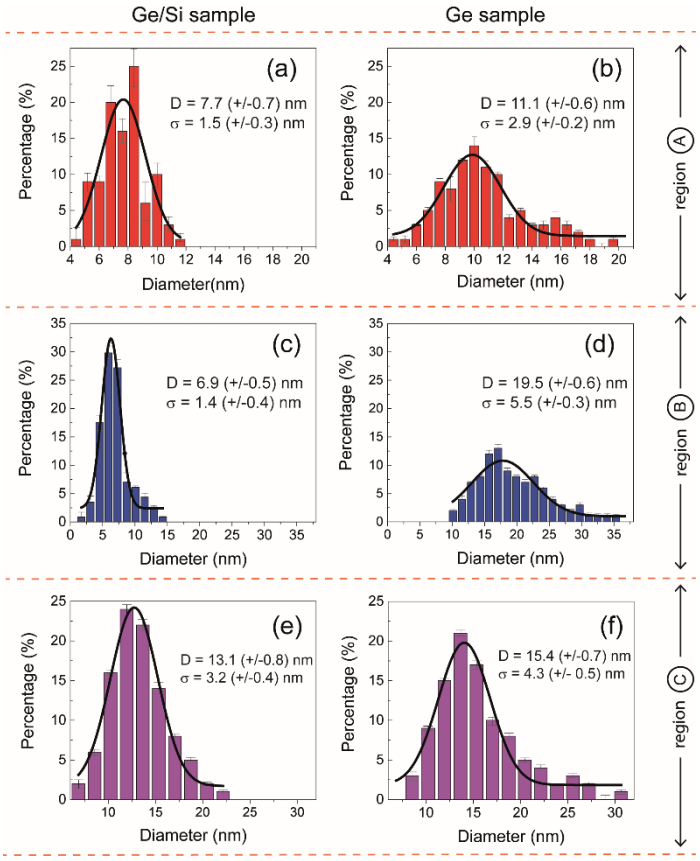

Figure 2: Size-dispersion of the nanoparticles formed in the different regions of the Ge/Si sample (on the left) and pure Ge sample (on the right).

The size distribution of the nanocrystals as measured by TEM in each sample region is presented for Ge/Si and Ge samples, in figures 2a/2c/2e and figures 2b/2d/2f, respectively. In the pure Ge sample, larger nanoclusters generally form in the sample regions where the local concentration of implanted Ge is highest. Such a feature is consistent with Ge-ncs synthesized at higher ion implantation doses, [24, 29] although this increase in size can also strongly depend on the annealing temperature and the presence of chemical dangling bounds inside the silicon oxide matrix. [17, 18, 21, 26]

The average diameters (D) and size-dispersions (σ) of the nanoclusters measured by TEM in Ge/Si and Ge samples are reported in figure 2 in each observation zone. Our statistical analyses were conducted on 100-200 nanoscaled objects, spatially distributed inside rectangular parallelepipeds having a constant thickness of ~10 nm, with base areas of 300 × 50 nm^2 (for zone A), 300 × 70 nm^2 (zone B), and 300 × 100 nm^2 (zone C). The vertical bars reported on the top of each histogram refer to the accuracy of the nanoparticle size measurements, which is +/- 0.25 nm for the Ge sample and +/-0.50 nm for the Ge/Si sample, respectively. The data shown in figure 2 indicate that except in zone C, where the very low concentration of co-implanted Si in the Ge/Si sample makes this region comparable to the one of the Ge sample, both the size and the size-dispersion of the nanoparticles formed in regions A and B are significantly reduced in the presence of co-implanted Si. As already mentioned,

[15-18] this results from a strong decrease of the Ge thermal diffusion coefficient in Si-implanted or Si-enriched SiO_2. Using the relationship established by Maeda, who determined that the average size of Ge-ncs varies as the cubic root of the diffusion coefficient, [30] the reduction in nanoparticle dimension reported in the Ge/Si sample could be associated with a reduction of the Ge thermal diffusion by up to 75 % in zone A, and more than 95 % in zone B. Such features mean that only several percent of excess Si inside silicon oxide are sufficient to block the Ge diffusion. These values are quantitatively consistent with the increase in retained Ge atoms that have been previously measured in Ge/Si co-implanted systems, [15-16] and silicon oxide films containing a greater concentration of Si dangling bonds. [18]

The critical effect induced by co-implanted Si on the nanoparticle dimensions raises some important questions regarding the structure and chemical composition of the formed clusters. As presented in figure 3, high-resolution TEM imaging was conducted in each sample region to shed light on the microstructure of the formed nanoclusters. The average distances measured between the observed atomic planes, identified as interplanar {111} spacings, [14] are reported on each micrograph. In agreement with figures 1a-b and figures 2a-d, the size and crystallinity of the nanoparticles formed in regions A and B (figures 3a-d) are found to be quite smaller and more disordered in the Ge/Si sample than in Ge sample. In pure Ge sample, the formed nanoparticles are very similar to the Ge-ncs observed in SiO_2/Si systems implanted at equivalent Ge concentration and annealed at 1100 °C for 1 h. The formation of dislocations, stacking faults and point defects inside the observed Ge-ncs can be attributed to the coalescence of small nanoclusters into larger aggregates as well as volume expansion effects. [31]

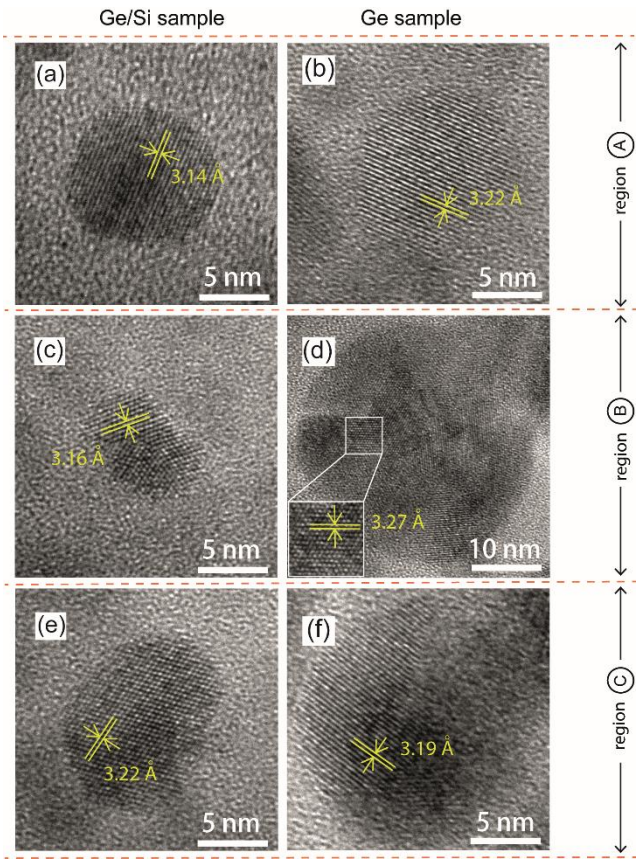

Figure 3: High-resolution TEM micrographs of nanoparticles formed at different depths in the Ge/Si sample (left) and Ge sample (right).

The d-spacing between each atom plane is also ~2-3% smaller in SiO_2 sublayers where Si ions have been co-implanted (figures 3a and 3c). On the other hand, no significant variation regarding the size and inner atomic ordering of the nanoclusters located in zone C was observed between the two studied samples (figure 3e and figure 3f), as expected for host matrices into which only a few amount or no co-implanted Si ions have penetrated (figure 1c). These results are consistent with the predominant formation of Ge/Si nano-alloys (Ge/Si-ncs) in the regions A and B of the Ge/Si sample, and the principal formation of pure Ge-ncs in region C. [17, 32, 33] Hence, the decrease in lattice parameter that is measured in the Ge/Si sample is consistent with higher rates of formation of Ge-Si and Si-Si chemical bonds, whose interatomic distance is ~3 % smaller than for Ge-Ge. [34] Since the displacement of implanted Si during thermal annealing is less than a few nanometers, [10] we also stipulate that the Raman signature of Si-Si chemical bonds observed in figure 1d (peak 4) originates from Si-ncs located in the regions A and B of the Ge/Si sample. The presence of a compressive mechanical stress exerted by the surrounding SiO_2 matrix on the formed nanocrystals, [14, 32, 35] as well as its release for Ge-ncs containing Si, [33] make the use of Vegard's laws irrelevant to determine the relative concentration of Ge/Si from the lattice parameters given in figure 3. [34] Nevertheless, using the SRIM depth-profiles reported in Fig. 1c and the Raman measurements displayed in figure 1d, we infer that the Si content inside the Ge/Si nanoclusters shown in figures 3a and 3c exceeds 50%.

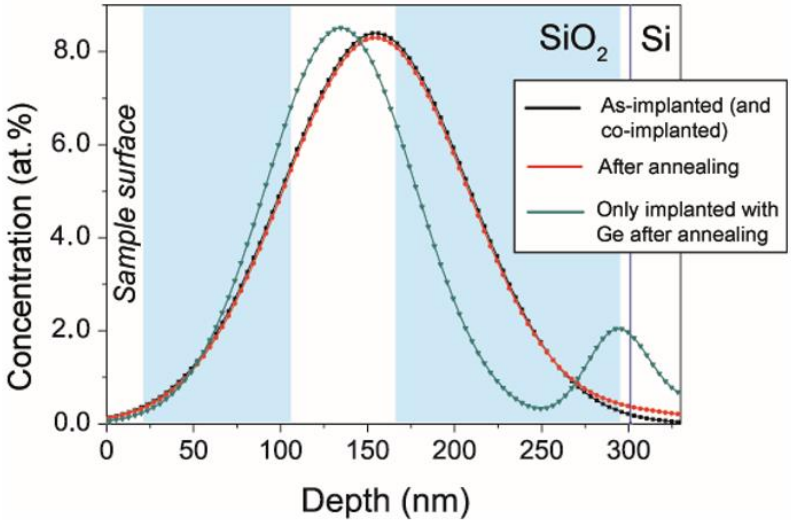

Figure 4: RBS analyses showing the blocking of the Ge diffusion in wet SiO_2 films using two diffusion barriers of co-implanted Si, located in both sides of the implanted Ge depth-distribution.

After demonstrating that the co-implanted of Si can be used to create a thermal diffusion barrier for Ge and reduce the size of the formed Ge and Ge/Si nanoclusters, we exploited this technique to produce nanoparticles of specific dimensions, selectively distributed within a commercial SiO_2 thin film of 350 nm thickness, thermally grown by wet oxidation. In these experiments, one first silicon co-implantation was performed at an ion dose of 6×10^{16} Si^+/cm^2 and an energy of 170 keV, followed by an implantation of Ge at an ion dose of 8×10^{16} Ge^+/cm^2 and an energy of 230 keV, and a second co-implantation of Si at an ion dose of 6×10^{16} Si^+/cm^2 and an energy of 35 keV. This sample is then annealed for 1 h at 1100 °C and compared to a sample only implanted with Ge annealed in same conditions. The projected ranges of Si ions

estimated by SRIM-TRIM for acceleration voltages of 35 kV and 170 kV are determined to be around 50 nm and 230 nm, respectively. [20] For the Ge implantation at 230 keV, the Ge distribution is centered with respect to an averaged depth of ~170 nm. The implantation parameters chosen in these experiments were set to generate a variation of the Si concentration inside the implanted SiO_2 layer, in order to monitor both the thermal diffusion of Ge toward the sample surface and the Ge in-depth diffusion.

Figure 4 illustrates the results of three RBS analyses performed on the sample only implanted with Ge after annealing, and the sample implanted with Ge and doubly co-implanted with Si, before and after annealing. The light blue areas in the both sides of the implanted Ge distribution denote sample regions where Si ions have been introduced. After thermal treatment, while the Ge is found to diffuse simultaneously towards the sample surface and the SiO_2/Si interface in the pure Ge sample, its depth-distribution remained practically unchanged in the sample doubly co-implanted with Si. We infer that such a feature results from the blocking of diffusing Ge by the two Si diffusion barriers, located between 20-100 nm and 180-250 nm depths, respectively.

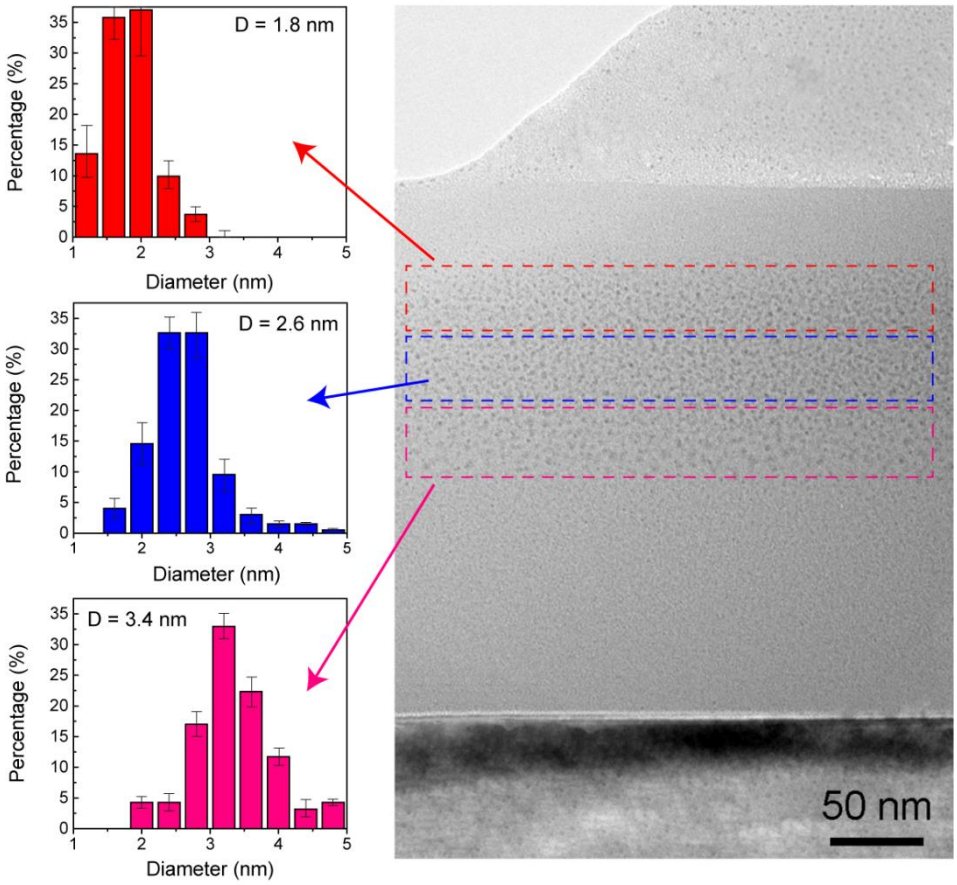

Figure 5: TEM micrograph and analysis, evidencing the synthesis of vertical stacked SiO_2 sublayers containing Ge-based nanocrystals of uniform sizes, obtained by multiple co-implantations of silicon.

The doubly co-implanted sample was also characterized by TEM after annealing. The micrograph shown in figure 5 reveals the formation of nanoclusters relatively uniform, whose dimensions increases continuously with their position in depth. The measurement of the nanoparticle dimensions is reported with an accuracy of +/- 0.25 nm. Small Ge-ncs and/or

Ge/Si-ncs are observed in the vicinity of the sample surface, while larger nanoscale aggregates are observed in deeper sample regions. Average diameters (D) of the observed nanocrystals are found to be: D = 1.8 (+/- 0.2) nm, between 40 and 80 nm depths, D = 2.6 (+/- 0.3) nm, between 80 nm and 120 nm, and D = 3.4 (+/- 0.2) nm, between 120 nm and 160 nm, with standard deviations of 0.34 nm, 0.65 nm and 0.77 nm, respectively. Such a vertically stacked arrangement of nanoparticles over a single SiO_2 monolayer illustrates nanostructured systems containing Ge-based nanoparticles of specific dimensions. This example allows to implement Si co-implantation to design new advanced and monolithically integrated devices, by controlling the thermal diffusion of Ge.

IV. Conclusions and Perspectives

We investigated both the size and the crystallinity of Ge and Ge/Si nanoclusters synthesized by Ge^+ and Si^+ ion implantation into SiO_2. Our work highlights the reduction of the Ge thermal diffusion inside SiO_2 sublayers co-implanted with Si, which can be used to control the size of the formed nanoclusters. Si-enriched regions were found to act as diffusion barriers for Ge atoms and prevent Ge desorption during thermal annealing conducted at 1100 ^oC. It is found that the nanocrystals formed in the sample region co-implanted with Si are smaller and contain a greater concentration of structural defects, due to the presence of Si impurities inside Ge-ncs and the formation Ge/Si nanoclusters. The Si co-implantation technique can be implemented to achieve stacked nanostructured Ge-based systems, selectively depth-distributed as a function of their sizes inside single SiO_2 monolayers. These new advanced devices can be used for applications in photonics and photovoltaics, where the development of monolithically integrated systems allows the fabrication of more compact and more performant devices.

ACKNOWLEDGMENT

This work was supported by the IX^{th} Québec-Wallonie-Bruxelles Workgroup (project 09.801). F.R. acknowledges PRIMA Québec for financial support (Project R10-006), as well as NSERC for funding through an individual Discovery Grant and partial salary support from the Canada Research Chairs program. F.R. is also grateful to the Government of China for a Chang Jiang (short term) scholar award and Sichuan Province for a short term 1000 talent award.

REFERENCES

[1] Green, M. A., Bremner, S. P. (2017). *Energy conversion approaches and materials for high-efficiency photovoltaics*. Nature Materials, 16, 23–34. https://doi.org/10.1038/nmat4676

[2] Yedji, M., Demarche, J., Terwagne, G., Delamare, R., Flandre, D., Barba, D., Koshel, D., Ross, G. G. (2011). *Method for fabricating third generation photovoltaic cells based on Si quantum dots using ion implantation into SiO_2.* J. Appl. Phys., 109(8), 084337. https://doi.org/10.1063/1.3575325

[3] Beard, M. C., Knustsen, K. P., Yu, P., Song, Q., Luther, J., Ellingson, R., Nozik, A. J. (2007). *Multiple exciton generation in colloidal silicon nanocrystals*. *Nano Lett.*, *7*, 2506–2512. https://doi.org/10.1021/nl071486l

[4] Trinh, M. T., Limpens, R., de Boer, W. D. A. M., Schins, J. M., Siebbeles, L. D. A., Gregorkiewicz, T. (2012). *Direct generation of multiple excitons in adjacent silicon nanocrystals revealed by induced absorption.* Nature Photonics, 6(5), 316–321. https://doi.org/10.1038/nphoton.2012.36

[5] Liu, Z., Yang, M., Chen, T. P., Liu, Y., & Zhang, H. Y. (2015). *Dielectric engineering of Ge nanocrystal/SiO_2 nanocomposite thin films with Ge ion implantation: Modeling and measurement.* Materials and Design, 83, 713–718. https://doi.org/10.1016/j.matdes.2015.05.071

[6] Zschintzsch, M., von Borany, J., Jeutter, N. M., & Mücklich, A. (2011). *Stacked Ge nanocrystals with ultrathin SiO_2 separation layers.* Nanotechnology, 22(46), 465302. https://doi.org/10.1088/0957-4484/22/46/465302

[7] Fang, C.-Y., Liu, Y.-L., Lee, Y.-C., Chen, H.-L., Wan, D.-H., & Yu, C.-C. (2013). *Nanoparticle Stacks with Graded Refractive Indices Enhance the Omnidirectional Light Harvesting of Solar Cells and the Light Extraction of Light-Emitting Diodes.* Adv. Funct. Mater., 23(11), 1412–1421. https://doi.org/10.1002/adfm.201201949

[8] Wang, Y. Q., Smirani, R., Ross, G. G., & Schiettekatte, F. (2005). *Ordered coalescence of Si nanocrystals in SiO_2.* Phys. Rev. B*, 71(16), 1–4*. https://doi.org/10.1103/PhysRevB.71.161310

[9] Zhu, J. G., White, C. W., Budai, J. D., Withrow, S. P., & Chen, Y. (1995). *Growth of Ge, Si, and SiGe nanocrystals in SiO_2 matrices.* J. Appl. Phys. 78(7), 4386–4389. https://doi.org/10.1063/1.359843

[10] Minke, M. V., Jackson, K. A. (2005). *Diffusion of germanium in silica glass*. J. Non-Crystalline Solids, 351(27–29), 2310–2316. https://doi.org/10.1016/j.jnoncrysol.2005.04.052

[11] Markwitz, A., Schmidt, B., Matz, W., Grötzschel, R., Mücklich, A. *(1998). Microstructural investigation of ion beam synthesised germanium nanoclusters embedded in SiO_2 layers.* Nucl. Instrum. Methods Phys. Res. B, 142(3), 338–348. https://doi.org/10.1016/S0168-583X(98)00283-3

[12] Beyer, V., von Borany, J. (2008). *Elemental redistribution and Ge loss during ion-beam synthesis of Ge nanocrystals in SiO_2 films*. Phys. Rev. B, 77(1), 014107. https://doi.org/10.1103/PhysRevB.77.014107

[13] Barba, D., Martin, F., Demarche, J., Terwagne, G., & Ross, G. G. (2012). *Nanocavities and germanium nanocrystals produced by Ge ion implantation in fused silica.* Nanotechnology, 23(14). https://doi.org/10.1088/0957-4484/23/14/145701

[14] Li, C., Feng, H., Liu, B., Liang, W., Liu, G., Ross, G. G., Wang, Y., & Barba, D. (2017). *Effect of nanocavities on Ge nanoclustering and out-diffusion in SiO_2.* Nanotechnology, 28(3), 035707. https://doi.org/10.1088/1361-6528/28/3/035707

[15] Barba, D., Demarche, J., Martin, F., Terwagne, G., Ross, G. G. (2012). *Trapping of diffusing germanium by silicon excess co-implanted into fused silica.* Appl. Phys. Lett., 101(14), 143107. https://doi.org/10.1063/1.4757291

[16] Barba, D., Demarche, J., Martin, F., Terwagne, G., & Ross, G. G. (2013). *Control of the Ge nanocrystal synthesis by co-implantation of Si^+.* J. Appl. Phys., 114(7), 074306. https://doi.org/10.1063/1.4817667

[17] Cai, R. S., Wang, Y. Q., Shang, L., Liu, X. H., Zhang, Y. J., Ross, G. G., & Barba, D. (2014). *Inhibitive formation of nanocavities by introduction of Si atoms in Ge nanocrystals produced by ion implantation.* Journal of Applied Physics, 115(20). https://doi.org/10.1063/1.4880661

[18] Barba, D., Cai, R. S., Demarche, J., Wang, Y. Q., Terwagne, G., Rosei, F., Ross, G. G. (2014). *Influence of silicon dangling bonds on germanium thermal diffusion within SiO_2 glass.* Appl. Phys. Lett., 104(11), 111901. https://doi.org/10.1063/1.4868721

[19] Marstein, E. S., Gunnæs, A. E., Serincan, U., Jørgensen, S., Olsen, A., Turan, R., & Finstad, T. G. (2003). *Mechanisms of void formation in Ge implanted SiO_2 films.* Nucl. Instrum. Methods Phys. Res. B, 207(4), 424–433. https://doi.org/10.1016/S0168-583X(03)00965-0

[20] Ziegler, J. F., Ziegler, M. D., Biersack, J. P. (2010). *SRIM – The stopping and range of ions in matter (2010).* Nucl. Instrum. Methods Phys. Res. B, 268(11–12), 1818–1823. https://doi.org/10.1016/j.nimb.2010.02.091

[21] Rodríguez, A., Ortiz, M. I., Sangrador, J., Rodríguez, T., Avella, M., Prieto, A. C., Torres, A., Jiménez, J., Kling, A., & Ballesteros, C. (2007). *Comparative study of the luminescence of structures with Ge nanocrystals formed by dry and wet oxidation of SiGe films.* Nanotechnology, 18(6), 065702. https://doi.org/10.1088/0957-4484/18/6/065702

[22] Pagès, O., Souhabi, J., Torres, V. J. B., Postnikov, A. V., & Rustagi, K. C. (2012). *Re-examination of the SiGe Raman spectra: Percolation/one-dimensional-cluster scheme and ab initio calculations.* Physical Review B, 86(4), 045201. https://doi.org/10.1103/PhysRevB.86.045201

[22] Vasin, A. S., Vikhrova, O. V., & Vasilevskiy, M. I. (2015). *Effects of alloy disorder and confinement on phonon modes and Raman scattering in Si_xGe_{1-x} nanocrystals: A microscopic modeling.* J. Appl. Phys. 115, 143505. Journal of Applied Physics, 118(18), 189902. https://doi.org/10.1063/1.4935816

[24] Barba, D., Martin, F., & Ross, G. G. (2008). *Evidence of localized amorphous silicon clustering from Raman depth-probing of silicon nanocrystals in fused silica.* Nanotechnology, 19(11), 115707. https://doi.org/10.1088/0957-4484/19/11/115707

[25] Mestanza, S. N. M., Rodriguez, E., & Frateschi, N. C. (2006). *The effect of Ge implantation dose on the optical properties of Ge nanocrystals in SiO_2.* Nanotechnology, 17(18), 4548–4553. https://doi.org/10.1088/0957-4484/17/18/004

[26] Faraci, G., Gibilisco, S., Russo, P., Pennisi, A. R., & La Rosa, S. (2006). *Modified Raman confinement model for Si nanocrystals.* Physical Review B - Condensed Matter and Materials Physics, 73(3), 1–4. https://doi.org/10.1103/PhysRevB.73.033307

[27] Barba, D., Koshel, D., Martin, F., Ross, G. G., Chicoine, M., Schiettekatte, F., Yedji, M., Demarche, J., & Terwagne, G. (2010). *Silicon nanocrystal synthesis by implantation of natural Si isotopes.* Journal of Luminescence, 130(4), 669–673. https://doi.org/10.1016/j.jlumin.2009.11.014

[28] Cardona, M. (2000). *Isotopic Effects in the Phonon and Electron Dispersion Relations of Crystals.* Physica Status Solidi (B), 220(1), 5–18. https://doi.org/10.1002/1521-3951(200007)220:1<5::AID-PSSB5>3.0.CO;2-K

[29] Ge, L. H., Wang, C., Cai, R. S., Liang, W. S., Wang, Y. Q., Ross, G. G., & Barba, D. (2017). *Effect of Ge Concentration on the Microstructure of Germanium Nanocrystals Produced by Ion Implantation in SiO_2.* Nanosci. Nanotechno., 17(3), 2196–2200. https://doi.org/10.1166/jnn.2017.12858

[30] Maeda, Y. (1995). *Visible photoluminescence from nanocrystallite Ge embedded in a glassy SiO_2 matrix: Evidence in support of the quantum-conf.* Phys. Rev. B, 51(3), 1658–1670. https://doi.org/10.1103/PhysRevB.51.1658

[31] Zhang, M., Cai, R., Zhang, Y., Wang, C., Wang, Y., Ross, G. G., & Barba, D. (2014). *Evolution of microstructural defects with strain effects in germanium nanocrystals synthesized at different annealing temperatures.* Mat. Char., 93(308), 1–9. https://doi.org/10.1016/j.matchar.2014.03.010

[32] Rodríguez, A., Rodríguez, T., Prieto, Á. C., Jiménez, J., Kling, A., Ballesteros, C., & Sangrador, J. (2010). *Crystallization of Amorphous $Si_{0.6}Ge_{0.4}$ Nanoparticles Embedded in SiO_2: Crystallinity Versus Compositional Stability.* J. Elec. Mat., 39(8), 1194–1202. https://doi.org/10.1007/s11664-010-1254-9

[33] Liu, L. Z., Gao, F., Wu, X. L., Li, T. H., & Chu, P. K. (2009). *Influence of GeSi interfacial layer on Ge–Ge optical phonon mode in SiO_2 films embedded with Ge nanocrystals.* Appl. Phys. Lett., 95(17), 171105. https://doi.org/10.1063/1.3257379

[34] Dismukes, J. P., Ekstrom, L., & Paff, R. J. (1964). *Lattice Parameter and Density in Germanium-Silicon Alloys*. *J. Phys. Chem., 68(10), 3021–3027.* https://doi.org/10.1021/j100792a049

[35] Sharp, I. D., Yi, D. O., Xu, Q., Liao, C. Y., Beeman, J. W., Liliental-Weber, Z., Yu, K.M., Zakharov, D.N., Ager, J.W., Chrzan, D.C., & Haller, E. E. (2005). *Mechanism of stress relaxation in Ge nanocrystals embedded in SiO_2.* Applied Physics Letters, 86(6), 063107. https://doi.org/10.1063/1.1856132

IV.3 Formation of large Ge-ncs by Si co-implantation

We showed that our co-implantation of silicon and germanium ions provides, in well-defined conditions, solutions to control both diffusion and nanoclustering of germanium implanted in a SiO_2/Si film. However, for the photovoltaic application targeted by this work, the key is not only to increase the photogeneration of electron/hole pairs but also to effectively collect them, as discussed in **section II.5**. To improve charge carriers collection, the distance between the source of carriers and their collection must be reduced. In this context, Ge nanocrystals must be formed at the vicinity of the SiO_2/Si interface (~300 nm), therefore increasing the probability of electrons/holes injection into the silicon substrate. As already discussed, optimization of the absorption of solar spectrum requires nanocrystals diameters increasing as a function of the depth to improve conversion efficiency.

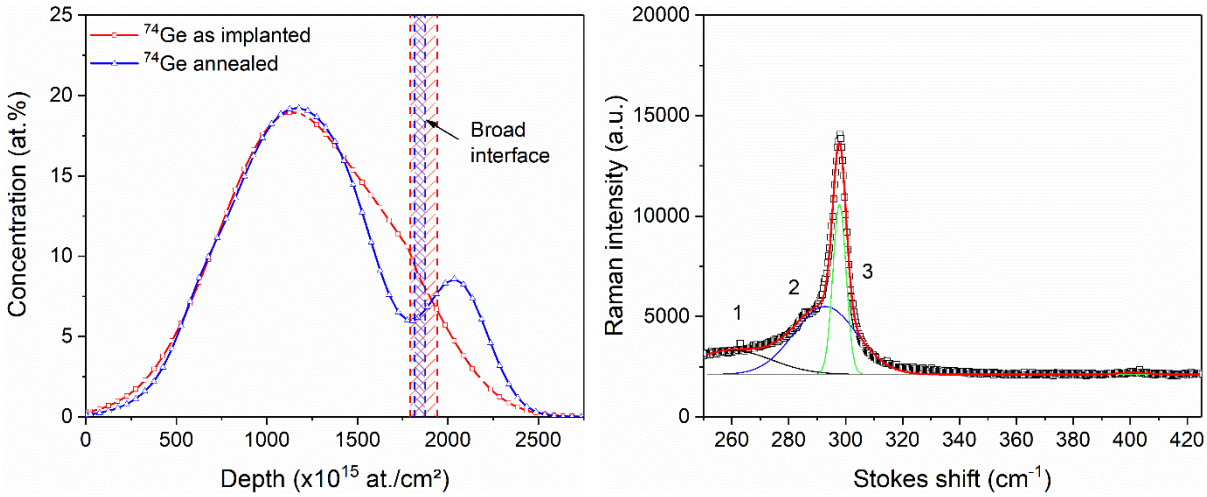

Figure 51 : Ge depth-profiles extracted from RBS spectra before (red) and after (blue) annealing and Raman spectrum after annealing for a sample solely implanted with 2 × 10^{17} Ge/cm² in SiO_2 (300 nm). The formation of Ge-ncs and diffusion are thermally activated (1100 °C, 60'). Measurement conditions: RBS ($E_\alpha = 2\ MeV, \theta = 165°$, incidence 7°, $Q = 10\mu C$), Raman ($\lambda_{Laser} = 514\ nm$, objective lens ×100).

Ge projected ranges closer to the interface have been obtained with an energy of 325 keV, corresponding to an average depth of ~225 nm (~1200 × 10^{15} at./cm²) according to SRIM-TRIM simulations. A high fluence of approximately 2.1 × 10^{17} Ge/cm² was chosen to overtake the diminution of concentration due to straggling at higher energies and to form relatively large nanocrystals. These conditions of implantation correspond to a concentration of approximately 20 at.% at maximum. The formation of Ge-ncs is thermally activated by annealing at 1100 °C for 60 minutes under N_2.

Due to the high Ge fluence, germanium mobility is almost annihilated between the sample surface and the projected range because of ion-induced damage and formation of Ge-Si bonds. Therefore, Ge redistribution only occurs in the second half of the germanium depth-profile, at the vicinity of the SiO_2/Si interface. **Figure 51** shows that, when germanium is implanted close to the SiO_2/Si interface, this interface is perturbed and is no longer a sharp interface but spreads over several tens of nanometers (represented by hashed boxes, 5 nm ≅

33.3 × 10^{15} atoms/cm²), because of damage induced by heavy ions. RBS analyses show that the width of this interface tends to shrink during annealing (**Figure 51**).

Raman measurements performed on this sample (and thereafter co-implanted samples) exhibit up to six peaks in the spectral range of 250 – 425 cm^{-1}. These Raman signatures have already been presented and correspond to a-Ge (peak 1, ∼260 cm^{-1}), Ge-Ge* (peak 2, ∼290 cm^{-1}), Ge-Ge (peak 3, ∼300 cm^{-1}), Ge-^{30}Si (peak 4, ∼391 cm^{-1}), Ge-^{29}Si (peak 5, ∼398 cm^{-1}) and Ge-^{28}Si (peak 6, ∼406 cm^{-1}).

Fluence (at./cm²)	1 (a-Ge)	2 (Ge-Ge*)	3 (Ge-Ge)	4 (Ge-^{30}Si)	5 (Ge-^{29}Si)	6 (Ge-^{28}Si)
0	42134	93448	49341	0	0	1190
3.5 × 10^{16}	170899	211624	170948	39495	22772	16904
9.1 × 10^{16}	263585	365305	340901	110796	34119	99557

Table 4 : Integrals of the Raman peaks for samples implanted with 2.1 × 10^{17} Ge/cm² and co-implanted with ^{30}Si whose fluence varies from 0 to 9.1 × 10^{16} Si/cm².

For the sample presented in **Figure 51**, solely implanted with germanium, only Raman signals related to Ge nanocrystals are observed. As shown in **Table 4**, the formation of contaminated nanocrystals (Ge-Ge*, peak 2) dominates the formation of pure Ge nanocrystals. These observations agree with RBS spectra highlighting the poor Ge mobility in this sample due to the high density of Ge-Ge and Ge-Si chemical bonds at high Ge fluences, and with the reduction of Ge diffusion associated with the increase of Ge fluence highlighted in **article I**.

To ensure the formation of a size gradient with small nanocrystals closer to the sample surface and large nanocrystals in the vicinity of the SiO_2/Si interface, a silicon co-implantation localized between the sample surface and the germanium projected range have been performed. ^{30}Si ions have been implanted prior to Ge ions with an energy of 100 keV and a measured fluence ranging from 3.5 to 9.1 × 10^{16} Si/cm². In these conditions, silicon projected range corresponds to ∼140 nm (∼500 × 10^{15} at./cm²). If silicon co-implanted behind the germanium projected range drastically reduces the redistribution of Ge due to trapping effects and damages (see **article III**), Si co-implanted in the first half of the Ge depth-profile is expected to force the formation of small nanocrystals in this part if the Ge profile, while letting germanium more mobile and likelier to form large nanocrystals closer to the SiO_2/Si interface. ^{30}Si depth-profiles have been verified by RNRA using the nuclear reaction already presented in the 3rd manuscript: ^{30}Si(p,γ)^{31}P at 620 keV.

Figure 52 shows that, more than just limiting Ge mobility in the regions where both implantation profiles overlap, Si co-implantation surprisingly enhances Ge redistribution in the oxide region between Si projected range and the SiO_2/Si interface. However, if we think once again in terms of recoiled atoms, ^{30}Si implantation will mostly give rise to an oxygen redistribution by kicking O atoms deeper in depth, *i.e.,* in the oxide region where germanium concentration is maximum. Moreover, the ratio ^{30}Si/Ge and the overlapping of both depth-profiles is weak in this region, limiting the efficacity of Ge/^{30}Si trapping effects.

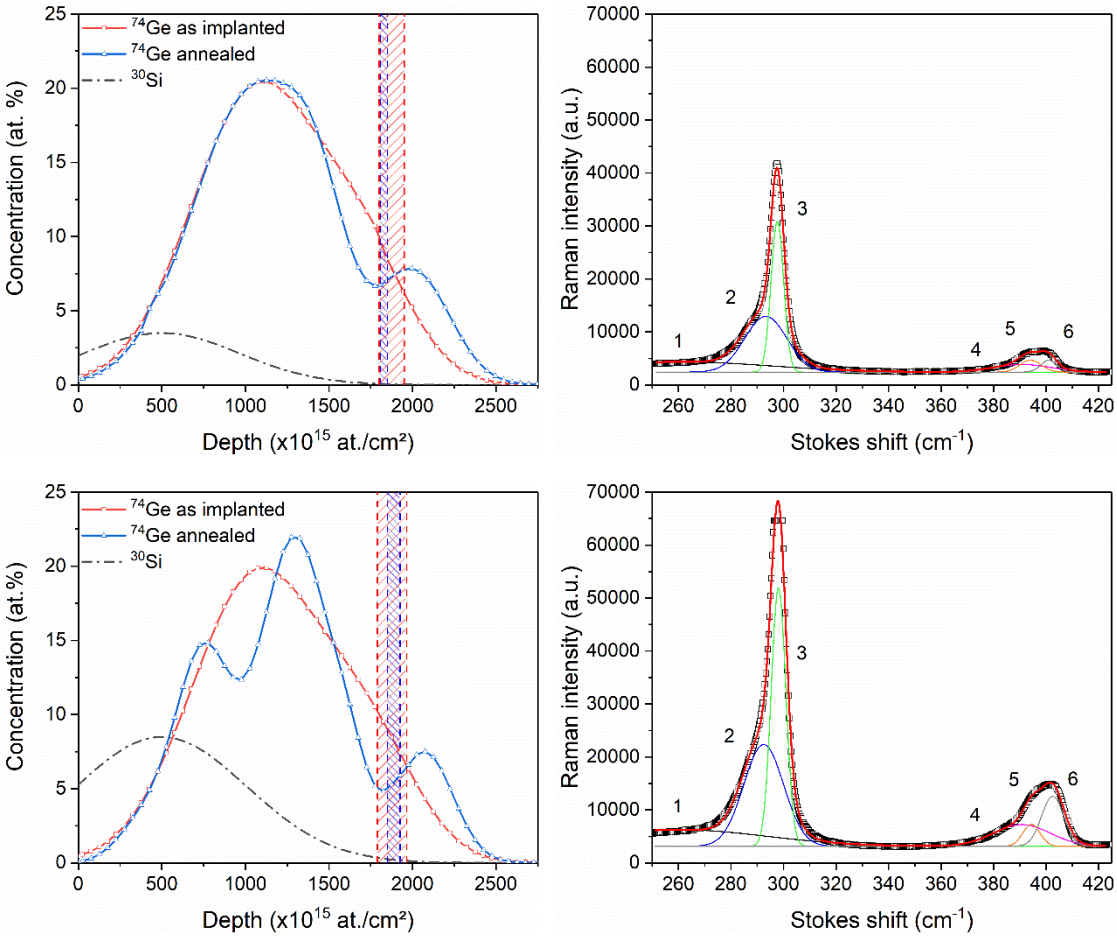

Figure 52 **:** Ge depth-profiles extracted from RBS spectra before (red) and after (blue) annealing and Raman spectra after annealing for samples co-implanted with 3.5 (top) and 9.1 × 10^{17} ^{30}Si/cm² (bottom). Measurement conditions: RBS ($E_\alpha = 2\ MeV, \theta = 165°$, incidence 7°, $Q = 10\mu C$), Raman ($\lambda_{Laser} = 514\ nm$, objective lens ×100).

As previously shown, germanium mobility is enhanced in the presence of oxygen, and especially in an oxygen-saturated SiO_2 layer, which is already observed for not co-implanted sample (**Figure 51**). As RBS results suggest that ^{30}Si co-implantation accentuates oxygen redistribution in depth, this leads to an enhancement of germanium mobility while ^{30}Si fluence increases. Raman spectra show that the density of Ge-Ge and Ge-Ge* signatures increase with the ^{30}Si fluence with a greater growth of pure nanocrystals compared to Si-containing nanocrystals (Ge-Ge*, peak 2). This agrees with an enhancement of germanium mobility, resulting in a more efficient formation of large nanocrystals. Raman spectra obviously indicate that the density of Ge-Si chemical bonds (peaks 4, 5 and 6) increases as the ^{30}Si fluence increases, with a nearly linear dependence on Ge-^{30}Si bonds (**Table 4**). The increase of the density of Ge-^{30}Si bonds is mainly due to the co-implantation of ^{30}Si ions. The increase of Ge-^{28}Si and Ge-^{29}Si bonds is probably due to an increase of irradiation-induced damage and to the inability of the SiO_2 layer to fully restore its stoichiometry because of the silicon excess brought by the co-implantation of ^{30}Si. This leads to an increase of interstitial atoms (not necessarily ^{30}Si) free to chemically bind to germanium.

XRD measurements, focused on high intensity Ge (111) signal around 27.4°, confirm that the average diameter of germanium nanocrystals drastically increases with the fluence of co-implanted ^{30}Si. The average diameters reported in **Figure 53** have been estimated using Scherrer's formula (**equation III.46**).

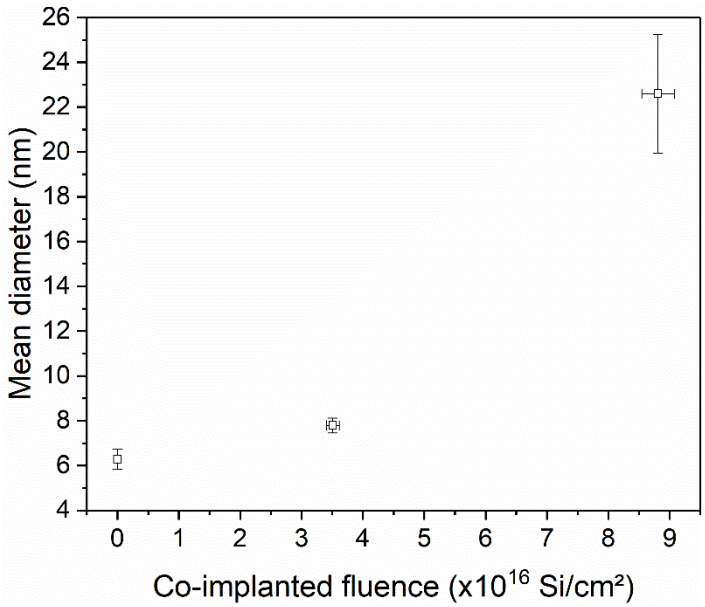

Figure 53 : Ge nanocrystals average diameter as a function of co-implanted Si fluence estimated by XRD measurements, using Scherrer's equation (**Equation III.46**), with Cu Kα source (1.5406 Å x-rays, rotating sample, inclination 2° to limit substrate contribution).

As already discussed in **article IV**, TEM measurements confirm that Ge nanocrystals are smaller in the oxide regions presenting a silicon excess (**Figure 54**), *i.e.,* oxide regions where both implantation profiles overlap or the regions most impacted by irradiation-induced damage.

TEM measurements show that the sample solely implanted with Ge ions already presents a size gradient with small nanocrystals closer to the sample surface and larger quantum dots in depth. The band of quantum dots extends to the SiO_2/Si interface, confirming the right choice of implantation energies.

On the other hand, **Figure 54** confirms the higher Ge mobility in depth observed by RBS. These results confirm that co-implantation of silicon in the conditions described above could be used to modify the distribution of nanocrystals sizes as a function of depth. This Si co-implantation enables to achieve very large nanostructures in depth with small nanocrystals closer to the sample surface. However, the conditions of implantation (energy, fluences) of both species could be optimized to remove larger nanocrystals closer to the oxide/substrate interface. **Figure 54** shows that a sublayer of smaller Ge-ncs remains close to the interface, while the aim is to form a size gradient of quantum dots increasing as a function of depth. This could be achieved by optimizing the conditions of implantation and by implanting in a thinner oxide layer. Lower fluences must also be considered, as the formation of quantum dots as large as 50 nm are not necessary according to the gap/size relation presented in **Figure 11**, as the confinement effect is lost at such diameters.

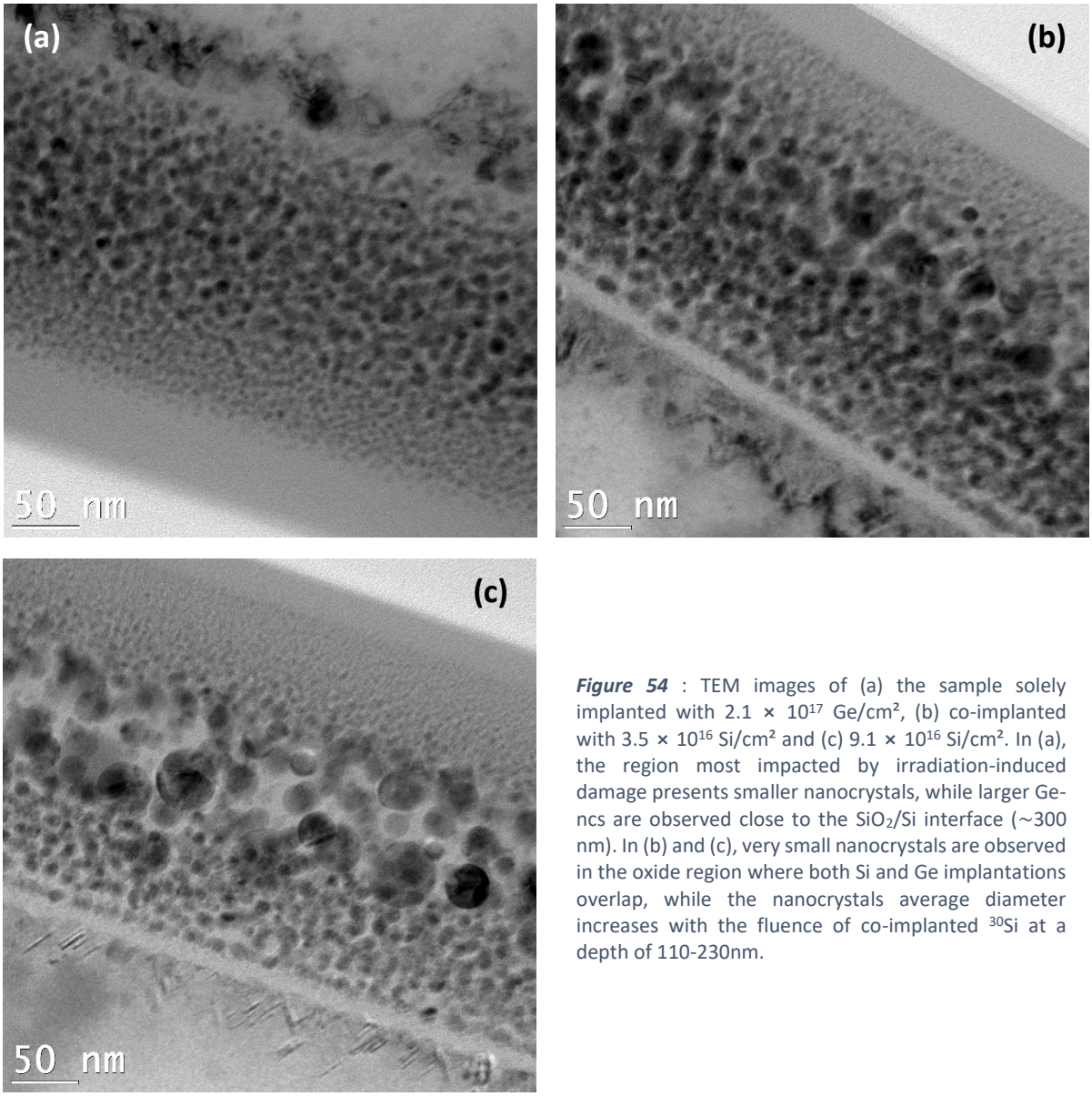

Figure 54 : TEM images of (a) the sample solely implanted with 2.1 × 10^{17} Ge/cm², (b) co-implanted with 3.5 × 10^{16} Si/cm² and (c) 9.1 × 10^{16} Si/cm². In (a), the region most impacted by irradiation-induced damage presents smaller nanocrystals, while larger Ge-ncs are observed close to the SiO_2/Si interface (∼300 nm). In (b) and (c), very small nanocrystals are observed in the oxide region where both Si and Ge implantations overlap, while the nanocrystals average diameter increases with the fluence of co-implanted ^{30}Si at a depth of 110-230nm.

If the energy of ^{30}Si ions is incremented, the overlapping of both Ge and Si depth-profiles increases. **Figure 55a** shows depth-profiles extracted from RBS spectra of a sample co-implanted with Si of 140 keV instead of 100 keV, for a fluence of 1.5 × 10^{17} Si/cm². In these conditions, TRIM simulations indicate a ^{30}Si projected range of ~196 nm.

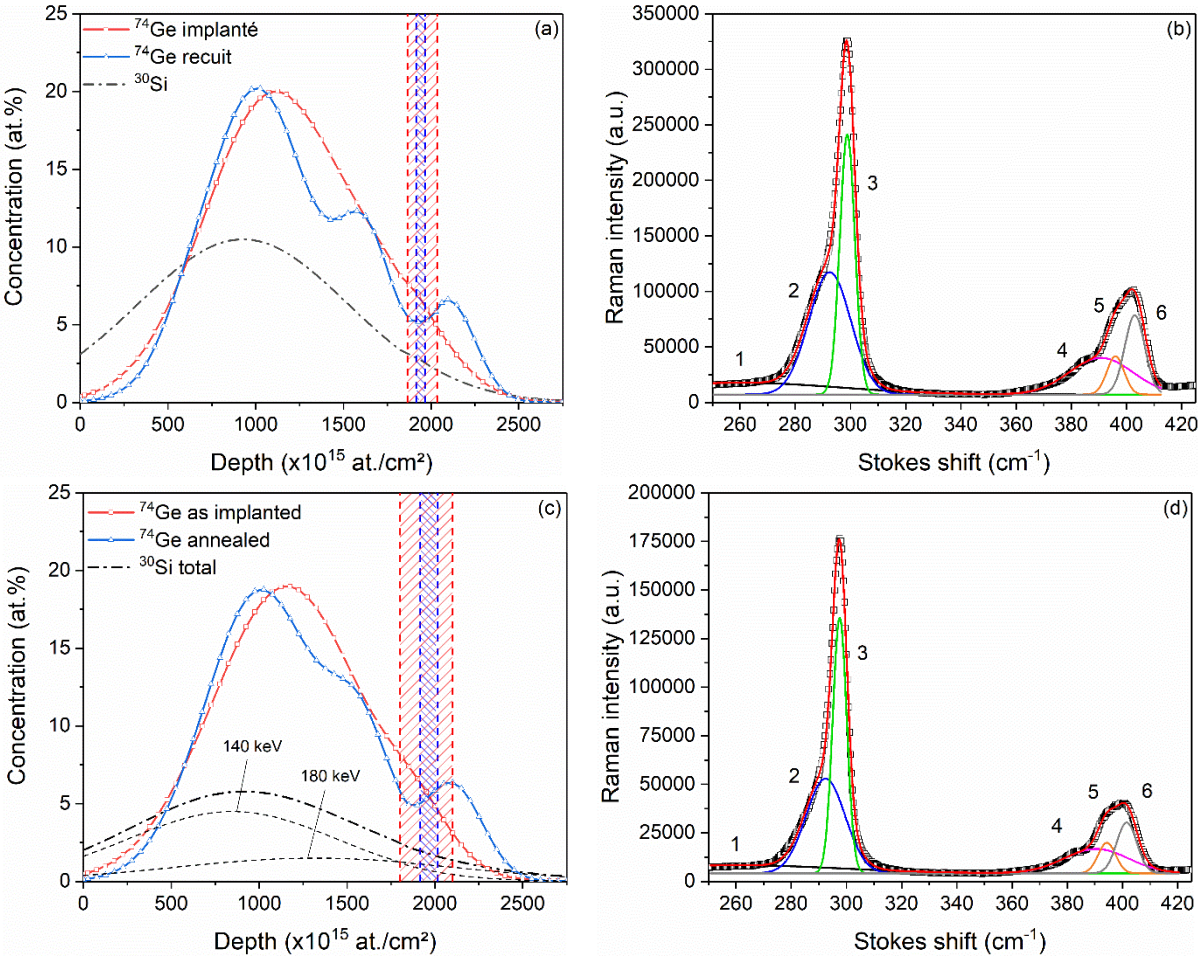

Figure 55 : (a),(b) Ge depth-profiles (RBS) and Raman spectra for a sample implanted with 2.1 × 10^{17} Ge/cm² at 325 keV and co-implanted with 1.5 × 10^{17} ^{30}Si/cm² at 140 keV. (c),(d) RBS and Raman spectra for a sample implanted with 2.1 × 10^{17} Ge/cm² at 325 keV and co-implanted with 6.2 × 10^{16} and 2.8 × 10^{16} ^{30}Si/cm² at 140 and 180 keV respectively. Measurement conditions : RBS ($E_\alpha = 2\ MeV, \theta = 165°$, incidence 7°, $Q = 10\ \mu C$), Raman ($\lambda_{Laser} = 514\ nm$, objective lens ×100).

This leads to the decrease of germanium mobility, as shown in Ge depth-profiles measured by RBS, because of a higher concentration of Ge-Si bonds due to a higher overlap of both implantation profiles, as discussed in **article III**. µ-Raman measurement, shown in **Figure 55b**, confirms the high concentration of Ge-Si chemical bonds, between 365 and 420 cm^{-1} (peaks 4, 5 and 6), responsible of the lower Ge mobility.

Double co-implantation of ^{30}Si has also been carried out with energies of 140 and 180 keV for fluences of 6 and 2 × 10^{16} Si/cm² respectively. The depth-profiles extracted from RBS and RNRA measurements are presented in **Figure 55c**. Once more, co-implanted ^{30}Si atoms locally enhance the formation of Ge-Si bonds, as indicated by µ-Raman (**Figure 55d**), forcing the formation of small Ge nanocrystals in surface and larger nanocrystals close to the oxide/substrate interface (**Figure 56**).

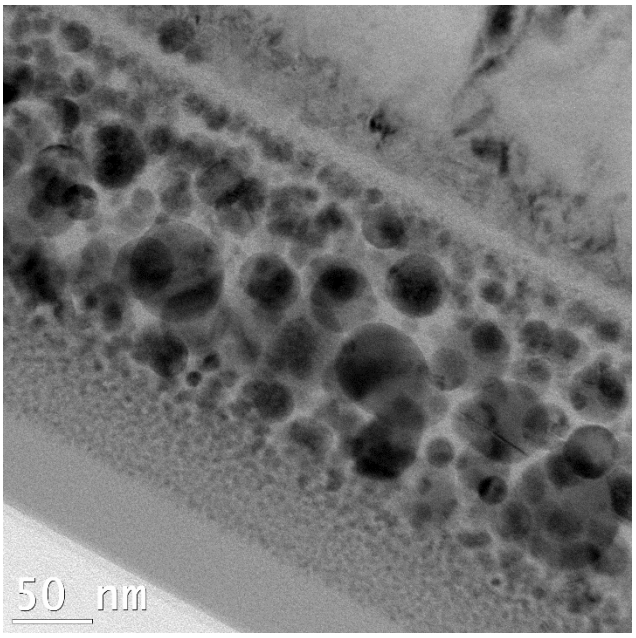

Figure 56 : TEM images of a sample implanted with 2.1×10^{17} $^{74}Ge/cm^2$ at 325 keV and co-implanted with 6 and 2×10^{16} $^{30}Si/cm^2$ at 140 and 180 keV respectively.

Chapter V

Formation of crystalline $Si_{1-x}Ge_x$ top layers by $^{74}Ge^+$ implantation in crystalline silicon

In the previous chapter, we discussed about several possibilities to control the growth and size of germanium quantum dots inside a SiO_2/Si film. From the point of view of PV cells, charge carriers generated inside a dielectric layer and, furthermore, far from the SiO_2/Si interface, appear hard to collect. A possibility is to count on tunnelling effects between close nanocrystals to reach the c-Si substrate, as discussed in **section II.5**. To solve this issue, charge carriers should be photogenerated in a semiconductor matrix, such as silicon, which will better conduct the electric charges.

As the results presented in **chapter IV** highlighted the poor mobility of germanium atoms in the presence of silicon excess, germanium ions implanted in crystalline silicon have weak chances to nucleate after diffusing through the semiconductor material. Moreover, the miscibility of germanium in silicon makes it difficult to form Ge nanocrystals embedded in a silicon matrix. However, even if the formation of Ge nanocrystals seems to be impossible, it would remain interesting to achieve to form crystalline $Si_{1-x}Ge_x$ alloys. From a photovoltaic point of view, $Si_{1-x}Ge_x$ alloys could slightly improve the solar cells efficiency as the energy gap of the alloy can be tuned as a function of the germanium concentration, although E_g would only vary between that of pure silicon and that of pure germanium. Fully relaxed $Si_{1-x}Ge_x$ top layers are also commonly implemented as "virtual substrates" for the growth of strained silicon layers for electronic devices. These strained layers are widely studied as a possibility to improve the mobility of electrons and holes in electronic devices.

To overcome the low Ge mobility, low-energy $^{74}Ge^-$ ions are implanted near the sample surface. This enables to reach high concentrations in thin layers and, consequently, Ge atoms very close to each other. Ge ions are implanted with an energy of 36 keV, for fluences varying from 5×10^{15} to 1.5×10^{17} Ge/cm². At this energy, Ge atoms are mainly localized in the first 35 nanometres from the sample surface, as shown by TEM measurements in **Figure 57**.

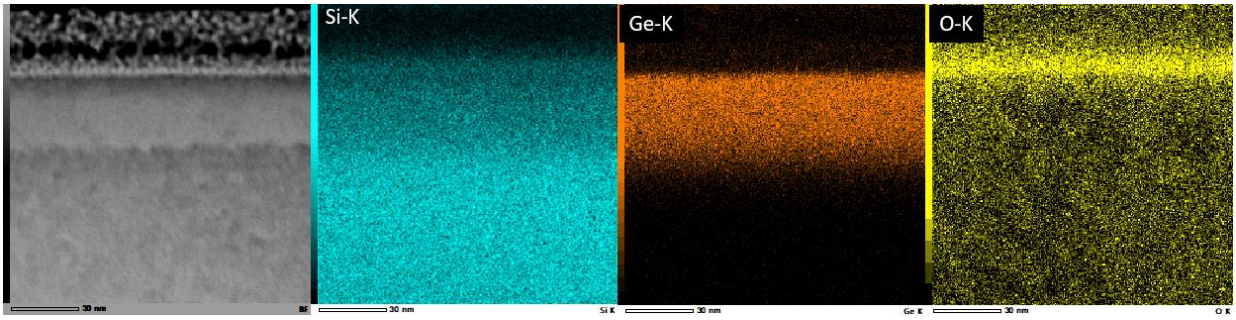

Figure 57 : STEM-HAADF micrographs of a sample implanted with a fluence of 1.5×10^{17} Ge/cm² annealed at 800°C during 30 minutes (scale: 30 nm).

Three distinct parameters have been studied:

1. Ge concentration (implantation fluence),
2. Annealing temperature,
3. Annealing time.

V.1 Influence of germanium concentration

For the low projected range of germanium ions at 36 keV, a saturation of Ge implanted ions concentration is expected to occur for the higher Ge fluences. From a threshold value, as many Ge ions are added than sputtered. This is confirmed by RBS analyses (**Figure 58**) indicating a rapid germanium saturation for fluences higher than 8 × 10^{16} Ge/cm². The maximum concentration reached is about 30-31 at.% for 1.5 × 10^{17} Ge/cm², as measured by RBS. TRIM simulations, treated to take into account sputtering and swelling effects discussed in **section III.1**, support this observation as shown in **Figure 58a** (in red). Retained doses are simulated using a sputtering yield of 2.34 atoms/ion extracted from TRIM simulations. The small deviation between measured and simulated values could be explained by the change in sputtering yield during implantation, the sample surface being no longer composed of pure silicon.

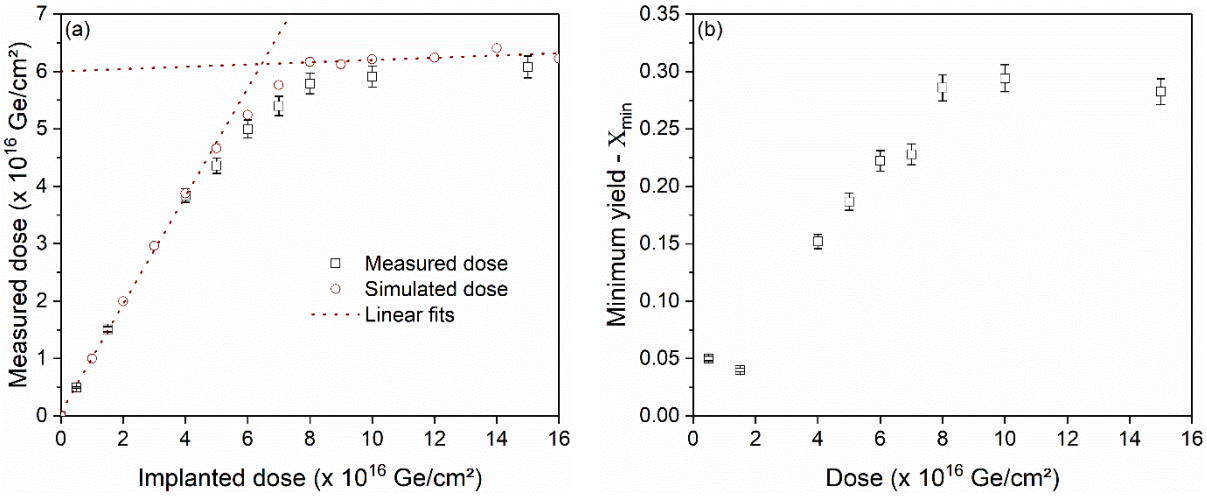

Figure 58 **:** (a) Measured dose (RBS) versus implanted dose, compared to TRIM simulations taking into account sputtering and swelling effects. (b) Ratio of Ge peak integrals measured by RBS in channeled (<100>) and random orientations.

RBS measurements, performed before and after annealing at 800°C (N_2, 30 minutes), did not highlight any germanium diffusion or desorption, which confirms the very poor mobility of Ge atoms implanted in silicon.

RBS/C measurements have been carried out according to <100> and <110> crystallographic orientations (see **Figure 39** in **section III.5** for a schematic representation of the ion beam alignment with both <100> and <110> orientations). Regions of interest (ROI) have been chosen around the Ge signal, for the $Si_{1-x}Ge_x$ layer, and in the Si signal, just after the alloy, for the substrate. The results of channeling along the <100> axis are presented in **Figure 58b** and **59**. RBS/C indicates that the crystallinity of the $Si_{1-x}Ge_x$ layer deteriorates when the Ge fluence increases, *i.e.,* with the composition *x*. This is highlighted by the evolution of the χ_{min} value, representing the ratio of peaks integrals between channeled and random orientations (**Figure 58b**). This effect is also visible in the inserts of **Figure 59**, representing the evolution of RBS signal as a function of the incident angle θ, characterized by dips in crystalline samples and constant values in amorphous samples. χ_{min} is equal to the minimum of the dip,

whose value decreases for a better crystallinity. RBS/C also indicates that germanium is incorporated in the crystal network in substitutional sites during thermal treatment, as well-defined dips are observed. This result was expected, as germanium and silicon are completely miscible. The dips corresponding to the $Si_{1-x}Ge_x$ layer and the Si substrate are superimposed in both crystallographic orientations, indicating an identical crystallography in the alloy and the substrate (inserts in **Figure 59**).

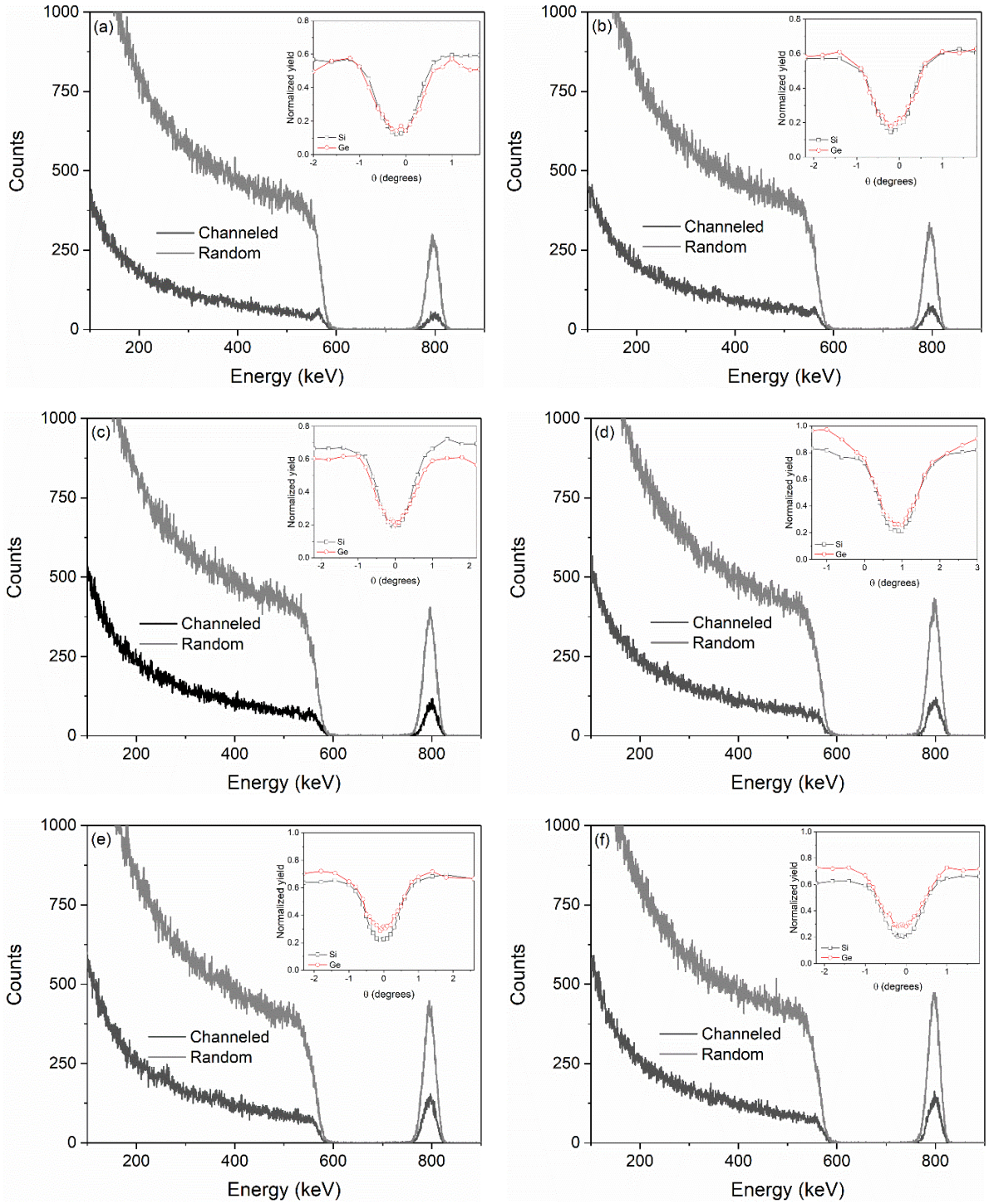

Figure 59 : RBS/C in <100> orientation of annealed samples (800°C - 30 minutes) implanted with (a) 4 ×10^{16} Ge/cm², (b). 5 ×10^{16} Ge/cm², (c) 6 ×10^{16} Ge/cm², (d) 7 ×10^{16} Ge/cm², (e) 8 ×10^{16} Ge/cm², (f) 1.5 ×10^{17} Ge/cm². The insert represents angular scans for ROI in the Si substrate (behind the $Si_{1-x}Ge_x$ layer) and in the Ge peak (*i.e.* inside the $Si_{1-x}Ge_x$ film).

The chemistry of the samples has been studied by Raman spectroscopy (**Figure 60**). Raman spectrum of virgin c-Si exhibits three characteristic peaks at ~302.6 cm^{-1}, ~434 cm^{-1} and ~520.7 cm^{-1}, which correspond respectively to LA, LO and TO vibration modes of crystalline silicon (yellow solid line). Three additional peaks appear after annealing (800°C, 30 minutes, N_2) for Ge-implanted samples. These peaks are located around 286 cm^{-1}, 405 cm^{-1} and in the range 500-520 cm^{-1} corresponding to Ge-Ge*, Ge-Si and Si-Si* Raman signatures respectively. Si-Si* is generally associated to a strained silicon layer, Si-ncs or crystalline silicon containing germanium impurities. In **articles II**, **III** and **IV**, Ge-Ge* Raman signature has been associated to small Ge-ncs containing Si impurities in Ge-implanted SiO_2. In the case of a silicon matrix, these Ge-Ge* phonons must rather be associated to Ge-Ge bonds contaminated by Si atoms that seems too small to be considered as nanocrystals.

Figure 60 shows that an $Si_{1-x}Ge_x$ alloy is formed even for very low germanium fluences (already for 3 × 10^{16} Ge/cm²), while Ge-Ge* signal is only measurable for fluences at least equal to 5 × 10^{16} Ge/cm². This can be explained by the weak mobility of Ge in silicon, as only spatially close germanium atoms are able to bond to each other. This probability increases as the Ge fluence increases.

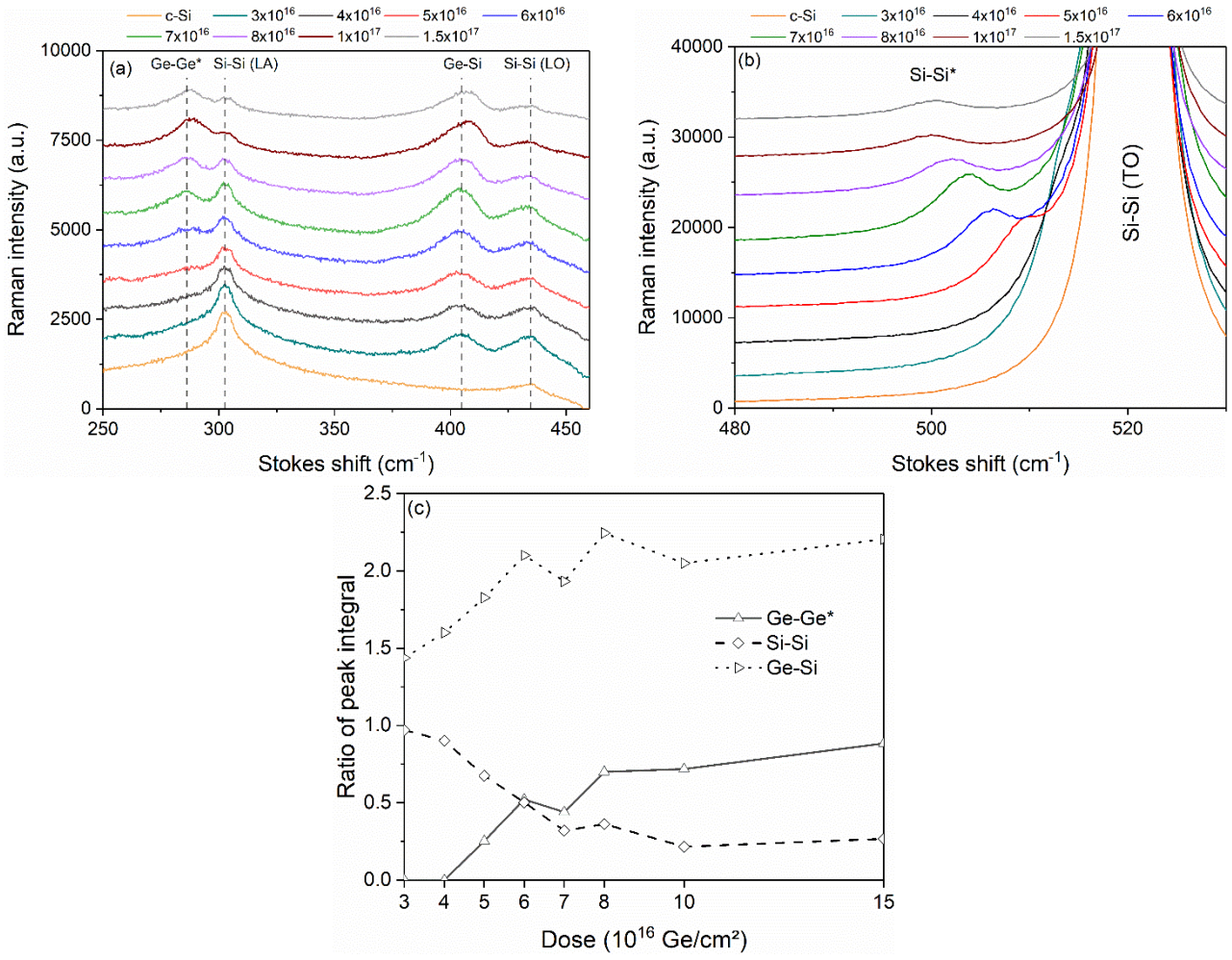

Figure 60 : Raman spectra of samples annealed 30 minutes at 800°C for fluences varying from 0 to 1.5 × 10^{17} Ge/cm² in the range (a) 250-460 cm^{-1} and (b) 480-540 cm^{-1}. (c) Integrals of Ge-Ge*, Ge-Si and Si-Si (LA) Raman signals (Lines are only there to guide the eye). The peaks integrals are divided by the integral of the signal at ~434 cm^{-1} from the substrate (Si-Si LO) in order to enable a comparison between measurements.

The evolution of the integral of the Ge-related peaks (Ge-Ge*, Ge-Si and Si-Si*) depends on the Ge content, and is very similar to that observed for the Ge concentration in RBS, presenting a linear evolution followed by a saturation for germanium fluences higher than 8 × 10^{16} Ge/cm².

In addition to the composition *x* of the alloy, the position of Raman peaks strongly depends on the presence of tensile or compressive strain in the $Si_{1-x}Ge_x$ layer. Therefore, the germanium concentration and layer strain must be determined to estimate if the peak shift is only due to changes in the film composition or to strain effects. RBS and XRD can independently estimate the average germanium concentration inside the $Si_{1-x}Ge_x$ layer. Lattice parameter, which depends on the alloy composition, is deduced from the peak position in XRD measurements. As germanium is incorporated in the silicon network in substitutional sites, XRD measurements focused on the major signal of the substrate, which is (400) around 69.1°. A peak corresponding to the $Si_{1-x}Ge_x$ alloy appears between the expected signals of pure Si and Ge, corresponding to 69.1° and 66.0° respectively (**Figure 61a**). This peak position is related to the interplanar distance, from which the lattice constant a_{SiGe} of the alloy film can be deduced (see **Equation III.45** in **chapter III**). This lattice parameter depends on the composition *x* of the $Si_{1-x}Ge_x$ film according to Dismukes law (**Equation II.3**). **Figure 61b** shows that the peak position follows the same trend than the Ge concentration measured by RBS.

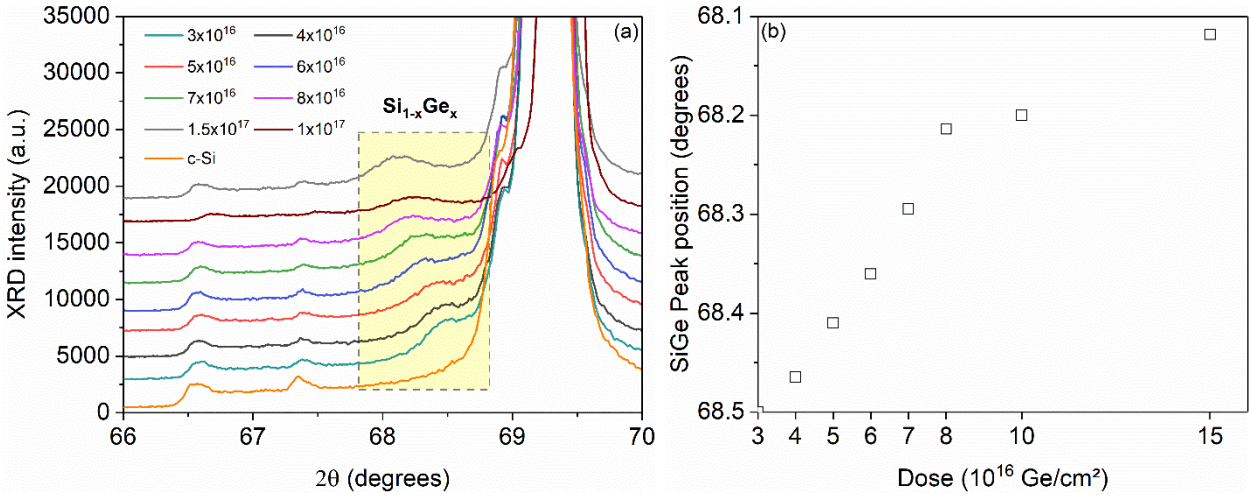

Figure 61 : (a) XRD spectra of samples implanted with fluences ranging from 3 × 10^{16} to 1.5 × 10^{17} Ge/cm², annealed at 800°C 30 minutes. (b) Evolution of SiGe (400) peak position as a function of Ge fluence.

The germanium average concentration of each sample was also estimated by RBS over the 30-35 first nanometers. The values obtained by both techniques are compared in **Table 5**, showing relatively close concentrations. This is a first indication of the absence of high strain in the direction normal to the sample surface, as XRD is sensitive to strain while RBS is not. In a strained layer, the position of the XRD peaks is shifted, what should have distorted the estimation of *x*.

As discussed in **section III.5**, RBS/C can be useful to highlight layer strain. The dips in the $Si_{1-x}Ge_x$ film and in the Si substrate should be shifted relative to each other in the <110> direction in the presence of a strained layer on top of a relaxed substrate. According to reference (111), the shifts should be higher than 0.30 degrees considering the film thickness

and the composition of our samples. As the dips observed in the <110> crystal orientation are weakly shifted, the larger shift observed being 0.08 degrees (**Table 5**), this confirms that the $Si_{1-x}Ge_x$ films are weakly strained after annealing.

The tetragonal strain and the lattice parameters ratio $a_{//}/a_{\perp}$ can be estimated by comparing the angular scans in <100> and <110> directions (**Table 5**), as explained in **section III.5**. The weak negative values of ε_T and the fact that $a_{//}/a_{\perp}$ is just smaller than 1 indicate a very weak tensile strain in the perpendicular direction. Moreover, the increase of χ_{min} with Ge fluence indicates that the films relax during thermal treatment, probably by the formation of extended defects such as dislocations. As the formed alloys are in a metastable state after the implantation process due to the composition and thickness of the films (see **Figure 6** in **chapter II**), they are likely to relax under high temperature. This agrees with the RBS/C results, which indicates that the crystallinity is not entirely recovered after annealing, as χ_{min} varies between 0.15 and 0.30 over the range of Ge fluences, while a perfect silicon <100> crystal has a minimum yield lower than 0.05 for 1 MeV alpha particles.

Implanted fluence ($\times 10^{16}$ Ge/cm²)	XRD (at.%)	RBS (at.%)	$\Delta\theta_{<100>}$ (degrees)	$\Delta\theta_{<110>}$ (degrees)	ε_T (%)	$a_{//}/a_{\perp}$	
						Film	Substr.
3	19.3 ± 0.5	/	/	/	/	/	/
4	20.3 ± 0.8	18.5 ± 0.6	0.02	0.08	-0.205	0.963	0.966
5	22.1 ± 0.8	21.1 ± 0.6	0.005	0.06	-0.131	0.961	0.964
6	23.5 ± 1.2	23.9 ± 0.7	0.006	0.04	-0.088	0.964	0.965
7	25.6 ± 0.7	26.0 ± 0.8	0.04	/	/	/	/
8	28.1 ± 0.6	28.3 ± 0.8	0.007	0.05	-0.107	0.96	0.962
10	28.6 ± 0.7	28.6 ± 0.9	0.006	0.08	-0.172	0.995	0.998
15	31.1 ± 0.4	30.1 ± 0.9	0.01	0.07	-0.106	1.022	1.024

Table 5 : Germanium concentrations estimated by XRD and RBS, and shifts between Si and $Si_{1-x}Ge_x$ dips measured by RBS/C in <100> and <110> directions and tetragonal strain.

Assuming $\varepsilon_{//} \sim 0$ (the calculated values of strain are of the order of $\sim 10^{-3}$-10^{-4}), the peak position of Ge-Ge*, Ge-Si and Si-Si* phonons have been adjusted by the following equations:

$$\omega_{Ge-Ge^*} = 282.0 + 0.149\,x - B^{Ge-Ge^*}\varepsilon_{//}$$

$$\omega_{Ge-Si} = 400.45 + 0.155\,x - B^{Si-Ge}\varepsilon_{//}$$

$$\omega_{Si-Si^*} = 520.72 - 0.66\,x - B^{Si-Si^*}\varepsilon_{//}$$

which are the linear fits of our experimental data (dashed lines in **Figure 62**). The fixed values $B^{Ge-Ge^*} \sim 400$ cm^{-1}, $B^{Ge-Si} \sim 550$ cm^{-1} and $B^{Si-Si^*} \sim 800$ cm^{-1} are close to those reported in literature (128), (129), (130), (131), (132), (133), (134). **Figure 62** (top) compares the present results with other experimental works in literature for fully relaxed samples as a function of

Ge concentration. **Figure 62** (bottom) compares our experimental data with fully relaxed and fully strained films. This clearly confirms that the $Si_{1-x}Ge_x$ top layers formed in this work are fully relaxed.

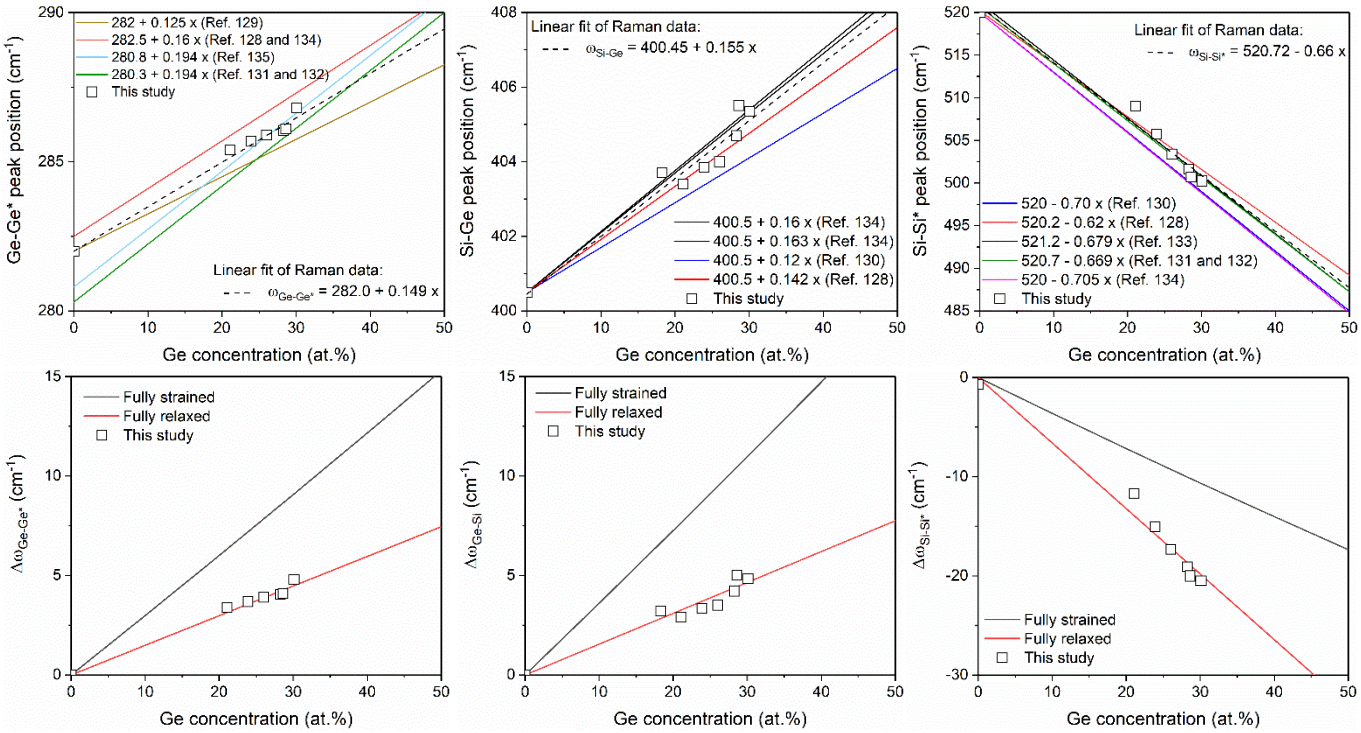

Figure 62 : Evolution of Raman peaks position as a function of Ge concentration. Top - Comparison with other studies for fully relaxed films *(128)*, *(129)*, *(130)*, *(131)*, *(132)*, *(133)*, *(134)*, *(135)*. Bottom – Comparison with a fully strain and a fully relaxed layer.

Figure 63 shows TEM measurements of a sample implanted with a fluence of 1×10^{17} Ge/cm² and annealed 30 minutes at 800°C under N_2. As observed by the combination of XRD, RBS/C and Raman measurements, TEM confirms the formation of a crystalline $Si_{1-x}Ge_x$ layer on top of the c-Si substrate. Darker and brighter structures, observed in bright and dark field modes respectively, indicate the possible presence of nanostructures, extended defects or both. In particular, **Figure 63c** highlights the presence of a large density of defects at the film/substrate interface and throughout the film, which could be associated to misfit and threading dislocations respectively.

The crystallinity of the $Si_{1-x}Ge_x$ layer is confirmed by electron diffraction patterns (insert in **Figure 63a**), showing well-separated spots in the substrate as well as in the $Si_{1-x}Ge_x$ film, characteristic of single crystalline samples.

In conclusion, fully relaxed $Si_{1-x}Ge_x$ films, probably containing dislocations, are formed by this fabrication process (800°C, N_2, 30 minutes). The gain in Ge concentration, and therefore in the ability of the $Si_{1-x}Ge_x$ to strain a Si layer deposited on top of this virtual substrate, becomes negligible for implantations fluences exceeding 1×10^{17} Ge/cm² due to saturation effects occurring above 8×10^{16} Ge/cm². Moreover, **Table 5** indicates that the germanium concentrations measured by RBS and XRD are very similar, which means that all germanium atoms could be involved in the formation of the $Si_{1-x}Ge_x$ alloy, confirming the difficulty in forming Ge nanocrystals in silicon.

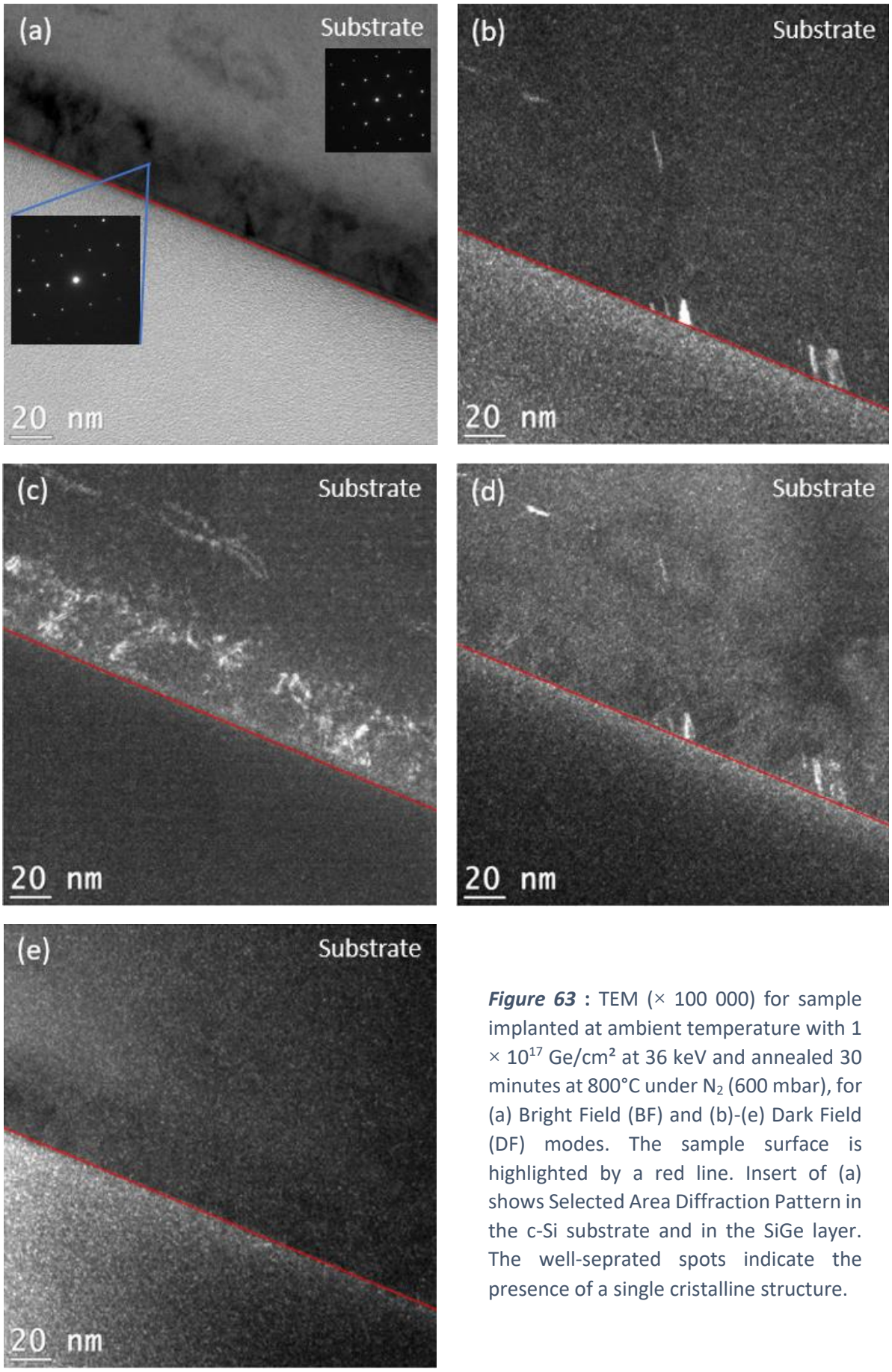

Figure 63 **:** TEM (× 100 000) for sample implanted at ambient temperature with 1 × 10^{17} Ge/cm² at 36 keV and annealed 30 minutes at 800°C under N_2 (600 mbar), for (a) Bright Field (BF) and (b)-(e) Dark Field (DF) modes. The sample surface is highlighted by a red line. Insert of (a) shows Selected Area Diffraction Pattern in the c-Si substrate and in the SiGe layer. The well-seprated spots indicate the presence of a single cristalline structure.

V.2 Influence of annealing temperature

For annealing temperatures under 500°C, only amorphous germanium is observed whether by RBS/C or Raman. Annealing has to be carried out above 500°C to beget the crystallization of germanium, while silicon recrystallization already occurs at lower temperatures (108).

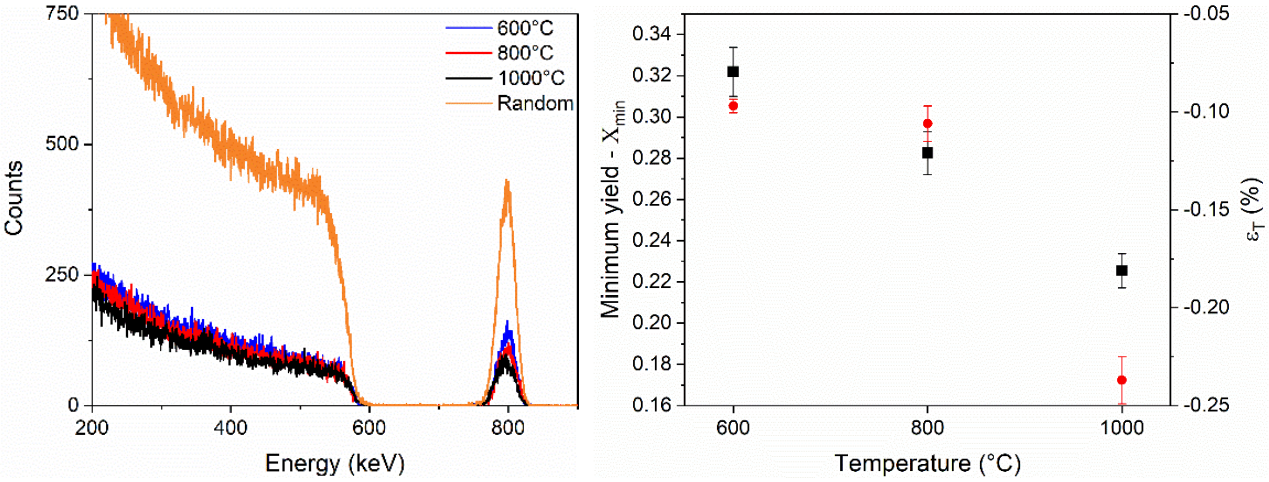

Figure 64 : Left – RBS/C of samples (1.5×10^{17} Ge/cm²) annealed for temperatures ranging from 600 to 1000°C, for random and channeled orientations (<100> is shown here). Right – χ_{min} as a function of the temperature (black squares) and tetragonal strain (red dots).

Figure 64 shows that, for a fixed annealing time (30 minutes), the crystallinity of the $Si_{1-x}Ge_x$ layer increases the more the annealing temperature is high, which is characterized by a diminution of χ_{min} in both <100> and <110> crystallographic orientations. This enhanced crystallinity is accompanied by an increase of strain in the $Si_{1-x}Ge_x$ layer, although the latter remains relatively low. This diminution of χ_{min} and increase of strain could indicate a better assimilation of germanium in the $Si_{1-x}Ge_x$ network and a lower formation of dislocations at higher temperatures.

Temperature (°C)	Fluence (Ge/cm²)	C_{Ge} - RBS (at.%)	C_{Ge} - XRD (at.%)	ε_T (%)
600	1.5×10^{17}	29.7 ± 0.9	30.4 ± 0.5	-0.097
800		30.5 ± 0.9	31.1 ± 0.4	-0.106
1000		28.9 ± 0.9	27.2 ± 0.5	-0.237
600	8×10^{16}	28.6 ± 0.9	27.2 ± 1.2	-0.093
800		27.7 ± 0.8	28.1 ± 0.6	-0.107
1000		29.4 ± 0.9	28.4 ± 0.3	-0.114

Table 6 : Ge concentration measured by RBS and XRD, and strain values measured by RBS/C as a function of fluence and temperature for 30 minutes of annealing.

The same trend is observed, for χ_{min} as well as strain, for germanium fluences of 4, 6 and 10 × 10^{16} Ge/cm² for annealing temperatures ranging from 600 to 1200°C for a fixed annealing time.

On the other hand, the integral of Ge-Ge* Raman peak systematically decreases while the crystallinity of the $Si_{1-x}Ge_x$ film increases when annealing temperature is elevated from 600 to 1000°C, as shown in **Figure 65** for two different germanium fluences. Ge-Si peak generally decreases at 1000°C because of a better interstitial diffusion of Si atoms compared to Ge atoms for temperatures higher than 900°C. Moreover, an optimum in annealing time is also observed, which is temperature-dependent, while the same duration is used here for the three temperatures (see next paragraph).

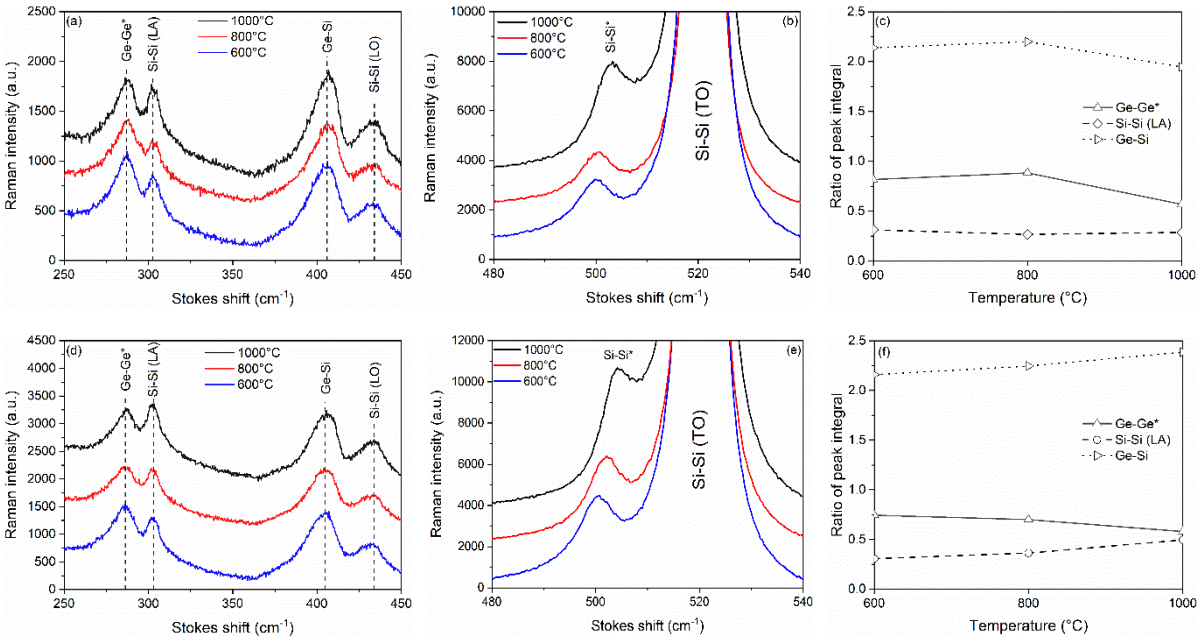

Figure 65 : Raman spectra of samples annealed 30 minutes for different temperatures and implanted with (a)-(b) 1.5 × 10^{17} and (d)-(e) 8 × 10^{16} Ge/cm². Integrals of Raman peaks divided by the peak at ~434 cm^{-1} (Si-Si LO) for fluences of (c) 1.5 × 10^{17} and (f) 8 × 10^{16} Ge/cm².

We can deduce from these results that increasing the temperature above 800°C improves the crystallinity of our films and the incorporation of Ge in the silicon network.

V.3 Influence of annealing time

Annealing times ranging from 2 to 180 minutes have been investigated. **Figure 66** shows the evolution of Raman peaks integrals and positions as a function of the annealing duration for samples implanted with 1 × 10^{17} Ge/cm² and annealed at 800 and 1000°C under N_2. For the sample annealed at 800°C, it is found that both the integral and the position of the peaks present the same evolution, *i.e.,* a "bell-like" shape. An optimum is reached at this temperature between 60 and 120 minutes whether for the integral or the position of the peaks.

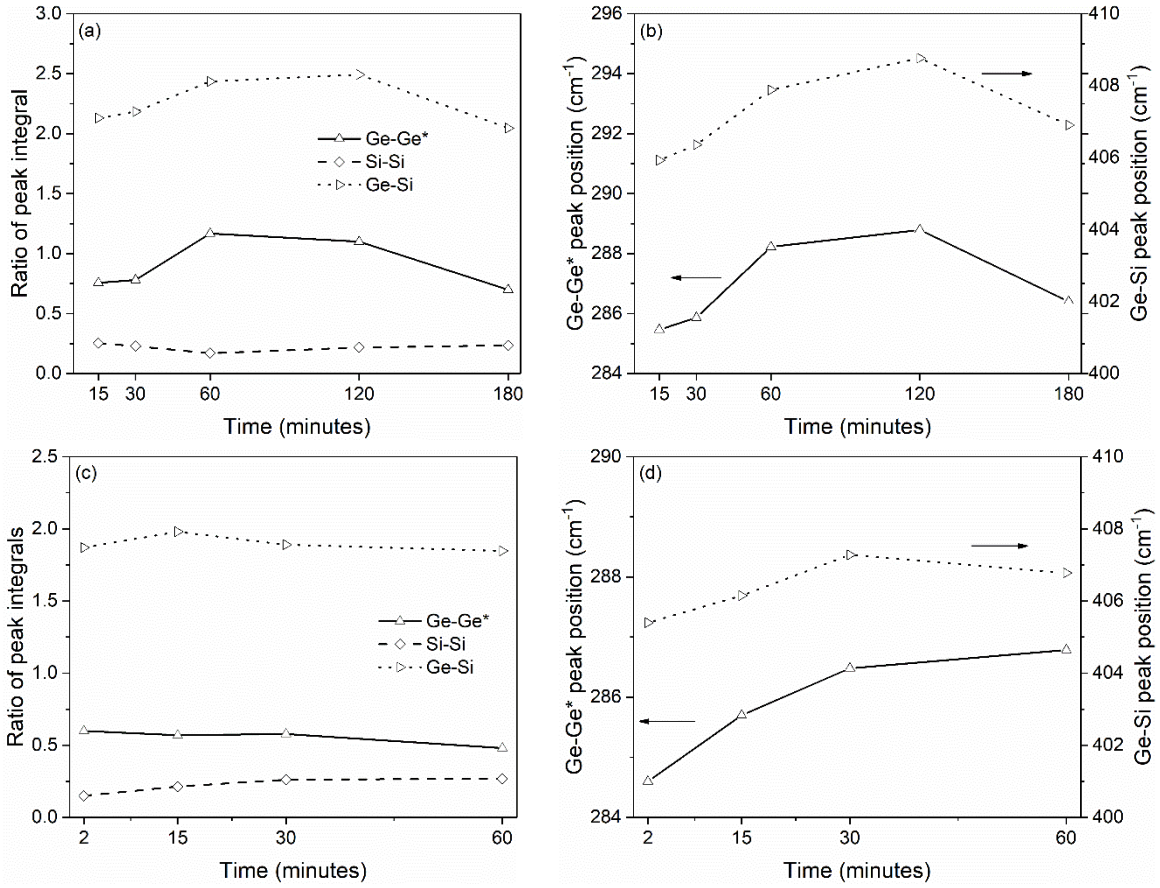

Figure 66 : Evolution of Raman peaks integrals and positions as a function of annealing time for samples implanted with 1 × 10^{17} Ge/cm² annealed at (a),(b) 800°C and (c),(d) 1000°C. The peaks integrals are divided by the integral of the signal at ~434 cm^{-1} (Si-Si LO) from the substrate in order to enable a comparison between measurements.

For higher temperatures (1000°C), the optimum in peaks position (**Figure 66d**) seems to be reached earlier compared to annealing at 800°C. Moreover, the Ge-related peaks are redshifted, meaning that the composition *x* of the $Si_{1-x}Ge_x$ alloy is lower than the one at 800°C. The peaks integrals continuously decrease while the annealing time increases. For annealing at 1200°C with the same fluence, the optimum is rapidly reached, as Ge-Ge* signal is observable after 2 minutes but is no longer detectable after 30 minutes of annealing.

In conclusion, an optimum can be found for each temperature, with an optimal annealing time which decreases while the temperature increases.

V.4 Implantation under high temperatures

In the previous samples, the germanium concentration is very similar whether measured by XRD or by RBS. This suggests that, due to the perfect miscibility of Ge in silicon, all germanium atoms participate to the formation the $Si_{1-x}Ge_x$ alloy. An attempt has been done to limit the incorporation of Ge in the silicon network to favour the potential formation of Ge-ncs by heating the samples during the implantation. This avoids the amorphization of silicon by Ge ions, which favours the formation of the alloy during the post-annealing step. As the poor germanium mobility is due to the formation of strong Ge-Si chemical bonds, which already takes place during implantation, heating the samples during the implantation could preserve the silicon network, reducing the density of Si dangling bonds.

Heated samples were implanted at Université de Montréal (UdeM) with a sample holder which can reach a temperature of 600°C. These temperatures are too low to efficiently form Ge-ncs, but are high enough to instantly beget the recrystallization of silicon.

Implantations have been carried out with an energy of 36 keV for a single Ge fluence of 1×10^{17} at./cm², for a heating temperature of 600°C measured at the sample surface.

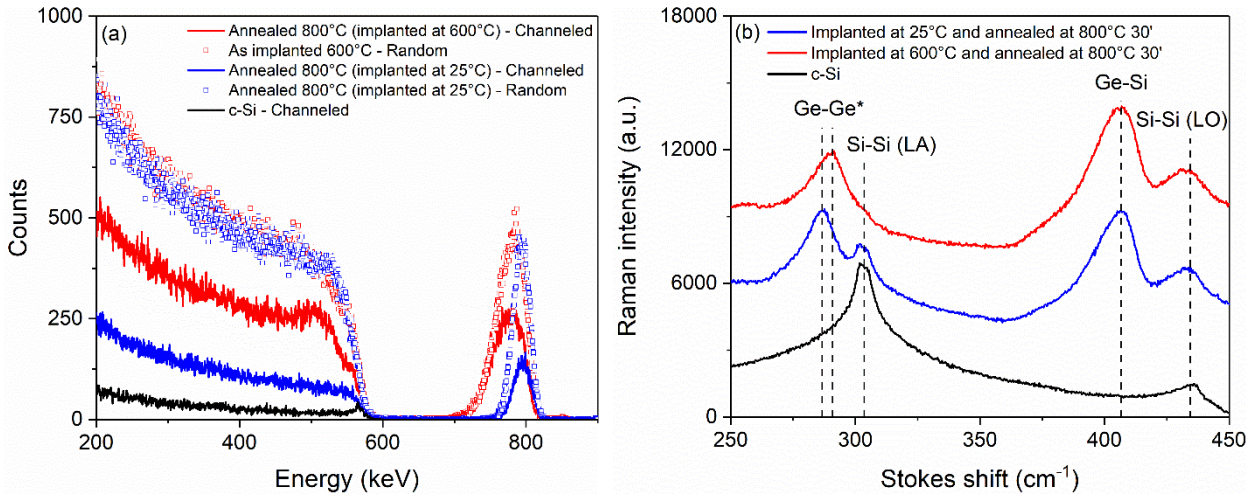

Figure 67 : RBS/C and Raman spectra of samples implanted with 1×10^{17} Ge/cm² at ambient temperature and at 600°C before 30 minutes of annealing at 800°C. (a) RBS/C spectra with 1 MeV α particles in random and channeled orientations for a detection angle of 165°. (b) Raman spectra with 514 nm laser and x100 objective lens.

Figure 67a compares the RBS spectra of samples implanted at ambient temperature (in blue) and at 600°C (in red), in random (squares) and channeled (lines) conditions after a post-implantation annealing at 800°C (30 minutes, N_2). Random spectra show that the Ge profile is more extended in depth for the sample implanted at 600°C. As the energy of the ions is the same in both samples, this indicates that Ge is able to diffuse in depth during the implantation at 600°C compared to the implantation at ambient temperature. This Ge diffusion probably occurs in the preserved Si network through interstitial jumps. This prevents from Ge saturation effects due to sputtering, as the fluence of the sample implanted at 600°C has been measured by RBS as being exactly the implanted fluence ($1.01 (\pm 0.03) \times 10^{17}$

Ge/cm²). Channeled spectra (**Figure 67a**) also reveals a worst alloy crystallinity, or a high concentration of interstitial atoms, in the sample implanted at 600°C.

Raman spectra, presented in **Figure 67b**, show that, after annealing at 800°C, Ge-Ge* signal is blueshifted by ~4.2 cm^{-1} for the sample implanted at 600°C compared to the sample implanted at ambient temperature. However, RBS and XRD measurements give a lower average germanium concentration in the $Si_{1-x}Ge_x$ film. Therefore, this shift cannot be associated to an increase of Ge content *x* in the $Si_{1-x}Ge_x$ layer, what is confirmed by the position of the Si-Ge peak (~405 cm^{-1}), which is invariant from one sample to the other. This could indicate a less efficient incorporation of Ge atoms in the silicon network, favouring the formation of Ge-Ge bonds.

Figure 68 shows TEM imaging performed on the sample implanted at 600°C. TEM observations of the sample implanted at ambient temperature have already been shown in **Figure 63**. For comparison, observation conditions of **Figure 68a**, **b** and **c** correspond to conditions (except for the scale) in **Figure 63b**, **e** and **a** respectively.

The higher density of defects highlighted by RBS/C for implantation at 600°C (**Figure 67a**) is confirmed by TEM, showing a large band of dislocations at a depth between 80 and 160 nm in **Figure 68a**. These dislocations extend up to the end of the germanium depth-profile tail. **Figure 68b** reveals the presence of brighter dots, which could be associated to small spherical nanostructures with a higher Z than silicon. The depth position of the nanostructures mainly corresponds to the depth of the dislocations layer. This could indicate that the germanium mobility is locally enhanced by the presence of structural defects, such as dislocations, leading to the accumulation of Ge close to these defects.

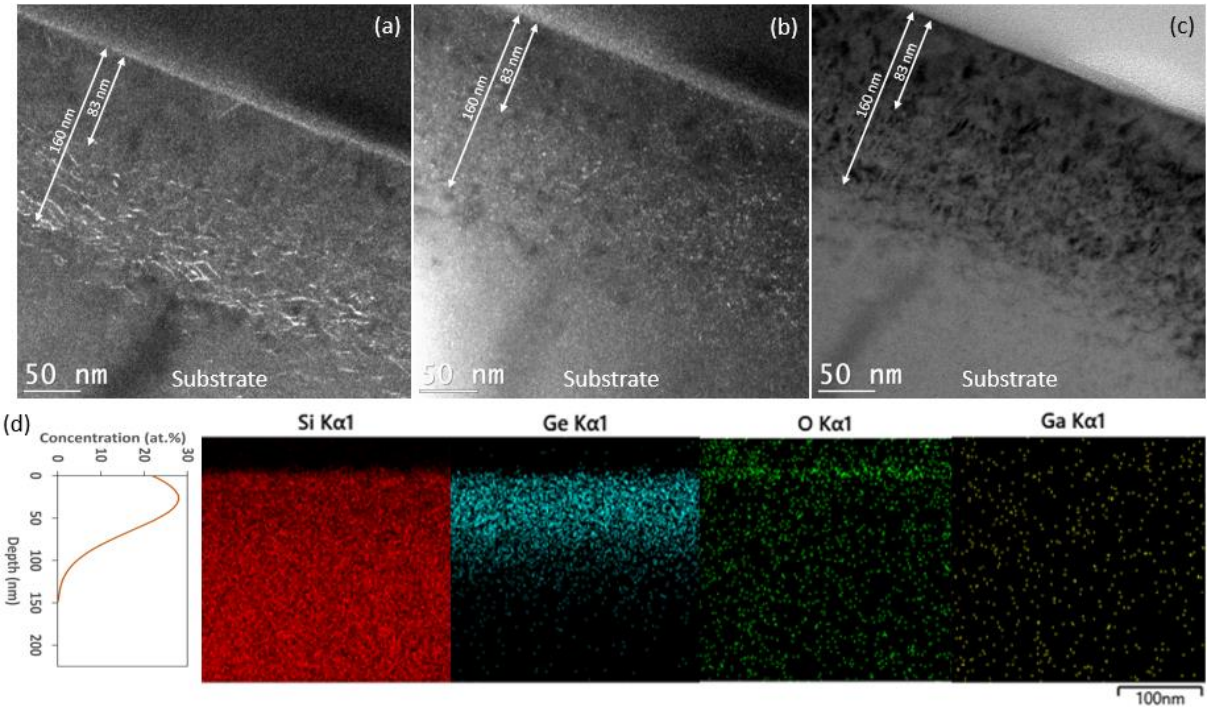

Figure 68 : TEM measurements (× 60 000) for a sample implanted at 600°C with 1 × 10^{17} Ge/cm² and annealed at 800°C during 1h under N_2, in (a)-(b) DF and (c) BF modes. (d) Ge depth-profile measured by RBS (1 MEV, α, detector 165°) and STEM-EDS analyses for Si, Ge, O and Ga. The presence of Ga is due to the sample preparation by focused ion beam (FIB).

Due to the very small dimensions of the nanostructures and the difficulty of image processing programs, such as ImageJ (136), to automatically differentiate these nanoclusters from the host matrix, a manual treatment allows us to assume an average diameter of about 1-2 nm. Note that this is not possible with the present results to affirm that the observed nanostructures are Ge quantum dots. Moreover, it is not excluded that at least a part of the nanostructures observed in **Figure 68** could be due to the nanoclustering of Ga atoms implanted during the focused ion beam process carried out during the sample preparation for TEM.

Chapter VI

Conclusions and perspectives

The development of nanoelectronics and optoelectronic devices such as solar panels, lasers or memory devices at the nanoscale is a very current research topic. In this thesis, we focused on the stabilization and characterization of germanium nanocrystals in Si-based host matrices. Through this work, a major effort has been made to experimentally study the capacities of ion implantation as being a leading technique in the manufacture of such devices, using original approaches such as the use of isotopic markers or co-implantations.

The mechanisms of Ge diffusion in implanted SiO_2 films have been brought to light in **article I**. Combination of IBA and XPS measurements allowed us to highlight the influence of irradiation-induced damage on the stoichiometry of the SiO_2 film as well as the Ge oxidation state after the implantation process, as a function of the Ge fluence. It has been showed that Ge mobility is reduced in under-stoichiometric SiO_x films ($x < 2$) compared to oxides containing an excess of oxygen, mainly due to the formation of Ge-Si bonds and GeO molecules respectively. This was used to explain the asymmetric diffusion of germanium in SiO_2 films highlighted by RBS.

The influence of oxygen on this asymmetric diffusion of germanium has been studied in **article II** with the stable isotope ^{18}O. We experimentally showed how the presence of a small oxygen contamination of the annealing atmosphere, as low as 1% of the total gas pressure, drastically changes the diffusion kinetics of germanium. Our results demonstrated the inward diffusion of oxygen atoms and their interaction with germanium, leading to the oxidation of Ge atoms or their out-diffusion through both the regeneration of the SiO_2 stoichiometry and the formation of GeO compounds. These results, in perfect agreement with theoretical models proposed in references (122), (123) and (127), were the first ever to experimentally study the correlation between the diffusion of both oxygen and germanium species. A new three-process model has been proposed in **article II** to explain the role of oxygen originating from the annealing atmosphere on germanium redistribution through the SiO_2 layer.

It has been shown, in **article I**, that a co-implantation of oxygen atoms in the oxide region most impacted by irradiation-induced damage could limit the formation of small nanocrystals while favouring the formation of larger ones. It has been demonstrated that O co-implantation increases the mobility of Ge through the formation of GeO until the over-saturation of the SiO_2 layer. Beyond this threshold, the gain is limited by the formation of not mobile GeO_2.

Solutions have been proposed to control the diffusion of germanium and, consequently, the formation of Ge nanocrystals. **Article III** showed that a silicon co-implantation highly influences both the Ge diffusion and nucleation. A local excess of silicon, as low as 1.6 at.%, is able to completely annihilate Ge diffusion, for a Ge implantation in the middle of a 300 nm thick SiO_2 layer and a fluence of 8×10^{16} at./cm². The results exhibit a high dependence on experimental parameters, the important factors to take into account for a co-implantation being:

- The projected range of all species and the overlapping of their depth-profiles. As shown in **articles III**, **IV** and in **section IV.3**, these two parameters define if the co-implanted Si atoms participate to the blocking of Ge diffusion or, on the contrary, to its local enhancement.

- The relative concentrations of the co-implanted species. The local effects of Si co-implantation are proportional to relative concentrations of implanted silicon and germanium atoms.

It has been shown in **article IV** that, in well-defined conditions, our co-implantation of silicon can be used to obtain a well-distributed size gradient of Ge nanocrystals. This was used to form very small nanocrystals closer to the sample surface and larger ones in depth, which is the best possible configuration that can be implemented to optimize the absorption of the solar spectrum. The main goal of this thesis has been achieved, as we proposed an experimental method for forming a dense gradient of Ge-ncs ranging from less than 1 to 4-5 nm, covering almost the entire solar spectrum.

Now that the possibility of locally controlling the formation and depth-distribution of germanium nanocrystals by co-implantation of silicon or oxygen has been demonstrated, the next step should be to implement it in solar cells to estimate how it could improve their efficiency, with the opportunity of mimicking multi-junction PV cells. One of the limiting factors for the integration of Ge quantum dots in photovoltaic cells should be the high temperature annealing required to give rise to their formation. From my knowledge of the fabrication process of such PV cells, the implantation of Ge ions, and the subsequent annealing, could be introduced in the first steps of the process without being influenced by the rest of the process. The temperatures and annealing times required for the diffusion and activation of dopants being not sufficient to affect the stable state of the Ge nanocrystals already formed.

It would also be interesting to co-implant Ge and Si atoms in thinner SiO_2 layers. This will reduce straggling effects occurring at higher energies. The SiO_2/Si interface will be less impacted by the implantation, which leads to the formation of defects in the first layers of the silicon substrate. This also enables a gain in time by reducing the fluence.

The particular study of irradiation-induced defects could be carried out further. In the case of triple implantations presented in **article III**, it would be interesting to separately study the effects of both ^{29}Si and ^{30}Si implantations on the symmetrical Ge redistribution observed in deposited samples. It would confirm once more that defects, such as Si dangling bonds, generated during the implantation process participate actively to the annihilation of Ge diffusion highlighted in co-implanted samples, especially for the high-energy implantation.

The possible influence of H atoms on Ge diffusion could also be investigated further. Some authors suggest that the presence of H atoms, contained in the wet SiO_2 film or coming from the annealing atmosphere, could influence the diffusion of Ge atoms through the formation of highly volatile GeH_4 molecules. Although this difference between dry and wet

oxides has not been investigated so much during this thesis, we noted the possible contamination of our samples during the implantation process (**Figure 69**). ERDA measurements showed that the Ge^+ beam could carry hydrogen during its travel through the vacuum line and that this hydrogen leaves the sample during the annealing step. The possible influence of hydrogen on Ge diffusion could be highlighted the same way we did for oxygen in this thesis, with a co-implantation of H.

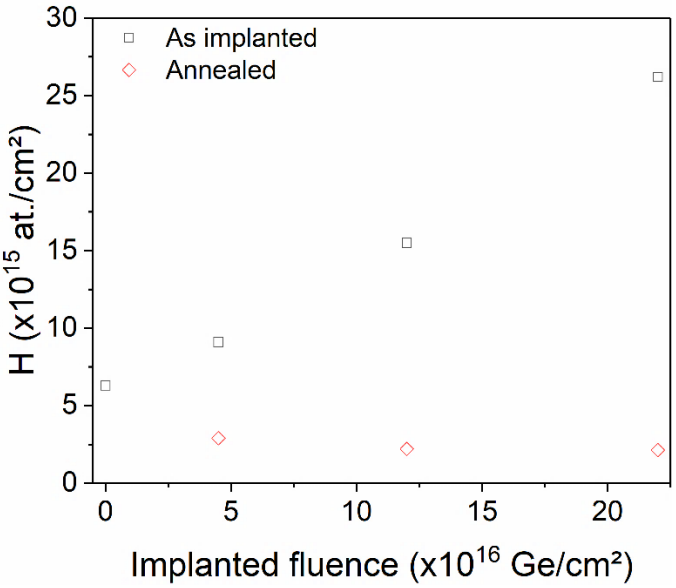

Figure 69 : Elastic Recoil Detection Analysis (ERDA) of H content before and after annealing for wet SiO_2 films implanted with Ge ions at 230 keV for different fluences.

The difficulty of collecting charge carriers generated in Ge quantum dots embedded in SiO_2 films has been discussed in chapters **II**, **IV** and **V**. This led to Ge implantations in semiconducting substrates, with the idea of enhancing the collection of the photogenerated charges. The preliminary results obtained for Ge implantations in silicon confirmed the hard challenge of forming Ge nanocrystals in a silicon matrix. This was expected at the light of the results obtained for Si co-implantations in SiO_2. Due to the miscibility of germanium in silicon, we principally observed the formation of a $Si_{1-x}Ge_x$ alloy rather than Ge nanocrystals embedded in a Si matrix. It has been shown that this epilayer was monocrystalline, as Ge atoms are incorporated in the silicon matrix in substitutional sites, and fully relaxed. Therefore, these $Si_{1-x}Ge_x$ top layers could be used as “virtual substrates” for the growth of strained Si layers.

However, concerning the formation of Ge-ncs in silicon, the last samples indicate that a glimmer of hope could be brought by the implantation under high temperature. A damper must be pointed out for photovoltaic applications, as a high density of dislocations are generated at the film/substrate interface. These extended defects could limit the implementation of Ge-ncs in silicon in PV cells as they are known to be particular sites for electrons/holes recombination.

Implantation of heated samples must be explored further, notably at higher temperatures. As shown in samples implanted at ambient temperature, increasing the

temperature of the post-implantation annealing could help to improve the crystallinity of the films.

Chapter VII

Bibliography

1. ***Detailed balance limit of efficiency of p-n junction solar cells.*** **Shockley, William and Queisser, Hans J. 3, s.l. : J. of appl. phys., 1961, Vol. 32.**

2. ***A review on solar cells from Si-single crystals to porous materials and quantum dots.*** **Badawy, W.A. 2015, J. Adv. Res., Vol. 6. , 2.**

3. http://www.ourworldindata.org. [Online]

4. IEA. ***"Renewables 2019".*** **Paris : s.n., 2019.**

5. Demarche, Julien. ***Synthèse et caractérisation fondamentale de nanocristaux de silicium et germanium synthétisés par implantation ionique pour le développement de capteurs hotovoltaïques à haut rendement.*** **s.l. : Presses universitaires de Namur, 2012.**

6. Michaelides, Efstathios E. ***Alternative energy sources.*** **s.l. : Springer, 2012.**

7. Jäger, Klaus, et al. ***Solar energy : fundamentals, technology and systems.*** **s.l. : Delft university of technology, 2014.**

8. Shi, Donglu, Guo, Zizheng and Bedford, Nicholas. ***Nanomaterials and devices - chapter 4 : Semiconductors quantum dots.*** **s.l. : William Andrew, 2015. pp. 83-104.**

9. Mishra, U. and Singh, J. ***Semiconductor device physics and design.*** **Dordrecht : Springer, 2008.**

10. ***Silicon photonics based on monolithic integration of II-V nanostructures on silicon.*** **Nguyen Thanh, T. 2013.**

11. Kitai, A. ***Principles of solar cells, LEDs and Diodes.*** **s.l. : Wiley, 2011.**

12. Kissiner, Gudrun and Pizzini, Sergio. ***Silicon, germanium and their alloys.*** **s.l. : CRC Press - Taylor | Francis Group, 2015.**

13. ***Die konstitution der mischkristalle und die raumfüllung der atome.*** **Vegard, L. 1921, Z. Phys., Vol. 5. , 17-26.**

14. ***Lattice parameter and density in germanium-silicon alloys.*** **Dismukes, J.P., Ekstrom, L. and Paff, R.J. 1964, J. Phys. Chem., Vol. 68.**

15. Ayers, J.E. ***Heteroepitaxy of semiconductors : theory, growth and characterization.*** **Boca Raton : CRC Press, Taylor & Francis Group, 2007.**

16. ***Defects in Epitaxial multilayers : misfit dislocations.*** **Matthews, J.W. and Blakeslee, A.E. 1974, J. Cryst. Grow., Vol. 27. , 118.**

17. ***Calculation of critical layer thickness versus lattice mismatch for Ge_xSi_{1-x}/Si strained-layer heterostructures.*** **People, R. and Bean, J.C. 1985, Appl. Phys. Lett., Vol. 47. , 322.**

18. Mastari, M. ***Growth and characrterization of SiGe alloys on nanometer-size structures for microelectronics applications.*** **2020.**

19. Haddara, Y.M., Ashburn, P. and Bagnall, D.M. ***Silicon-germanium : properties, growth and applications. In: Kasap S., Capper P. (Eds) Springer Handbook of Electronic and Photonic Materials. Springer Handbooks. Springer, Cham. https://doi.org/10.1007/978-3-319-48933-9_22.*** **2017.**

20. ***Solar photovoltaics R&D at the tipping point : a 2005 technology overview.*** **Kazmerski, Lawrence L. s.l. : J. electron spectrosc. , 2006, Vol. 150.**

21. ***Optical quantum confinement ans photocatalytic properties in two-, one- and zero-dimensional nanostructures.*** **Edvinsson, T. s.l. : R. Soc. open sci., 2018, Vol. 5.**

22. ***Quantum confinement in Si and Ge nanostructures.*** **Barbagiovanni, E. G., et al. s.l. : J. Appl. phys., 2012, Vol. 111.**

23. ***Multiple exciton generation in semiconductor quantum dots.*** **Beard, Matthew C. s.l. : J. Phys. Chem. Lett., 2011, Vol. 2.**

24. ***Photoluminescence of silicon nanoclusters with reduced size dispersion produced by laser ablation.*** **Patrone, L., et al. s.l. : J. Appl. Phys., 2000, Vol. 87.**

25. ***Quantum confinement in Si and Ge nanostructures : theory and experiment.*** **Barbagiovanni, Eric G., et al. s.l. : Appl. Phys. Rev., 2014, Vol. 1.**

26. ***Silicon quantum dot nanostructures for tandem photovoltaic cells.*** **Conibeer, Gavin, et al. s.l. : Thin Solid Films, 2008, Vol. 516.**

27. ***Multiple exciton generation in semiconductor quantum dots.*** **Nozik, A.J. 2008, Chem. Phys. Lett., Vol. 457. , 1-3.**

28. ***Mechanisms for photogenration and recombinaition of multiexcitons in semiconductor nanocrystals: implications for lasing and solar energy conversion.*** **Klimov, Victor I. s.l. : J. Phys. Chem., 2006, Vol. 110.**

29. ***Multiple exciton generation in colloidal nanocrystals.*** **Smith, Charles and Binks, David. s.l. : Nanomaterials, 2014, Vol. 4.**

30. ***Carrier multiplication in bulk and nanocrystalline semiconductors : mechanism, efficiency and interest for solar cells.*** **Delerue, Christophe, et al. s.l. : Phys. Rev. B, 2010, Vol. 81.**

31. ***Carrier multiplication yields of CdSe and CdTe nanocrystals by transient photoluminescence spectroscopy.*** **Nair, Gautham and Bawendi, Moungi G. s.l. : Phys. Rev. B, 2007, Vol. 76.**

32. ***Role of impact ionization in multiple exciton generation in PbSe nanocrystals.*** **Allan, G. and Delerue, C. s.l. : Phys. rev. B, 2006, Vol. 73.**

33. ***High-efficiency carrier multiplication through direct photogeneration of multi-excitons via virtual single-exciton states.*** **Schaller, Richard D., Agranovich, Vladimir M. and Klimov, Victor I. s.l. : Nature Physics, 2005, Vol. 1.**

34. ***Highly efficient multiple exciton generation in colloidal PbSe and PbS quantum dots.*** **Ellington, Randy J., et al. 5, s.l. : Nano Lett., 2005, Vol. 5.**

35. ***Multiexciton generation by a single photon in nanocrystals.*** **Shabaev, A., Efros, Al. and Nozik, A. 12, s.l. : Nano. Lett., 2006, Vol. 6.**

36. ***Direct generation of multiple excitons in adjacentsilicon nanocrystals revealed by induced absorption.*** **Trinh, Tuan M., et al. s.l. : Nat. Photonics, 2012, Vol. 6.**

37. ***Silicon nanostructures for third generation photovoltaic solar cells.*** **Conibeer, G., et al. s.l. : Thin Solid Films, 2006, Vols. 511-512.**

38. Boer, K. ***Survey of semiconductors physics.*** **s.l. : Springer, 1990.**

39. ***One step towards the fabrication of a nanscale Si-nc based laser cavity.*** **Koshel, D., et al. s.l. : J. Lumin., 2011, Vol. 131.**

40. ***Ionoluminescence induced by low-energy proton excitation of Si nanocrystals embedded in silica.*** **Demarche, J., et al. s.l. : Nucl. Instrum. Methods Phys. Res. B, 2012, Vol. 272.**

41. ***Silicon quantum wire array fabrication by electrochemical and chemical dissolution of wafers.*** **Canham, L. T. s.l. : Appl. Phys. Lett. , 1990, Vol. 57.**

42. ***Porous silicon formation : a quantum wire effect.*** **Lehmann, V. and Gösele, U. s.l. : Appl. Phys. Lett., 1991, Vol. 58.**

43. ***Quantum confinement in germanium nanocrystals.*** **Niquet, Y.M., et al. 2000, Appl. Phys. Lett., Vol. 77. , 8.**

44. ***Exciton states and photoluminescence in Ge quantum dots.*** **Kaganovich, E.B., et al. 2007, Nanotechnology, Vol. 18. , 295401.**

45. ***Luminescence characteristics of Ge nanocrystals embedded in SiO_2 matrix.*** **Ray, S.K. and Das, K. 2005, Opt. Mater., Vol. 27. , 948.**

46. ***Visible photoluminescence from nanocrystallite Ge embedded in a glassy SiO_2 matrix : Evidence in support of the quantum confinement mechanism.*** **Maeda, Y. 1995, Phys. rev. B, Vol. 51.**

47. ***Characterization of size-controlled and red luminescent Ge nanocrystals in multilayered superlattive structure.*** **Zhang, B., et al. 2010, Thin Solid Films, Vol. 518. , 5483.**

48. ***Size-dependent near-infrared photoluminescence from Ge nanocrystals embedded in SIO_2 matrices.*** **Takeoka, S., et al. 1998, Phys. Rev. B, Vol. 58. , 12.**

49. ***A review on Ge nanocrystals embedded in SIO_2 and high-k dielectrics.*** **Lehninger, D., Beyer, J. and Heitmann, J. 2018, Phys. Status Solidi A. , 1701028.**

50. ***Quantum size effects in germanium nanocrystals and amorphous nanoclusters in $GeSi_xO_y$ films.*** **Gambaryan, M.P., et al. 2020, Phys. Solid State, Vol. 62. , 3.**

51. ***The origin of photoluminescence in Ge-implanted SiO_2 layers.*** **Kim, H.B., et al. 1999, J. Lumin., Vol. 80. , 281.**

52. ***On the origin of visible photoluminescence in nanometer-size Ge crystallites.*** **Kanemitsu, Y., et al. 1992, Appl. Phys. Lett., Vol. 61. , 18.**

53. ***Visible photoluminescence from Ge nanocrystal embedded into a SiO_2 matrix fabricated by atmospheric pressure chemical vapor deposition.*** **Dutta, A.K. 1996, Vol. 68. , 9.**

54. ***Role of surface defect states in visible luminescence from oxidized hydrogenated amorphous Si/hydrogenated amorphous Ge multilayersz.*** **Xu, J., et al. 1999, Appl. Phys. Lett., Vol. 74. , 25.**

55. ***Improving solar cell efficiencies by down-conversion of high-energy photons.*** **Trupke, T., Green, M. A. and Würfel, P. s.l. : J. Appl. Phys., 2002, Vol. 92.**

56. ***Modeling improvement of spectral response of solar cells by deployment of spectral converters containing semiconductor nanocrystals.*** **van Sark, W., et al. 8, s.l. : Semiconductors, 2004, Vol. 38.**

57. ***Silicon nanocrystals as a photoluminescence down shifter for solar cells.*** **yuan, Zhizhong, et al. s.l. : sol. Energy Mater. Sol. Cells, 2011, Vol. 95.**

58. ***Method for fabricating third generation photovoltaic cells based on Si quantum dots using ion implantation into SiO2.*** **Yedji, M., et al. s.l. : J. Appl. Phys., 2011, Vol. 109.**

59. ***Embedded Ge nanocrystals in SiO_2 synthesized by ion implantation.*** **Baranwal, V., et al. s.l. : J. Appl. Phys., 2015, Vol. 118.**

60. ***Nanocavities and germanium nanocrystals produced by Ge ion implantation in fused silica.*** **Barba, D., et al. 2012, Nanotechnology, Vol. 23.**

61. ***Microstructural investigation of ion beam synthesised germanium nanoclusters embedded in SiO_2 layers.*** **Markvitz, A., et al. s.l. : Nucl. instr. Meth. B, 1998, Vol. 142.**

62. ***silicon nanocrystal synthesis by implantation of natural Si isotopes.*** **Barba, D., et al. 2010, J. Lumin., Vol. 130.**

63. ***Method for fabricating third generation photovoltaic cells based on Si quantum dots using ion implantation into SiO_2.*** **Yedji, M., et al. 2011, J. Appl. phys., Vol. 109.**

64. ***Size-controlled highly luminescent silicon nanocrystals : a SiO/SiO_2 superlattice approach.*** **Zacharias, M., et al. 4, s.l. : Appl. Phys. Lett., 2002, Vol. 80.**

65. ***Correlation between luminescence and structural properties of Si nanocrystals.*** **Icona, F., Franzo, G. and Spinella, C. 2000, J. Appl. phys., Vol. 87. , 1295.**

66. ***Annealing characteristics of Si-rich SiO_2 films.*** **Nesbit, L.A. 1985, Appl. Phys. Lett., Vol. 46. , 38.**

67. ***Si quantum dot formation with low-pressure chemical vapor deposition.*** **Nakajima, Anri, et al. s.l. : Jpn J. appl. Phys., 1996, Vol. 35.**

68. ***Effect of nucleation parameters of Ge quantum dots grown over silicon oxide by LPCVD.*** **Mestanza, S.N.M., Doi, I. and Frateschi, N.C. 2007, J. Integr. Circ. Syst., Vol. 2. , 2.**

69. ***Sperical SiGe quantum dots prepared by thermal evaporation.*** **Liao, Yu-Cheng, et al. s.l. : Appl. Phys. Lett. , 2000, Vol. 77.**

70. ***Evolution with annealing treatments of the size of silicon nanocrystallites embedded in a SiN_x matrix and correlation with opticla properties.*** **Molinari, M., et al. 2003, Mater. Sci. Eng. B, Vol. 101. , 186.**

71. ***Evidence of light-emitting amorphous silicon clusters confined in a silicon oxide matrix.*** **Rinnert, H. and Vergnat, M. 2001, J. Appl. Phys., Vol. 89. , 237.**

72. ***Super-high density Si quantum dot thin film utilizing a gradient Si-rich oxide multilayer structure.*** **Kuo, Kuang-Yang, Huang, Pin-Ruei and Lee, Po-Tsung. s.l. : Nanotechnology, 2013, Vol. 24.**

73. ***Photoluminescence spectra of clusters of group IV elements embedded in SiO_2 matrices.*** **Hayashi, S., et al. 1993, Z. Phys. D, Vol. 26. , 144.**

74. ***Evolution of Si suboxides into Si nanocrystals during rapid thermal annealing as revealed by XPS and Raman studies.*** **Zhang, W., et al. 2009, J. Cryst. Growth, Vol. 311. , 1296.**

75. ***Temperature dependence of photoluminescence from mono-dispersed Si nanocrystals.*** **Orii, T., et al. 2003, Eur. Phys. J. D, Vol. 24. , 119.**

76. ***Nucleation and growth of Si nanocrystals in an amorphous SiO_2 matrix.*** **Riabinina, D., et al. 2006, Phys. Rev. B, Vol. 74. , 075334.**

77. ***Molecular beam epitaxy of silicon-germanium nanostructures.*** **Pchemyakov, O.P., et al. 2000, Thin Solid Films, Vol. 367. , 75.**

78. ***Formation of single-cystalline silicon nanostructures by self-assembling growth with molecular beam epitaxy.*** **Baumgartner, H., et al. 1998, Appl. Surf. Sci., Vol. 130. , 747.**

79. ***Ge nanocrystals in magnetron sputtered SiO_2.*** **Skov Jensen, J., et al. 2006, Appl. Phys. A, Vol. 83. , 41.**

80. Pucker, Georg, Serra, Enrico and Jestin, Yoann. ***Silicon quantum dots for photovoltaics : a review.*** **s.l. : IntechOpen, 2012.**

81. ***Effect of Ge concentration on the microstructure of germanium nanocrystals produced by ion implantation in SiO_2.*** **Ge, L.H., et al. 2016, J. Nanosci. Nanotechnol., Vol. 16.**

82. ***Inhibitive formation of nanocavities by introduction of Si atoms in Ge nanocrystals produced by ion implantation.*** **Cai, R.S., et al. 2014, J. Appl. phys., Vol. 115.**

83. ***Ostwald ripening of Ge precipitates elaborated by ion implantation in SiO_2.*** **Bonafos, C., et al. 2000, Mater. Sci. Eng. B, Vols. 69-70. , 380.**

84. ***Effect of nanocavities on Ge nanoclustering and outdiffusion in SiO_2.*** **Li, C., et al. s.l. : Nanotechnology, 2017, Vol. 28.**

85. ***Evolution of microstructural defects with strain effects in germanium nanocrystals synthesized at different annealing temperatures.*** **Zhang, M., et al. 2014, Mater. Charact., Vol. 93.**

86. ***Matrix role in Ge nanoclusters embedded in Si_3N_4 or SiO_2.*** **Mirabella, S., et al. 2012, Appl. phys. Lett., Vol. 101. , 011911.**

87. ***SRIM - the stopping and range of ions in matter.*** **Ziegler, J. F., Ziegler, M. D. and Biersack, J. P. s.l. : Nucl. Instrum. Methods Phys. Res. B, 2010, Vol. 268.**

88. SUSPRE. [Online] [Cited: 11 Févirer 2021.] https://www.surrey.ac.uk/ion-beam-centre/research/interactions-energetic-particles.

89. Axcelis. [Online] https://www.axcelis.com/.

90. [Online] [Cited: 30 June 2021.] https://www.dow.com/en-us/pdp.syltherm-800-stabilized-heat-transfer-fluid.39260z.html.

91. Tilley, Richard J.D. ***Defects in solids.*** **s.l. : Wiley, 2008.**

92. Baudrant. ***Implantation ionique et traitements thermiques en technologie du silicirm.*** **s.l. : Lavoisier, 2011.**

93. ***Norgett, M.J., Robinson, M.T. and Torrens, I.M. 1975, Nucl. Eng. Design, Vol. 33, pp. 50-54.***

94. Kinetics of solid phase crystallization in amorphous silicon. Olson, G.L. and Roth, JA. 1988, Materials Science Reports, Vol. 3. , 1.

95. Kuech, T.F. Handbook of crystal growth. Thin films and epitaxy: basic techniques. 2nd edition. Boston : Elsevier North-Holland, 2015. Vols. III, part A.

96. Salh, R. Defect related luminescence in silicon dioxide network : a review. Crystalline silicon - properties and uses. 2011.

97. General relationship for the thermal oxidation of silicon. Deal, B.E. and Grove, A.S. 1965, J. Appl. phys., Vol. 36.

98. http://www.tf.uni-kiel.de/matwis/amat/elmat_en/kap_6/backbone/r6_2_1.html. [Online]

99. Wolf, H.F. Silicon semiconductor data. New York : Pergamon Press, 1969.

100. Review of oxide formation in a plasma. Gourrier, S. and Bacal, M. 1981, Plasma Chem. Plasma Process., Vol. 1.

101. Anodic oxide films, in "Physics of thin films" by H.A. Francombe, R.W. Hoffmann, col.6, Academic Press, New York, 1971. Dell'Oca, C.J., Pulvrey, D.L. and Young, L.

102. Nastasi, Y. Wang and M. Handbook of modern ion beam materials analysis. s.l. : Materials Research Society, 2009.

103. Rutherford Backscattering Spectroscopy (RBS). Mayer, M. 2003. Lectures given at the Workshop on Nuclear Data for Science and Technology : Materials Analysis.

104. SIMNRA, a simulation program for the analysis of NRA, RBS and ERDA. Mayer, M. 1999, AIP Conf. Proc.

105. Characterization of carbon nitride compounds synthesized by simultaneous implantation of carbon and nitrogen in copper. Colaux, J.L. 2009, Doctoral dissertation, University of Namur.

106. Feldman, Léonard C., Mayer, James W. and Picraux, Thomas S. Materials analysis by ion channeling. s.l. : Academic press, 1982.

107. Morgan, D.V. Channeling : theory, observation and applications. s.l. : John Wiley & Sons, 1973.

108. Channeling effect measurements of the recrystallization of amorphous Si layers on crystal Si. Csepregi, L., Mayer, J.W. and Sigmon, T.W. 1975, Phys. Lett., Vol. 54A. , 2.

109. Strain in AlGaN layer studied by Rutherford backscattering/channeling and x-ray diffraction. Wu, M.F., et al. 1999, J. Vac. Sci. Technol. B, Vol. 17. , 1502.

110. Ge_xSi_{1-x} strained-layer superlattice grown by molecular beam epitaxy. Bean, J.C., et al. 1984, J. Vac. Technol. A, Vol. 2.

111. Crystallinity, strain, and thermal stability of heteroepitaxial $Si_{1-x}Ge_x$/Si (100) layers created using pulsed laser induced epitaxy. Kramer, K.-J., et al. 1992, Appl. Phys. Lett., Vol. 61. , 7.

112. Narrow nuclear resonance position or cross section shape measurements with a high precision computer controlled beam energy scanning system. Amsel, G. , et al. 1998, Nucl. Instrum. and Meth. B, Vols. 136-138, p. 545.

113. Larkin, P. Infrared and Raman spectroscopy : principles and spectral interpretation. San Diego : Elsevier, 2011. 2011008524.

114. [Online] [Cited: 17 02 2021.] https://www.edinst.com/blog/what-is-raman-spectroscopy/.

115. X-ray diffraction cristallography. Waseda, Yoshio, Matsubara, Eiichiro and Shinoda, Kozo. s.l. : Springer, 2011.

116. XPS simplified. [Online] [Cited: 29 03 2021.] https://xpssimplified.com/elements/germanium.php.

117. Electron microscopy. [Online] [Cited: 29 03 2021.] https://mmegias.webs.uvigo.es/02-english/6-tecnicas/6-electronico.php.

118. [Online] 19 05 2021. https://www.eag.com/techniques/.

119. Diffusion of germanium in silica glass. Minke, M.V. and Jackson, K.A. s.l. : J. Non-Cryst. Solids, 2005, Vol. 351.

120. Control of the Ge nanocrystal synthesis by co-implantation of Si^+. Barba, D., et al. 2013, J. Appl. phys., Vol. 114.

121. Influence of silicon dangling bonds on germanium thermal diffusion within SiO_2 glass. Barba, D., et al. s.l. : Appl. Phys. Lett., 2014, Vol. 104.

122. Elemental redistribution and Ge loss during ion-beam synthesis of Ge nanocrystals in SiO_2 films. Beyer, V. and von Borany, J. s.l. : Phys. Rev. B, 2008, Vol. 77.

123. Precipitation, ripening and chemical effects during annealing of Ge^+ implanted SiO_2 layers. Heinig, K.H., et al. s.l. : Nucl. Instrum. Methods Phys. Res. B, 1999, Vol. 148.

124. Multimodal impurity redistribution and nanocluster formation in Ge implanted silicon dioxide films. von Borany, J., et al. s.l. : Appl. Phys. Lett., 1997, Vol. 71.

125. XPS investigation with factor analysis for the study of Ge clustering in SiO_2. Oswald, S., Schmidt, B. and Heinig, K.H. s.l. : Surf. Interface Anal., 2000, Vol. 29.

126. trapping of diffusion germanium by silicon excess co-implanted into fused silica. Barba, D., et al. 2012, Appl. Phys. lett., Vol. 101.

127. Modeling of Ge nanocluster evolution in ion-implanted SiO_2 layer. Borodin, V.A., Heinig, K.-H. and Schmidt, B. 1999, Nucl. Instr. and Meth. in Phys. Res. B, Vol. 147. , 286.

128. Measurements of alloy composition and strain in thin Ge_xSi_{1-x} layers. Tsang, J.C., et al. 1994, J. Appl. Phys., Vol. 75. , 8098.

129. Raman scattering in GeSi alloys. Brya, W.J. 1973, Solid State Commun., Vol. 12. , 253.

130. Raman spectra of c-$Si_{1-x}Ge_x$ alloys. Alonso, M.I. and Winer, K. 1989, Phys. Rev. B, Vol. 39. , 10056.

131. Raman spectroscopy determination of composition and strain in $Si_{1-x}Ge_x$/Si heterostructures. Pezzoli, F., et al. 2008, Mater. Sci. Semicond. Process., Vol. 11. , 279.

132. Strain-induced shift of phonon modes in $Si_{1-x}Ge_x$ alloys. Pezzoli, F., et al. 2006, Mater. Sci. Semicond. Process., Vol. 9. , 541.

133. Strain in coherent-wave SiGe/Si superlattices. Shin, H.K., Lockwood, D.J. and Baribeau, J.-M. 2000, Solid State Commun., Vol. 114. , 505.

134. Composition and strain in thin $Si_{1-x}Ge_x$ virtual substrates measured by micro-Raman spectroscopy and x-ray diffraction. Perova, T.S., et al. 2011, J. Appl. Phys., Vol. 109. , 033502.

135. Strained-layer epitaxy of germanium-silicon alloys. Bean, J.C. s.l. : Science, 1985, Vol. 230.

136. NIH Image to ImageJ : 25 years of image analysis. Schneider, C.A., Rasband, W.S. and Eliceiri, K.W. 2012, Nature mathods, Vol. 9. , 7, PMID 22930834, version 1.4.

137. Díez, Víctor Alarcón. Development of charged particle detection systems for materials analysis with rapid ion beams : large solid angle detectors and numerical nuclear pulse processing. s.l. : Université Pierre et Marie Curie - Paris VI, 2016.

138. Ferraro, John R. , Nakamuto, Kazuo and Brown, Chris W. Introductory raman spectrocopy. 2003 : Elsevier.

139. Raman imaging from microscopy to macroscopy : quality and safety control of biological materials. Lohumi, Santosh, et al. s.l. : Trend. Anal. Chem, 2017, Vol. 93. 183-198.

140. https://www.nrel.gov/pv/cell-efficiency.html. NREL. [Online]

141. Overview of stabilizing ligands for biocompatible quantum dot nanocrystals. Zhang, Yanjie and Clapp, Aaron. s.l. : Sensors, 2011, Vol. 11.

142. Mehrer, Helmut. Diffusion in solids. s.l. : springer, 2007.

143. Uematsu, M. Silicon-germanium (SiGe) nanostructures - chapitre 12 : Self-diffusion and dopant diffusion in germanium (Ge) and silicon-germanium (SiGe) alloys. s.l. : Woodhead publishing, 2011.

144. Energy conversion approaches and materials for high-efficiency photovoltaics. Green, M.A. and Bremmer, S.P. 2017, Nat. Mater., Vol. 16.

145. Dielectric engineering of Ge nanocrystal/SiO_2 nanocomposite thin films with Ge ion implantation : Modling and measurement. Liu, Z., et al. 2015, Mater. Des., Vol. 83.

146. Zschintzsh, M.Z., et al. 2011, Nanotechnology, Vol. 22.

147. Nanoparticle stacks with graded refractive indices enhance the omnidirectional light harvesting of solar cells and the light extraction of light-emitting diodes. Fang, C.Y., et al. 2013, Adv. Funct. Mater., Vol. 23.

148. Ordered coalescence of Si nanocrystals in SiO_2. Wang, Y.Q., et al. 2005, Phys. Rev. B, Vol. 71.

149. Growth of Ge, Si, and SiGe nanocrystals in SiO_2 matrices. Zhu, J.G., et al. 1995, J. Appl. Phys., Vol. 78.

150. Mechanisms of void formation in Ge implanted SiO_2 films. Marstein, E.S., et al. 2003, Nucl. Instrum. Methods Phys. Res. B, Vol. 207.

151. Comparative study of the luminescence of structures with Ge nanocrystals formed by dry and wet oxidation of siGe films. Rodriguez, A., et al. 207, Nanotechnology, Vol. 18.

152. Re-examination of the SiGe Raman spectra : Percolation/one-dimensional-cluster scheme and ab initio calculations. Pages, O., et al. 2012, Phys. Rev. B, Vol. 86.

153. Effects of alloy disorder and confinement on phonon modes and Raman scattering in Si_xGe_{1-x} nanocrystals : A microscopic modeling. Vasin, A.S., Vikhrova, O.V. and Vasilevskiy, M.I. 2014, J. Appl. Pjys., Vol. 115.

154. Evidence of localized amorphous silicon clustering from Raman depth-probing of silicon nanocrystals in fused silica. Barba, D., Martin, F. and Ross, G.G. 2008, Nanotechnology, Vol. 19.

155. The effect of Ge implantation dose on the optical properties of Ge nanocrystals. Mestanza, S.N.M., Rodriguez, E. and Frateschi, N.C. 2006, Nanotechnology, Vol. 17.

156. Modified Raman confinement model for Si nanocrystals. Faraci, G., et al. 2006, Phys. Rev. B, Vol. 73.

157. Isotopic effect in the phonon and electron dispersion relations of crystals. Cardona, M. 2000, Phys. Status Solidi B, Vol. 220.

158. Crystallization of amorphous $Si_{0.6}Ge_{0.4}$ nanoparticles embedded in SiO_2 : Crystallinity versus compositional stability. Rodriguez, A., et al. 2010, J. electron. Mater., Vol. 39.

159. Influence of GeSi interfacial layer on Ge-Ge optical phonon mode in SiO_2 films embedded with Ge nanocrystals. Liu, L.Z., et al. 2009, Appl. phys. Lett., Vol. 95.

160. Mechanism of stress relaxation in Ge nanocrystals embedded in SiO_2. Sharp, I.D., et al. 2005, Appl. Phys. Lett., Vol. 86.

161. Lide, D.R. CRC Handbook of physics and chemistry. 85th ed. Boca Raton : Press, CRC, 2005.

162. Nélis, A., Haye, E. and Terwagne, G. 2021, (under submission).

163. Vickridge, I. and Amsel, G. 1990, Nucl. Instr. and Meth. B 45, 6-11.

164. Lide, David R. CRC Handbook of Chemistry and Physics, internet version 2005. Boca Raton, FL : CRC Press, 2005.

165. Oh, J. and Campbell, J.C. 2004, J. Electron. Mater., Vol. 33. , 4.

166. Takeoka, S., et al. 2000, Phys. Rev. B, Vol. 61. , 23.

167. Choi, W.K., et al. 2001, Mater. Sci. Eng. C, Vol. 16.

168. Multiple exciton generation in colloidal silicon nanocrystals. Beard, M.C., et al. 2007, Nano Lett., Vol. 7. , 2506.

169. Control of germanium diffusion using low quantities of co-implanted silicon isotopes. Nélis, A., Barba, D. and Terwagne, G. 2020, J. Appl. Phys, Vol. 128. , 125705.

170. Modeling of Si self-diffusion in SiO_2 : effect of the Si/SiO_2 interface including time-dependent diffusivity. Uematsu, M. et al. 2004, Appl. Phys. Lett. 84, 876-878.

171. Germanium diffusion and nanocrystals formation in silicon oxide on silicon substrate under rapid thermal annealing. Choi, W. K. et al. 2005, Appl. Phys. Lett. 86, 143114.

172. Microanalysis of the stable isotopes of oxygen by means of nuclear reactions. Amsel, G. and Samuel, D. 1967, Anal. Chem. 39, 1689-1698.

173. An ^{18}O study of the interaction between carbon monoxide and dry thermal SiO_2 at 1100°C. Deville Cavellin, C. et al. 2009, J. appl. Phys. 105, 033501.

174. Use of ^{18}O isotopic labelling to study thermal dry oxidation of silicon as a function of temperature and pressure. Trimaille, I. and Rigo, S. 1989, Appl. Surf. Sci. 39, 65-80.

175. A very narrow resonance in $^{18}O(p,alpha)^{15}N$ near 150 keV : application to isotopic tracing. Battistig, G. et al. 1991, Nucl. Instr. and Meth. B 61, 369-376.

176. Diffusion of near surface defects during the thermal oxidation of silicon. Ganem, J.-J., et al. 1997, J. Appl. Phys., Vol. 81. , 12.

177. Formation of Ge^0 and GeO_x nanoclusters in Ge^+-implanted SiO_2/Si thin-film heterostructures under rapid thermal annealing. Zatsepin, A.F., et al. 2015, Appl. Surf. Sci., Vol. 349. , 780.

178. Kinetics of structural and phase transformations in thin SiO_x films in the course of a rapid thermal annealing. Dan'ko, V.A., et al. 2005, Semiconductors, Vol. 39. , 10.

179. Distinctly different thermal decomposition pathways of ultrathin oxide layer on Ge and Si surfaces. Prabhakaran, K., et al. 2000, Appl. Phys. Lett., Vol. 76. , 2244.

180. Outdiffusion and subsequent desorption of volatile SiO molecules during annealing of thick SiO_2 films in vacuum. Takakuwa, Y., Nihei, M. and Miyamoto, N. 1993, Jpn J. Appl. Phys., Vol. 32.

181. Permeation of gaseous oxygen through vitreous silica. Norton, J. F. 1961, Nature (London) 191, 701.

182. Elemental thin film depth profiles by ion beam analysis using simulated annealing - a new tool. Jeynes, C., et al. 2003, J. Phys. D Appl. Phys. 36.

183. Quantum dots for electro-optic devices. Nann, T. and Skinner, W.M. 2011, ACS Nano, Vol. 5. , 5291.

184. Fast and long retention-time nano-crystal memory. Hanafi, H.I., Tiwari, S. and Khan, I. 1996, IEEE Trans. Electron Devices, Vol. 43. , 1553.

185. Characterization of implantation induced defects in Si-implanted SiO_2 films. Hao, X., et al. 2008, Nanosci. Nanotechno., Vol. 8. , 1350.

186. X-ray photoelectron spectroscopy : towards reliable binding energy referencing. Greczynski, G. and Hultman, L. 2020, Prog. Mater Sci., Vol. 107. , 100591.

187. Using ammonia for reactive magnetron sputtering, a possible alternative to HiPIMS? Rassinfosse, L., et al. 2020, Appl. Surf. Sci., Vol. 502. , 144176.

188. Direct formation of large-scale multi-layered germanene on Si substrate. Tsai, et al. 2015, Phys. Chem. Chem. Phys., Vol. 17. , 33.

189. Silicon (100)/SiO_2 by XPS. Jensen, D.S., et al. 2013, Surf. Sci. Spectra, Vol. 20. , 36.

190. Damage center formation in SiO_2 thin films by fast electron irradiation. Pfeffer, R.L. 1985, J. Appl. Phys., Vol. 57. , 5176.

191. Direct characterization of nanocrystal size distribution using Raman spectroscopy. Dogan, I. and van de Sanden, M.C.M. 2013, J. appl. Phys., Vol. 114. , 134310.

192. Knoll, G.F. Radiation detection and measurement, 3rd edition. s.l. : John Wiley & Sons, 2000.

193. Nélis, A., Barba, D. and Terwagne, G. s.l. : J. Appl. Phys., Vol. 128.

194. Influence of oxygen co-implantation on germanium out-diffusion and nanoclustering in SiO_2/Si films. Nélis, A., Haye, E. and Terwagne, G. 2021, J. Appl. Phys., Vol. 130, 105701.